Near-Fields in Attenuating Media



Son C. Chu

Harris Manchester College

University of Oxford

A thesis submitted for the degree of

Doctor of Philosophy

Michaelmas 2019

For my little boys, Harris and Harvey

Acknowledgements

A DPhil/PhD journey always begins with receiving an offer letter from the university and ends with submitting a complete thesis to the university. My start point is somewhat mysterious to me even to this day. But "it does not matter how you begin - what matters is how you end". I took this opportunity to produce something useful and make sure that my supervisors would not regret accepting me as their DPhil student. Doing DPhil means pushing the boundary of existing knowledge. It is rare that pushing that boundary can be accomplished without the help of others, and it is fortunate that a DPhil student can find support along their way whenever needed. I have been a lucky one.

First and foremost, every thank belongs to The Buddha - the most Beneficent, the most Compassionate and Benevolent for his peace and blessing. I will forever be grateful to all my spiritual masters, both external and internal.

I would like to express my sincere gratitude to my supervisors Prof Chris Stevens and Prof Ekaterina Shamonina who without their inspiration, vision, guidance, and encouragement this research would not have been started nor completed. I owe a deep sense of thankfulness to Emeritus Prof Laszlo Solymar for his suggestions and fruitful discussions with him, which helped shape my intuition in electromagnetism. Thanks also are due to Dr Andrea Vallecchi who guided me through the most difficult time - my first two years - and taught me how to work in an academically competitive environment. I am especially indebted to two "random" champs on the internet, Mark Luloff and Md Nazmul Hasan, whom I made contact when I read his master thesis and watched his Youtube tutorials, respectively. I am deeply touched and honoured by their willingness to share any knowledge and research experiences that they may have with me. Moreover, I am very grateful to my fellow lab-mates and colleagues, especially Angelina Yan, Kailun Xu, Paramin Sangwongngam, Vincent Lee, and Grahame Faulkner for their creative advice, helpful comments, and encouragement during my DPhil. I would also like to thank all university and Harris Manchester College staff for their support and willingness to share any and all information requested.

My acknowledgement would be incomplete without thanking the biggest source of my strength, my family. I have been blessed with a very loving and supportive family. I would like to give thanks to my wonderful parents Chu Cong Can and

Nguyen Thu Ha for funding my course and loving me unconditionally. Moreover, I also wish to express my appreciation to my beloved wife Bin Tran, my two little boys Harris and Harvey, and other family's member, especially Linh "Que" Chu, Trang "Do" Pham, and Huyen "Trui" Nguyen, for their unwavering and unselfish love and support given to me at all times.

Last but not least, some special words of gratitude go to my friends who have always been with me at my best, and at my worst. BFF: Linh "Ti" and Tai Minh; Sheffield Hallam classmates: Milan Stefko and Bach "Prince" Tran; London Flat 9: Jethro "Uncle" Lee and Tung "Spaeman" Le; Hoi ba con chim: Son be and Minh be; VOX anh Phi Anh "The Dealer" Phan, Tuan Anh Le, Minh Cong Tran, Khanh Vu Do, Quang Anh Tran, Hoang "The Bank" Vu, anh Viet "James" Do, Hien Phan, Chau "The Wall" Nguyen, Hoan "Chat" Nguyen, Hien "Goblin" Ngo, Phuong "Zucchini" Pham, Van "The Shortest" Le and others.

There were many more who have helped me along the way, some old, some new, I apologize for any oversight on my behalf.

Abstract

Metamaterials are artificial materials that can exhibit extraordinary electromagnetic properties that have never been observed in nature. By engineering elements of metamaterials, one can achieve a so-called left-handed or double-negative medium, enabling new physics and new potential applications. Applications can be found in a wide variety of fields, such as invisibility cloaking, wireless power and data transfer, magnetic resonance imaging and body area networking. In addition, metamaterials are known to support magnetoinductive (MI) waves. By their very nature, magnetoinductive waves with strong inter-element coupling offers low loss and wide bandwidth channels. Recently, one of the new directions of research is low-frequency communications in RF-challenging environments (i.e., underground/underwater or in vivo medical diagnosis and treatment applications) with the aid of MI waves, due to their advantages over other transverse electromagnetic (TEM) wave-based techniques in penetrating lossy medium. Underground/underwater, or human body and tissues, are an extreme challenge for the conventional wireless links using TEM waves. TEM waves interact strongly with the lossy background medium resulting in high ohmic losses, the need for large antenna size and often rapid attenuation which increases in severity with frequency.

The use of arrays of resonating circuits forming MI waveguides therefore has been proposed in communications in lossy medium to achieve longer ranges as well as robust channels of transmission. Elsewhere, modelling of propagation of low frequency waves in a lossy medium has been paid increasing attention to embedded biomedical systems and body area networking for health-related applications, due to the fact that the human body and organs are relatively conductive from about 0.05 S/m to about 1.5 S/m at microwave frequencies. In terms of signal propagation, the attenuation of a signal in a given medium is the most important parameter. The radiation of TEM waves in conductors was understood and described a long time ago by Maxwell's equations. However, there is as yet no theoretical or numerical model to express the penetration of MI waves in conductive environments.

The main aims of this research are (i) firstly, to investigate the impact of an intervening conductive medium on the magnetic coupling of two low frequency coils which is usually presented by a questionable assumption in most literature, (ii) secondly to examine the field distribution and the mutual coupling, and by

that, the attenuation and phase delay between two low frequency coils embedded in a homogeneous dissipative medium and (iii) finally, study a completed circuit model, that takes into account all the effects of the background medium on coils coupled in close proximity and thereby, derive a new dispersion equation for the MI waves in these media. Since the dispersion equation is known, the propagation of MI waves will be fully understood and some relevant applications can be proposed. Besides, with the novel equivalent circuit model being considered, this research has laid the foundation for the theory of wireless power transfer in non-conventional environments.

Preface

This thesis is an account of work carried out by the author in the Department of Engineering Sciences, University of Oxford between October 2015 and August 2019, under the supervision of Professor Christopher Stevens and Professor Ekaterina Shamonina. No part of this work has been previously submitted for a degree at this or any other university. The submission of this thesis is in accordance with the requirements for the award of the degree of '*Doctor of Philosophy*' under the auspices of the University.

Some of the work in this thesis have been published/submitted/in preparation in the following journals:

1. **S. Chu**, M. S. Luloff, J. Yan, C. J. Stevens, and E. Shamonina "Magnetoinductive waves in attenuating media", *Nature Communications*, 2020 (**submitted**).

2. **S. Chu**, C. J. Stevens, and E. Shamonina, "Wireless power transfer in non-ideal media", *IEEE Transactions on Circuits and Systems II: Express Briefs*, 2020 (**in preparation**).

3. A. Vallecchi, **S. Chu**, C. J. Stevens, E. Shamonina and L. Solymar, 'Coupling between coils in the presence of conducting medium', *IET Microwaves, Antennas & Propagation*, vol. 13, no. 1, 2018.

4. **S. Chu**, A. Vallecchi, C. J. Stevens and E. Shamonina, 'Fields and coupling between coils embedded in conductive environments', *EPJ Applied Metamaterials*, vol. 5, no. 2, 2018 (**invited**).

Some of the work in this thesis have been published in the following conference proceedings:

5. **S. Chu**, C. J. Stevens and E. Shamonina,'A complete circuit model for two coils inside a dissipative medium', in *Proceedings of 12th International Congress on Engineered Materials Platforms for Novel Wave Phenomena (Metamaterials)*, Espoo, Finland, 2018, , pp. 78-80.

6. **S. Chu**, A. Vallecchi, C. J. Stevens and E. Shamonina,'Analytical solution for the magnetic coupling of two coils immersed in a conductive medium', in *Proceedings of 11th International Congress on Engineered Materials Platforms for Novel Wave Phenomena (Metamaterials)*, Marseille, France, 2017, pp. 58-60.

7. A. Vallecchi, **S. Chu**, C. J. Stevens and E. Shamonina,'Impact of a conducting medium on the coupling of meta-atoms', *Proceedings of 10th International Congress on Advanced Electromagnetic Materials in Microwaves and Optics (Metamaterials)*, Crete, Greece, 2016, pp. 385-387.

Contents

List of Figures **xii**

List of Abbreviations **xxvi**

1 Introduction **1**

1.1 Metamaterials 1

1.2 Coupling Mechanism between Meta-Atoms 4

1.3 Magnetoinductive Waves 6

1.4 Applications of Magnetoinductive Waves 12

1.4.1 Underground/Underwater Communications 13

1.4.2 Medical Devices 16

1.5 Research Challenges and Thesis Structure 18

1.5.1 Research Challenges 18

1.5.2 Thesis Structure 19

2 Impact of an Intervening Attenuating Medium **21**

2.1 Limitations of Current Models: Plane-Wave Approximation 22

2.2 Generalised Field Solutions 25

2.3 CST Models and Simulations Results 29

2.3.1 CST Models 30

2.3.2 Simulations Results 31

2.3.2.1 Magnetic Field Distribution 31

2.3.2.2 Poynting Vector 34

2.3.2.3 Mutual Inductance 38

2.4 Experiments 44

2.4.1 Experimental Apparatus 44

2.4.2 Experimental Results 46

2.5 Conclusions 49

3 Field Model of Coupled Coils in Homogeneous Dissipative Media 51
3.1 Circuit Model of Coupled Coils inside a Dissipative Medium 53
3.2 Complex Kirchhoff Coefficients: a New Field Solution 55
3.3 Simulation Results: Complex Kirchhoff Coefficients 60
3.3.1 CST Models 60
3.3.2 Simulations Results 61
3.3.2.1 Impact of Medium Conductivity 63
3.3.2.2 Impact of Vertical Distance 68
3.3.2.3 Impact of Horizontal Separation 71
3.4 Conclusions 76

4 Network Analysis of Coupled Resonators in Dissipative Media 80
4.1 Quality factor and Resonant Frequency 81
4.2 Frequency Splitting 86
4.3 Current Distribution 89
4.4 Power Conservation 94
4.5 Conclusions 98

5 Wireless Power Transfer via Coupled Resonators in Dissipative Media 100
5.1 Introduction 101
5.2 System Modelling 101
5.3 System Optimization 104
5.3.1 Optimal Load 104
5.3.2 Optimal Working Frequency 105
5.4 Simulation Results 106
5.5 Criteria for the Frequency Switching 113
5.6 Conclusions 116

6 Magnetoinductive Waves in Homogeneous Dissipative Media 118
6.1 Dispersion Equation 119
6.2 Simulation Results 121
6.3 Laboratory Experiments 126
6.3.1 Experimental Design 126
6.3.1.1 Dissipative Media 127
6.3.1.2 Split Ring Resonators 128
6.3.1.3 Dielectric Cavities, Cantilevers, and Immersion Level 131
6.3.2 Retrieving Dispersion Constants 135
6.3.3 Experimental Results 136
6.4 Conclusions 139

7 Conclusions and Future Work **141**
7.1 Conclusions 141
7.2 Future Work 145
7.2.1 Possible Model Improvement 145
7.2.2 Possible Applications 147

Appendices

A Field Solutions for a Coil above an Infinitely Wide Slab **149**

B Field Solutions for a Coil inside a Dissipative Medium **152**
B.1 Transmitting coil problem 152
B.2 Receiving coil problem 154

C Lorentzian Fit **156**

D Retrieving Dispersion Constants from Experimental Data **158**

References **160**

List of Figures

1.1 The first fabricated metamaterial with simultaneous negative permittivity and permeability composed of resonant split rings and straight wires. This figure is taken from [14]. 3
1.2 A general model for RF coupled resonators. 4
1.3 A schematic representation (top) and photographs of a section (bottom) of (a) an axial line and (b) a planar line. The photographs are taken from [37]. 6
(a) 6
(b) 6
1.4 Calculated dispersion relationship by using (1.6) in (a) 1-D coaxial waveguide of a positive magnetic coupling coefficient ($\kappa > 0$) and (b) coplanar 1-D waveguide of a negative magnetic coupling coefficient ($\kappa < 0$) in a very low-loss case ($Q = 1000$). The solid orange lines represent the nearest neighbour interaction ($p = 1$) while the dash green lines represent the interactions up to the third nearest neighbours ($p = 3$). The distance between two neighbour coil is $d = 20$ mm. 9
(a) 9
(b) 9
1.5 Calculated dispersion relationship by using (1.6) in a coaxial 1-D waveguide with a magnetic coupling coefficient of $\kappa = 1.6$ with the nearest neighbour approximation in a very low-loss case ($Q = 1000$). The distance between two neighbour coils is $d = 20$ mm. The vertical asymptote is $\beta = 0.715\pi$. 11
1.6 The normalised group velocity of MI waves calculated from Fig. 1.5. The result is normalised to the velocity of light in vacuum $c = 3 \times 10^8$ m/s. 11
1.7 Attenuation of an EM wave when crossing a conductive medium. . 14
1.8 The swallowable capsule and its schematic graphs. The capsule is used to measure the gas level along the gastrointestinal tract of human or animals [59]. 18

2.1 The general schematic diagram of a WUCN, consisting of a pair of transmitting and receiving coils. 23

2.2 Typical ranges of conductivity (S/m) for selected Earth materials and human organic matter [79–81]. 26

2.3 The cross-section of the configuration investigated consisting of two circular air core coils with the same orientation intervened by an infinitely wide conducting slab of varying conductivity. 27

2.4 The basic configuration investigated in CST EMS, consisting of a conductive material placed centrally-aligned between two coaxial identical circular air core coils. 29

2.5 Simulated amplitude and polarization of the total magnetic field generated by a transmitting coil (a) in air and (b) in the presence of a non-conducting dielectric block in the yz-plane. The cylindrical block has a dimension of $D = 90$ mm, thickness of $t = 30$ mm and relative permittivity of $\epsilon_r^{(\mathbf{III})} = 78$. Polarization ellipses are normalised at a sampling step of 5 mm along the y and z axes. Black dash lines mark the cross sections of the block while black dots represent transmitter (top) and receiver (bottom) coils. 32

(a) Air ($\epsilon_r = 1$ and $\sigma = 0$ S/m) 32

(b) Lossless Dielectric ($\epsilon_r = 78$ and $\sigma = 0$) 32

2.6 Simulated amplitude and polarization of the total magnetic field generated by a transmitting coil above a conducting cylindrical block in the yz-plane for different conductivity (a) $\sigma^{(\mathbf{III})} = 4$ S/m and (b) $\sigma^{(\mathbf{III})} = 1000$ S/m. The conducting cylindrical block has a dimension of $D = 90$ mm, thickness of $t = 30$ mm and relative permittivity of $\epsilon_r^{(\mathbf{III})} = 78$. Polarization ellipses are normalised at a sampling step of 5 mm along the y and z axes. Black dash lines mark the cross sections of the block while black dots represent transmitter (top) and receiver (bottom) coils. 33

(a) Conducting block ($\epsilon_r = 1$ and $\sigma = 4$ S/m) 33

(b) Conducting block ($\epsilon_r = 1$ and $\sigma = 1000$ S/m) 33

2.7 Capacitive compensation circuits to maximize the transferred power through two identical coupled coils. The values of capacitors are determnined by using Keysight ADS. Yellow blocks indicate 50 Ω impedance ports. 35

2.8 The power flow density and streamlines of the time-averaged Poynting vector generated from a pair of transmitting and receiving coils in the presence of a conducting cylindrical block in the yz-plane for different conductivity (a) $\sigma^{(\mathbf{III})} = 0$ (b) $\sigma^{(\mathbf{III})} = 4$ S/m and (b) $\sigma^{(\mathbf{III})} = 1000$ S/m. The conducting cylindrical block has a dimension of $D = 90$ mm, thickness of $t = 30$ mm and relative permittivity of $\epsilon_r^{(\mathbf{III})} = 78$. Black dash lines mark the cross sections of the block while black dots represents transmitter (top) and receiver (bottom) coils. The power transfer efficiency, $\eta = |S_{21}|^2 =$ (a) 48.8%, (b) 3.9 %, and (c) 0%. . . 36
(a) Air ($\epsilon_r = 1$ and $\sigma = 0$ S/m) 36
(b) Conducting block ($\epsilon_r = 1$ and $\sigma = 4$ S/m) 36
(c) Conducting block ($\epsilon_r = 1$ and $\sigma = 1000$ S/m) 36
2.9 Simulated modulus of the mutual inductance as a function of the conducting block diameter for the block conductivity $\sigma^{(\mathbf{III})} = 1.5, 4, 10$ and 1000 S/m. Two coaxial coils are displaced by $d = 37$ mm. The conducting cylindrical block has a dimension of $D = 90$ mm, thickness of $t = 30$ mm and relative permittivity of $\epsilon_r^{(\mathbf{III})} = 78$. 38
2.10 (a) Real part, (b) imaginary part, and (c) modulus of the mutual inductance between two coaxial circular coils versus the block conductivity from $\sigma^{(\mathbf{III})} = 10^{-3}$ to $\sigma^{(\mathbf{III})} = 10^8$ S/m. Two coaxial coils are displaced by $d = 37$ mm. The conducting cylindrical block has a dimension of $D = 90$ mm, thickness of $t = 30$ mm and relative permittivity of $\epsilon_r^{(\mathbf{III})} = 78$. CST EMS simulation results are compared with those obtained with the PW approximation, the D&D solution [71], the generalised field solution. 40
(a) 40
(b) 40
(c) 40
2.11 (a) Real part, (b) imaginary part, and (c) modulus of the mutual inductance between two coaxial circular coils versus the block thickness from $t = 0$ to $t = 32$ mm. Two coaxial coils are displaced by $d = 37$ mm. The conducting cylindrical block has a dimension of $D = 90$ mm, conductivity of $\sigma^{(\mathbf{III})} = 4$ S/m and relative permittivity of $\epsilon_r^{(\mathbf{III})} = 78$. CST EMS simulation results are compared with those obtained with the PW approximation, the D&D solution [71], the generalised field solution. 42
(a) 42
(b) 42
(c) 42

2.12 (a) Real part, (b) imaginary part, and (c) modulus of the mutual inductance between two coaxial circular coils versus the block relative permittivity from $\epsilon_r = 1$ to $\epsilon_r = 80$. Two coaxial coils are displaced by $d = 37$ mm. The conducting cylindrical block has a dimension of $D = 90$ mm, thickness of $t = 30$ mm, and conductivity of $\sigma^{(\mathbf{III})} = 4$ S/m. CST EMS simulation results are compared with those obtained with the PW approximation, the D&D solution [71], the generalised field solution. 43
(a) 43
(b) 43
(c) 43
2.13 (a) Schematic view of the laboratory experiment and (b) the block diagram of the measurement system. 44
(a) 44
(b) 44
2.14 A magnetic probe used in the experiment. 45
2.15 Measured (a) real part, (b) imaginary part, (c) modulus and (d) phase of the mutual inductance between two coaxial circular coils versus the solution conductivity from $\sigma = 0$ to $\sigma = 20$ S/m. Two coaxial coils are displaced by $d = 37$ mm. The aqueous solution has a dimension of $D = 90$ mm, thickness of $t = 30$ mm, and relative permittivity of $\epsilon_r = 78$. Comparisons are made with results obtained with the PW approximation, the D&D solution [71], the generalised field solution, and CST EMS simulations. 47
(a) 47
(b) 47
(c) 47
(d) 47
2.16 Measured (a) real part, (b) imaginary part, (c) modulus and (d) phase of the mutual inductance between two coaxial circular coils versus the solution thickness from $t = 0$ to $t = 32$ mm. Two coaxial coils are displaced by $d = 37$ mm. The aqueous solution has a dimension of $D = 90$ mm, conductivity of $\sigma = 4$ S/m and relative permittivity of $\epsilon_r = 78$. Comparisons are made with results obtained with the PW approximation, the D&D solution [71], the generalised field solution, and CST EMS simulations. 48
(a) 48
(b) 48
(c) 48

(d) 48

3.1 General schematic diagram of two coupled coils in proximity with the same orientation completely immersed inside an infinite homogeneous dissipative medium. Each coil is insulated by a small dielectric cavity. 54

3.2 Cross-section of the configuration investigated consists of two circular transmitting and receiving coils with the same orientation spaced apart a certain distance in an infinite homogeneous dissipative medium. (a) The finite size dielectric cavities used in the actual configuration, are considered as infinite dielectric layers (b) in the theoretical model. 56

(a) 56

(b) 56

3.3 Configuration investigated consisting of two identical circular air core coils with dielectric enclosures placed inside an infinite, linear, homogeneous, isotropic, and dissipative environment. 62

3.4 Modulus of the complex self inductance $|\,\Delta\mathcal{L}\,|$ as a surface function of the working frequency and the medium conductivity. The medium conductivity is from $\sigma^{(\mathbf{I})} = 0.01$ to $\sigma^{(\mathbf{I})} = 20$ S/m while the working frequency ranges between $f = 37$ to $f = 55$ MHz. (Top left) The analytical value obtained with (3.18) is compared to CST EMS simulation results for three different sizes of the insulators: (Top right) $R = 1.1r_0$, (Bottom left) $R = 2.0r_0$, and (Bottom right) $R = 3.0r_0$. 64

3.5 Modulus of the complex mutual inductance $|\,\mathcal{M}\,|$ as a surface function of the working frequency and the medium conductivity. The medium conductivity is from $\sigma^{(\mathbf{I})} = 0.01$ to $\sigma^{(\mathbf{I})} = 20$ S/m while the working frequency ranges between $f = 37$ to $f = 55$ MHz. (Top left) The analytical value obtained with (3.19) is compared to CST EMS simulation results for three different sizes of the insulators: (Top right) $R = 1.1r_0$, (Bottom left) $R = 2.0r_0$, and (Bottom right) $R = 3.0r_0$. 64

3.6 Real parts and imaginary parts of the complex Kirchhoff coefficients $\Delta\mathcal{L}$ and $\mathcal{M}$ as a surface function of the working frequency and the medium conductivity. The medium conductivity is from $\sigma^{(\mathbf{I})} = 0.01$ to $\sigma^{(\mathbf{I})} = 20$ S/m while the working frequency ranges between $f = 37$ to $f = 55$ MHz. (Top left) The analytical value obtained with (3.18) and (3.19) is compared to CST EMS simulation results for three different sizes of the insulators: (Top right) $R = 1.1r_0$, (Bottom left) $R = 2.0r_0$, and (Bottom right) $R = 3.0r_0$. 65

(a) Real part of $\Delta\mathcal{L}$ 65
(b) Imaginary part of $\Delta\mathcal{L}$ 65
(c) Real part of $\mathcal{M}$ 65
(d) Imaginary part of $\mathcal{M}$ 65
3.7 Average relative errors of the analytical solutions for the complex Kirchhoff coefficients in terms of their moduli and phases with respect to CST EMS simulation results for several different sizes of the dielectric cavities. 66
3.8 (a) Real part, (b) imaginary part, and (c) modulus of the complex self inductance $\Delta\mathcal{L}$ as a function of the normalised vertical separation d/r_0. The dissipative medium has a conductivity of $\sigma^{(\mathbf{I})} = 4$ S/m and the horizontal displacement is $\Delta d = 0$ mm. CST EMS simulation results for three different sizes of the insulators: $R = 1.1r_0$, $2r_0$, and $3r_0$ are compared with those obtained with the analytical solution (3.18). 69
(a) 69
(b) 69
(c) 69
3.9 The (a) real part, (b) imaginary part, and (c) modulus of the complex self inductance $\mathcal{M}$ as a function of the normalised vertical separation d/r_0. The dissipative medium has a conductivity of $\sigma^{(\mathbf{I})} = 4$ S/m and the horizontal displacement is $\Delta d = 0$ mm. CST EMS simulation results for three different sizes of the insulators: $R = 1.1r_0$, $2r_0$, and $3r_0$ are compared with those obtained with the analytical solution (3.19). 70
(a) 70
(b) 70
(c) 70
3.10 The (a) real part, (b) imaginary part, and (c) modulus of the complex self inductance $\Delta\mathcal{L}$ as a function of the normalised horizontal displacement $\Delta d/r_0$. The dissipative medium has a conductivity of $\sigma^{(\mathbf{I})} = 4$ S/m and the distance between the two coils is $d = 30$ mm. CST EMS simulation results for three different sizes of the insulators: $R = 1.1r_0$, $2r_0$, and $3r_0$ are compared with those obtained with the analytical solution (3.18). 72
(a) 72
(b) 72
(c) 72

3.11 The (a) real part, (b) imaginary part, and (c) modulus of the complex mutual inductance $\mathcal{M}$ as a function of the normalised horizontal displacement $\Delta d/r_0$. The dissipative medium has a conductivity of $\sigma^{(\mathbf{I})} = 4$ S/m and the distance between the two coils is $d = 30$ mm. CST EMS simulation results for three different sizes of the insulators: $R = 1.1r_0$, $2r_0$, and $3r_0$ are compared with those obtained with the analytical solution (3.19). 73
(a) 73
(b) 73
(c) 73

3.12 Simulated polarization ellipses and magnitude of the total magnetic field produced by the transmitter coil. Ellipse axes are normalised and plotted at a sampling step of 5 mm along the y and z directions. Black dash lines mark the cross sections of the dielectric cavities. (a) The medium (a) is free space and (b) has relative permittivity of $\epsilon_r = 78$, relative permeability of $\mu_r = 1$, and conductivity $\sigma = 4$ S/m (seawater). The mutual inductances are (a) $M \approx 0.6572\underline{/-22^\circ}$ and (b) $M \approx 0.7572\underline{/-0.02^\circ}$. 75
(a) Free Space 75
(b) Seawater ($\sigma = 4$ S/m, and $\epsilon_r = 78$) 75

3.13 Contour maps of the modulus of H_z components of the magnetic fields illustrated in Fig 3.12b and Fig 3.12a respectively. Black dash lines mark the cross sections of the insulating cavities. 76
(a) Free space 76
(b) Seawater ($\sigma = 4$ S/m, and $\epsilon_r = 78$) 76

4.1 Calculated normalised resonant frequency of a coil inside an infinite medium background with a variable conductivity from $\sigma = 10^{-3}$ to $\sigma = 10^2$ S/m. The result obtain with (4.1) is normalised to the resonance of the coil in vacuum. 83

4.2 Calculated normalised Q-factor of a coil insulated by a small dielectric cavity and immersed completely inside an infinite medium background with a variable conductivity from $\sigma = 10^{-3}$ to $\sigma = 10^2$ S/m. The result obtain with (4.2) is normalised to the Q-factor of the coil in vacuum. 84

4.3 The normalised (a) resonant frequency and (b) Q-factor of a coil in a practical WUSN investigated in [51, 91]. The coil has dimensions: mean radius of $r_0 = 150$ mm, height of $l = 7.25$ mm, thickness of $w = 1.45$ mm, and five turns $N = 5$. The resonant frequency and the Q-factor in free space are: $f_0 = 7$ MHz and $Q = 1284$. The cylindrical dielectric cavity providing insulation for the coils has a height of $2h + l = 9.25$ mm. The soil's electromagnetic properties are relative permittivity of $\epsilon_r = 1$, relative permeability of $\mu_r = 1$, and variable conductivity from $\sigma = 10^{-3}$ to $\sigma = 10^2$ S/m. The red stars indicate the value of soil's conductivity ($\sigma = 1e - 2$ S/m, dry soil) investigated in [91]. The results are normalised to those of the coil in vacuum. 85

(a) 85

(b) 85

4.4 The configuration investigated consisting of two identical coils with dielectric enclosures placed inside a dissipative environment. The coils are placed coaxially with a distance of 30 mm apart from each other. 86

4.5 Comparison of the theoretical values and simulation results for splitting resonant frequencies of two coupled coils inside a dissipative environment. The two coils are insulated by a small dielectric cavity and immersed completely inside an infinite medium background with a relative permittivity of $\epsilon_r = 78$, relative permeability of $\mu_r = 1$, and variable conductivity from $\sigma = 10^{-3}$ to $\sigma = 10^2$ S/m. The coil has dimensions: mean radius of $r_0 = 11$ mm, height of $l = 5$ mm, thickness of $w = 1$ mm, one turn $N = 1$ and the resonant frequency of $f_0 = 46$ MHz. To isolate the effects of the medium, the internal resistance of the coils is negligible, $R_0 = 0$. The cylindrical dielectric cavity providing insulation for the coils has a height of $2h + l = 7$ mm. The results are normalised by $f_0 = 46$ MHz. 88

4.6 Calculated normalised magnitude of the current distribution versus frequency and medium conductivity in the transmitting coil: (a) the 3-D waterfall map and (b) colour-map for the configuration of two circular coils of mean radius $r_0 = 11$ mm, height of $l = 5$ mm, thickness of $w = 1$ mm, number of turns $N = 1$, separated by a vertical distance $d = 30$ mm and horizontal displacement $\Delta d = 0$ inside a dissipative medium with a relative permittivity of $\epsilon_r = 78$, relative permeability of $\mu_r = 1$, and conductivity $\sigma = 4$ S/m. The resonant frequency and the Q-factor in free space are: $f_0 = 46$ MHz and $Q = 432$. The cylindrical dielectric cavity providing insulation for the coils has a height of $2h+l = 7$ mm. The result is normalised to the maximum value of the transmitter current when the transmission medium is vacuum. 90
(a) 90
(b) 90
4.7 Calculated normalised magnitude of the current distribution versus frequency and medium conductivity in the receiving coil: (a) the 3-D waterfall map and (b) colour-map for the configuration of two circular coils of mean radius $r_0 = 11$ mm, height of $l = 5$ mm, thickness of $w = 1$ mm, number of turns $N = 1$, separated by a vertical distance $d = 30$ mm and horizontal displacement $\Delta d = 0$ inside a dissipative medium with a relative permittivity of $\epsilon_r = 78$, relative permeability of $\mu_r = 1$, and conductivity $\sigma = 4$ S/m. The resonant frequency and the Q-factor in free space are: $f_0 = 46$ MHz and $Q = 432$. The cylindrical dielectric cavity providing insulation for the coils has a height of $2h + l = 7$ mm. The result is normalised to the maximum value of the receiver current when the transmission medium is vacuum. 91
(a) 91
(b) 91
4.8 Comparison of (a) the calculated active power (real part) and (b) reactive power (imaginary part) of three volt-amperes versus frequency: S_f (feedback loss due to the medium), S_1 (leaving the transmitter), and S_2 (entering the receiver). The coil configuration is: two coaxial identical coils separated by a distance $d = 30$ mm with the resonant frequency $f_0 = 46$ MHz, the quality factor $Q = 432$, and dimensions: mean radius $r_0 = 11$ mm, height of $l = 5$ mm, thickness of $w = 1$ mm, number of turns $N = 1$. The cylindrical dielectric cavity providing insulation for the coils has a height of $2h + l = 7$ mm. The transmission medium is vacuum. 96

(a) 96
(b) 96
4.9 Comparison of the input active power and the power dissipated in the coils as heat versus frequency for the configuration stated in Fig. 4.8 96
4.10 Comparison of (a) the calculated active power (real part), (b) reactive power (imaginary part), and (c) apparent power (modulus) of three volt-amperes versus frequency: S_f (feedback loss due to the medium), S_1 (leaving the transmitter), and S_2 (entering the receiver). The coil configuration is: two coaxial identical coils separated by a distance $d = 30$ mm with the resonant frequency $f_0 = 46$ MHz, the quality factor $Q = 432$, and dimensions: mean radius $r_0 = 11$ mm, height of $l = 5$ mm, thickness of $w = 1$ mm, number of turns $N = 1$. The cylindrical dielectric cavity providing insulation for the coils has a height of $2h + l = 7$ mm. The properties of the transmission medium are relative permittivity of $\epsilon_r = 78$, relative permeability of $\mu_r = 1$, and conductivity $\sigma = 1$ S/m. 97
(a) 97
(b) 97
(c) 97
4.11 Comparison of the input active power and the power dissipated in the coils and the ambient environment versus frequency for the configuration stated in Fig. 4.10 98

5.1 Equivalent circuit model of a WPT system consisting of two resonant coils with series-series capacitive compensation topology. 103
5.2 Calculated colour map of the output power P_L as a surface function of the normalised working frequency f and the load resistance R_L. The frequency is normalised by the resonance of the coils in the isolated case. The WPT system operates in free space. 108
(a) 108
(b) 108
5.3 (a) Calculated active power at load at the optimal frequency and the resonance, (b) the corresponding efficiency, (c) optimal frequency, and (d) optimal load resistance. The output power in the case study is compared when the compensation capacitances are kept the same as in free space (non-retuned) and when the compensation capacitances are added according to the prediction of the detuning effect based on the novel circuit model (retuned). 109
(a) 109
(b) 109

(c) 109
(d) 109
5.4 Calculated colour map of the output power P_L as a surface function of the normalised working frequency f and the load resistance R_L. The frequency is normalised by the resonance of the coils in the isolated case. The WPT system operates inside a medium with the conductivity of (a) $\sigma = 0.01$, (b) $\sigma = 0.1$, (c) $\sigma = 1$, and $\sigma = 10$. . . 111
(a) $\sigma = 0.01$ S/m 111
(b) $\sigma = 0.1$ S/m 111
(c) $\sigma = 1$ S/m 111
(d) $\sigma = 10$ S/m 111
5.5 Calculated colour map of the output power P_L as a surface function of the normalised working frequency f and the load resistance R_L. The frequency is normalised by the resonance of the coils in the isolated case. The WPT system operates inside a medium with the conductivity of (a) $\sigma = 0.01$, (b) $\sigma = 0.1$, (c) $\sigma = 1$, and $\sigma = 10$. The coils are retuned to the original resonance inside the medium by adding suitable capacitors. 112
(a) $\sigma = 0.01$ S/m 112
(b) $\sigma = 0.1$ S/m 112
(c) $\sigma = 1$ S/m 112
(d) $\sigma = 10$ S/m 112
5.6 Optimal frequency for the maximum output power at load for three extreme cases of the configuration: $R_1 = 0$, $R_2 = 0$, and $R_1 = R_2 = 0$. 113
5.7 Calculated colourmap guidance by using (5.14) for the optimal frequency selection as a fuction of the receiver resistance and the medium conductivity. The solid line refers to the values when the output powers at the original resonance and upper resonance are equal. 115

6.1 General schematic diagram of a coaxial MI waveguide consisting of a finite number of capacitively-loaded split ring resonators immersed in a dissipative environment. Each element is placed centrally in an insulating volume. 119
6.2 Calculated dispersion relationship (a) attenuation and (b) phase constant in a coaxial 1-D waveguide with a distance between two adjacent resonators of $d = 30$ mm embedded in free-space ($\sigma = 0$ S/m) and a dissipative medium with relative permittivity of $\epsilon_r = 78$, relative permeability $\mu_r = 1$ and conductivity of $\sigma = 1.5$ S/m in a very low-loss case ($Q = 1000$). Each element is placed centrally in an insulating cavity. The magnetic interaction is taken up to the fifth nearest neighbour. 122

(a) 122
(b) 122
6.3 Calculated coupling constants $\kappa_n = 2M_n/L$ in the complex plane as a function of frequency between five neighbour resonant elements in the MI waveguide configurations shown in Fig. 6.2. The surrounding medium is (a) free space and (b) a dissipative medium with relative permittivity of $\epsilon_r = 78$, relative permeability $\mu_r = 1$ and conductivity of $\sigma = 1.5$ S/m. The working frequency is from $0.9\omega_0$ to $1.1\omega_0$. Black arrows indicate the progression of the frequency. 124
(a) Free space ($\epsilon_r = 1$ and $\sigma = 0$ S/m) 124
(b) Medium ($\epsilon_r = 78$ and $\sigma = 1.5$ S/m) 124
6.4 Calculated dispersion relationship of (left) attenuation and (right) phase constant in a coaxial 1-D waveguide with a distance between two adjacent resonators of (a) $d = 30$ mm and (b) $d = 20$ mm embedded in free-space ($\sigma = 0$ S/m) and a dissipative medium with relative permittivity of $\epsilon_r = 78$, relative permeability $\mu_r = 1$ and different conductivity of $\sigma = 0.055$, 1.5, 4, and 10 S/m in a very low-loss case ($Q = 1000$). Each element is placed centrally in an insulating cavity. 125
(a) $d = 30$ mm 125
(b) $d = 20$ mm 125
6.5 Schematic diagram of the experiment set-up to measure the dispersion constants of MI waveguides inside a dissipative surrounding medium. 127
6.6 (a) Schematic diagram of a split ring resonator and (b) its actual photograph. The ring is loaded with a capacitor of polystyrene film type at the gap. 128
6.7 Measurement set-up to measure the quality factor of the fabricated split ring resonators (a) alone and (b) in combination with their corresponding insulating cavities. 129
(a) 129
(b) 129
6.8 The modulus of the measured transmission coefficients for manufactured split ring resonators with and without their corresponding insulating cavities. 130
6.9 Schematic diagram of the dielectric cavity providing the insulation for the split ring resonators. 132
6.10 Vertical immersion level of the split ring resonators in the experiment.133

6.11 Normalised (a) modulus and (b) phase of the lossy self inductance as a function of the immersion level for the configuration of two coaxial identical circular coils shown in Fig. 6.6, separated by a vertical distance $d = 30$ mm inside a dissipative medium with a relative permittivity of $\epsilon_r = 78$, relative permeability of $\mu_r = 1$, and variable conductivity $\sigma = 0.055$, 1.5, 4, and 10 S/m. The insulating cavities shown in Fig. 6.9 have a height of 7 mm. CST EMS simulation results are normalised to that of the case when the surrounding dissipative medium is infinite and the insulators are in perfectly cylindrical shape. 133
(a) . . . 133
(b) . . . 133
6.12 Normalised (a) modulus and (b) phase of the lossy mutual inductance as a function of the immersion level for the configuration of two coaxial identical circular coils shown in Fig. 6.6, separated by a vertical distance $d = 30$ mm inside a dissipative medium with a relative permittivity of $\epsilon_r = 78$, relative permeability of $\mu_r = 1$, and variable conductivity $\sigma = 0.055$, 1.5, 4, and 10 S/m. The insulating cavities shown in Fig. 6.9 have a height of 7 mm. CST EMS simulation results are normalised to that of the case when the surrounding dissipative medium is infinite and the insulators are in perfectly cylindrical shape. . . . 134
(a) . . . 134
(b) . . . 134
6.13 3D printed (top) U-shaped cantilevers, the (bottom right) body and (bottom left) cap of an insulating cylindrical cavity with a split ring resonator inside. . . . 134
6.14 Laboratory measurement of an MI waveguide consisting of 11 elements with the distance between two adjacent elements of $d = 30$ mm submerged in an aqueous solution of sodium chloride with suitable conductivity. (a) Side view, and (b) top view. . . . 136
(a) . . . 136
(b) . . . 136
6.15 Log-magnitude of transmission coefficients, S_{21} in dB scale measured along the waveguide shown in Fig. 6.14 submerged in an aqueous solution with different conductivity of (a) $\sigma = 0.055$, (b) $\sigma = 1.5$, (c) $\sigma = 4$, and (d) $\sigma = 10$ S/m. . . . 137
(a) $\sigma = 0.055$ S/m . . . 137
(b) $\sigma = 1.5$ S/m . . . 137
(c) $\sigma = 4$ S/m . . . 137

(d) $\sigma = 10$ S/m 137
6.16 Comparison of the experimental and theoretical (left) attenuation constant and (right) phase constant in a coaxial 1-D waveguide with a distance between two adjacent resonators of $d = 30$ mm embedded in an aqueous solution with different conductivity of (a) $\sigma = 0.055$, (b) $\sigma = 1.5$, (c) $\sigma = 4$, and (d) $\sigma = 10$ S/m. Each element is placed centrally in an insulating cavity with the radius equalling to three times ring radius. The shaded area represents the spread in the theoretical results due to the 7% uncertainty in the lossy Kirchhoff coefficients ($\Delta\mathcal{L}$ and $\mathcal{M}$). 138
(a) $\sigma = 0.055$ S/m 138
(b) $\sigma = 1.5$ S/m 138
(c) $\sigma = 4$ S/m 138
(d) $\sigma = 10$ S/m 138

List of Abbreviations

BAN . . . . . Body area networking

D&D . . . . . Dodd and Deeds

EI . . . . . Electroinductive

EM . . . . . Electromagnetic

LHM . . . . . Left-handed metamaterials

MI . . . . . Magnetoinductive

MM . . . . . Metamaterials

MRI . . . . . Magnetic resonance imaging

RF . . . . . Radio frequency

TEM . . . . . Transverse Electromagnetic

VNA . . . . . Vector Network Analyser

WPT . . . . . Wireless power transfer

WUCN . . . . Wireless underground/underwater communications network

1 Introduction

Contents

1.1 Metamaterials 1
1.2 Coupling Mechanism between Meta-Atoms 4
1.3 Magnetoinductive Waves 6
1.4 Applications of Magnetoinductive Waves 12
1.4.1 Underground/Underwater Communications 13
1.4.2 Medical Devices 16
1.5 Research Challenges and Thesis Structure 18
1.5.1 Research Challenges 18
1.5.2 Thesis Structure 19

1.1 Metamaterials

Worldwide, scientists have been drawing a huge attention to metamaterials (MM) since the first invention in the early 21st century [1–4]. To understand the concept of MM, one might need to refer to the prevailing knowledge of electromagnetic (EM) properties of natural materials. Generally speaking, all materials existing in nature are comprised of tiny atoms. As an incident transverse EM wave of a certain frequency, or wavelength, penetrates in a structure, there are two possibilities, i.e., the wavelength is either comparable to or much longer than the particle separation of the structure. In the former case, Bragg diffraction [5] occurs and thus that

material is considered as a discrete medium. Otherwise, in the latter case, when the wavelength is much larger than the atomic spacing, the lattice structure of the material no longer plays an important role in defining the interaction of the material with incident EM waves. Alternatively, one may neglect the microscopic details and conceptually replace a discrete structure by a homogeneous and continuous material, which is macroscopically described by only two crucial electromagnetic parameters, namely magnetic permeability μ, and electric permittivity ϵ. Basically, μ and ϵ are of positive values for almost all natural materials. A few exceptions include metals or ferrites at some particular frequencies. For example, gold and silver may have negative ϵ at frequencies below their plasma frequency [6] while nickel—zinc (NiZn) ferrite exhibit negative μ at microwave frequency, around 0.7 GHz [7].

A similar situation arises in the case of artificial materials, wherein atoms and molecules are substituted by macroscopic, engineered elements. Even the dimensions of the engineered components now may be larger than that of natural material particles, the segregation rule above is still valid. When the wavelength is approximate to the inter–element distance, the Bragg effect should be taken into account and then one has a so-called photonic bangap materials [8–10]. Otherwise, if the element separation is relatively small in comparison to the incident wavelength, the effective-medium approximation can be applied and hence the medium is referred to as a metamaterial [1–4]. In general, by tailoring individual elements, also known as, meta-atoms and the interaction between them, it is possible to engineer the permittivity and permeability of the structure, resulting in extraordinary electromagnetic properties, which have not been observed in natural materials.

The overall picture of MM has been presented. Scientists, however, are still struggling to give a general definition and classification for MM [4]. The most well-known type of metamaterial is left-handed metamaterial (LHM) that simultaneously exhibits negative values of ϵ and μ, forming the left-handed $\left(\overrightarrow{E}, \overrightarrow{H}, \overrightarrow{k}\right)$ triplet [1] inside the medium [1]. The marvellous electromagnetic properties of such media were theoretically predicted in 1964 by Velesago [11]. Nonetheless, because there is

[1] $\overrightarrow{E}$ is the electric field vector, $\overrightarrow{H}$ is the magnetic field vector and $\overrightarrow{k}$ is the wave vector

no such material in nature that could provide both negative ϵ and μ, this research field remained theoretical until the works of Pendry et al. [12, 13] three decades later. In those works, two types of periodic configurations of conducting components were investigated, such as a collection of thin wires [12] and split ring arrays [13], to present non-positive values of ϵ_r and μ_r respectively due to near-field couplings. Inspired by Pendry et al. [12, 13], Smith et al. [14] concluded that a superposition of the two kinds of structures above could lead to a so-called double-negative medium. The first bulky MM, shown in Fig. 1.1, was then fabricated and examined to verify Smith's hypothesis. A proof of a negative index of refraction was published thereupon [15].



Figure 1.1: The first fabricated metamaterial with simultaneous negative permittivity and permeability composed of resonant split rings and straight wires. This figure is taken from [14].

The pioneering discovery of LHM realizes the theoretical analysis predicted by Velesago. Thus, it enables new physics, one of which is the reversal of Snell's law of refraction, and opens the floodgates of new potential applications. By adjusting the inter-element interaction, applications of MM nowadays can be found in a wide variety of fields, ranging from some extreme applications, such as super lens [16, 17], cloaking at all range of frequencies [2, 18, 19], and to some down-to-earth

applications, such as antennas [20, 21], absorbers [22, 23], wireless power transfer [24, 25], magnetic resonance imaging [26] and biosensing [27].

1.2 Coupling Mechanism between Meta-Atoms

The key to form MM, as stated in Section 1.1, is to design meta-atoms and therefore, the mutual coupling between them, resulting in negative values of ϵ or μ at a certain range of frequencies. At radio frequencies (RF), meta-atoms are usually in the form of coupled resonant circuits [18, 20–23, 25]. Fig. 1.2 illustrates a general model for a pair of coupled resonators discussed in [28].

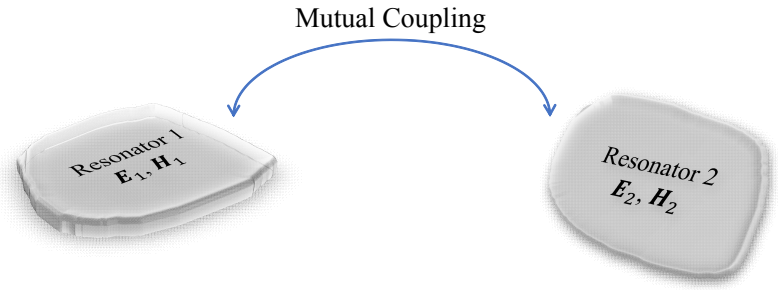


Figure 1.2: A general model for RF coupled resonators.

Often, the mutual coupling between two resonators is described by a dimensionless physical quantity – the coupling coefficient k, which represents the degree of coupling. It is defined by a ratio of coupled energy to stored energy where all electromagnetic fields $\mathbf{E}$ and $\mathbf{H}$ are calculated at resonant frequencies, and the volume integrals are taken over the entire effective region with permittivity ϵ and permeability μ [28].

$$k = \frac{\iiint \epsilon \mathbf{E}_1 \cdot \mathbf{E}_2 \, \mathrm{d}v}{\sqrt{\iiint \epsilon |\mathbf{E}_1|^2 \, \mathrm{d}v \times \iiint \epsilon |\mathbf{E}_2|^2 \, \mathrm{d}v}} + \frac{\iiint \mu \mathbf{H}_1 \cdot \mathbf{H}_2 \, \mathrm{d}v}{\sqrt{\iiint \mu |\mathbf{H}_1|^2 \, \mathrm{d}v \times \iiint \mu |\mathbf{H}_2|^2 \, \mathrm{d}v}} \tag{1.1}$$

The first fraction defines the coupling via the electric fields whereas the second fraction defines the coupling via the magnetic fields. Since (1.1) described the electric coupling and magnetic coupling by the dot operation of their respective vector fields, their signs can be either negative or positive. A raise in the stored energy compared to an uncoupled system results in a positive coupling coefficient and vice

versa. As a result, the electric coupling and magnetic coupling may have either the same or opposite effect when they have the same or opposite signs, respectively.

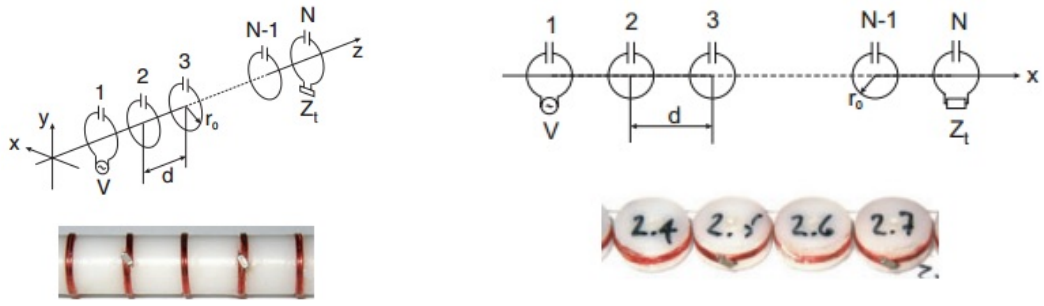
As discussed in [29], it is pointed out that the nature of coupling mechanism between meta-atoms depends heavily on the range of EM frequency. At MHz region or lower, analytical calculations and experimental measurements prove in most cases, the electric coupling might be negligible, leading to sole magnetic coupling [4]. The electric coupling, on the other hand, starts playing a large part when the frequency moves up to the GHz region as there is non-uniform charge distributions in meta-atoms [30, 31]. At higher frequency, e.g., THz range, a term of kinetic inductance participates into the process, making the coupling further complicated [31]. In such a manner, the overall coupling may consist of either the magnetic coupling or electric coupling or both of them, depending on the working frequency and the geometry of the configuration.

Apart from the influence upon the penetration of conventional EM radiation, due to the inter-element coupling, MM shows a capability of supporting other types of waves, such as magnetoinductive (MI) waves [32] and their dual counterpart - electroinductive (EI) waves [33]. These waves are slow and longitudinal with the wavelengths being much smaller than that of the EM wave [34]. Their names obviously indicate their origins. Magnetic coupling in MM leads to the existence of MI waves whilst the EI waves are produced by capacitive coupling between meta-atoms in the so-called complementary MM, in which the constituent metallic parts are replaced by the dielectric and vice versa.

Being known to support two slow and longitudinal types of waves, the research of the guiding property has become a significant branch added to the main subject of MM. This thesis, however, focuses in particular on MI waves with the aid of magnetic MM (comprising resonators with a strong magnetic response) at radio frequencies, especially at the lower region between 3 kHz and 3 GHz.

1.3 Magnetoinductive Waves

MI waves were first postulated analytically nearly 20 years ago [32]. A one-dimensional array of capacitively loaded metallic coils along the axle of a dielectric rod was chosen as a supporting medium for the propagation of MI waves. Shortly after that, Wiltshire et al [35] demonstrated experiments to prove the existence of these waves. Hence, these evidences led to a proof that MI waves will exist in periodic structures when magnetic couplings are present. The dispersion characteristics of MI waves has been studied theoretically and experimentally in all one, two and three dimensions [32, 35–37]. Fig. 1.3 illustrates the schematic and practical configuration of coaxial and coplanar capacitively-loaded-loop waveguides with a finite number of elements. In the former case, the axis of resonant components is normal to the plane where the components are lying whilst the axis in the latter case is in the same plane as the components.



(a) **(b)**

Figure 1.3: A schematic representation (top) and photographs of a section (bottom) of (a) an axial line and (b) a planar line. The photographs are taken from [37].

MI waves propagate in both cases within the waveguides due to the magnetic coupling, or in other words, mutual inductance between elemental resonators in the array. However, the orientation of the resonators distinguishes two prototypes. In axial waveguides, the magnetic flux enters two adjacent elements in the same direction but in the opposite direction in planar waveguides, yielding positive and negative mutual inductances respectively. A forward wave, which travels with

positive group velocity ($v_g = \mathrm{d}\omega/\mathrm{d}\beta$) [2], therefore, comes as a consequence of positive coupling in an axial chain of resonators. Otherwise, a backward wave, which travels with negative group velocity can be observed in a planar configuration with negative coupling.

The array of capacitively-loaded split rings consists of $\mathcal{N}$ elements. Fundamentally, each ring can be modelled as a resonator or a RLC series circuit [38]. The impedance of the n-th coil is given by: $Z_n = R_n + j\omega L_n + 1/(j\omega C_n)$ where R_n is the resistance, L_n is the self-inductance, and C_n is the capacitance of the n-th coil and ω is the angular frequency. The mutual impedance between the n-th element and the m-th element is directly proportional to the mutual inductance $Z_{n,m} = j\omega M_{n,m}$ where $M_{n,m}$ is the mutual inductance whose expression can be found in practically every textbook on Electromagnetic Theory, e.g., [39]. Applying Kirchhoff's voltage law, the relationship between current and voltage in the n-th ring is obtained by:

$$Z_n I_n + \sum_{n \neq m} I_n Z_{n,m} = V_n \tag{1.2}$$

where I_n is the current in n-th ring, V_n is the voltage applied to the n-th ring. The general relationship of the waveguide thus can be rewritten in the matrix form:

$$\mathbf{V} = \mathbf{ZI} \tag{1.3}$$

$$\Longleftrightarrow \begin{bmatrix} V_1 \\ V_2 \\ \dots \\ V_n \\ \dots \\ V_{\mathcal{N}} \end{bmatrix} = \begin{bmatrix} Z_1 & Z_{12} & Z_{13} & \dots & Z_{1n} & \dots & Z_{1\mathcal{N}} \\ Z_{12} & Z_2 & Z_{23} & \dots & Z_{2n} & \dots & Z_{2\mathcal{N}} \\ \dots & \dots & \dots & \dots & \dots & \dots & \dots \\ Z_{n1} & Z_{n2} & Z_{n3} & \dots & Z_n & \dots & Z_{n\mathcal{N}} \\ \dots & \dots & \dots & \dots & \dots & \dots & \dots \\ Z_{\mathcal{N}1} & Z_{\mathcal{N}2} & Z_{\mathcal{N}3} & \dots & Z_{\mathcal{N}n} & \dots & Z_{\mathcal{N}} \end{bmatrix} \begin{bmatrix} I_1 \\ I_2 \\ \dots \\ I_n \\ \dots \\ I_{\mathcal{N}} \end{bmatrix} \tag{1.4}$$

where $\mathbf{Z}$ is the symmetrical $\mathcal{N} \times \mathcal{N}$ impedance matrix of the configuration, $\mathbf{V}$ is the $\mathcal{N} \times 1$ applied voltage vector and $\mathbf{I}$ is the $\mathcal{N} \times 1$ current vector. As a result, if the impedance of all the coils, the mutual inductance between any two coils, and the excitation signal are known, the currents in each loop can be easily determined by matrix inversion.

[2] v_g is the group velocity, ω is the angular frequency and β is the angular wavenumber

The excitation is an external voltage V_0 applied in coil 1 of the MI waveguide. To simplify the configuration, it is assumed that all elements in the chain are identical ($R = R_n$, $L = L_n$ and $C = C_n$). Consequently, the simple wave solution is applied to (1.2) due to the attenuation of magnetic field, resulting the current of the n-th coil in the form:

$$I_n = I_0 e^{-n\gamma d} \tag{1.5}$$

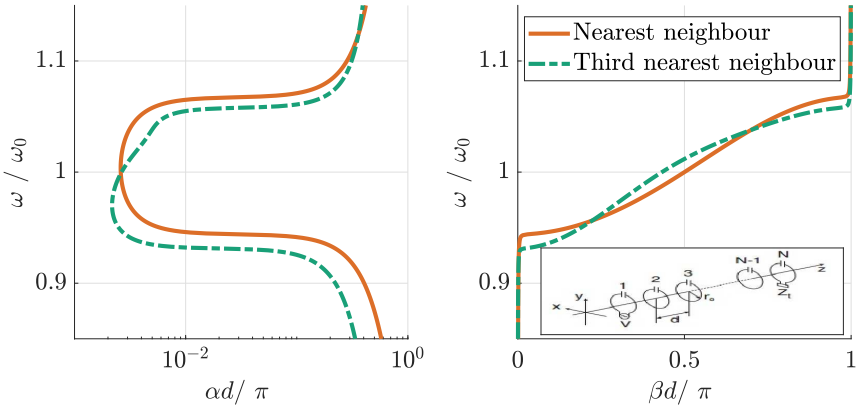
where I_0 is a constant, d is the separation between two adjacent elements, $\gamma = \alpha + j\beta$ is the propagation constant, α is the attenuation coefficient and β is the wave number. The dispersion relationship is finally derived by substituting (1.5) into (1.2) [32, 36]:

$$\frac{\omega_0^2}{\omega^2} + \frac{j}{Q}\frac{\omega_0}{\omega} - 1 = \sum_{n=1}^{p} \kappa_n \cosh(n\gamma d) \tag{1.6}$$

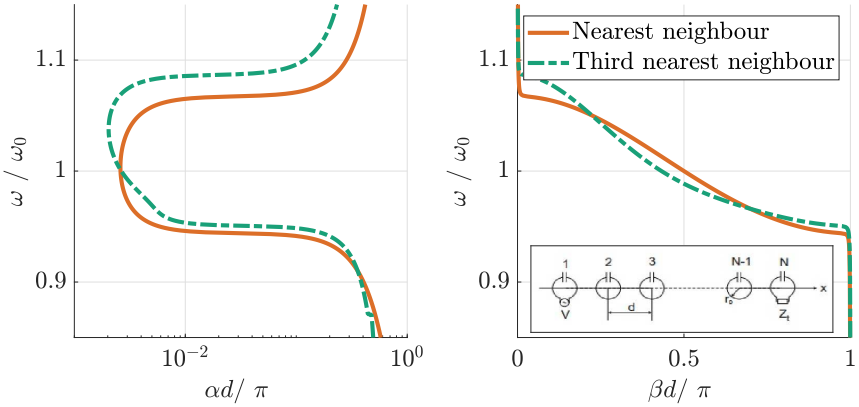
where $\omega_0 = 1/\sqrt{LC}$ is the fundamental resonant frequency of the capacitively-loaded split ring, $Q = \omega_0 L/R$ is the Q-factor, $\kappa_n = 2M_n/L$ is the mutual coupling coefficient, M_n is the mutual inductance between two loops located at a distance of nd apart from each other, p is the upper limits of the summation, depending on how far the elements can interact magnetically before their coupling becomes negligible. In fact, due to the rapid attenuation of magnetic field, if the distance between two adjacent elements is large enough, it is sufficient to consider nothing but the nearest neighbour magnetic coupling ($p = 1$). Therefore, in the lossless case ($Q \to \infty$), (1.6) can be reduced by applying the nearest neighbour approximation:

$$\frac{\omega_0^2}{\omega^2} - 1 = \kappa \cosh(\gamma d) \tag{1.7}$$

where $\kappa = 2M/L$ and M are the mutual coupling and mutual inductance of two adjacent loops, respectively. Fig. 1.4 shows the dispersion relationship ω/ω_0 as a function of αd and βd using the nearest-neighbour approximation and using the third-nearest-neighbour approximation in a coaxial 1-D structure of a positive coupling ($\kappa > 0$) and a coplanar 1-D structure of a negative coupling ($\kappa < 0$) in a very low-loss case ($Q = 1000$).



(a)



(b)

Figure 1.4: Calculated dispersion relationship by using (1.6) in (a) 1-D coaxial waveguide of a positive magnetic coupling coefficient ($\kappa > 0$) and (b) coplanar 1-D waveguide of a negative magnetic coupling coefficient ($\kappa < 0$) in a very low-loss case ($Q = 1000$). The solid orange lines represent the nearest neighbour interaction ($p = 1$) while the dash green lines represent the interactions up to the third nearest neighbours ($p = 3$). The distance between two neighbour coil is $d = 20$ mm.

It can be concluded from the dispersion curve that MM, particularly capacitively-loaded split rings in this case, can carry a slow type of waves with novel dispersion characteristics. There is a bandpass around the resonant frequency of the meta-atoms where MI waves can propagate along the structure whilst MI waves are evanescent outside this band with βd being either 0 or π. In the forbidden band, the currents of all elements are in phase when $\beta d = 0$ whereas currents of two adjacent elements are always of opposite phase when $\beta d = \pi$. Both cases exhibit strong attenuation of currents away from the source. In addition, as mentioned

before, a coaxial structure supports forward waves via a positive coupling coefficient. The phase velocity $v_p = \omega/\beta$ and group velocity $v_g = d\omega/d\beta$ of forward waves can be seen in the same direction from Fig. 1.4a. On the other hand, the backward waves, which have opposite sign of group velocity and phase velocity, exists in a coplanar structure, as shown in Fig. 1.4b.

In the passband, the propagation constant γ is purely imaginary for a lossless medium. The expression of bandpass of 1-D MI waveguide in relation to the magnetic coupling coefficient can be derived from (1.7) by setting $\cosh(\gamma d) = \cos(\beta d) = \pm 1$:

$$\frac{1}{\sqrt{1+|\kappa|}} \leqslant \frac{\omega_{pass-band}}{\omega_0} \leqslant \frac{1}{\sqrt{1-|\kappa|}} \tag{1.8}$$

Clearly, the magnitude of magnetic coupling among meta-atoms is the most important factor which determines the effectiveness of MM to assist the existence of MI waves. The coupling coefficient between any two elements, κ_n, however, is constrained by the magnetic flux conservation ($\kappa_n < 2$), or in other words, the mutual inductance must be less than self-inductance of a single element.

Interestingly, based on the (1.8), infinite bandwidth can be achieved when $\kappa > 1$. The lower-frequency cut-off definitely still exists but there will be no upper boundary of the passband as it expands to infinity with a vertical asymptote calculated by [32, 36]:

$$\beta d = \arccos(-\frac{1}{\kappa}) \tag{1.9}$$

Fig. 1.5 visualises one example of an infinite passband when $\kappa = 1.6$. It is assumed that there is extremely-low loss in structure and only the nearest neighbour interaction is taken into account. The dispersion curve exhibits an extremely sharp increase towards the vertical asymptote $\beta d = 0.715\pi$. It leads to an unlimited passband with the phase constant being almost unchanged as the frequency tends to infinity. The result suggests an almost ideal transmission waveguide of minimum dispersion at high frequencies when $\kappa > 1$. However, the circuit theory is only valid when the size of the circuit is much smaller compared to the wavelength. At higher frequency, the coil is no longer small in terms of electrical size, the

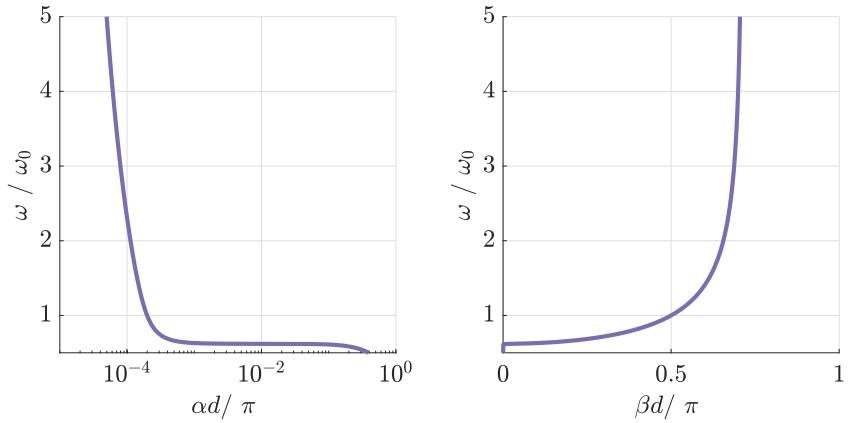


Figure 1.5: Calculated dispersion relationship by using (1.6) in a coaxial 1-D waveguide with a magnetic coupling coefficient of $\kappa = 1.6$ with the nearest neighbour approximation in a very low-loss case ($Q = 1000$). The distance between two neighbour coils is $d = 20$ mm. The vertical asymptote is $\beta = 0.715\pi$.

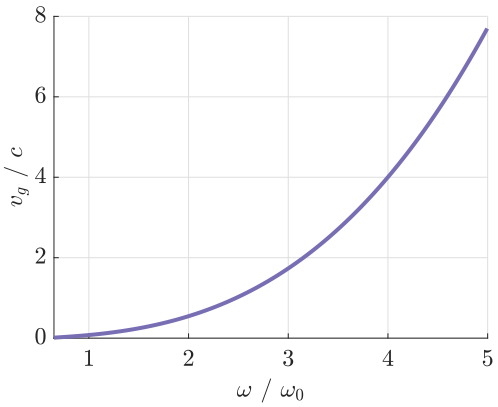


Figure 1.6: The normalised group velocity of MI waves calculated from Fig. 1.5. The result is normalised to the velocity of light in vacuum $c = 3 \times 10^8$ m/s.

current flowing is no longer uniform, and the retardation effect must be taken into account. This limitation can be shown clearly in the Fig. 1.6 of the group velocity. Obviously, from frequency $\omega/\omega_0 \approx 2.5$, the group velocity becomes larger than the velocity of light in vacuum. This result contradicts special relativity where signal speed is at most equal to the velocity of light in vacuum. Thus, the coupled circuit model for MI waves collapses unless the size of circuit are much smaller than the wavelength in free-space.

To sum up, the main features of dispersion relationship of MI waves have been enumerated in the case of one-dimension MM. At around the fundamental resonant

frequency of the waveguide elements, circuit theory is sufficient to understand and appreciate the phenomenon of these waves. For more details of MI waves in 2-D and 3-D dimension, see [4, 36].

1.4 Applications of Magnetoinductive Waves

In addition to applications exploring the unusual electromagnetic properties of MM as listed in Section 1.1, its guiding property has been received a great deal of attention since MM are shown to support the penetration of MI waves [34, 37]. MI waves exhibit several exciting advantages that may be exploited for potential applications, such as the simplicity of design, the relatively simple mathematical description of their operation, the full-dimensional penetration (existing in the form of 1-D, 2-D and 3-D waveguide structures), and the wide range of operating frequency, from the MHz to the THz region [34]. Various subwavelength devices are then successively proposed by employing the characteristics of MI waves, namely waveguides [32, 36, 40], near-field lenses [41–43], delay lines [44], directional couplers and phase shifter [37, 45, 46].

Additionally, MI waves can be exploited in the field of wireless data and power transfer. The experiments in [47] revealed that it is possible to achieve a data rate of approximately 60 Mpbs (for an assumed input signal-to-noise ratio of 10^4) and 305 Mbps (for an assumed input signal-to-noise ratio of 10^2) with the aid of 1-D coplanar MI waveguides and 2-D MI waveguides, respectively. Interestingly, it is advised that direct signal path is not the limitation of MI waves [48] as similar to the conventional wireless signals, resulting in a significant potential improvement of the flexibility and usability of networks by applying MIMO technique. MI waves can also be employed to do the job of wireless power transfer. Stevens et al. [49, 50] suggest that the relay coil system can be considered as a magnetic metamaterial waveguide that supports MI waves and thus, one can describe them by the properties of MI waves. Therefore, these works offer insights to redesign conventional near-field coupled systems based on the characteristics of MI waves in order to achieve a larger communication bandwidth, larger data capacity and better power transfer.

Another possible application of MI waves, that has emerged recently, is to support communication channels in attenuating media, such as underground/underwater [51, 52] or human body and tissue [53]. Conventional EM waves show numerous difficulties in dissipative media, especially at high frequency, which will be addressed in the next section. On the contrary, MI waves, by their nature, can solve these challenges, becoming a promising alternative technique for communications [54]. These advantages, for example, have been investigated in the petroleum industry since the 1940s. This technique is often called induction logging [55], with the original goal of non-destructive testing for the formation resistivity in oil-based-mud-boreholes or in air-drilled boreholes. By evaluating the interaction between two, or generally several coils placed coaxially in a borehole, it is possible to determine the conductivity of the surrounding soil that could reveal the existence of oil-bearing strata. Besides, since the human body and tissue are relatively conductive at microwave frequency, MI waves show a great potential for various medical applications, such as detections for magnetic resonance imaging (MRI) [56], body area networking [57, 58], wireless power for implants [59].

1.4.1 Underground/Underwater Communications

Apart from a regular wireless communications network operating in free-space or air, wireless underground/underwater communication networks (WUCNs) have been promising a huge variety of applications in military and civilian [51, 52]. These networks comprise devices that function below the surface of ground or water. Their recent applications include soil condition monitoring, border patrol and security, landscape management, submarine communications, ocean exploration, location and positioning [54]. Underground/underwater, or in general, conducting media, however, present an extreme limitation for wireless links since the environment is no longer an insulator. The EM wireless signals interact strongly with the surrounding environment, eventually encountering three significant issues, such as high path loss, low channel condition quality and large antenna size [54]. The wireless system using EM technique is then restricted.

The propagation of TEM waves in a general conductive environment is illustrated in Fig. 1.7. When the waves move in z-direction, their attenuation when propagating through a medium is expressed by the equation:

$$\mathbf{E} = \mathbf{E}_0 e^{j(\omega t - \gamma z)} = \mathbf{E}_0 e^{j(\omega t - \beta z)} e^{-\alpha z} \tag{1.10}$$

where $\mathbf{E}$ is the electric field vector, $\mathbf{E}_0$ is the spatial amplitude vector of the electric field, $\gamma = \alpha + j\beta$ is the propagation constant, α is the attenuation constant, β is the phase constant, $e^{j(\omega t - \beta z)}$ is the variation of the field with space and time, $e^{-\alpha z}$ is the exponential decay due to the skin depth effect, and ω is the angular frequency.

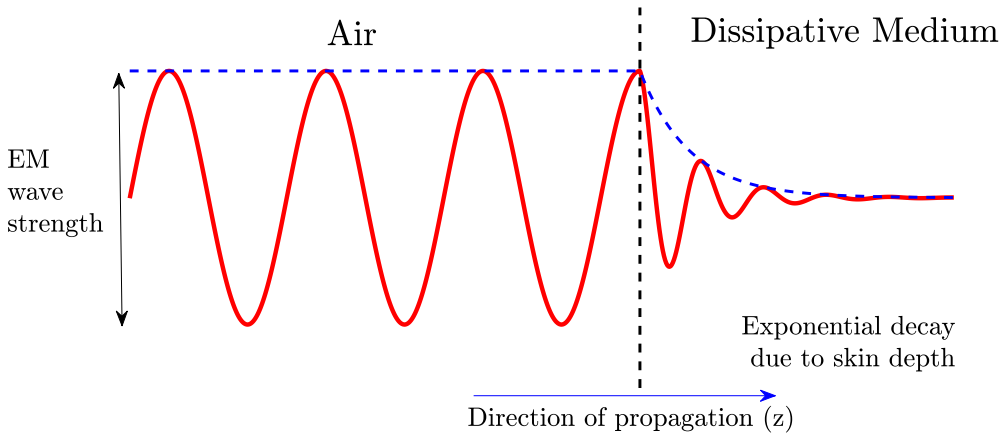


Figure 1.7: Attenuation of an EM wave when crossing a conductive medium.

The general solution of the propagation constants of a plane wave can be found by solving the homogeneous wave equation in the far-fields [60]:

$$\begin{cases} \alpha = \omega \sqrt{\dfrac{\mu\epsilon}{2}\left[\sqrt{1+\left(\dfrac{\sigma}{\omega\epsilon}\right)^2} - 1\right]}, \\ \beta = \omega \sqrt{\dfrac{\mu\epsilon}{2}\left[\sqrt{1+\left(\dfrac{\sigma}{\omega\epsilon}\right)^2} + 1\right]}. \end{cases} \tag{1.11}$$

where ϵ, μ, and σ are the permittivity, permeability, and conductivity of medium, respectively. The skin depth indicates the distance from the surface of the medium at which the field strength of travelling waves decays by an amount of $1/e$, expressed

as the reciprocal of the attenuation constant:

$$\delta = \frac{1}{\alpha} = \frac{1}{\omega\sqrt{\frac{\mu\epsilon}{2}\left[\sqrt{1+\left(\frac{\sigma}{\omega\epsilon}\right)^2}-1\right]}}. \tag{1.12}$$

In good conductors ($\sigma \gg \omega\epsilon$), by neglecting the displacement current term, the propagation constants in (1.11) and the skin depth in (1.12) reduce to

$$\begin{cases} \alpha = \beta = \sqrt{\frac{\omega\mu\sigma}{2}}, \\ \delta = \frac{1}{\alpha} = \sqrt{\frac{2}{\omega\mu\sigma}}. \end{cases} \tag{1.13}$$

From (1.10), TEM waves face a challenge of extremely rapid attenuation because of the absorption of the medium background. Not only that, the waves are shortened in wavelength, resulting in slower velocity while travelling in the conductive medium. Moreover, the path loss of EM waves is seen to depend exponentially on the conductivity of the environment which is usually unpredictable over time and space. A typical example is as follows. Properties of soil may fluctuate with time, affected by weather or geological activities while in a given short distance, the change of elements of which soil is composed, e.g., sand, water, minerals, organic matter and etc., leads to a drastic modification of soil properties. As a result, channel conditions are often spatially and temporally anisotropic. Finally, there has been a trade-off in antenna designs. It is usually expected to shift the operating frequency lower to attain a practical transmission distance of several meters as the medium conductivity increases [54]. The antennas size, in turn, become larger for efficiently transmitting and receiving signals.

MI waves, on the other hand, are capable of resolving three challenging problems above, emerging as a better substitute of conventional EM waves for WUCNs. Technically, as stated in the Section 1.3, MI waveguides carry signals that utilise near-field magnetic couplings between resonant elements, relying mostly on the relative permeability of the medium, μ_r. Since the permeabilities of most soil, liquid or ordinary supporting environments do not usually deviate from that of free-space, $\mu_r = 1$ [54], some properties of medium, e.g., texture, structure, density and etc.,

can be then excluded, reducing the complexity of the networks and easing the signal processing. By tailoring the MI wave parameters, one can even minimize further the path loss. Hence, this feature of MI waves properly addresses the high path loss of EM waves and also their variable channel conditions with time and space. In the MI waveguide system, transmission links are established by chains of small coils where each coil may be regarded as a magnetic dipole. Thus, there is no theoretical lower limit for the size of the transmitting and receiving antennas. In spite of working at low frequency, the antennas in systems using MI waves can be maintained significantly smaller than that of systems using transverse EM waves. In addition to three major advantages over EM waves, MI waveguides might be preferable due to their discrete structure having spatially isolated resonant circuits. Unlike usual continuous waveguides, MI waveguides are fairly flexible and easy to manufacture, install, maintain, replace and deploy.

1.4.2 Medical Devices

Another promising field of MI waves is medical diagnosis and treatment applications because human organs and tissue are moderately conductive. Early on, Shamonina et al. [32], when they proposed the first MI waveguide, predicted that it would likely contribute to the well-established clinical MRI technique. Many devices or methods employing MI waves are then proposed to improve MRI, such as MI catheter receiver [61], and MI data-transferring cables inside MRI system [56]. It is also suggested that the common routine of image recovery via Fourier transform might be replaced by point-to-point near field transfer that is able to reconstruct subwavelength information, which is evanescent over the former process [35].

The future research direction, however, might focus primarily on medical devices related to communications on or inside human body. This research field is often known as body area networking (BAN) [57, 58]. In principle, BAN is a technology at the human scale which enables wireless communications between sensors placed on or inside the body and a central unit. One main BAN application is real-time monitoring and devices of health services. Such networks employ a collection of

wireless sensors worn or implanted on the body to collect real-time vital physical and physiological parameters of patients, i.e., heart rate, blood pressure, body temperature, respiration rate and so forth [58]. While EM radiation has been a predominant technique for BAN, it still has several drawbacks. Current sensor technology requires battery power and also, EM signals have a limited range in dissipative media. Apart from that, channel modelling is extremely difficult for practical implants and wearable devices; and antenns are constrained by size, materials, shape, etc. [57]. Moreover, even the general effect of a long RF exposure on human health is still officially undetermined [62], there are several recent researches [63, 64] showing evidences of RF exposure being responsible for some terrifying diseases, such as cancer or brain damage. MI communications with the aid of MI waves, as a result of these downsides, has emerged as a suitable candidate to the job of BAN in health services. Wireless power transfer by near field couplings in poor media can address the question of power limitations. MI communications systems have been shown to have a longer transmission range than conventional EM systems in conducting materials [51]. Finally, as explained in section 1.4.1, since almost all organic matters are impermeable, the channel conditions and the fear of harmful RF can be solved.

One novel example of systems using MI communications is 'Swallowable capsule' [59], as captured in Fig. 1.8. The capsule enters human or animal body through their mouth to measure the gas level in the digestive system. The sensor inside the capsule converts the analogue measured data into digital signals in order to transmit through a wireless system. Each capsule has a coil, acting as an antenna to convey the data from inside the body to outside components via near field magnetic couplings. Such a sensor could also use its coil to communicate with MI-wave-based power and data networks, recharging its battery as required.



Figure 1.8: The swallowable capsule and its schematic graphs. The capsule is used to measure the gas level along the gastrointestinal tract of human or animals [59].

1.5 Research Challenges and Thesis Structure

1.5.1 Research Challenges

In terms of signal transmission, the propagation of a signal in a given medium is the most important parameter. The radiation of TEM waves in conductors was understood and described a long time ago by the Maxwell's equations. However, impact of a conductive environment on near-field coupling is not well described by the skin effect model. There is as yet no theoretical or numerical model to express the penetration of MI waves in attenuating environments. To the best of my knowledge, there is no theoretical or numerical model to express the penetration of MI waves in attenuating environments. All the equations in section 1.3 are valid if and only if the medium is free-space. The exact effects of conducting media upon magnetic channels are still unknown in most current literature. It has been a difficulty for applications using MI waves working inside an attenuating environment. Most applications require real time, stable and accurate communications with extremely strict constraints in size and power. Also, when there are numerous devices, the bandwidth of the network can become another problem. Thus, without the knowledge of MI propagation within a conductive medium, some parameters of the network cannot be optimized. This may lead to inefficient and costly systems. In conclusion, it is essential to establish an adequate model of the attenuation of MI waves for the near-field communications in dissipative media.

1.5.2 Thesis Structure

This thesis is organised as follows.

- Chapter 2 examines the effects of an interposing attenuating medium on the magnetic coupling between two low-frequency coils in close proximity. The most popular current model based on an approximation of plane waves travelling in a conductor is reinvestigated. Then, the analytical solutions available in literature are generalised by including retardation effects in order to take into account an arbitrary permittivity of the conductive medium. Simulation results obtained by CST and experimental data are then reported and compared to the analytical values and the plane-wave approximation.

- Chapter 3 reports a new field model as a combination of circuit theory and the field theory - for two coils coupled inside an infinite homogeneous attenuating medium. It is then proved that apart from a change in the mutual inductance, there indeed exists an alteration in self-inductance via the impact of eddy currents in the environment background (lossy self-inductance). CST simulations are conducted and compared to the analytical method.

- Chapter 4 presents the network analysis for a system of two coupled coils in a dissipative environment with the circuit model developed in Chapter 3. The impact of the medium background on important circuit parameters, such as the self resonance, and the Q-factor, is presented. Furthermore, the frequency splitting, current responses and power conversation are addressed in detail.

- Chapter 5 analyses the characteristic of an MI waveguide structure inside a dissipative medium. A general dispersion equation of MI waves is derived from the equivalent circuit model. Laboratory experiments are conducted to validate the proposed theory.

- Chapter 6 considers one potential application of the novel circuit model: wireless power transfer via coupled resonators in RF-challenging environments.

The conditions for optimal working frequency are established. Based on these conditions, several guidelines for system design are proposed.

- Chapter 7 outlines the summary and final conclusions of this thesis. Then, some limitations of the developed model are discussed, followed by several suggestions for future works.

2

Impact of an Intervening Attenuating Medium

Contents

2.1 Limitations of Current Models: Plane-Wave Approximation 22
2.2 Generalised Field Solutions 25
2.3 CST Models and Simulations Results 29
2.3.1 CST Models 30
2.3.2 Simulations Results 31
2.4 Experiments 44
2.4.1 Experimental Apparatus 44
2.4.2 Experimental Results 46
2.5 Conclusions 49

A brief introduction of MI waves in metamaterials is given in the previous chapter. From the dispersion relationship of MI waves, mutual coupling is the key parameter to determine the characteristic of MI waves. In Chapter 2, the impact of an intervening dissipative medium of the mutual coupling between two coupled coils is investigated. Section 2.1 discusses the limitations of a current model used in most literature – plane-wave approximation. In Section 2.2, by including the displacement current term, the analytical solution for a coil above an infinite conductive block is generalised in order to cover the higher range of frequency and

the diversity of material conductivity. Section 2.3 shows the simulation results for the magnetic field, Poynting vector and mutual inductance in CST studio. The measurements to verify the simulations and analytical data are reported in Section 2.4. The main contribution of this Chapter is to examine the validity of the plane-wave approximation. Some of the work in this chapter have been published in the following journals/conference proceedings:

- A. Vallecchi, **S. Chu**, C. J. Stevens, E. Shamonina and L. Solymar, 'Coupling between coils in the presence of conducting medium', *IET Microwaves, Antennas & Propagation*, vol. 13, no. 1, 2018.

- A. Vallecchi, **S. Chu**, C. J. Stevens and E. Shamonina,'Impact of a conducting medium on the coupling of meta-atoms', *Proceedings of 10th International Congress on Advanced Electromagnetic Materials in Microwaves and Optics (Metamaterials)*, Crete, Greece, 2016, pp. 385-387.

2.1 Limitations of Current Models: Plane-Wave Approximation

The impact of a nearby dissipative medium on the magnetic channel between two low-frequency coils is usually assumed to be described by the TEM waves in most literature. In the model of some early researches on WUCNs, the medium background is considered to have little-to-no effect on the magnetic channels and thus, assumed to be free-space [51, 52, 65–67]. The lay-out of such a system is illustrated in Fig. 2.1. Two coils acting as a pair of transmitting and receiving antennas are exploited to establish a communications channel in a lossy medium. Each coil is placed inside an insulating box to prevent direct contacts with the environment. It is assumed that the coils are made of a plurality of multiple filamentary turns [51, 52, 65–67].

In these works, the coils are considered as magnetic dipoles and thus, the mutual inductance between them is derived from the magnetic vector potential generated by

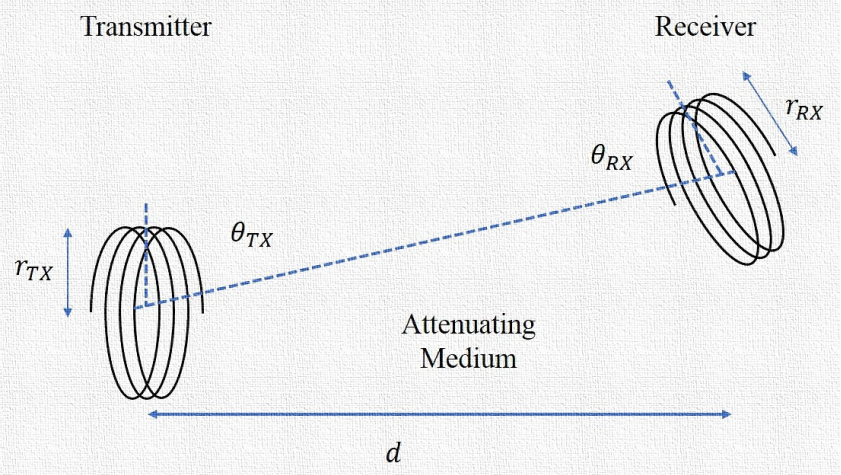


Figure 2.1: The general schematic diagram of a WUCN, consisting of a pair of transmitting and receiving coils.

magnetic dipoles in free space. However, the authors have made a simple assumption that the path loss is independent on the medium's properties [51, 52, 65–67]. In other words, the mutual inductance of two coils in an attenuating medium does not differ from that in vacuum, given approximately by [66]:

$$M \approx \mu\pi N_t N_r \frac{r_{TX}^2 r_{RX}^2}{4d^3} \left(2 \sin\theta_{TX} \sin\theta_{RX} + \cos\theta_{TX} \cos\theta_{RX}\right) \tag{2.1}$$

where μ is the permeability of the medium, N_t, N_r, a_t, and a_r are the number of turns and the radii of the transmitting coil and receiving coil respectively, θ_{TX} and θ_{RX} are the angles between the coil radial directions and the line connecting the coil centres, and d is the horizontal distance between two coils, as shown in Fig. 2.1. Obviously, this poor assumption makes the model invalid in practice, especially for highly conductive media.

Later, a more realistic transmission model has been developed, wherein the effect of medium-based losses is taken into account [68, 69]. From the electromagnetic points of view, the time-varying magnetic field generated by a current loop induces eddy currents in conductors nearby due to Faraday's law of induction. Thus, in the case of WUCNs, there are eddy currents induced in the medium background, causing an additional attenuation for the initial magnetic field, as expected from Lenz's law. A scaling factor G, as a result, is introduced to (2.1) to represent the

extra loss factor due to the eddy currents. Here, an assumption is made that the magnetic field strength decays at the same rate of an EM plane wave propagating in a conducting material, i.e., $G = \exp(-d/\delta)$, where δ is the skin depth [69]. Thus, mutual inductance is rewritten as [69]:

$$M \approx \mu\pi N_t N_r \frac{r_{TX}^2 r_{RX}^2}{4d^3} \left(2\sin\theta_{TX}\sin\theta_{RX} + \cos\theta_{TX}\cos\theta_{TX}\right) e^{\frac{-d}{\delta}}. \tag{2.2}$$

Since underground/underwater is a poorly conductive environment ($\sigma \ll \omega\epsilon$), the skin depth is calculated as in (1.12):

$$\delta = \frac{1}{\omega\sqrt{\frac{\mu\epsilon}{2}\left(\sqrt{1+\frac{\sigma^2}{\omega^2\epsilon^2}}-1\right)}} \tag{2.3}$$

where ω is the angular frequency, and ϵ and σ is the permittivity and conductivity of the medium respectively. Apparently, the "model with attenuation" by (2.2) has a better reliability rather than the "model without attenuation" by (2.1). This assumption might be called 'plane wave' (PW) approximation since it is assumed that the near field magnetic field decays at the same rate as a plane-wave travelling in a conductor.

Experiments under realistic soil conditions to compare these two models are conducted in [70]. However, even though the value obtained with the "model with attenuation" is in better agreement with the measurement data, Ma et al. noticed with deep concern that:

> "Whereas, it is possible that the "model with attenuation" presented in this section does not constitute the optimal model. Specifically, the attenuation characteristic G is valid for far-zone electromagnetic waves but might not hold true for near-zone magnetic fields. Therefore, further investigation is needed to model the attenuation characteristics of MI channels more precisely." [70]

In my view, the attenuation of MI waves due to the eddy currents in conductive media cannot be described simply by the properties of EM plane waves in conductors. Mutual inductance between coils is a near-field rather than a far-field phenomenon. Although it is expected that the propagation depth is inversely proportional to

the medium conductivity, a current loop or a magnetic dipole does not provide a plane-wave type of magnetic field in the near regions. Also, key amongst the differences this implies is that the main component of the magnetic field in MI communications systems is parallel rather than perpendicular to the direction of wave penetration. The validity of the plane-wave assumption, therefore, needs to be tested again by other independent methods. These methods will be further explained in the next three sections.

2.2 Generalised Field Solutions

To understand the attenuating effects of the medium, the most common approach is to formulate the differential equation that illustrates the electromagnetic fields of the system. In 1968, Dodd and Deeds (D&D) first formulated and solved mathematically a classical study of circular air core coils over a semi-infinite conducting block [71]. This method is then a milestone for solving an eddy-current probe-coil problem which can be further extended for various applications and scenarios [72–77]. Since the D&D method mostly considers applications in the field of non-destructive eddy current testing at very low frequency (typically kHz) for highly conductive materials or components (especially metals), displacement currents are often much less than conduction currents and therefore are negligible. The ideal quasi-static approximation[1] is always performed. Here, instead, the displacement currents are taken into account to cover the higher range of frequency and the diversity of material conductivity, from that of dry sand ($\sigma \approx 10^{-3}$ S/m) to that of a fictitious conducting material ($\sigma \approx 10^{8}$ S/m). Also, because this thesis is primarily interested in applications for communications in RF-challenging environments (underground/underwater, human body and tissue, etc.), the range of conductivity between 0 and 10 S/m is crucial due to the fact that conductivity

[1]Quasi-static approximation: when the dimensions of the physical structure are much smaller than the electromagnetic wavelength associated with the dominant timescale of the problem, the fields often satisfy the Laplace equation (static field) even all the fields are time-dependent. The quasi-static approximation can be performed by neglecting the displacement current term [78].

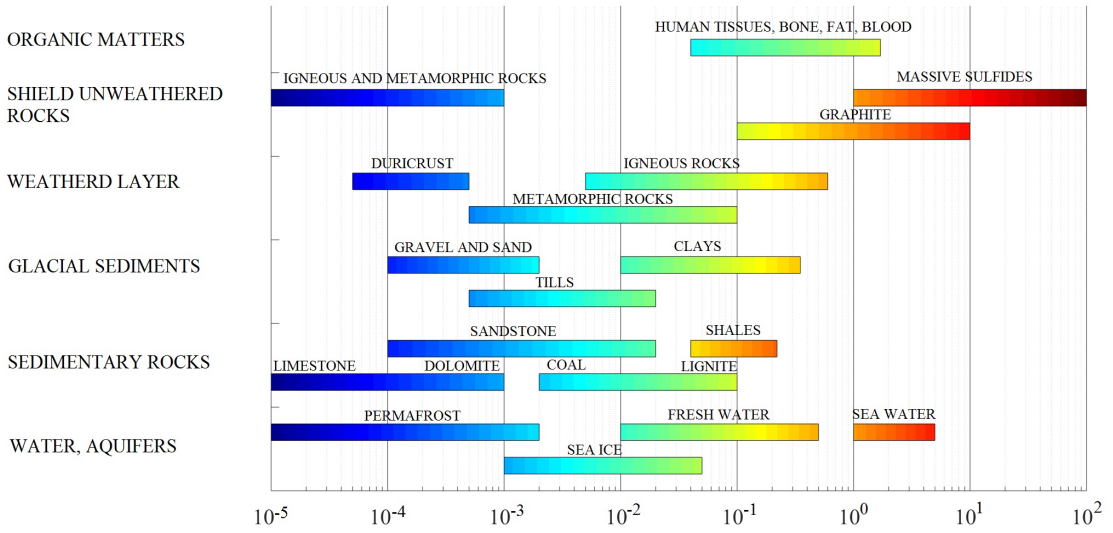


Figure 2.2: Typical ranges of conductivity (S/m) for selected Earth materials and human organic matter [79–81].

of most earth-material, human tissue and organics lie down in that range [79–81], as shown in Fig. 2.2.

Here, a special case of filamentary coils is considered. The cross section of the configuration investigated is shown in Fig. 2.3: an infinitely wide slab of conductivity σ and thickness c is placed between two coils of radii r_1 and r_2 with the same orientation at a certain distance apart from each other. Space is divided into the four regions labelled with Roman numbers: above the coil (**I**), below the coil but above the slab (**II**), the conducting slab (**III**), and below the slab (**IV**). To simplify the configuration, the regions (**I**), (**II**), and (**IV**) are assumed to be vacuum.

The transmitting coil is driven by a current density $\boldsymbol{J_0}$ while the receiving coil is left open circuited. At low frequency, the current density in the wire cross section is principally uniform and then is approximated by a filamentary current. For most eddy current problems, it is convenient to solve the boundary conditions in cylindrical coordinates [82]. All the media are assumed to be linear, isotropic and homogeneous. Hence, the differential equation for the magnetic vector potential

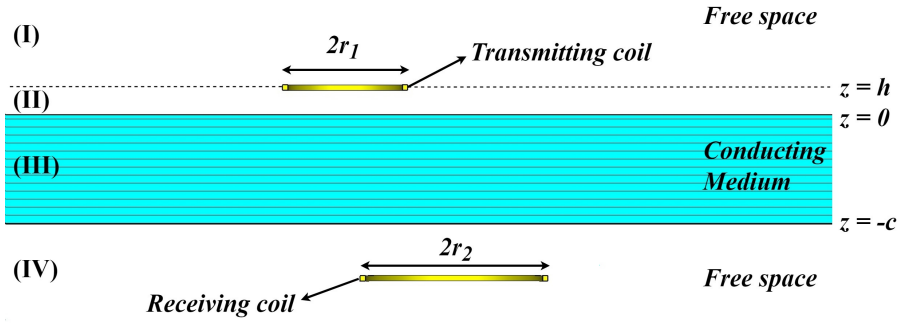


Figure 2.3: The cross-section of the configuration investigated consisting of two circular air core coils with the same orientation intervened by an infinitely wide conducting slab of varying conductivity.

$\mathbf{A}$ in region n due to an applied current density $\boldsymbol{J_0}$ is derived as [71]:

$$\begin{aligned}\boldsymbol{\nabla}^2\mathbf{A}^{(n)} &= \begin{bmatrix} \frac{\partial^2 A_\rho^{(n)}}{\partial z^2} + \frac{\partial^2 A_\rho^{(n)}}{\partial \rho^2} + \frac{1}{\rho}\frac{\partial A_\rho^{(n)}}{\partial \rho} - \frac{A_\rho^{(n)}}{\rho^2} + \frac{1}{\rho^2}\frac{\partial^2 A_\rho^{(n)}}{\partial \varphi^2} - \frac{2}{\rho^2}\frac{\partial A_\varphi^{(n)}}{\partial \varphi} \\ \frac{\partial^2 A_\varphi^{(n)}}{\partial z^2} + \frac{\partial^2 A_\varphi^{(n)}}{\partial \rho^2} + \frac{1}{\rho}\frac{\partial A_\varphi^{(n)}}{\partial \rho} - \frac{A_\varphi^{(n)}}{\rho^2} + \frac{1}{\rho^2}\frac{\partial^2 A_\varphi^{(n)}}{\partial \varphi^2} + \frac{2}{\rho^2}\frac{\partial A_\rho^{(n)}}{\partial \varphi} \\ \frac{\partial^2 A_z^{(n)}}{\partial z^2} + \frac{\partial^2 A_z^{(n)}}{\partial \rho^2} + \frac{1}{\rho}\frac{\partial A_z^{(n)}}{\partial \rho} + \frac{1}{\rho^2}\frac{\partial^2 A_z^{(n)}}{\partial \varphi^2} \end{bmatrix}^{\boldsymbol{T}} \begin{bmatrix} \widehat{\boldsymbol{\rho}} \\ \widehat{\boldsymbol{\varphi}} \\ \widehat{\boldsymbol{z}} \end{bmatrix} \\ &= -\mu_0 \boldsymbol{J_0} + \mu^{(n)}\sigma^{(n)}\frac{\mathrm{d}\,\mathbf{A}^{(n)}}{\mathrm{d}\,t} + \mu^{(n)}\epsilon^{(n)}\frac{\mathrm{d}^2\,\mathbf{A}^{(n)}}{\mathrm{d}\,t^2} \end{aligned} \tag{2.4}$$

where $[\mathbf{X}]^{\boldsymbol{T}}$ is the transpose matrix of a matrix $[\mathbf{X}]$, ρ, φ, and z are the radial, azimuthal, and axial coordinates, $\widehat{\boldsymbol{\rho}}$, $\widehat{\boldsymbol{\varphi}}$, and $\widehat{\boldsymbol{z}}$ are the corresponding unit vectors in cylindrical coordinates, μ_0 is the permeability of free space, $\mu^{(n)}$, $\epsilon^{(n)}$, and $\sigma^{(n)}$ are the permeability, permittivity, and conductivity of the n-th region respectively, and t is the time variable. Basically, the induced eddy current density must be in the same direction as the magnetic vector potential. With the assumption of an axially symmetric conductor geometry, the induced eddy currents has only one spatial component along the azimuthal angle φ and so is the magnetic vector potential, i.e., $\mathbf{A}^{(n)}(0, A_\varphi^{(n)}, 0)$ and $\partial\mathbf{A}^{(n)}/\partial\varphi = 0$. Hence, (2.4) reduces to:

$$\begin{aligned}\boldsymbol{\nabla}^2\mathbf{A}^{(n)} &= \left(\frac{\partial^2 A_\varphi^{(n)}}{\partial z^2} + \frac{\partial^2 A_\varphi^{(n)}}{\partial \rho^2} + \frac{1}{\rho}\frac{\partial A_\varphi^{(n)}}{\partial \rho} - \frac{A_\varphi^{(n)}}{\rho^2}\right)\widehat{\boldsymbol{\varphi}} \\ &= \left(-\mu_0 J_0 + \mu^{(n)}\sigma^{(n)}\frac{\mathrm{d}\,A_\varphi^{(n)}}{\mathrm{d}\,t} + \mu^{(n)}\epsilon^{(n)}\frac{\mathrm{d}^2\,A_\varphi^{(n)}}{\mathrm{d}\,t^2}\right)\widehat{\boldsymbol{\varphi}}\end{aligned} \tag{2.5}$$

By using the mathematical method adapted in [71] to solve (2.5) (see Appendix A), the magnetic vector potential in each region is expressed in the general form:

$$A_{\varphi}^{(n)}(\rho, z, \omega) = \int_0^{\infty} \left(X^{(n)} e^{-\alpha_n z} + Y^{(n)} e^{\alpha_n z} \right) \mathrm{J}_1(\alpha\rho)\, \mathrm{d}\alpha \tag{2.6}$$

where $X^{(n)}$ and $Y^{(n)}$ are functions of the separation constant α, and J_1 is the Bessel function of the first kind and the first order. Here, the main contribution of this thesis is to generalise the analytical solution by including the displacement current term instead of using the quasi-static approximation as in [71], i.e., $\alpha_n = \sqrt{\alpha + j\omega\mu^{(n)}\sigma^{(n)} - \omega^2\mu^{(n)}\epsilon^{(n)}}$ in place of $\alpha_n = \sqrt{\alpha + j\omega\mu^{(n)}\sigma^{(n)}}$ in [71]. Once the magnetic vector potential is known, the induced electromotive force in the receiving coil may be obtained as:

$$\begin{aligned} \mathcal{E} &= j\omega \oint \boldsymbol{A}^{(\mathbf{IV})} \cdot \mathrm{d}\boldsymbol{l} \\ &= j\omega \int \rho\, A_{\varphi}^{(\mathbf{IV})}(\rho, z)\, \mathrm{d}\varphi \end{aligned} \tag{2.7}$$

where $\mathrm{d}\boldsymbol{l} = \mathrm{d}\rho\, \widehat{\boldsymbol{\rho}} + \rho \mathrm{d}\varphi\, \widehat{\boldsymbol{\varphi}} + \mathrm{d}z\, \widehat{\boldsymbol{z}}$ is the line element of the coil winding path. Recalling that the Cartesian coordinates of the points along the circumference of the receiving coil are $(x,\, y) = (x_2 + r_2 \cos\theta,\, y_2 + r_2 \sin\theta)$, where $(x_2,\, y_2)$ is the centre point of the receiving coil, r_2 is the receiving coil radius, and θ is a local angular coordinate varying from 0 to 2π. The induced voltage can be rewritten as:

$$V = j\omega \int_0^{2\pi} r_2 \cos(\varphi - \theta)\, A_{\varphi}^{(\mathbf{IV})}(\rho, z)\, \mathrm{d}\theta \tag{2.8}$$

where

$$\begin{cases} \rho &= \sqrt{(x_2 + r_2\cos\varphi)^2 + (y_2 + r_2 \sin\varphi)^2} \\ \varphi &= \arctan\left(\dfrac{y_2 + r_2 \sin\theta}{x_2 + r_2 \cos\theta} \right) \end{cases} \tag{2.9}$$

Finally, the mutual inductance between two coils is determined as the ratio of the induced electromotive force in the receiver over the total current in the transmitter:

$$M = \frac{\mathcal{E}}{j\omega I}. \tag{2.10}$$

2.3 CST Models and Simulations Results

In this section, the magnetic field distribution and the mutual inductance of two low-frequency coils in the presence of an attenuating material will be studied intensively. Four different approaches are employed to determine the mutual inductance: the PW approximation in Section 2.1, the quasi-static solution derived by D&D for an infinitely wide conducting slab [71], the evolved field solution to include the displacement current described in Section 2.2, and the finite numerical simulation provided by CST EM Studio (CST EMS) [83] using low-frequency and static package. Throughout the simulations and calculations, the geometry of the coil configuration, as shown in Fig. 2.4, is maintained the same. Two identical coils, acting as a transmitter (above) and a receiver (below), are placed coaxially with the distance between centres being $d = 37$ mm. The coil has a mean radius $r_0 = 11$ mm, a square cross-section $w = 1$ mm. A conductive cylindrical block of a diameter D mm and a thickness of t is inserted between two coils.

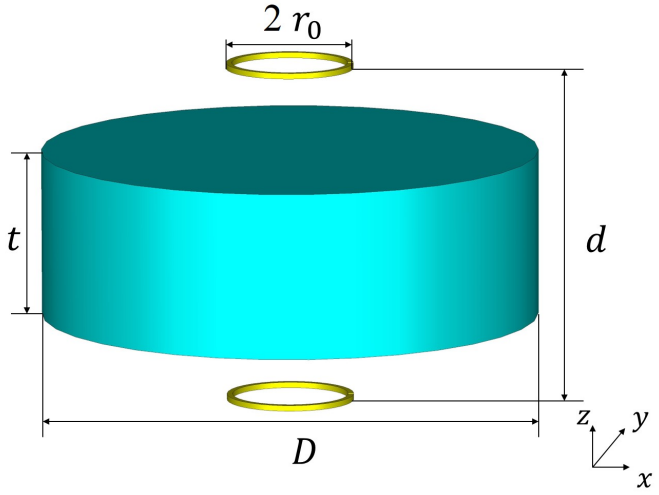


Figure 2.4: The basic configuration investigated in CST EMS, consisting of a conductive material placed centrally-aligned between two coaxial identical circular air core coils.

In this work, I shall cover the full range of conductivity of the block from $\sigma^{(\mathbf{III})} = 0$ to $\sigma^{(\mathbf{III})} = 10^8$, the range of relative permittivity from that of air ($\epsilon_r^{(\mathbf{III})} = 1$) to that of tap water ($\epsilon_r^{(\mathbf{III})} = 78$) [84, 85] and the range of thickness from

a thin plate to the one filling nearly the whole space between the coils. Due to the fact that most of the applications involving conductive media employs near-field coupled coils with uniform currents, the working frequency can be up to values where the coils are electrically small. In other words, the wavelength should be less than one tenth of the coil's circumference [86]. For simplicity and without loss of generality, all results presented in Section 2.3 are calculated at the angular frequency $\omega = 10^9$ rad/s corresponding to $f \approx 159$ MHz.

2.3.1 CST Models

In near-field systems, the absorption of power to produce a current in the receiver can cause a change in the load of the transmitter. Therefore, to simulate the impact of the conductive medium on the impedance of the transmitter as well as the induced electromotive force at the receiver, the near-field feedback effects due to the receiver's current must be neutralized. For this purpose, the transmitting coil in CST EMS is excited by using a lumped port, injecting an alternating current of a constant amplitude of 1 A while the receiving coil is connected to a current port of 0 A. These ideal ports aim to eliminate the conduction current in the receiver, leaving only the induced electromotive force in the receiver to be measured and thus, resulting in no feedback effect from the receiver to the transmitter, as can be seen from (2.11).

$$\begin{bmatrix} Z & j\omega M \\ j\omega M & Z \end{bmatrix} \begin{bmatrix} 1 \\ 0 \end{bmatrix} = \begin{bmatrix} Z \\ j\omega M \end{bmatrix} = \begin{bmatrix} V_1 \\ V_2 \end{bmatrix} \tag{2.11}$$

where Z is the self-impedance of the coils, M is the mutual inductance between them, V_1 and V_2 is the voltage at the current ports of coil 1 and coil 2 respectively. The mutual inductance can be directly calculated from the voltage at the current port in coil 2.

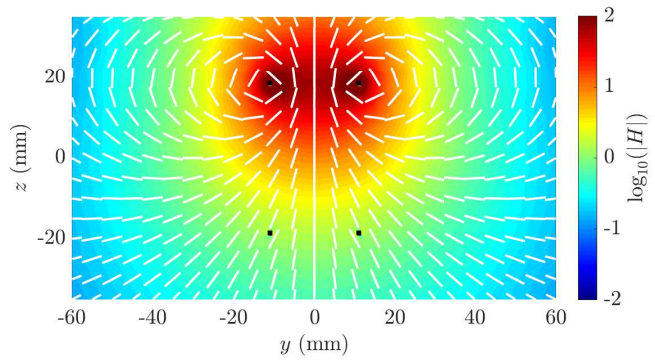
$$M = \frac{V_2}{j\omega} \tag{2.12}$$

2.3.2 Simulations Results

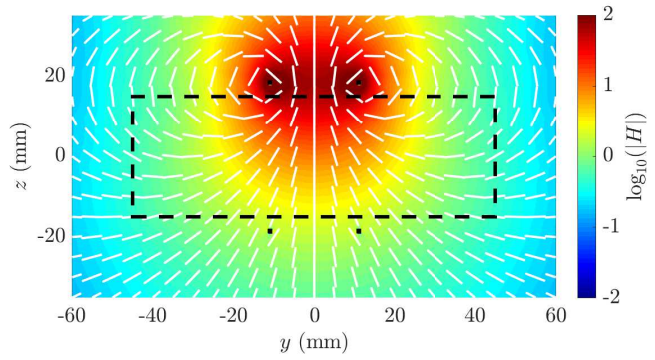
2.3.2.1 Magnetic Field Distribution

The magnetic field distribution of the configuration is illustrated to understand the details of the underlying physics. Fig. 2.5 shows the amplitude and polarisation[2] of the total magnetic field produced by an air core circular coil in air and in the presence of a non-conductive block. Numerical results are obtained with CST EMS. In general, the time-varying magnetic field generated by the transmitting coil in vacuum is linearly polarised or in other words, non-rotating. The polarization ellipses of the magnetic field collapse to straight lines, as shown in Fig. 2.5a. The simulated mutual inductance then has a negligible imaginary part which associates with the retardation effect, $M = 0.4636\angle{-0.01^\circ}$ nH. When inserting a non-conductive material with a higher relative permittivity ($\epsilon_r^{(\mathbf{III})} = 78$), i.e., de-ionized water, the magnetic field seems to remain unchanged in the polarization but to increase in magnitude. As a consequence, the simulated mutual inductance changes to $M = 0.5692\angle{-0.01^\circ}$. The reason behind that trend is because the intervening dielectric slab magnify the displacement currents between two coils. Therefore, the mutual inductance increases due to the change in the electrical length. This phenomenon validates the argument in section 2.3 to include the displacement currents into the field solutions for poorly conductive media.

[2]The polarisation refers to the orientation of the field vector that may be in a constant direction or may vary with time [87].



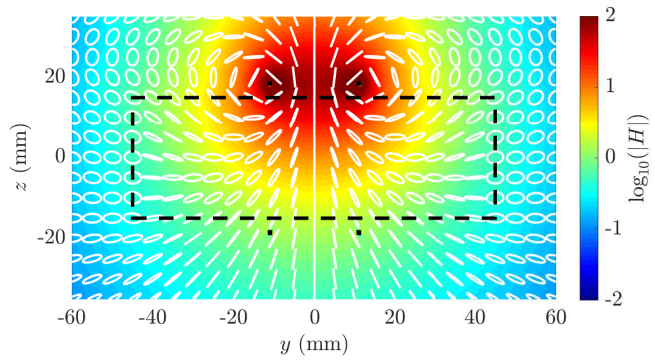
(a) Air ($\epsilon_r = 1$ and $\sigma = 0$ S/m)



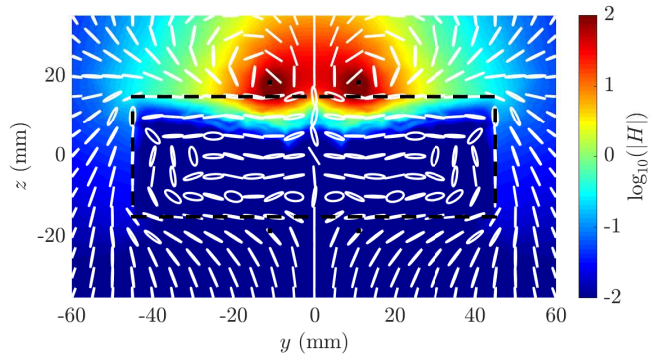
(b) Lossless Dielectric ($\epsilon_r = 78$ and $\sigma = 0$)

Figure 2.5: Simulated amplitude and polarization of the total magnetic field generated by a transmitting coil (a) in air and (b) in the presence of a non-conducting dielectric block in the yz-plane. The cylindrical block has a dimension of $D = 90$ mm, thickness of $t = 30$ mm and relative permittivity of $\epsilon_r^{(\mathbf{III})} = 78$. Polarization ellipses are normalised at a sampling step of 5 mm along the y and z axes. Black dash lines mark the cross sections of the block while black dots represent transmitter (top) and receiver (bottom) coils.

Next, the magnetic field distribution in the presence of a slab with a finite conductivity is investigated. Fig. 2.6 illustrates numerical simulations of the magnetic field distribution obtained with CST EMS for two different conductivities. In the presence of an intervening attenuating block with the same relative permittivity, eddy currents are excited inside the medium and eventually produce an induced field which opposes the primary field due to Lenz's law. That secondary field might have a significant phase shift with respect to the field generated by the transmitting coil. The total magnetic field being a superposition of the primary field generated by the transmitting coil and the induced field generated by eddy currents, as a result, becomes elliptically polarised. Correspondingly, the mutual inductance between



(a) Conducting block ($\epsilon_r = 1$ and $\sigma = 4$ S/m)



(b) Conducting block ($\epsilon_r = 1$ and $\sigma = 1000$ S/m)

Figure 2.6: Simulated amplitude and polarization of the total magnetic field generated by a transmitting coil above a conducting cylindrical block in the yz-plane for different conductivity (a) $\sigma^{(\mathbf{III})} = 4$ S/m and (b) $\sigma^{(\mathbf{III})} = 1000$ S/m. The conducting cylindrical block has a dimension of $D = 90$ mm, thickness of $t = 30$ mm and relative permittivity of $\epsilon_r^{(\mathbf{III})} = 78$. Polarization ellipses are normalised at a sampling step of 5 mm along the y and z axes. Black dash lines mark the cross sections of the block while black dots represent transmitter (top) and receiver (bottom) coils.

two coils will be necessarily complex. In Fig. 2.6a, the finite element calculations demonstrate the magnetic field distributions in the presence of a block with a relative permittivity of $\epsilon_r^{(\mathbf{III})} = 78$ and conductivity of $\sigma^{(\mathbf{III})} = 4$ S/m (similar to those of sea water [79, 84]), thickness of $t = 30$ mm and diameter of $D = 90$ mm symmetrically placed between two coils a distance of $d = 37$ mm apart. Since the conductivity is relatively small and eddy currents are insignificant, the magnetic field clearly penetrates the conducting material and the phase lag of induced currents rapidly increases with penetration depth due to the large propagation wavenumber in the block as compared to the insulator. Because of the significant phase shift of the magnetic field at the receiving coil, the corresponding simulated mutual

inductance is a complex quantity $M = 0.4182\angle{-61.45^\circ}$ nH. For the same size block with a conductivity of $\sigma = 1000$ S/m (similar to highly doped polymers, e.g., Methanesulfonic acid (CH_3SO_3H) doped polyphenylene vinylene (PPV) [88]), the effect of eddy currents is distinguishably stronger than in the previous case, making the normal component of the magnetic field at the bottom of the block almost vanishing as expected from Lenz's law. Meanwhile, the tangential component just outside the periphery of the block is nearly doubled. In other words, the slab has become almost impermeable to magnetic fields. As can be seen from Fig. 2.6b, most of the magnetic field lines skirt the periphery of the block as one would expect from a diamagnetic material. The corresponding simulated mutual inductance is drastically smaller than in the previous case $M = 0.00275\angle{-25.81^\circ}$ nH.

The physics underlying the variation of the magnetic fields can be explained by a combination of the primary field generated by the transmitter and the induced field generated by the eddy currents inside the conducting block. Alternatively, one could claim that the propagation of the magnetic field is inversely proportional to medium conductivity because of larger skin effects.

2.3.2.2 Poynting Vector

To the greatest extent, the study of a physical phenomenon is incomplete unless the movement of energy is considered. For electromagnetic fields, the energy conservation is described by Poynting's theorem whose derivation in integral or differential form can be found in most textbooks on electromagnetism, e.g., [82]. Here, regarding near-field problems, where the geometry is on a scale relatively small to the wavelength, the best approach to understand the physics is visualizing the streamlines of the time-averaged Poynting vector. They manifest how the power propagates from the source to where it is absorbed. In principle, the time-averaged Poynting vector is calculated from the electric field and magnetic field phasors, $\mathbf{E}$ and $\mathbf{H}$, $\mathbf{S} = 1/2\,\mathrm{Re}\,[\mathbf{E} \times \mathbf{H}^*]$. The power distribution between two magnetically coupled coils is then simulated in CST Microwave Studio (CST MWS). In the simulations, S-parameter ports are used instead of ideal current ports. In order to maximize the

transferred power, the two coils are matched to 50 Ω impedance by using a simple capacitive compensation circuit, as shown in Fig. 2.7. The values of the capacitors C_1 and C_2 are determined by using Keysight Advanced Design System (ADS) [89].

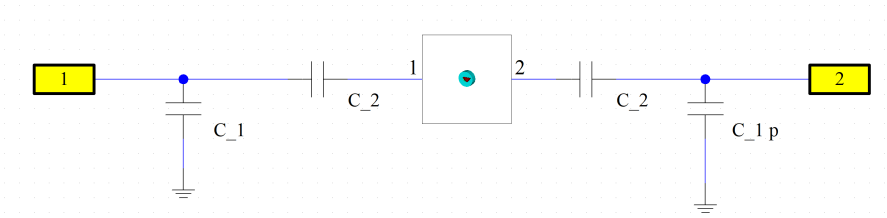
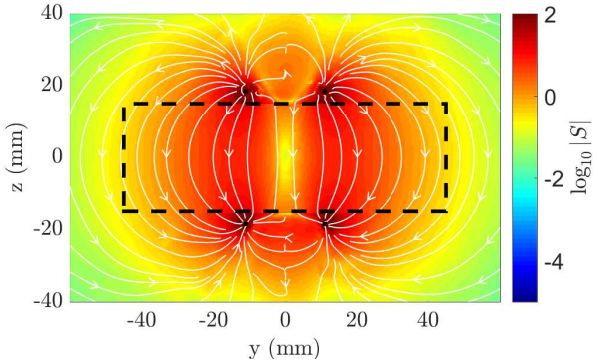
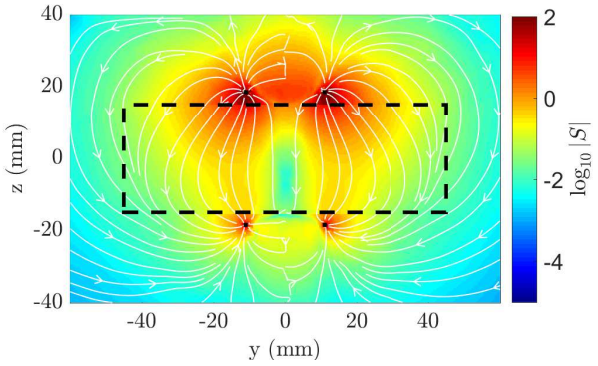


Figure 2.7: Capacitive compensation circuits to maximize the transferred power through two identical coupled coils. The values of capacitors are determnined by using Keysight ADS. Yellow blocks indicate 50 Ω impedance ports.

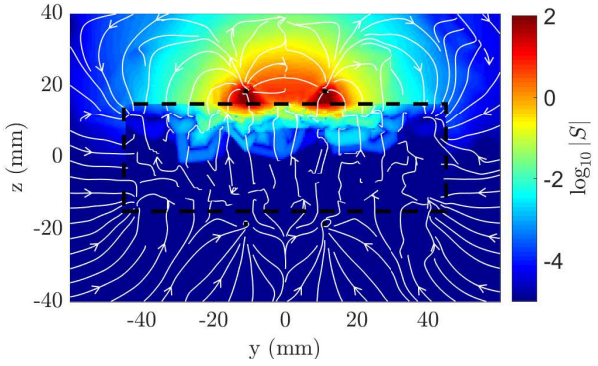
Fig. 2.8 exhibits the full-wave simulation results of the power flow density (modulus) and the streamlines (direction) of the time-averaged Poynting vector for the two configurations shown in Fig. 2.6. Also, the case when the intervening block is non-conductive ($\sigma^{(\mathbf{III})} = \text{S/m}$) but has a high permittivity ($\epsilon_r^{(\mathbf{III})} = 78$) is presented as a reference in Fig. 2.8a.



(a) Air ($\epsilon_r = 1$ and $\sigma = 0$ S/m)



(b) Conducting block ($\epsilon_r = 1$ and $\sigma = 4$ S/m)



(c) Conducting block ($\epsilon_r = 1$ and $\sigma = 1000$ S/m)

Figure 2.8: The power flow density and streamlines of the time-averaged Poynting vector generated from a pair of transmitting and receiving coils in the presence of a conducting cylindrical block in the yz-plane for different conductivity (a) $\sigma^{(\mathbf{III})} = 0$ (b) $\sigma^{(\mathbf{III})} = 4$ S/m and (b) $\sigma^{(\mathbf{III})} = 1000$ S/m. The conducting cylindrical block has a dimension of $D = 90$ mm, thickness of $t = 30$ mm and relative permittivity of $\epsilon_r^{(\mathbf{III})} = 78$. Black dash lines mark the cross sections of the block while black dots represents transmitter (top) and receiver (bottom) coils. The power transfer efficiency, $\eta = |S_{21}|^2$ = (a) 48.8%, (b) 3.9 %, and (c) 0%.

When the transmitting coil is excited with an AC voltage and the block is non-conductive, the physics is clear. The Poynting vector's streamlines spring from the transmitter and terminate at the receiver by following a number of spatial paths, evident from Fig. 2.8a. The power density centres on the proximity of the coils and decays as further away from the source. When the conductivity of the block is different from zero, $\sigma^{(\mathbf{III})} \neq 0$, the conductive material introduces a significant attenuation on the power flow between the two coils even for a small value of conductivity (cf. Fig. 2.8b). Only some parts of the power generated from the transmitter reach the receiver while others are absorbed in the slab due to the generation of eddy currents. Besides this, the streamlines are noticeably distorted compared to the former case. As the conductivity further increases to $\sigma^{(\mathbf{III})} = 1000$ S/m, the Poynting vector not only decreases to a greater degree but also diverts its direction to be mostly parallel to the bases of the cylindrical block. This trend is in accordance with the behaviour of the magnetic field going around the block in Fig. 2.6b, where its normal component at the lower base is almost zero and its tangential component is doubled. Since the power appears at the receiving coil through longer paths, there must be a phase delay in the induced voltage at the sink and eventually, the mutual inductance between the two terminals.

Additionally, the colour-maps indicate the decay of power density through the slab in both cases of non-zero conductivities. It is worth noting that for higher conductivity, the power flow still penetrates through the conducting slab but is absorbed in a continuously reducing thickness from the top surface as expected from the literature of the skin effect. All things considered, the Poynting vector visualisation method reinforces tangible evidences of the complex mutual inductance as a consequence of the field rotation as shown in Fig. 2.5 and 2.6. Next, the variation of the mutual inductance as a function of medium's parametric properties is investigated.

2.3.2.3 Mutual Inductance

Clearly, the conducting block considered above is not infintely wide as in D&D [71]. In order to compare the CST simulations to D&D solutions, common sense suggests that the block needs to be sufficiently wide to electromagnetically represent an infinitely wide slab. The coil configuration in Fig. 2.4 remains unchanged. Fig. 2.9 shows the simulated mutual inductance as a function of the conducting block's width for several conductivities. It can be seen clearly that when the radius of the block is approximately 4 times lager than the coil radius, the mutual inductance seems independent of the block diameter. On the basis of these results, a conducting block of size $D = 90$ mm centre-aligned with the pair of coils is used in the simulation in the rest of this chapter.

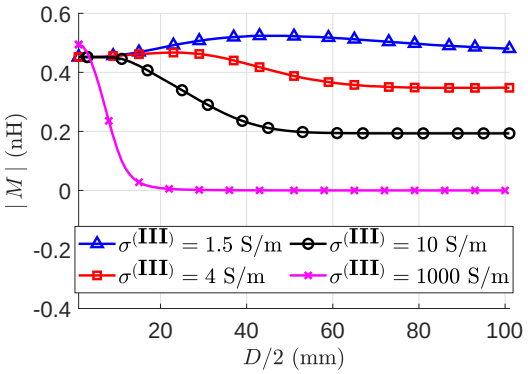


Figure 2.9: Simulated modulus of the mutual inductance as a function of the conducting block diameter for the block conductivity $\sigma^{(\mathbf{III})} = 1.5, 4, 10$ and 1000 S/m. Two coaxial coils are displaced by $d = 37$ mm. The conducting cylindrical block has a dimension of $D = 90$ mm, thickness of $t = 30$ mm and relative permittivity of $\epsilon_r^{(\mathbf{III})} = 78$.

It may be concluded that the permittivity of the slab seems to boost the mutual inductance while the conductivity of the block, on the other hand, is attenuating it. In the literature, especially in the field of communications engineering, the plane-wave approximation has been widely assumed [68, 69, 90–93]. It is suggested that the mutual inductance between two coils decays at the same rate of the path loss for a plane wave penetrating in a half-space conductor. Accordingly, the mutual

inductance can be written in the form [69]:

$$M \approx M_0 e^{\frac{-d}{\delta}}. \tag{2.13}$$

where M_0 is the mutual inductance between two coils in air, and δ is the skin depth, whose expression can be found in (2.3). This simple approximation overestimates the effect of conductive medium on the near field and thus, causes difficulties in the design of applications involving conductive media. Here, three other independent methods are performed to assess the PW approximation. They are: the quasi-static solution by D&D [71], the generalised field solution stated in section 2.2 to include retardation effects, and finally the finite-element simulation with CST EMS.

Fig. 2.10 shows the influence of the medium's conductivity on the real (Fig. 2.10a) and imaginary parts (Fig. 2.10b) and the modulus (Fig. 2.10c) of the mutual inductance between two air core circular coils. The conductive slab has a diameter of $D = 90$ mm, thickness of $t = 30$ mm and varying conductivity from $\sigma^{(\mathbf{III})} = 10^{-3}$ to $\sigma^{(\mathbf{III})} = 10^{8}$ S/m. The values of the mutual inductance obtained with the PW approximation are compared to the D&D solution, generalised solution, and finite numerical simulations. Clearly, the amplitude of the mutual inductance is a monotonically decreasing function of the medium conductivity due to the stronger opposing effects of eddy currents. Among the analytical solutions, the generalised approach shows an excellent agreement to the full-wave simulation from CST EMS whereas the D&D solution appears to be inaccurate for poorly conducting media with conductivity varying from $\sigma^{(\mathbf{III})} = 10^{-3}$ to $\sigma^{(\mathbf{III})} = 10$ S/m. Within that range, the condition for quasi-statics approximation ($\sigma^{(\mathbf{III})} \ll \omega\epsilon_0\epsilon_r^{(\mathbf{III})}$) are not satisfied. Thus, the displacement currents are not negligible, leading to a large discrepancy between the D&D solution and simulated results. At higher conductivities, conduction currents usually dominate the displacement ones even in a medium with high permittivity. The D&D solution then coincides with the generalised solution. In addition, the curve from the PW method is apparently different from others. Arguably, this model has no physical basis. In a near distance from the radiation sources, the fields are never as uniform as in considerably far

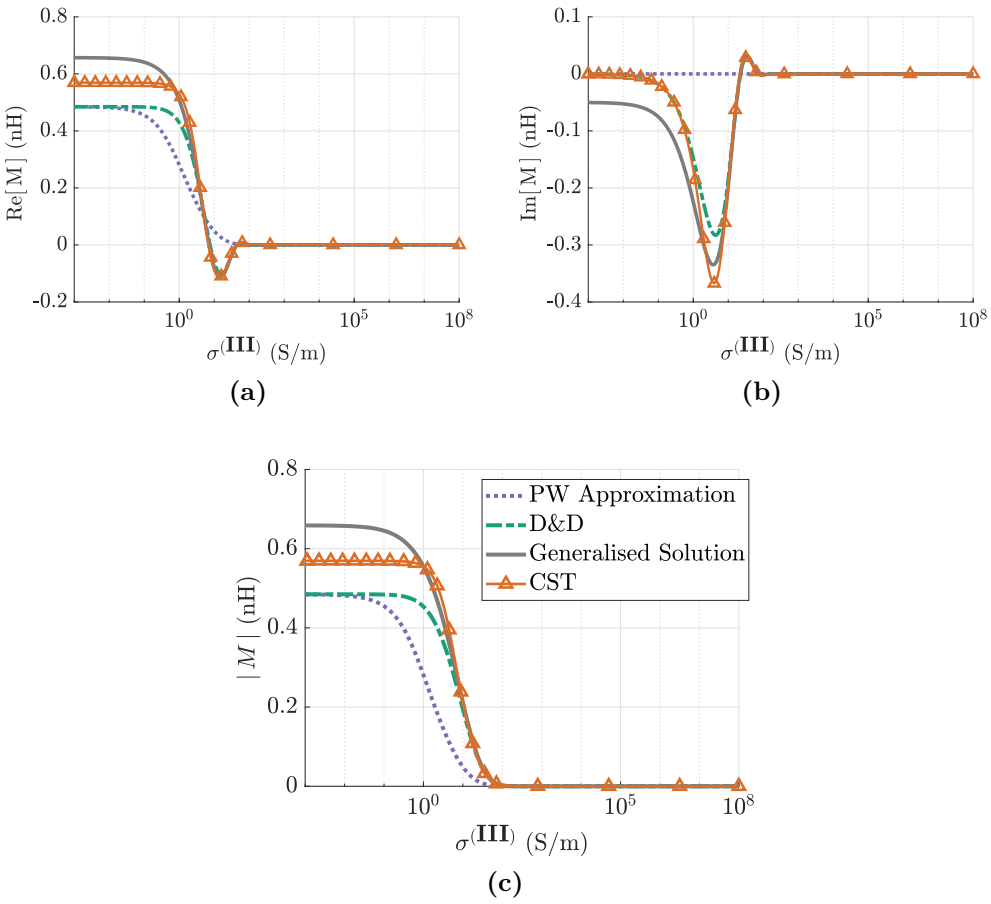


Figure 2.10: (a) Real part, (b) imaginary part, and (c) modulus of the mutual inductance between two coaxial circular coils versus the block conductivity from $\sigma^{(\mathbf{III})} = 10^{-3}$ to $\sigma^{(\mathbf{III})} = 10^{8}$ S/m. Two coaxial coils are displaced by $d = 37$ mm. The conducting cylindrical block has a dimension of $D = 90$ mm, thickness of $t = 30$ mm and relative permittivity of $\epsilon_r^{(\mathbf{III})} = 78$. CST EMS simulation results are compared with those obtained with the PW approximation, the D&D solution [71], the generalised field solution.

distances. Criteria to distinguish the reactive near-fields, transition fields and far fields are stated clearly in electromagnetism textbooks [86]. Accordingly, the behaviour of eddy currents - a pure near-field phenomenon - must not be described by an ideal case of a plane wave. Also, the polarization of the far fields of an electromagnetic wave, not depending on the location of observation points, is either linear, circular or elliptical. Contrariwise, all three types of polarization can coexist in the near-field magnetic field. The type of polarization of the magnetic field seems to depend solely on the spatial position of the observation points from the source, as shown in Fig. 2.6. As a result of falling short of describing the field

rotation, the PW approximation exhibits zero phase change since it entirely neglects the imaginary part of the mutual inductance. Positively, the PW model might be applied when the conductivity is sufficiently large, for instance $\sigma^{(\mathbf{III})} > 10^2$ S/m in this configuration, the material becomes impermeable and blocks mostly the magnetic flux. Another applicable scenario might be when very electrically large coils are employed. The electrically larger coils produce a likely plane-wave type of magnetic field. However, these conditions are unlikely to meet in practice. The PW approximation appears to be inadequate for actual applications.

The generalised field solution, however, exhibits an unsatisfactory agreement to the finite element simulations for $\sigma < 1$ S/m. The reason behind this is that in the analytical method, the conducting slab is an infinitely wide half-space while in the simulations, the cylindrical slab has a finite diameter, $D = 90$ mm. Indeed, for nearly vanishing conductivity, the medium behaves as a lossy dielectric block with high permittivity, whose shielding effect depends profoundly on its physical size. The larger the size of the slab, the more it enlarges the induced field generated by the displacement currents until reaching the saturation point of an infinitely large slab. Consequently, the predictions for the mutual coupling based mathematical generalised field solutions for an infinitely wide layer are always higher than those obtained with numerical simulations in this situation.

The mutual inductance between coils as a function of the medium thickness are reported in Fig. 2.11. Similar to Fig. 2.10, three analytical methods are performed: the approximation-based PW properties, the quasi-static D&D solution, the generalised solution. Those results are justified to the full-wave simulations. The mutual inductance shows an inverse proportion to the thickness of the conducting material. A larger thickness, of course, suggests a bulkier slab - a bigger volume for eddy currents to exist. It leads to a decay in the mutual coupling following an increase in the induced electromotive force, analogously to the impact of larger values of conductivity related to stronger eddy currents. Additionally, the agreement between the generalised formula and CST results is desirable. The D&D is only capable of estimating the real part of the mutual coupling while coming short on the imaginary

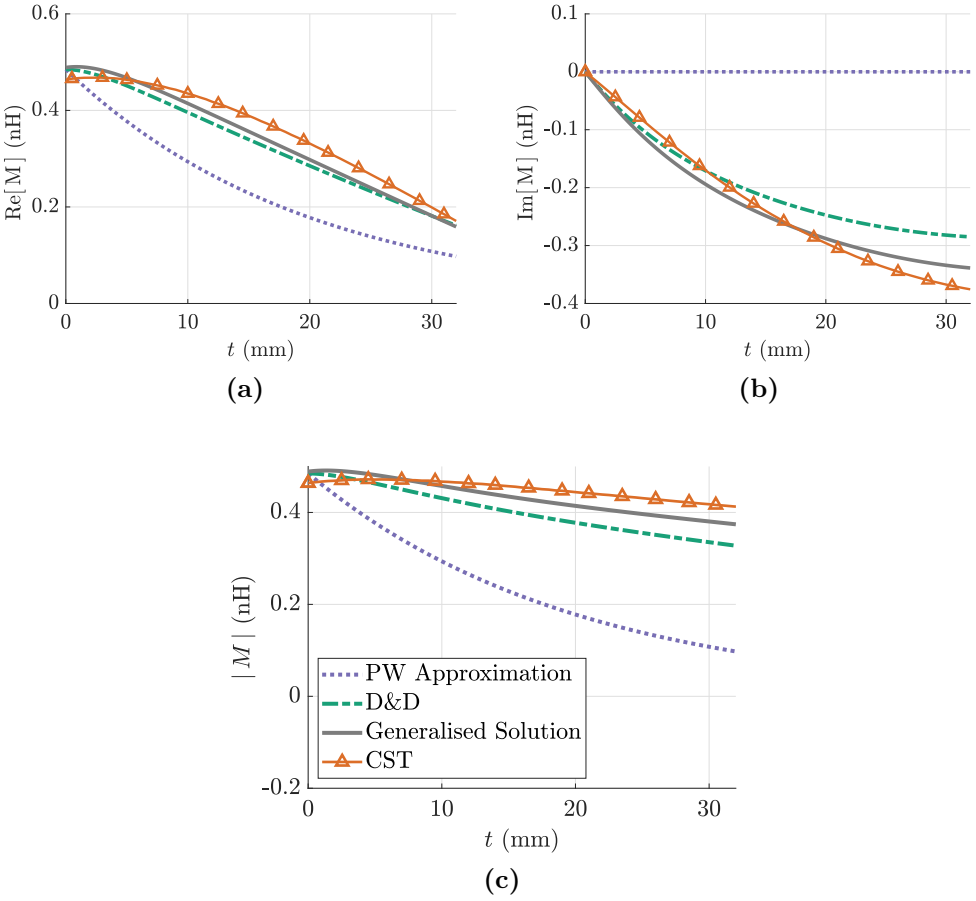


Figure 2.11: (a) Real part, (b) imaginary part, and (c) modulus of the mutual inductance between two coaxial circular coils versus the block thickness from $t = 0$ to $t = 32$ mm. Two coaxial coils are displaced by $d = 37$ mm. The conducting cylindrical block has a dimension of $D = 90$ mm, conductivity of $\sigma^{(\mathbf{III})} = 4$ S/m and relative permittivity of $\epsilon_r^{(\mathbf{III})} = 78$. CST EMS simulation results are compared with those obtained with the PW approximation, the D&D solution [71], the generalised field solution.

part. Contrarily, the PW approximation is yet to produce favourable results. It crudely overrates the shielding effect of the block even for small values of thickness.

Finally, the effect of the material's permittivity on the mutual coupling is investigated. At low frequencies, especially of interest for modern MI communications systems (typically kHz), conduction currents usually dominate over the displacement ones even in a medium with high permittivity. However, as the global trend is to increase the channel bandwidth necessary for higher data rates, the operating frequency is expected to move up to higher bands. At higher frequency, the amount

of magnetic flux produced by the displacement currents may be comparable to that produced by the conduction currents. Under this circumstance, the displacement currents should be considered to yield a precise solution for the mutual inductance. Here, the block's relative permittivity varies from that of air ($\epsilon_r^{(\mathbf{III})} = 1$) to that of tap water at room temperature ($\epsilon_r^{(\mathbf{III})} = 78$). Fig. 2.12 shows the influence of the block permittivity on the mutual inductance between two coils.

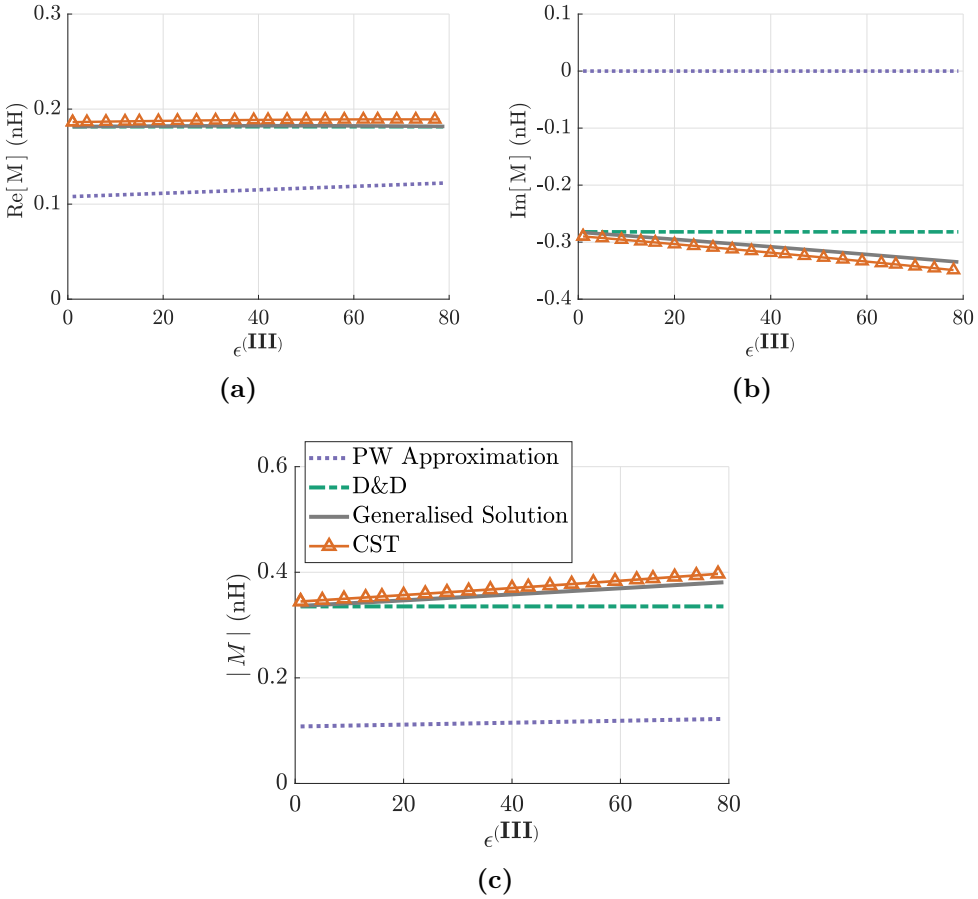


Figure 2.12: (a) Real part, (b) imaginary part, and (c) modulus of the mutual inductance between two coaxial circular coils versus the block relative permittivity from $\epsilon_r = 1$ to $\epsilon_r = 80$. Two coaxial coils are displaced by $d = 37$ mm. The conducting cylindrical block has a dimension of $D = 90$ mm, thickness of $t = 30$ mm, and conductivity of $\sigma^{(\mathbf{III})} = 4$ S/m. CST EMS simulation results are compared with those obtained with the PW approximation, the D&D solution [71], the generalised field solution.

Undoubtedly, the quasi-static solution from D&D gives a constant value for mutual coupling since the retardation effect is excluded. The generalised solution to consider the radiating term, on the other hand, exhibits an excellent agreement

with the CST simulation data. The plane-wave based approach unsurprisingly is providing inadequate results for the mutual inductance. Generally speaking, the permittivity of the medium boosts the total coupling by introducing more flux due to the displacement currents. This behaviour would offer an option to tailor the coupling suitable for a number of inductively-coupled-coil systems where dielectric materials are involved.

2.4 Experiments

2.4.1 Experimental Apparatus

To verify the simulation results, in this section, the laboratory measurements have been reported. A large number of experiments have been conducted to test the finite numerical calculations and three analytical methods. Fig. 2.13 illustrates the schematic and block diagram of the laboratory apparatus, representing the configuration in Fig. 2.4. The scattering parameters for signals transmitting between them are measured using a Vector Network Analyser (VNA) Keysight E5061B. The VNA is calibrated up to the connection with the probes with a set of standard terminations.

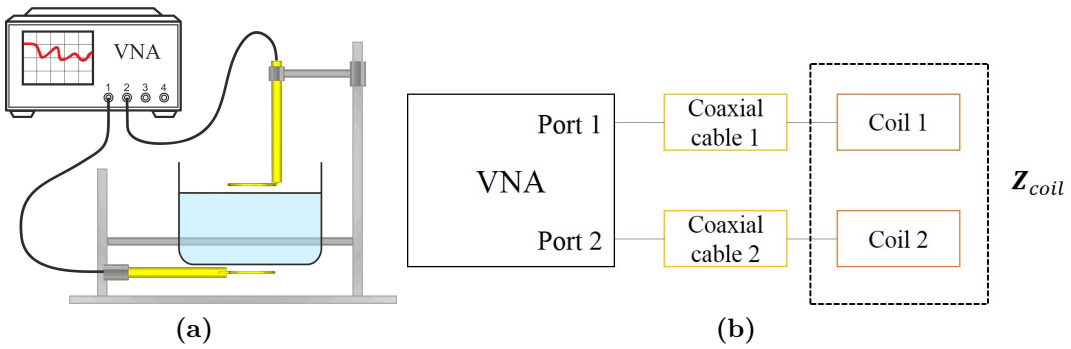


Figure 2.13: (a) Schematic view of the laboratory experiment and (b) the block diagram of the measurement system.

Each magnetic probe is a non-resonant loop antenna, manufactured from a semirigid coaxial cable (RG402/U 50 Ω) with one end being a 22-mm-diameter loop made from its inner conductor, as shown in Fig. 2.14. The position of the probes are fixed by using perspex clamps and polytetrafluoroethylene (PTFE) rods.



Figure 2.14: A magnetic probe used in the experiment.

The conductive medium is inserted centrally and symmetrically between two probes. Since there is no natural solid material which has variable electrical conductivity suitable for measurements, an alternative option is an aqueous solution of sodium chloride with variable concentration in a cylindrical plastic container to represent the conducting slab. The conductivity of the sample solution is assessed with a conductivity-meter calibrated with standard calibration solutions (HANNA HI-70030 12880 μS/cm). The largest conductivity of the aqueous solution in the experiments is 20 S/m, corresponding to the upper limit of the conductivity meter. At radio frequencies, the relative permittivity of the solutions is assumed to be about $\epsilon_r = 78$ at room temperature [84, 85].

To refine the experiments, a plastic fixture is used to align the equipment. The container is realized by an additive manufacturing technique (3D printing) with an acrylonitrile butadiene styrene (ABS) filament. Then the entire apparatus was placed inside an anechoic chamber to shield the probes from external electromagnetic interference. As can be seen from the block diagram in Fig. 2.13b, the impedance matrix Z_{coil} containing the mutual coupling between two coils can be converted from the S-parameters by using deembedding technique to abolish the effect of the coaxial cables. The deembedding procedure is as follows. The measured scattering parameters are converted into $ABCD$-matrix, $ABCD_{network}$ [87]. Then the $ABCD$-matrix of two magnetically coupled probes is obtained by the equation:

$$ABCD_{coil} = ABCD_{cable1}^{-1} \times ABCD_{network} \times ABCD_{cable2}^{-1} \tag{2.14}$$

where

$$ABCD_{cable} = \begin{bmatrix} \cosh(\gamma l) & Z_0 \sinh((\gamma l) \\ \frac{1}{Z_0} \sinh((\gamma l) & \cosh(\gamma l) \end{bmatrix} \tag{2.15}$$

is the $ABCD$-matrix of the semi-rigid cable, l is the cable length, $\gamma = \alpha + j\beta$ is the propagation constant which can be accessed from the manufacturing datasheet, and $Z_0 = 50\ \Omega$ is the characteristic impedance of the cable. Finally, the Z-parameters of two coupled coils is obtained by analytical conversion from ABCD-matrix [87]. Once the impedance matrix is known, the mutual coupling between two coils can then be derived by applying a simple equivalent circuit model. Given that the operating frequency is far below the coil self-resonant frequency, each coil can be modelled as a lossy inductor. Therefore, the Z_{coil} can be rewritten as:

$$Z_{coil} = \begin{bmatrix} R + j\omega L & j\omega M \\ j\omega M & R + j\omega L \end{bmatrix} \tag{2.16}$$

where R is the Ohmic losses, and L is the self-inductance of the coils, and M is the mutual inductance between them. Generally speaking, L and M are complex quantities with real and imaginary parts which take into account lossy and inductive contributions from the eddy currents respectively.

2.4.2 Experimental Results

Experimental results for mutual inductance M (real part, imaginary part, and modulus) versus the medium's conductivity are shown in Fig. 2.15. For the purpose of comparison, measured data are presented against the results of the three analytical methods and the finite numerical simulations mentioned above. Indeed, the measured mutual inductances are complex and in good agreement with the results obtained with CST EMS and the generalised field solutions. The modulus of the experimental data exhibits practically the same decay rate with them. Within the range of relatively small conductivity, the curve from the generalised field solution diverges from the measured and simulated data, as discussed in Fig. 2.10. Nevertheless, the simple analytical approximation based on the properties of a PW is hugely overestimating the shielding of one coil from another by the intervening medium, making it an unreliable model for MI communications.

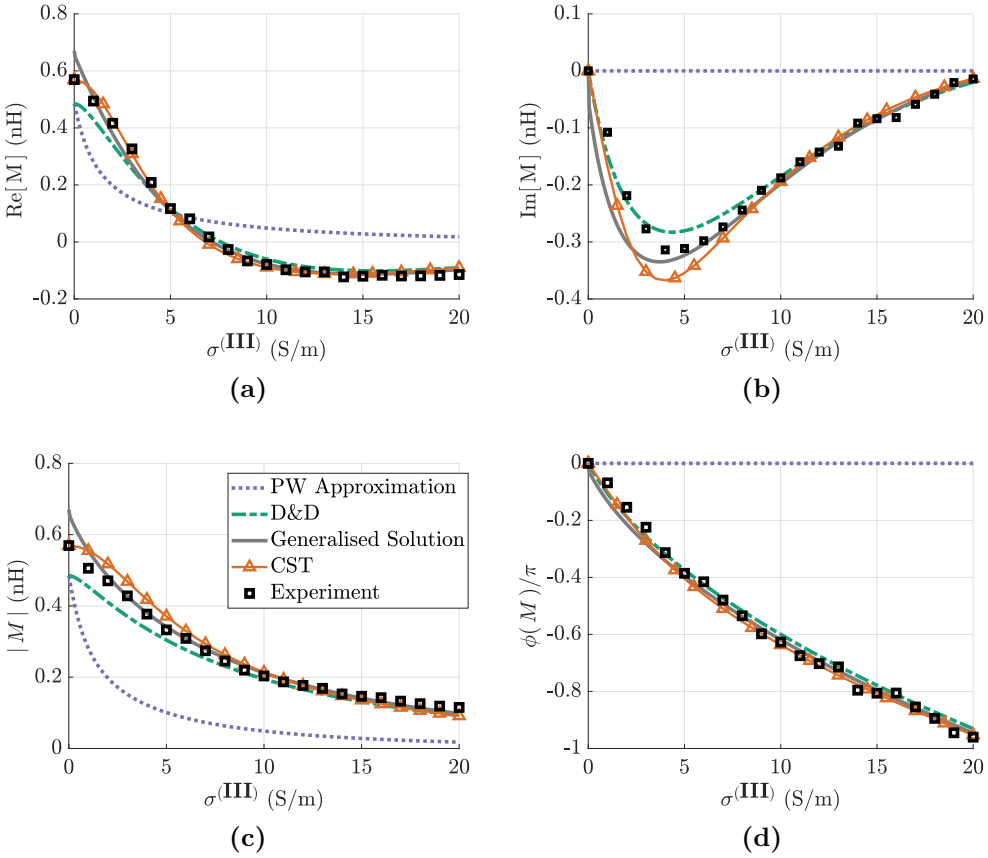


Figure 2.15: Measured (a) real part, (b) imaginary part, (c) modulus and (d) phase of the mutual inductance between two coaxial circular coils versus the solution conductivity from $\sigma = 0$ to $\sigma = 20$ S/m. Two coaxial coils are displaced by $d = 37$ mm. The aqueous solution has a dimension of $D = 90$ mm, thickness of $t = 30$ mm, and relative permittivity of $\epsilon_r = 78$. Comparisons are made with results obtained with the PW approximation, the D&D solution [71], the generalised field solution, and CST EMS simulations.

Fig. 2.16 reports the measured real part, imaginary part, and modulus of the mutual inductance as a function of medium's thickness. Experimental data are compared to three analytical predictions and results from CST EMS. Once again, the generalised field solution closely matches the mutual inductance in the presence of a medium with a variable thickness. Likewise, the curve from the PW approximation are a poor match for both simulated and measured values, estimating the coupling between coils at much lower values that those observed in practice.

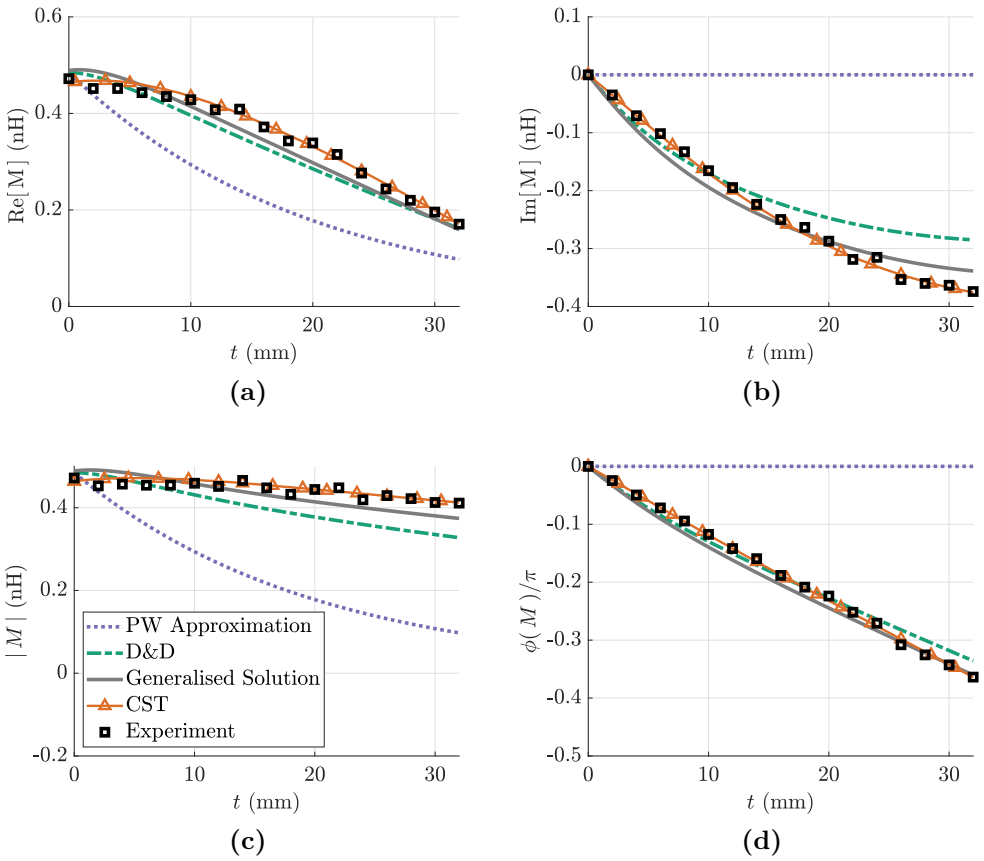


Figure 2.16: Measured (a) real part, (b) imaginary part, (c) modulus and (d) phase of the mutual inductance between two coaxial circular coils versus the solution thickness from $t = 0$ to $t = 32$ mm. Two coaxial coils are displaced by $d = 37$ mm. The aqueous solution has a dimension of $D = 90$ mm, conductivity of $\sigma = 4$ S/m and relative permittivity of $\epsilon_r = 78$. Comparisons are made with results obtained with the PW approximation, the D&D solution [71], the generalised field solution, and CST EMS simulations.

The final comment is that small discrepancies observed between the measured and simulated values was caused by a few minor aspects: the uncertainty in the measurement with hardware instruments (VNA and conductivity-meter), the uneven level of the aqueous solution due to the surface tension, the manufacturing imperfection of the semi-rigid cables and the loops, and the deembedding technique tolerance, to name but a few.

2.5 Conclusions

In Chapter 2, the variation of the mutual inductance between two air core circular coils in the presence of an intervening conducting material has been evaluated by using analytical, simulation and experimental methods. The simulations in CST EMS show that the magnetic field becomes elliptically polarised, owing its modification to the induced field generated by eddy currents inside the medium. As a result of the field rotation, the mutual inductance is no longer a real number, but a complex quantity. A larger number of simulations were carried out to examine the effects of medium conductivity, thickness and relative permittivity on the real part, imaginary part and modulus of the mutual inductance. Simulation results have shown that the conductivity and thickness of medium are attenuating the mutual coupling while the medium relative permittivity is enhancing the magnetic flux produced by the displacement currents and eventually increasing the total mutual coupling. In addition to this, it has been confirmed that the displacement current should be taken into account in the field solution to accurately estimate the mutual inductance for ordinary media with relatively low conductivity (less than 10 S/m), such as soil, sea water or human body and tissues.

Laboratory experiments have been conducted to validate the simulation data with CST EMS. The medium is an aqueous solution of sodium chloride with the relative permittivity of $\epsilon_r = 78$, conductivity from $\sigma = 0$ to $\sigma = 20$ S/m, and thickness from $t = 0$ to $t = 32$ mm. The measured results exhibit an excellent agreement with finite element simulations while a satisfactory agreement with the generalised field solution for an infinitely wide conducting slab. The reason for the discrepancy between experimental/simulated data and the curve from the generalised solution is mainly due to the finite size of the medium in experiments and simulations, as highlighted in the sections above. In addition, the credibility of the skin-depth-based model proposed in the literature [69] has been investigated. As things stand, this simple model is indeed inadequate. The PW approximation has neglected completely the imaginary part while overestimated the attenuation of the real part of the mutual inductance. In fact, the imaginary part of the mutual inductance is quite significant

because of the field polarization. Also, the real part and imaginary part of the mutual inductance may change sign from positive to negative values or vice versa at suitable medium conductivities. The PW approximation is, without a doubt, too simplistic and hence, impractical for applications employing MI communications technique. It can only be used when either the conductivity of the medium is sufficiently large, or the coils are electrically large. In the former case, the conductive medium becomes impermeable and blocks almost all of the magnetic flux toward the receiver, while in the latter case, the field produced by the transmitter coils appears more plane-wave-esque at the material interface.

Those findings are immediately relevant to the attenuation of MI waves in common conducting environments (e.g. soil, sea water), body area networking, implanted sensors for biological systems and wireless power transfer in lossy environments.

3

Field Model of Coupled Coils in Homogeneous Dissipative Media

Contents

3.1 Circuit Model of Coupled Coils inside a Dissipative Medium 53
3.2 Complex Kirchhoff Coefficients: a New Field Solution 55
3.3 Simulation Results: Complex Kirchhoff Coefficients . 60
3.3.1 CST Models 60
3.3.2 Simulations Results 61
3.4 Conclusions 76

As discussed through by numerical simulations and experimental data in Chapter 2, the presence of an intervening conducting block between two coils has two major effects on the magnetic field: firstly, it causes the polarization of the magnetic field to become elliptical, and secondly, it introduces a phase shift in the magnetic field that leads to a complex mutual inductance. However, the configuration considered in Chapter 2 was relevant to the case when a conductive slab is inserted between two coupled coils. In this chapter, more attention is paid to the case when the two coils are completely immersed in non-conventional media, e.g. buried in the ground or submerged in the water as in WUCNs. Section 3.1 proposes a novel equivalent circuit model for two coupled coils inside a dissipative medium.

In comparison to the model of two coupled coils in free space, there are two new Kirchhoff terms: complex self inductance and complex mutual inductance, which represent the impacts of induced eddy currents on the circuit model. Closed-form analytical solutions to calculate the complex Kirchhoff terms are presented in Section 3.2. Then, the solutions are justified by comparing to CST EMS simulations in Section 3.3. The main contribution of this chapter is to propose a novel equivalent circuit model for two coupled coils inside a dissipative medium, where the emerging complex Kirchhoff terms can be estimated analytically. In order to achieve closed-form analytical solutions, finite dielectric cavities providing coil insulation are considered as infinitely wide layers. Some of the work in this chapter have been published in the following journals/conference proceedings:

- **S. Chu**, A. Vallecchi, C. J. Stevens and E. Shamonina, 'Fields and coupling between coils embedded in conductive environments', *EPJ Applied Metamaterials*, vol. 5, no. 2, 2018 (**invited**).
- **S. Chu**, C. J. Stevens and E. Shamonina,'A complete circuit model for two coils inside a dissipative medium', in *Proceedings of 12th International Congress on Engineered Materials Platforms for Novel Wave Phenomena (Metamaterials)*, Espoo, Finland, 2018, , pp. 78-80.
- **S. Chu**, A. Vallecchi, C. J. Stevens and E. Shamonina,'Analytical solution for the magnetic coupling of two coils immersed in a conductive medium', in *Proceedings of 11th International Congress on Engineered Materials Platforms for Novel Wave Phenomena (Metamaterials)*, Marseille, France, 2017, pp. 58-60.

3.1 Circuit Model of Coupled Coils inside a Dissipative Medium

In the last century, there has been considerable interest in the subject of radiating systems embedded in dissipative media due to the need for submarine communications [94–98]. Uninsulated Hertzian dipoles in an infinite homogeneous conductive medium were first investigated in 1947 [94]. It has been concluded that a detectable field strength at some distant from the source can only be generated by a massive power due to the extremely large ohmic losses in the immediate neighbourhood of the dipole. The antenna therefore must be insulated in order to control the current distribution and radiation. Later, it was shown in [95] that the radiation efficiency of a magnetic dipole is higher than that of its electrical counterpart in attenuating environments. However, all these works have assumed a simple point dipole source concentrating on far-field propagation and usually ignoring the reactive near-fields.

In the intensive theoretical and experimental works for an insulated electric dipole in conductive media by King [99–102], it is stated that:

> " The near electric field of a bare or insulated dipole in a medium like muscle or the earth is much more involved than the far field because it is elliptically polarized. " [102]

Due to the symmetry of electromagnetic fields, one might expect the magnetic field of an insulated loop current inside those media to be elliptically polarized as well. This expectation is somewhat consistent with the results from Chapter 2, where the polarization of the total magnetic field generated by a coil above a conducting block becomes elliptical. Also, for near-field systems, the absorption of electromagnetic waves creates a feedback effect on the load of the transmitter. To include that phenomenon, the common method is to develop the equivalent circuit model of the system. The basic unit of this system consists of two identical coils with the same orientation placed in lossless dielectric cavities ($\sigma = 0$ S/m) in an infinite homogeneous dissipative environment ($\sigma \neq 0$), as illustrated in Fig. 3.1. The purpose of the insulators is to prevent the current leakage to the medium background and direct conduction currents from the transmitter.

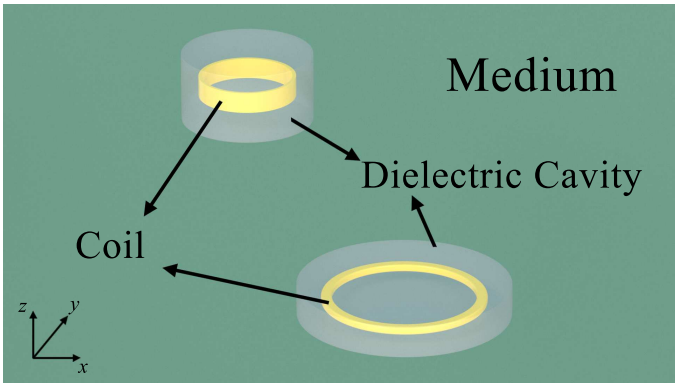


Figure 3.1: General schematic diagram of two coupled coils in proximity with the same orientation completely immersed inside an infinite homogeneous dissipative medium. Each coil is insulated by a small dielectric cavity.

From Chapter 2, the physics is clear that a conducting medium in proximity to two coupled coils can have significant impact on their near-fields. Here, when the two coils are completely embedded inside a dissipative medium, the mutual coupling is predictably attenuated due to induced eddy currents in the environment. Besides, elsewhere, in the field of non-destructive testing and evaluation, it was verified by experiments [103], that there is indeed a change in the resistance and the self impedance of a circular driving coil above a pair of long, non-ferromagnetic and conducting parallel plates. As a result, two new terms - complex self inductance and complex mutual inductance - will be introduced to describe the change in the self impedance and mutual inductance of two coils inside an attenuating medium. Applying Kirchhoff's voltage law, the general equivalent circuit model of this system is expressed by:

$$\begin{bmatrix} V_1 \\ V_2 \end{bmatrix} = \begin{bmatrix} Z_1 + j\omega\Delta\mathcal{L}_1 & j\omega\mathcal{M} \\ j\omega\mathcal{M} & Z_2 + j\omega\Delta\mathcal{L}_2 \end{bmatrix} \begin{bmatrix} I_1 \\ I_2 \end{bmatrix} \tag{3.1}$$

where V_1, V_2, I_1, and I_2 are the applied voltages, current responses of coil 1 and 2, respectively, Z_1 and Z_2 are self impedances in vacuum of coil 1 and 2 respectively, ω is the angular frequency, $\Delta\mathcal{L}_1$ and $\Delta\mathcal{L}_2$ are the complex self inductances of coil 1 and 2, representing the coupling of a coil and the eddy currents it generates, $\mathcal{M} = M_0 + M_E$ is the complex mutual inductance between two coils inside the medium, M_0 is the mutual inductance of two coils in free space, and M_E represents the coupling of a coil and the eddy currents generated by a nearby coil. When

the conductivity of the medium vanishes, i.e., $\sigma_{medium} = 0$ S/m, the medium has no impact on the magnetic channels and hence, all the additional coupling - the complex self inductance and the added mutual inductance - no longer exist, i.e., $\Delta\mathcal{L}_1 = \Delta\mathcal{L}_2 = 0$, $M_E = 0$ and $\mathcal{M} = M_0$. Consequently, (3.1) reduces to the circuit model (3.2) of two coils coupled in free space.

$$\begin{bmatrix} V_1 \\ V_2 \end{bmatrix} = \begin{bmatrix} Z_1 & j\omega M_0 \\ j\omega M_0 & Z_2 \end{bmatrix} \begin{bmatrix} I_1 \\ I_2 \end{bmatrix} \tag{3.2}$$

3.2 Complex Kirchhoff Coefficients: a New Field Solution

To calculate the complex coefficients, the most general approach is to formulate the differential equation for the magnetic vector potential, which describes the electromagnetic properties of the system. Once the magnetic vector potential is known, every other physically observable electromagnetic quantity can be determined, including the complex self and mutual inductance of the coils. The cross-section of the system under analysis is shown in Fig. 3.2a. To simplify the configuration, these cavities made of non-magnetic insulating material have little-to-no effect on the magnetic channels and thus are assumed to be free space. These dielectric cavities are then replaced by infinitely wide dielectric layers to derive a closed-form analytical solution for the magnetic vector potential. Thus, boundary value problem is divided into the five regions labelled with Roman numerals, as shown in Fig. 3.2b.

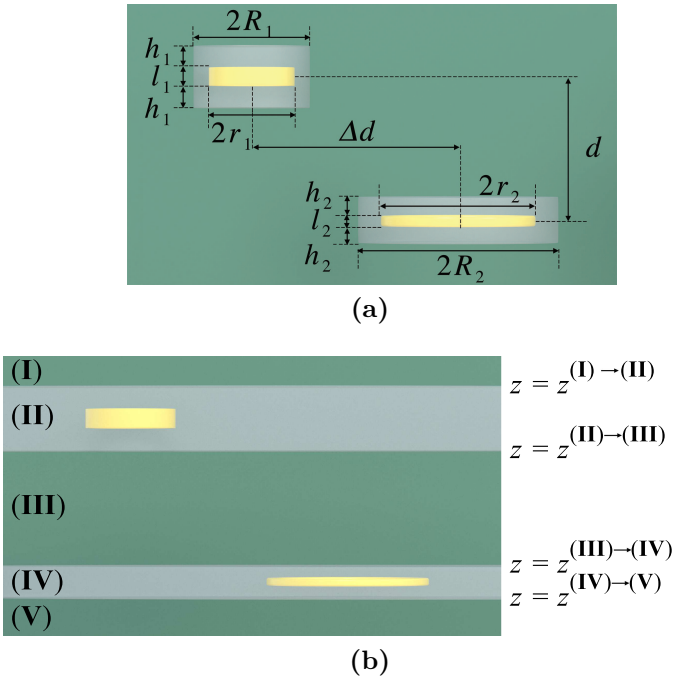


Figure 3.2: Cross-section of the configuration investigated consists of two circular transmitting and receiving coils with the same orientation spaced apart a certain distance in an infinite homogeneous dissipative medium. (a) The finite size dielectric cavities used in the actual configuration, are considered as infinite dielectric layers (b) in the theoretical model.

Here, the superposition theorem is performed to reduce complexity. The field solutions for a coil are formulated in the absence of the other coil. Similar to most eddy current problems, cylindrical coordinates are employed in this case to facilitate the boundary conditions. Following the argument of the symmetry of the configuration in Chapter 2, the magnetic vector potential has only one spatial component along the azimuthal angle φ, i.e., $\mathbf{A}^{(n)}(0, A_{\varphi}^{(n)}, 0)$. Thus, the differential equation for the magnetic vector potential of coil 1 due to an applied voltage $\boldsymbol{V}_0$ is expressed by:

$$\begin{aligned} \boldsymbol{\nabla}^2 \mathbf{A}_1^{(n)} &= \left(\frac{\partial^2 A_{1\varphi}^{(n)}}{\partial z^2} + \frac{\partial^2 A_{1\varphi}^{(n)}}{\partial \rho^2} + \frac{1}{\rho} \frac{\partial A_{1\varphi}^{(n)}}{\partial \rho} - \frac{A_{1\varphi}^{(n)}}{\rho^2} \right) \widehat{\boldsymbol{\varphi}} \\ &= \left(\mu^{(n)} \sigma^{(n)} \frac{\mathrm{d}\, A_{1\varphi}^{(n)}}{\mathrm{d}\, t} + \mu^{(n)} \epsilon^{(n)} \frac{\mathrm{d}^2\, A_{1\varphi}^{(n)}}{\mathrm{d}\, t^2} \right) \widehat{\boldsymbol{\varphi}} \end{aligned} \tag{3.3}$$

where $A_{1\varphi}^{(n)}$ is the vector potential of coil 1 in the region n, which for symmetry reasons only depends on the cylindrical coordinates ρ and z, $\widehat{\boldsymbol{\varphi}}$ are the azimuthal unit vectors

in cylindrical coordinates, $\mu^{(n)}$, $\epsilon^{(n)}$, and $\sigma^{(n)}$ are the permeability, permittivity, and conductivity of region n, respectively, and t is the time variable. To simplify the mathematical complexity, the magnetic vector potential in the time-domain is defined as the convolution of the Magnetic Vector Potential Impulse Response (MVPIR) function with the transient current in the respective coils [103, 104].

$$A_1(\rho, z, t) \equiv \widehat{A}_1(\rho, z, t) * i_1(t) \tag{3.4}$$

where

$$\widehat{A}_1(\rho, z, t) = \widehat{E}_1(\rho, z, t) + \widehat{\Psi}_1(\rho, z, t) = \widehat{E}_1(\rho, z, t) + \widehat{\Psi}_1(\rho, z)\,\delta(t)$$

are the MVPIRs, $\widehat{\Psi}_1(\rho, z, t)$ is the MVPIR generated by a unit impulse current in coil 1 in free space, $\widehat{E}_1(\rho, z, t)$ is the MVPIR generated by eddy currents in the medium, and $\delta(x)$ is the Dirac delta function of variable x. By using the mathematical method in [103], the solutions for MVPIR for coil 1 problem in each region in the frequency domain and the Hankel space (α-space) are summarized below. More details about the method can be found in Appendix B.

$$\widehat{A}_1(\alpha, z, \omega) = \begin{cases} \widehat{\Psi}_1(\alpha, z, \omega) + X_1^{(\mathbf{II})}(\alpha, \omega)\, e^{\alpha^{(\mathbf{II})} z} + Y_1^{(\mathbf{II})}(\alpha, \omega)\, e^{-\alpha^{(\mathbf{II})} z}, & \text{for n} = \mathbf{II}, \\ X_1^{(n)}(\alpha, \omega)\, e^{\alpha^{(n)} z} + Y_1^{(n)}(\alpha, \omega)\, e^{-\alpha^{(n)} z}, & \text{for n} \neq \mathbf{II}. \end{cases} \tag{3.5}$$

The unknown coefficients in (3.5) can be solved by applying the boundary conditions (3.6) and (3.7) from the continuity conditions for the electric and magnetic field components at the interfaces shown in (3.8). It is notable that the boundary conditions (3.6) – (3.8) cannot be applied unless the dielectric cavities is infinitely wide.

$$\widehat{A}^{(n)}(\alpha, z, \omega)\Big|_{z=z^{n\to n+1}} = \widehat{A}^{(n+1)}(\alpha, z, \omega)\Big|_{z=z^{n\to n+1}} \tag{3.6}$$

$$\frac{1}{\mu^{(n)}} \frac{\mathrm{d}\,\widehat{A}^{(n)}(\alpha, z, \omega)}{\mathrm{d}\,z}\bigg|_{z=z^{n\to n+1}} = \frac{1}{\mu^{(n+1)}} \frac{\mathrm{d}\,\widehat{A}^{(n+1)}(\alpha, z, \omega)}{\mathrm{d}\,z}\bigg|_{z=z^{n\to n+1}} \tag{3.7}$$

$$z^{n\to n+1} = \begin{cases} -2h_1 - l_1, & \text{for interface } \textbf{I-II}, \\ 0, & \text{for interface } \textbf{II-III}, \\ c, & \text{for interface } \textbf{III-IV}, \\ c + 2h_2 + l_2, & \text{for interface } \textbf{IV-V}. \end{cases} \tag{3.8}$$

where $z^{n\to n+1}$ is the location of the interface between consecutive zones n and $n+1$, c is the thickness of the medium in-between two coils, and $2h_2 + l_2$ is the height of the insulating cavity of coil 2. The expression of the unknown coefficients $X_1^{(n)}$ and $Y_1^{(n)}$ is derived in the Appendix B. Once all the coefficients are known, every other physically observable electromagnetic quantity can be calculated directly from the magnetic vector potential.

Here, the complex self inductance term is defined in the same manner with the self inductance. Whereas the self inductance represents the interaction between the source magnetic field produced by a coil with itself to produce an EMF, the complex self inductance can be referred as the interaction of the secondary magnetic field generated by the eddy currents with the coil. On the other hand, since the magnetic vector potential in the region of the second coil is an aggregate of the primary field generated by the first coil and the secondary field generated by the eddy currents, cf. (3.5), the complex mutual inductance is a summation of the original mutual inductance in free-space and the coupling between the second coil and the eddy currents generated by the first coil. In other words, it is the mutual inductance between two coils through the medium.

Consequently, the complex self inductance of coil 1 can be calculated by integrating the eddy-current-based MVPIRs arising from currents in coil 1 in the region containing the coil itself over its volume.

$$\Delta\mathcal{L}_1 = \frac{2\pi N_1}{w_1\, l_1} \int_0^{\infty} \int_{r_1 - w_1/2}^{r_1 + w_1/2} \int_{(-h_1 - l_1)}^{(-h_1)} \alpha\, r\, \mathrm{J}_1(\alpha r)\; \widehat{E}_1^{(\mathbf{II})}(\alpha, z, \omega)\, \mathrm{d}\alpha\, \mathrm{d}r\, \mathrm{d}z \tag{3.9}$$

Then, the complex mutual inductance is determined by integrating the eddy-current-based MVPIR arising from currents in a nearby coil in the region containing the secondary coil over its volume. Applying integral transformations in [105, 106] for

the mutual inductance of two coils with a horizontal offset, the complex mutual inductance can be calculated by:

$$\mathcal{M} = \mathcal{M}_{21} = \frac{2\pi N_2}{w_2\, l_2} \int_0^{\infty} \int_{r_2-w_2/2}^{r_2+w_2/2} \int_{c+h_2}^{c+h_2+l_2} \alpha\, r\, \mathrm{J}_0\left(\alpha \Delta d\right)\, \mathrm{J}_1\left(\alpha r\right)\, \widehat{E}_1^{(\mathbf{IV})}(\alpha, z, \omega)\, \mathrm{d}\alpha\, \mathrm{d}r\, \mathrm{d}z \tag{3.10}$$

where Δd is the horizontal displacement between two coils.

By proceeding analogously, the solutions for MVPIR for coil 2 problem in each region are obtained:

$$\widehat{A}_2(\alpha, z, \omega) = \begin{cases} \widehat{\Psi}_2(\alpha, z, \omega) + X_2^{(\mathbf{IV})}(\alpha, \omega)\, e^{\alpha^{(\mathbf{II})} z} + Y_2^{(\mathbf{IV})}(\alpha, \omega)\, e^{-\alpha^{(\mathbf{II})} z}, & \text{for n} = \mathbf{IV}, \\ X_2^{(n)}(\alpha, \omega)\, e^{\alpha^{(n)} z} + Y_2^{(n)}(\alpha, \omega)\, e^{-\alpha^{(n)} z}, & \text{for n} \neq \mathbf{IV}. \end{cases} \tag{3.11}$$

where

$$\widehat{\Psi}_2(\alpha, z, \omega) = \frac{\mu^{(\mathbf{II})}\, N_2}{2\, \alpha\, w_2\, l_2} \int_{r_2-w_2/2}^{r_2+w_2/2} \int_{c+h_2}^{c+h_2+l_2} r\, \mathrm{J}_1\left(\alpha r\right)\, e^{-\alpha |z-z'|}\, \mathrm{d}r\, \mathrm{d}z', \tag{3.12}$$

and $X_2^{(n)}(\alpha, \omega)$ and $Y_2^{(n)}(\alpha, \omega)$ can be found by solving the boundary conditions (3.6) – (3.8), see Appendix B. Then, the complex self inductance of coil 2 and the complex mutual inductance between coil 2 and coil 1 can be calculated by using the following equations:

$$\Delta \mathcal{L}_2 = \frac{2\pi N_2}{w_2\, l_2} \int_0^{\infty} \int_{r_2-w_2/2}^{r_2+w_2/2} \int_{c+h_2}^{c+h_2+l_2} \alpha\, r\, \mathrm{J}_1\left(\alpha r\right)\, \widehat{E}_2^{(\mathbf{IV})}(\alpha, z, \omega)\, \mathrm{d}\alpha\, \mathrm{d}r\, \mathrm{d}z \tag{3.13}$$

$$\mathcal{M} = \mathcal{M}_{12} = \frac{2\pi N_1}{w_1\, l_1} \int_0^{\infty} \int_{r_1-w_1/2}^{r_1+w_1/2} \int_{(-h_1-l_1)}^{(-h_1)} \alpha\, r\, \mathrm{J}_0\left(\alpha \Delta d\right)\, \mathrm{J}_1\left(\alpha r\right)\, \widehat{E}_2^{(\mathbf{II})}(\alpha, z, \omega)\, \mathrm{d}\alpha\, \mathrm{d}r\, \mathrm{d}z \tag{3.14}$$

3.3 Simulation Results: Complex Kirchhoff Coefficients

3.3.1 CST Models

To simulate the change in the impedance of the transmitter as well as the change in the induced electromotive force at the receiver, the near-field feedback effects due to the receiver's current must be neutralized. For this purpose, the transmitting coil in CST EMS is excited by using a lumped port injecting an alternating current of a constant amplitude of 1 A while the receiving coil is connected to a current port of 0 A. These ideal ports aim to eliminate the conduction current in the receiver, leaving only the induced electromotive force in the receiver to be measured and thus, resulting in no feedback effect from the receiver to the transmitter, as can be seen from (3.15).

$$\begin{bmatrix} V_1 \\ V_2 \end{bmatrix} = \begin{bmatrix} Z_0 + j\omega\Delta\mathcal{L} & j\omega\mathcal{M} \\ j\omega\mathcal{M} & Z_0 + j\omega\Delta\mathcal{L} \end{bmatrix} \begin{bmatrix} 1 \\ 0 \end{bmatrix} = \begin{bmatrix} Z_0 + j\omega\Delta\mathcal{L} \\ j\omega\mathcal{M} \end{bmatrix} \tag{3.15}$$

where Z_0 is the self impedance of the coils. Then, the complex self inductance and complex mutual inductance can be directly calculated from the simulated voltages at the current ports of coil 1 and coil 2 respectively.

$$\Delta\mathcal{L} = \frac{V_1 - Z_0}{j\omega} \tag{3.16}$$

$$\mathcal{M} = \frac{V_2}{j\omega} \tag{3.17}$$

In contrast to simulating the value of the complex mutual inductance, computing the complex self inductance may be challenging on grounds of numerical difficulty. Simulations with CST EMS are based on the Finite Element Method, which performs a spatial discretization in the given domain to approximately obtain solutions for the boundary-value problems [83]. The simulating structure is then subdivided into tiny and simple geometries through a mesh creation. Since the complex self inductance represents the ability of the eddy currents, which a coil induces to the medium, to produce a EMF back to the coil itself, it is often dominated by the self inductance. In conjunction with this problem, the boundary in the simulations also

need to imitate the effects of an infinite medium. Therefore, unless the solver, the mesh and the boundary are properly defined, it is impossible to accurately calculate the complex self inductance. Important settings in CST EMS for all simulations in this Chapter are listed in Table. 3.1. As a result of a very dense mesh and high accuracy solver order, the simulations are very computationally intensive as the simulation time for each configuration at a single frequency is about 8 to 10 hours.

Boundary condition	Open
Boundary size	A cube of at least $30r_0$
Solver type	Low frequency domain solver
Solver equation	Full wave
Solver order	3rd (high accuracy)
Mesh type	Tetrahedral
Adaptive mesh refinement: Passes	10
Computational time	$8 \sim 10$ **hours**

Table 3.1: Important settings in the CST EMS for all simulations in this Chapter.

3.3.2 Simulations Results

In this section, I shall justify the validity of the complex Kirchhoff coefficients by comparing those obtained with the analytical solutions and those obtained with CST EMS. Fig. 3.3 depicts the geometric arrangement investigated: two identical coils are immersed inside a conducting medium of conductivity $\sigma^{(\mathbf{I})}$ at a vertical distance d and a horizontal offset Δd apart from each other. The background medium is assumed to be infinite, linear, isotropic and homogeneous. Some geometric and electromagnetic parameters of the configuration listed in Table. 3.2, are kept constant throughout the simulations.

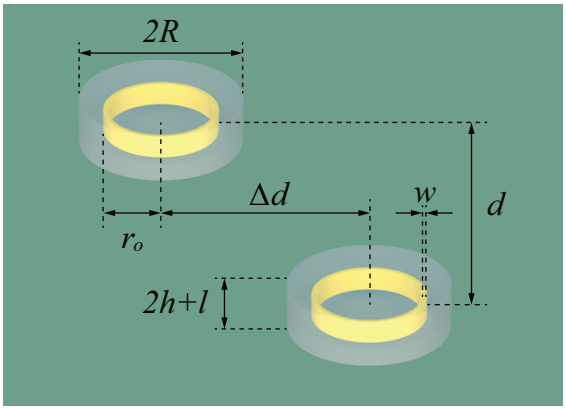


Figure 3.3: Configuration investigated consisting of two identical circular air core coils with dielectric enclosures placed inside an infinite, linear, homogeneous, isotropic, and dissipative environment.

Mean radius of coils, r_0	11 mm
Width of coils, w	1 mm
Height of coils, l	5 mm
Height of free-space cavities, $2h + l$	7 mm
Relative permittivity of medium, $\epsilon_r^{(\mathbf{I})}$	78
Relative permeability of medium, $\mu_r^{(\mathbf{I})}$ and	1

Table 3.2: Important settings in the CST EMS for all simulations in this Chapter.

Since two coils in the simulations are identical, the analytical equations for the complex coefficients can be recast as:

$$\Delta\mathcal{L} = \frac{2\pi N}{w\,l}\int_0^{\infty}\int_{r-w/2}^{r+w/2}\int_{(-h-l)}^{(-h)} \alpha\, r\, \mathrm{J}_1(\alpha r)\ \widehat{E}_1^{(\mathbf{II})}(\alpha, z, \omega)\,\mathrm{d}\alpha\,\mathrm{d}r\,\mathrm{d}z \tag{3.18}$$

$$\mathcal{M} = \frac{2\pi N}{w\,l}\int_0^{\infty}\int_{r-w/2}^{r+w/2}\int_{c+h}^{c+h+l} \alpha\, r\, \mathrm{J}_1(\alpha r)\ \mathrm{J}_0(\alpha\Delta d)\ \widehat{E}_1^{(\mathbf{IV})}(\alpha, z, \omega)\,\mathrm{d}\alpha\,\mathrm{d}r\,\mathrm{d}z \tag{3.19}$$

The theoretical predictions for the complex Kirchhoff coefficients are compared to those obtained by finite numerical simulations with CST EMS over a range of medium conductivity $\sigma^{(\mathbf{I})}$ (where the conductivity of most earth materials and organic matters is found [79–81, 107]), variable vertical distance d, and the variable

horizontal displacement Δd between two coils. The fundamental assumption of the mathematical method above is that the finite radius of the cylindrical dielectric cavities, providing coil insulation, tends to infinity. For this reason, in the simulations with CST EMS, the complex coefficients are calculated corresponding to three different sizes of insulators (cf. Fig. 3.2a), whose radius R is set to be $R = 1.1r_0$, $2r_0$, and $3r_0$.

3.3.2.1 Impact of Medium Conductivity

Firstly, the variation of the complex coefficients across a range of common medium conductivity is the main interest since the strength of the induced eddy currents depends heavily on the electrical conduction. As a further consideration, the separation constant $\alpha^{(n)} = \sqrt{\alpha^2 + j\omega\mu^{(n)}\sigma^{(n)} - \omega^2\mu^{(n)}\epsilon^{(n)}}$ in the Hankel transform is also a function of frequency. Accordingly, the complex Kirchhoff coefficients are frequency-dependent unlike normal inductive terms which are always considered constant at low frequency. Since one of the potential applications of MI waves is in magnetic resonance imaging, the central frequency is set to $f_c = 46$ MHz, equivalent to hydrogen MRI in 1.08 T magnetic field. The two coupled coils are then placed at a vertical distance of $d = 30$ mm and horizontal separation of $\Delta d = 0$ mm apart from each other inside a conductive medium with a variable conductivity $\sigma^{(\mathbf{I})} = 0.01$ to $\sigma^{(\mathbf{I})} = 20$ S/m.

Fig. 3.4 and Fig. 3.5 presents the modulus of the two complex terms obtained with (3.18) and (3.19) as a surface function of the conductivity of the surrounding environment and the working frequency. For the purpose of comparison, the simulation results obtained with CST EMS are included in those figures corresponding to three different insulator radii of $R = 1.1r_0$, $2r_0$, and $3r_0$ respectively.

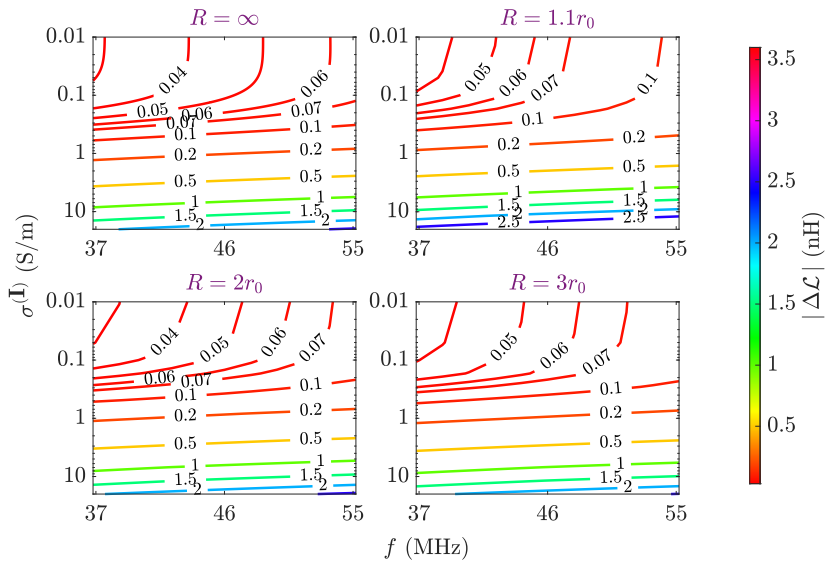


Figure 3.4: Modulus of the complex self inductance $|\Delta\mathcal{L}|$ as a surface function of the working frequency and the medium conductivity. The medium conductivity is from $\sigma^{(\mathbf{I})} = 0.01$ to $\sigma^{(\mathbf{I})} = 20$ S/m while the working frequency ranges between $f = 37$ to $f = 55$ MHz. (Top left) The analytical value obtained with (3.18) is compared to CST EMS simulation results for three different sizes of the insulators: (Top right) $R = 1.1r_0$, (Bottom left) $R = 2.0r_0$, and (Bottom right) $R = 3.0r_0$.

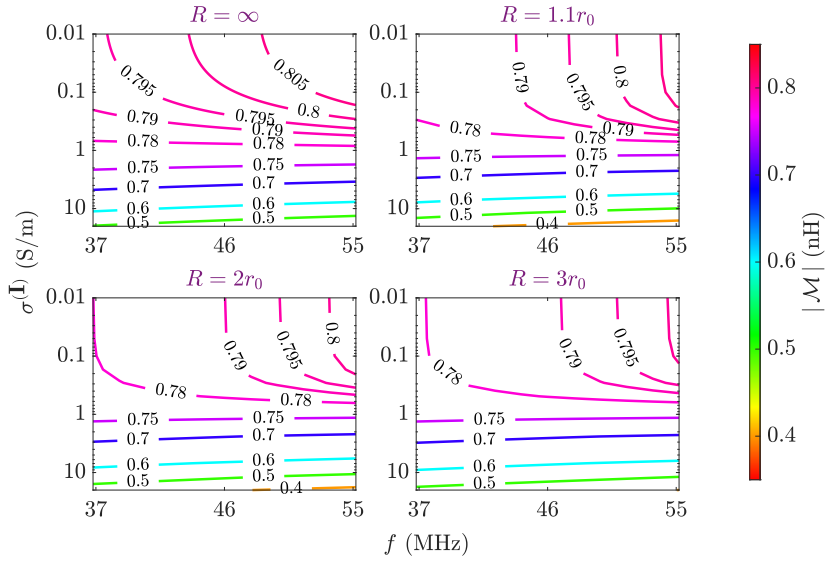
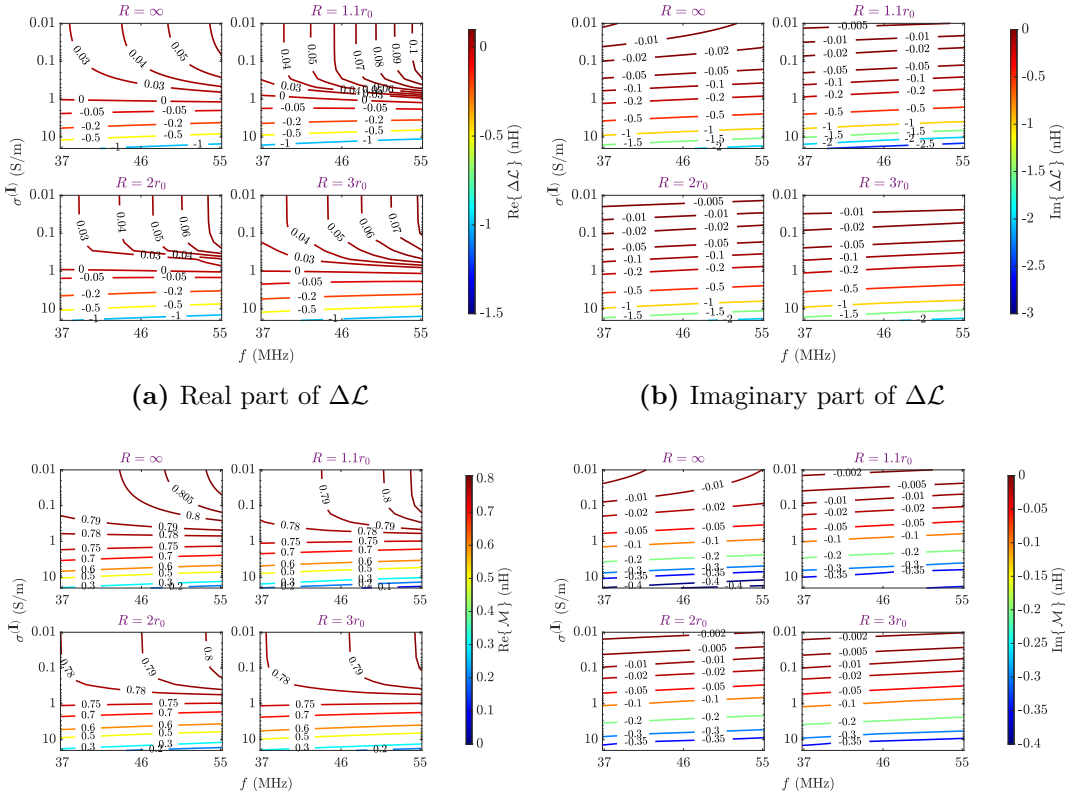


Figure 3.5: Modulus of the complex mutual inductance $|\mathcal{M}|$ as a surface function of the working frequency and the medium conductivity. The medium conductivity is from $\sigma^{(\mathbf{I})} = 0.01$ to $\sigma^{(\mathbf{I})} = 20$ S/m while the working frequency ranges between $f = 37$ to $f = 55$ MHz. (Top left) The analytical value obtained with (3.19) is compared to CST EMS simulation results for three different sizes of the insulators: (Top right) $R = 1.1r_0$, (Bottom left) $R = 2.0r_0$, and (Bottom right) $R = 3.0r_0$.

As apparent from these figures above, theoretical results calculated with (3.18) and (3.19) show the same trends as those determined with CST EMS for all three different sizes of the insulators. Both complex Kirchhoff coefficients are truly complex and frequency-dependent as confirmed by simulated data. In addition, it can be observed from the contour plots that larger radius of the insulators results in less discrepancies between the analytical solutions and the finite numerical simulations. Fig. 3.6 compares the real and imaginary parts of the complex coefficients obtained with the analytical approach and the CST EMS results for $R = 3r_0$.



(a) Real part of $\Delta\mathcal{L}$ **(b)** Imaginary part of $\Delta\mathcal{L}$

(c) Real part of $\mathcal{M}$ **(d)** Imaginary part of $\mathcal{M}$

Figure 3.6: Real parts and imaginary parts of the complex Kirchhoff coefficients $\Delta\mathcal{L}$ and $\mathcal{M}$ as a surface function of the working frequency and the medium conductivity. The medium conductivity is from $\sigma^{(\mathbf{I})} = 0.01$ to $\sigma^{(\mathbf{I})} = 20$ S/m while the working frequency ranges between $f = 37$ to $f = 55$ MHz. (Top left) The analytical value obtained with (3.18) and (3.19) is compared to CST EMS simulation results for three different sizes of the insulators: (Top right) $R = 1.1r_0$, (Bottom left) $R = 2.0r_0$, and (Bottom right) $R = 3.0r_0$.

It is clear that the larger the insulators are, the more accurate the infinite dielectric layer approximation provides. The deviation of the values obtained with formulae (3.18) and (3.19) with respect to those obtained with CST EMS for different cavity sizes are then analysed. A bar graph, Fig. 3.7, depicts the relative errors in the modulus and phase of the theoretical complex terms compared to the numerical simulations. It is worth noting that the results which have a phase less than 1° are excluded in the calculation for the relative error of the phase due to the error tolerance in simulation software. When the radius of the cavities is three times larger than the coil radius $R \geq 3r_0$, (3.18) and (3.19) are found to be in excellent agreement with the finite-element simulations in terms of modulus with average relative errors less than 5% over the simulated ranges of conductivity and working frequency. Meanwhile, the average relative error for the phases of the complex terms do not exceed 7%.

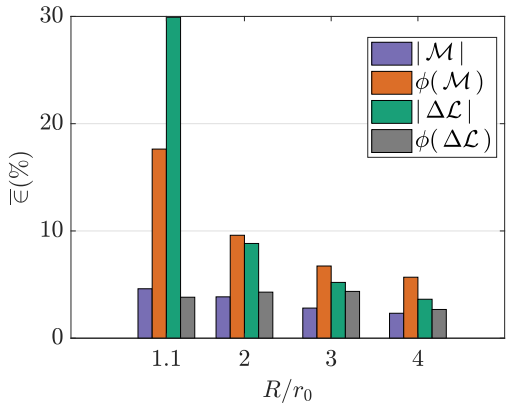


Figure 3.7: Average relative errors of the analytical solutions for the complex Kirchhoff coefficients in terms of their moduli and phases with respect to CST EMS simulation results for several different sizes of the dielectric cavities.

It is also noteworthy that the complex self inductance always has a negative imaginary part. Recall that $\Delta\mathcal{L} = \Delta\mathcal{L}' - j\Delta\mathcal{L}''$. The impedance of the coil (a RLC series resonant circuit), $\tilde{Z}$, while embedding inside a conductive medium

can be calculated by:

$$\begin{aligned}\tilde{Z} &= Z_0 + j\omega\Delta\mathcal{L} \\ &= (R_0 + \omega\Delta\mathcal{L}'') + j\omega\left(L_0 + \Delta\mathcal{L}'\right) + \frac{1}{j\omega C_0}\end{aligned} \tag{3.20}$$

where $Z_0 = R_0 + j\omega L_0 + 1/(j\omega C_0)$, R_0, L_0 and C_0 are the self impedance, resistance, inductance, capacitance of the coils in free-space respectively. From (3.20), it can be concluded that the imaginary part of the complex self inductance represents additional losses due to the conductive medium. Generally speaking, the real part of the complex self inductance represents the change in the reactance of the circuit. As the conductivity increases, the eddy currents induce an opposite EMF back to the transmitting coil as expected from Lenz's law so that the complex self inductance's real part is negative, representing the reduction in self-flux. When the ambient environment has a relatively small conductivity but a very high permittivity, i.e., lossy dielectric materials, the induced displacement currents overpower theirs counterpart – induced conduction currents. The real part of the complex self inductance astonishingly becomes positive. It indicates that the induced EMF due to the displacement currents has an opposite sign with the one due to the conduction currents. In any case, the complex self inductance alters the self inductance of the coils, making the coils resonant at different frequencies. Moreover, the absolute values of the real and imaginary parts of the complex self inductance is directly proportional to the working frequency, as shown in Fig. 3.6a and 3.6b, due to the stronger eddy current effects at higher frequencies. Else, the complex mutual inductance is indeed a complex quantity when the two coils are completely immersed in a conductive medium, analogous to the configuration discussed in Chapter 2. Since the eddy currents attenuate the primary fields generated by the transmitter, the modulus of the complex mutual inductance declines with the increasing frequency and medium conductivity, as shown in Fig. 3.5.

3.3.2.2 Impact of Vertical Distance

Both complex Kirchhoff coefficients exhibit an understandable frequency-dependent feature. For simplicity and without loss of generality, all results presented next are calculated at the frequency $f_c = 46$ MHz unless stated otherwise. Now, the effects of the vertical distance between the coils are investigated. Since the height of the dielectric insulators is kept constant, the vertical separation between the coils is actually related to the thickness c of the conductive layer (**III**) (cf., Fig. 3.2b). Fig. 3.8 and Fig. 3.9 show the complex Kirchhoff coefficients as a function of the normalised vertical separation between the two coils when the medium conductivity and the horizontal distance are set to $\sigma^{(\mathbf{I})} = 4$ S/m and $\Delta d = 0$ mm respectively. As in Fig. 3.5, a set of three numerical simulations corresponding to three different dielectric cavity radii is examined: $R = 1.1r_0$, $2r_0$, and $3r_0$. Again, the results look similar to those in Fig. 3.5 where the analytical solutions (3.18) and (3.19) appear to constitute good approximations.

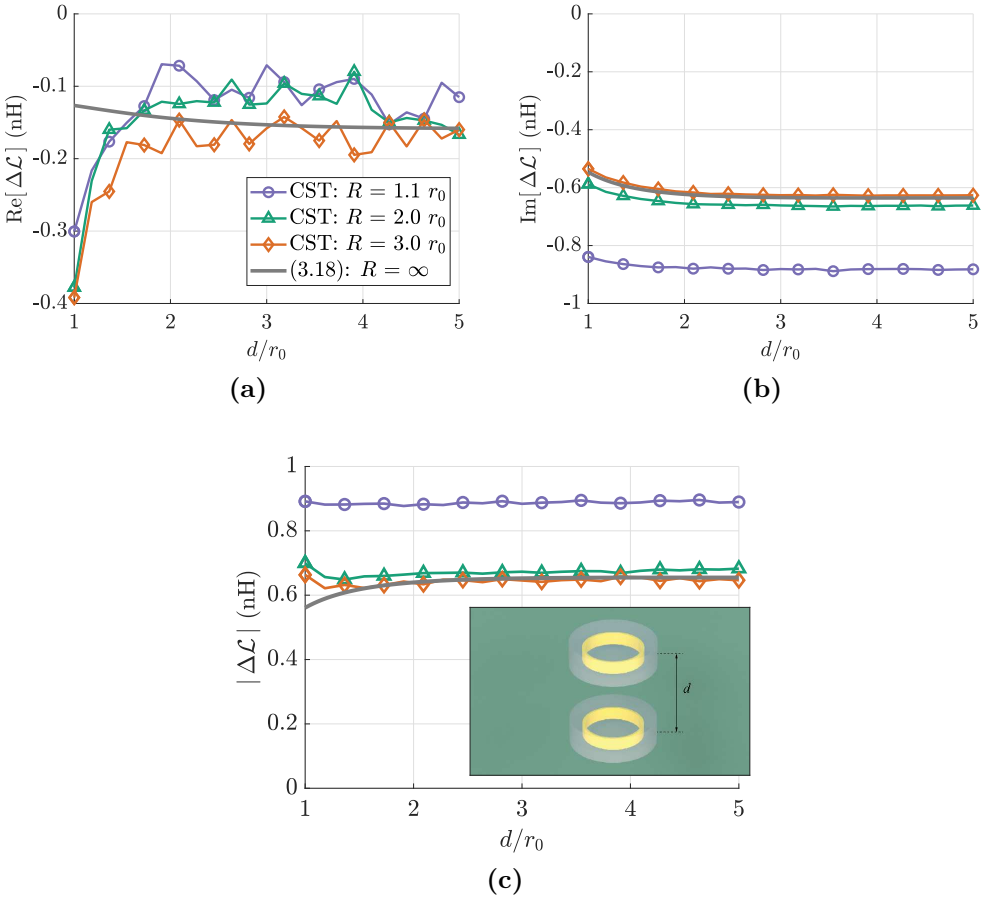


Figure 3.8: (a) Real part, (b) imaginary part, and (c) modulus of the complex self inductance $\Delta\mathcal{L}$ as a function of the normalised vertical separation d/r_0. The dissipative medium has a conductivity of $\sigma^{(\mathbf{I})} = 4$ S/m and the horizontal displacement is $\Delta d = 0$ mm. CST EMS simulation results for three different sizes of the insulators: $R = 1.1r_0$, $2r_0$, and $3r_0$ are compared with those obtained with the analytical solution (3.18).

The magnitude of the magnetic coupling declines as the separation between the coils increases. Indeed, the magnetic field decays quickly for increasing distance from the source following an inverse cube law. Moreover, an increase in distance means a thicker conductive layer between the coils which leads to bigger volume for eddy currents. The induced field therefore reduces the primary field generated by the transmitting coil and accordingly lowers the mutual inductance. Meanwhile, the complex self inductance seems to saturate when the vertical distance between coils tends to infinity. For the same reason that the magnetic field declines with the distance, the induced eddy current density in the conductive medium has its maximum strength at the region immediately neighbouring to the insulating

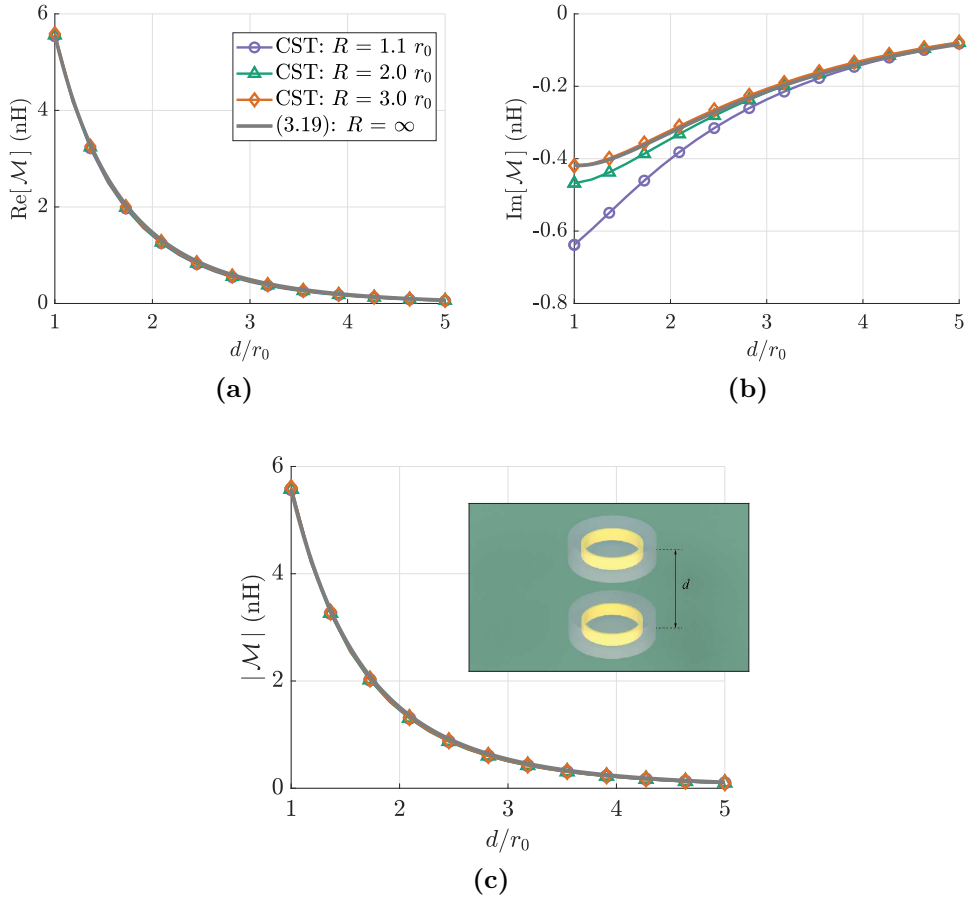


Figure 3.9: The (a) real part, (b) imaginary part, and (c) modulus of the complex self inductance $\mathcal{M}$ as a function of the normalised vertical separation d/r_0. The dissipative medium has a conductivity of $\sigma^{(\mathbf{I})} = 4$ S/m and the horizontal displacement is $\Delta d = 0$ mm. CST EMS simulation results for three different sizes of the insulators: $R = 1.1r_0$, $2r_0$, and $3r_0$ are compared with those obtained with the analytical solution (3.19).

enclosures and then decays further away. On that account, when the distance between coils are large enough, the amplitude of the nearby eddy currents generated by the transmitter is approximately steady and so is the complex self inductance. However, when the distance between two inductive circuits is small, i.e., less than $d < 1.5r_0$ for that particular coil arrangement, the analytical solutions show the credibility for estimating correctly the complex mutual inductance and the imaginary part of the complex self inductance but fail to compute its real part. It is a limitation of the analytical model where the infinite long layers of dielectric cavities are considered. Notably, the huge oscillations evident in the real part of the complex self inductance are due to the computational imperfection in the finite-element simulations.

To compute the change in the self inductance of the coil, a dense mesh as well as a high degree of solver accuracy are expected as stated in Table 3.1. Because of the relatively small electrical size of the coils in this configuration, the mesh seems to not be dense enough to provide accurate approximation for the small real part of the complex self inductance, around a few hundred pH. These oscillations can be improved by further increasing the adaptive mesh refinement in CST EMS but the trade-off will surely be a very long computational time. Nonetheless, the simulations offer a good understanding of the physical phenomenon since it can compute the imaginary part of the complex self inductance as well as the complex mutual inductance with ease. The rule of thumb $R \geq 3r_0$ is still valid given that the distance between two coils is far enough ($d \geq 1.5r_0$). The formulas give an approximate value of the magnetic coupling, which is accurate to better than a 5% average relative error in both magnitude and phase of the two complex terms compared to simulation results.

3.3.2.3 Impact of Horizontal Separation

Finally, the validity of the analytical solutions for the complex Kirchhoff coefficients is examined in the situation that the receiving coil is displaced by a distance Δd away from the coaxial alignment. The conductivity of the medium and the vertical distance are fixed at $\sigma = 4$ S/m and $d = 30$ mm, respectively. Fig. 3.10 and Fig. 3.11 present the simulation results for the complex Kirchhoff coefficients as a function of the normalised horizontal displacement between the transmitting and receiving coils. For the purpose of comparison, the data for the free space obtained with the analytical solutions is included.

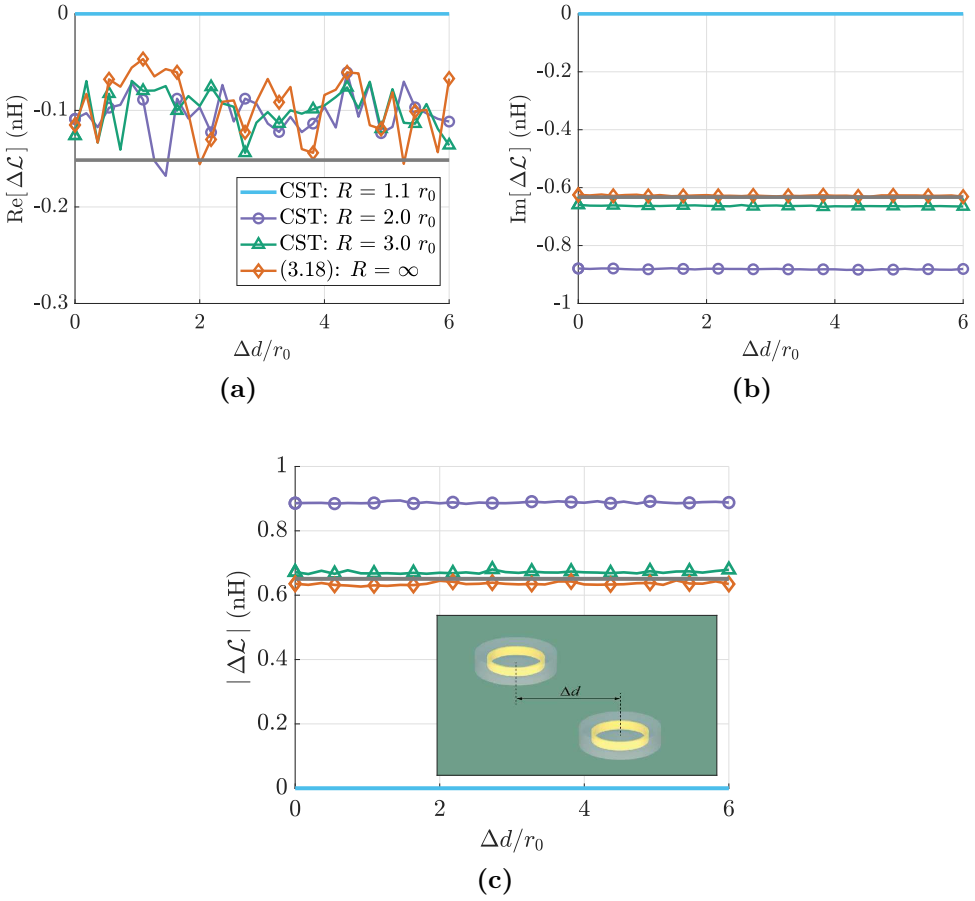


Figure 3.10: The (a) real part, (b) imaginary part, and (c) modulus of the complex self inductance $\Delta\mathcal{L}$ as a function of the normalised horizontal displacement $\Delta d/r_0$. The dissipative medium has a conductivity of $\sigma^{(\mathbf{I})} = 4$ S/m and the distance between the two coils is $d = 30$ mm. CST EMS simulation results for three different sizes of the insulators: $R = 1.1r_0$, $2r_0$, and $3r_0$ are compared with those obtained with the analytical solution (3.18).

Considering that the closed-form solution for the magnetic vector potential is derived under the assumption of infinite dielectric layers, the formula (3.18) for the complex self inductance does not fully account for the horizontal displacement of the receiver and its insulator. Despite that, Fig. 3.10 points out that the horizontal displacement in fact has little-to-no effect on the complex self inductance as the simulated modulus closely resembles a constant line over the displacement range for all three different insulator sizes. It follows the above reasoning that the eddy current strength decays rapidly from the area very close to the insulating cavities. Moreover, an interesting behaviour of the complex mutual inductance has been found when

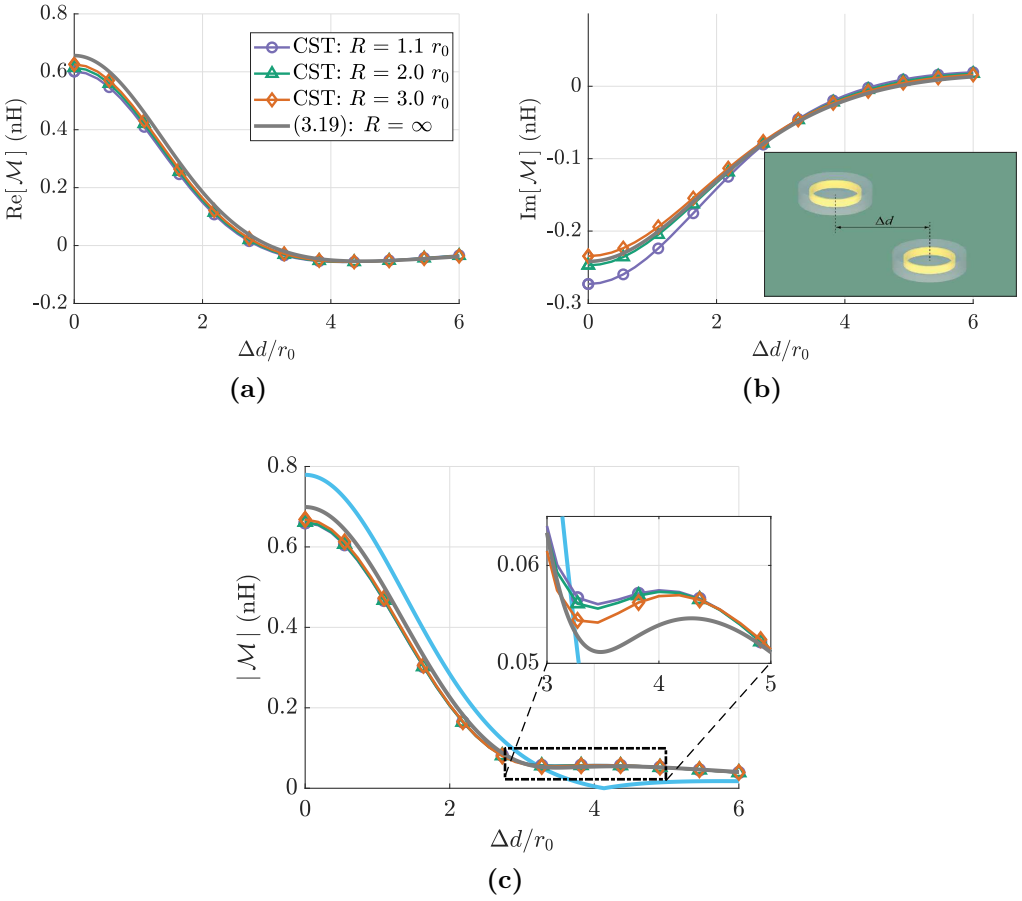


Figure 3.11: The (a) real part, (b) imaginary part, and (c) modulus of the complex mutual inductance $\mathcal{M}$ as a function of the normalised horizontal displacement $\Delta d/r_0$. The dissipative medium has a conductivity of $\sigma^{(\mathbf{I})} = 4$ S/m and the distance between the two coils is $d = 30$ mm. CST EMS simulation results for three different sizes of the insulators: $R = 1.1r_0$, $2r_0$, and $3r_0$ are compared with those obtained with the analytical solution (3.19).

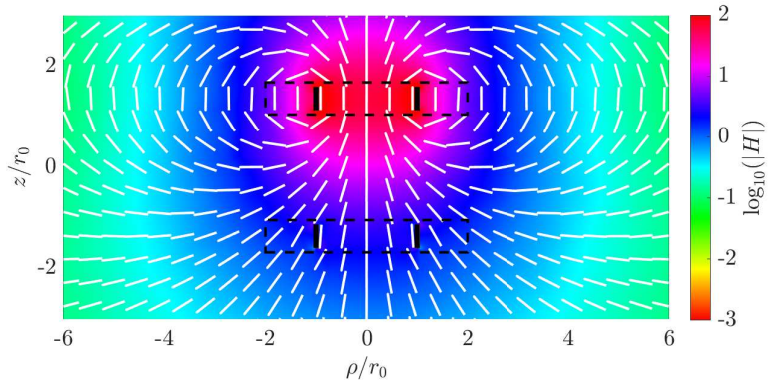
the circular symmetry is broken. In free space, the magnetic field generated by a uniform circular loop current is symmetric with the strongest magnetic flux density along the axis of the loop. When the receiver moves off the coaxial configuration, the modulus of the mutual inductance decreases proportionally with the increasing displacement from the receiving loop centre to the transmitter axis until reaching the zero-point where the net magnetic flux across the loop vanishes. Then its modulus starts increasing due to the out-of-phase coupling.

For the coil arrangement investigated, the zero-point occurs at about $\Delta d = 4.14r_0$. In contrast to the free space case, inside an ambient dissipative medium, the modulus

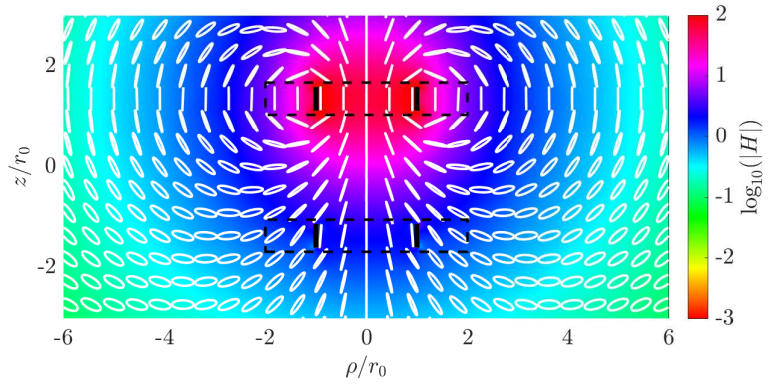
of the complex mutual inductance does not exhibit a monotonically decreasing function of the horizontal displacement before reaching the zero-point, as shown in Fig. 3.11c. In fact, there is no longer a zero-point in the magnetic flux generated by an insulated current loop embedded in a dissipative material. Instead, the mutual coupling may have both local minimum and maximum values over a certain range of the horizontal displacement. The reason underlying this trend can be clarified by examining the distribution of the magnetic field, see below. Nevertheless, the analytical solution (3.19) provides a good approximation of the complex mutual inductance as a function of the receiver horizontal displacement. Once again, excellent accuracy with an average relative error not exceeding 7% can be achieved for both complex terms when the insulator radius is at least three times larger than the coil radius, $R \geq 3r_0$.

The magnetic field generated by the transmitting coil in an arbitrary plane through the z-axis of the coaxial configuration is investigated. Fig. 3.12b shows the results of a finite-element calculation by CST EMS for the magnitude and polarization of the magnetic field generated by an insulated transmitting coil immersed in a dissipative medium. For the purpose of comparison, the field distribution when the medium is lossless is presented in Fig. 3.12a. Here, the position of the receiver is disregarded as the fields due to the conduction current in the receiver are disabled in CST EMS simulations.

Following the argument for the field polarization in the case where a conductive block is inserted between a pair of low frequency coils, the polarization of the magnetic field generated by a coil immersed inside a dissipative environment is generally elliptically polarised, i.e., its spatial components have a non-zero phase shift relative to one another. Unlike the linear polarization of the free space case in Fig. 3.12a, in the plane of the receiver, the axial ratio and tilt angle of the ellipses representing the polarization of the magnetic field illustrated in Fig. 3.12b change noticeably between $\rho = 2r_0$ and $\rho = 6r_0$. It means that the H_z component, which determines the value of the induced voltage at the coaxial receiver changes in modulus as well as in its relative phase with respect to the H_ρ component.



(a) Free Space

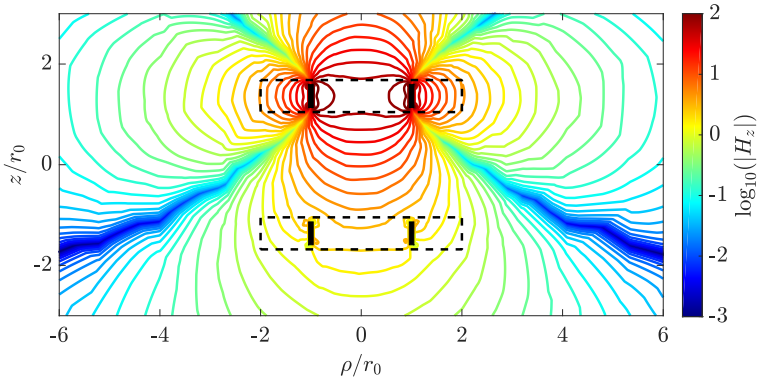


(b) Seawater ($\sigma = 4$ S/m, and $\epsilon_r = 78$)

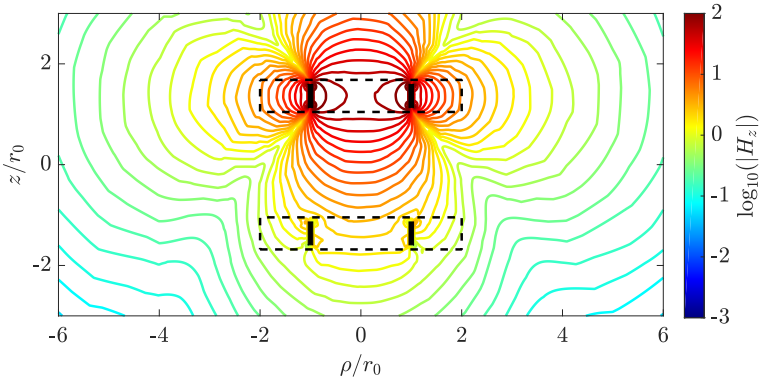
Figure 3.12: Simulated polarization ellipses and magnitude of the total magnetic field produced by the transmitter coil. Ellipse axes are normalised and plotted at a sampling step of 5 mm along the y and z directions. Black dash lines mark the cross sections of the dielectric cavities. (a) The medium (a) is free space and (b) has relative permittivity of $\epsilon_r = 78$, relative permeability of $\mu_r = 1$, and conductivity $\sigma = 4$ S/m (seawater). The mutual inductances are (a) $M \approx 0.6572\angle{-22°}$ and (b) $M \approx 0.7572\angle{-0.02°}$.

The distribution of the z-component of the simulated magnetic field shown in Fig. 3.12 is further explored in the contour plots of Fig. 3.13. These maps are consistent with the analytical prediction of the mutual inductance by the formula (3.19) and corresponding simulation results shown in Fig. 3.11. When the two coils are in free space, a region where the field vanishes appears at about $\Delta d \approx 4.14 r_0$, cf. Fig. 3.11c, similarly to $\rho \approx 4.14 r_0$ in Fig. 3.13a. Otherwise when the two coils are immersed in a dissipative environment, due to the interference between the primary field created by the transmitting coil and the reaction field produced by eddy currents in the medium, which can be substantially phase shifted with respect to the inducing field, the contour map of the magnitude of the H_z component no

longer exhibits null regions where the net flux of the magnetic field is evanescent but has instead a smoother quatrefoil distribution, as shown in Fig. 3.13b. Since the complex mutual inductance is calculated by integrating the H_z component over the area of the receiver, the quatrefoil geometry of the H_z component results in the local minimum and maximum points of the mutual inductance as a function of the horizontal displacement Δd, observed in Fig. 3.11.



(a) Free space



(b) Seawater ($\sigma = 4$ S/m, and $\epsilon_r = 78$)

Figure 3.13: Contour maps of the modulus of H_z components of the magnetic fields illustrated in Fig 3.12b and Fig 3.12a respectively. Black dash lines mark the cross sections of the insulating cavities.

3.4 Conclusions

A novel equivalent circuit model for two coupled coils insulated by small cylindrical cavities and completely immersed in an infinite homogeneous dissipative medium has been theorized as a combination of circuit theory and field theory. The

dissipative medium background in proximity to two low frequency coils is shown to have significant impact upon their near-fields, and the induced eddy currents are responsible for the change in their self impedance and the mutual inductance between them. The coupling interactions between the eddy currents and the currents flowing in the two coils may be represented by two complex inductive coefficients, namely complex self inductance and complex mutual inductance. These complex terms depend on the working frequency, geometry of the coils and medium's electromagnetic property. To derive closed-form solutions for these coefficients, the dielectric cavities providing insulation for the coils are considered as infinitely wide layers. The advantage of analytical solutions is the possibility to more accurately calculate the fields, and thereby the electromagnetic interactions of two low frequency coils coupled in non-conventional media.

A complete analysis of the complex Kirchhoff coefficients as functions of the working frequency, medium conductivity, vertical distance and horizontal displacement is conducted. Numerical simulations with CST EMS show that the analytical solutions could be used to accurately estimate the values of the complex coefficients over broad ranges of parameters. They exhibit remarkable accuracy with an average relative error not exceeding 7% in comparison to the finite-element simulations for reasonable values of the parameters, given that the radius of the insulating cavity is sufficiently large with respect to the coil radius, i.e., at least three times larger than the coil diameter $R \geq 3r_0$. In particular, the solution for the complex mutual inductance is capable of correctly reproducing an interesting behaviour of the complex mutual inductance as a function of coil horizontal displacement, which exhibits oscillations in the magnitude with local minima and maxima without vanishing as in free space case. This observation can be important in the research field of eddy current testing where the magnetic induction is utilized to detect or characterize some parameters of a conductive object, e.g., metal detectors.

Considering coupled coil system are usually excited by time-harmonic voltages with finite coil impedances, the analytical method used in [71], which considers one coil driven by a constant amplitude alternating current and the other coil

left open-circuited, is not always applicable. Superior to the constant amplitude alternating current approach, this method not only reduces the complexity of the system of linear equations representing the fields but also is capable of directly calculating the complex self inductance arose naturally from theory. The proposed approach is also versatile and can be easily adapted to various application scenarios, for instance, a submarine communications system consisting of two immersed coils close to the water surface. The sea may be considered as a conducting half-space and to derive a closed-form solution, an infinite layer of air should be added above the top of layer (**I**) and thus system (B.7) or (B.8) will contain 10 rather than 8 linear equations. Additionally, the approach is applicable when the dissipative layers have different conductivities, such as in free-floating wireless implantable neural recording [108, 109] where a transmitting coil is placed on the scalp while the neural recording sensors are implanted on the cortex area of the patient brain under the skull. In this case, layer (**I**) is air while layers (**III**) and (**V**), the skull and cortex respectively, may have different conductivities.

Moreover, it is reaffirmed that the electromagnetic properties of the medium indeed influence the coil resonators to a greater extent. Apart from the variation of the mutual inductance due to the field rotation, there exists the complex self inductance accounting for the change in the coil's self inductance. The imaginary part of the complex self inductance represents the additional losses added by the medium and its real part is associated with the change in the flux. As entitled to energy loss, the imaginary part of complex self inductance must be mathematically negative. The real part can be either positive or negative depending on the nature of the environment. For examples, when the medium is a dielectric material (highly permittivity but poor conductivity), the real part is positive due to the flux reinforcement of the displacement currents. When the medium supports the conduction eddy currents, they oppose the change in flux and cause a counter EMF to the transmitting coil, resulting in a negative real part of the complex self inductance.

To conclude, the new circuit model incorporates all electromagnetic coupling and feedback effects for two insulated coupled coils in non-conventional media. It will

undoubtedly be of interest in the network analysis and design for any magnetic induction system operating inside a dissipative medium, such as underground/underwater sensor networks, wearable/implanted sensors for biological systems, and wireless power transfer in harsh environments.

4

Network Analysis of Coupled Resonators in Dissipative Media

Contents

4.1 Quality factor and Resonant Frequency 81
4.2 Frequency Splitting 86
4.3 Current Distribution 89
4.4 Power Conservation 94
4.5 Conclusions 98

Having proved the merit of the novel analytical solutions (3.18) and (3.19) with a remarkable accuracy not exceeding 7% in terms of the relative error with respect to the CST simulated results for reasonable values of the parameters, only results from those expressions are considered in this chapter. It is equivalent to assuming the radius of the dielectric cavities is larger than at least three times the coil radius. With the equivalent circuit model for the two coils being changed significantly because of the additional coupling terms, Chapter 4 performs the network analysis of the two-coil system in detail. Often, the resonant frequency and the quality factor of the coils inside a dissipative medium have not been analysed whilst presuming they are unaffected by the surrounding environment. Section 4.1 analyses the impact of the medium on the resonant frequency and the quality factor of the coils. By

using the eigenvalue method, the splitting frequencies in strongly-coupled regimes are determined in Section 4.2, followed by the current distribution in Section 4.3. To conclude the chapter, Section 4.3 discusses the power conservation the emergence of the two complex Kirchhoff coefficients. The main contribution of this chapter is to perform the network analysis of a two-coupled-resonator system with the novel circuit model stated in Chapter 3. Some of the work in this chapter have been published in the following journals/conference proceedings:

- **S. Chu**, M. S. Luloff, J. Yan, C. J. Stevens, and E. Shamonina "Magnetoinductive waves in attenuating media", *Nature Communications*, 2020 (**submitted**).

4.1 Quality factor and Resonant Frequency

When embedding a resonator circuit in a conductive medium, the physical phenomenon is quite clear. The induced eddy currents introduce additional losses as well as change the self-flux of the circuit. Moreover, the displacement currents may result in a rise in the self inductance when the medium is a lossy dielectric material, i.e., $\sigma \leq \omega\epsilon_0\epsilon_r$. It surely causes a change in the resonant frequency, f_0, and a reduction in the quality factor, Q, of the circuit. The impedance of a coil when immersed in a medium background can be expressed by (3.20), where $R_0 + \omega\Delta\mathcal{L}''$ is the total losses of the circuit including the losses from the eddy currents, $L_0 + \Delta\mathcal{L}'$ is the total inductance of the circuit, $\Delta\mathcal{L} = \Delta\mathcal{L}' - j\Delta\mathcal{L}''$ is the frequency-dependent complex self inductance.

Here, the notations are as follows: x is the circuit parameter of the coil in free space while $\tilde{x}$ is that of the coil inside a dissipative medium. In principle, the resonant frequency occurs when the inductive reactance is equal to the capacitive reactance. Unlike the equivalent circuit theory where the electrical reactance elements are idealised to be frequency-independent for a certain range of frequency, the complex self inductance is instead dependent upon the working frequency. Therefore, the

resonant frequency of a coil immersed inside a conductive medium is the root of the following equation representing the total reactance equalling to zero:

$$2\pi\tilde{f}_0\left(L_0+\Delta\mathcal{L}'(\tilde{f}_0)\right)=\frac{1}{2\pi\tilde{f}_0C_0}\;\Leftrightarrow\;\tilde{f}_0{}^2\left(L_0+\Delta\mathcal{L}'(\tilde{f}_0)\right)-\frac{1}{4\pi^2C_0}=0 \tag{4.1}$$

Hence, its Q-factor inside the medium, $\tilde{Q}$, is then obtained by:

$$\tilde{Q}=\frac{2\pi\tilde{f}_0\left(L_0-\Delta\mathcal{L}'(\tilde{f}_0)\right)}{R_0+2\pi\tilde{f}_0\Delta\mathcal{L}''(\tilde{f}_0)} \tag{4.2}$$

Now let's consider a coil with the parameters listed in Table. 3.2. The expression for self inductance of the coil can be found with several different methods in most textbooks on the subject of electromagnetism, e.g., [82]. Here, the self inductance can also be calculated by integrating the magnetic vector potential generated by the coil itself over its volume in the α-space:

$$L_0=\frac{2\pi N}{w\,l}\int_0^{\infty}\int_{r-w/2}^{r+w/2}\int_{(-h-l)}^{(-h)}\alpha\,r\,\mathrm{J}_1(\alpha r)\;\widehat{\Psi}(\alpha,z,\omega)\,\mathrm{d}\alpha\,\mathrm{d}r\,\mathrm{d}z \tag{4.3}$$

Typically, the parasitic self capacitance of electromagnetic coils is of the order of pF, much smaller than the lumped capacitors required to tune the coils to resonate at lower frequencies. As a result, the self capacitance is usually disregarded and the value of tuning capacitors are then determined from the desired resonance and the self inductance. The resistance of the coil consists of the energy loss due to the skin and proximity effects. The proximity effect increases the resistance of a conductor due to the influences of adjacent AC currents causing a non-uniform current distribution over the its cross section [110]. A large number of papers investigated the proximity effect by analytical, numerical or semi-analytical methods [111–113]. However, this effect is beyond the scope of this thesis so it is neglected in the calculation of the coil resistance. Besides, to isolate the effects of the complex self inductance, the frequency dependence of the resistance due to the skin effect is presumably obsolete around the resonance, i.e., R_0 calculated at the resonance frequency is constant over a small range of frequency around the resonance. The formula for the resistance of a coil with rectangular cross-section is modified as:

$$R_0=\sqrt{\frac{\pi^3 f\mu_c}{\sigma_c}}\frac{2Nr_0}{w+h} \tag{4.4}$$

where μ_c and σ_c are the relative permeability and conductivity of the conductor material. Finally, assuming the coils are made of annealed copper ($\mu_c = 1$ and $\sigma_c = 5.8 \times 10^7$ S/m), the circuit parameters are as follows: $f_0 = 46$ MHz, $R_0 = 10.19$ mΩ, $L_0 = 30.46$ nH, $C_0 = 393$ pF, and $Q \approx 432$. The coil is then insulated by a lossless cylindrical cavity with a height of $h + 2l = 7$ mm and embedded in a medium with the relative permittivity of $\epsilon_r = 78$, relative permeability of $\mu_r = 1$ and variable conductivity from $\sigma = 10^{-3}$ to $\sigma = 10^2$ S/m. With that given coil geometry and medium's electromagnetic properties, the complex self inductance can be calculated accordingly with (3.18). Fig. 4.1 shows the influence of the medium conductivity on the resonant frequency of the particular coil design above.

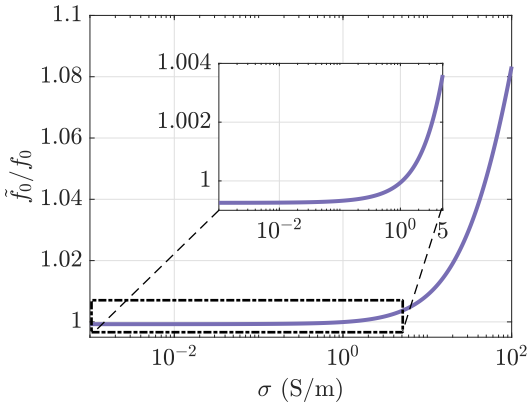


Figure 4.1: Calculated normalised resonant frequency of a coil inside an infinite medium background with a variable conductivity from $\sigma = 10^{-3}$ to $\sigma = 10^2$ S/m. The result obtain with (4.1) is normalised to the resonance of the coil in vacuum.

When the medium is a lossy dielectric material ($\sigma = 10^{-3}$ S/m and $\epsilon_r = 78$), the resonant frequency of the coil unsurprisingly reduces by a small amount in virtue of the strong effects of the displacement currents. As the environment allows the conduction currents to take place, the fields generated from the conduction eddy currents start cancelling out the self-flux of the coil, resulting in a decrease in the coil's self inductance. When the conductivity is still small, i.e., $\sigma \approx 1$ S/m, the flux cancellation from the conduction eddy currents balances out the flux reinforcement from the displacement eddy currents so that the resonant frequency tends to be unaffected. At higher conductivities, the impact of the conduction currents is more

profound. The real part of the complex self inductance becomes negative and also increases exponentially in magnitude, as discussed in Chapter 2. Hence, it lowers the coil's self inductance, tuning the resonance to higher frequencies.

In addition, another key characteristic parameter of the system - the quality factor of the coils - is investigated. For most of the current research going on in the field of WUSNs [68, 69, 90–93], the effects of the surrounding environment on the Q-factor are usually neglected. The losses on those system analyses are mainly assumed to associate with the decay of the transmitting signals or the path loss. However, from (3.20), the medium also introduces additional losses to the transmitting coil, represented by the imaginary part of the complex self inductance. Correspondingly, the Q-factor is expected to decline proportionally to the conductivity. Fig. 4.2 illustrates the relationship between the quality factor of the coil and the conductivity of the medium. Clearly from the graph, the quality factor seems to be strongly affected by the medium's conductivity even for a poorly conductive medium. When the conductivity is around $\sigma = 1.059$ S/m (mean value of that of living human brains [107]), the Q-factor of the coil decreases nearly 80% of its value in free-space. As the conductivity reaches $\sigma = 10^2$ S/m, the losses due to the medium mostly abolishes the Q-factor.

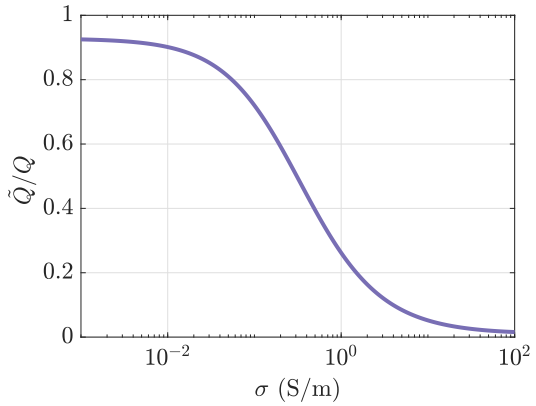


Figure 4.2: Calculated normalised Q-factor of a coil insulated by a small dielectric cavity and immersed completely inside an infinite medium background with a variable conductivity from $\sigma = 10^{-3}$ to $\sigma = 10^2$ S/m. The result obtain with (4.2) is normalised to the Q-factor of the coil in vacuum.

It is worth to mention that the coil investigated in the configuration has only one turn with quite small dimensions because this thesis mainly focuses on the applications of MI waves with metamaterials. The influence of the complex self inductance on resonant frequency and the quality factor should be conscientiously considered in applications employing bigger and longer coils, e.g., wireless power transfer technology [24] or WUSNs [51, 91]. The coils used in practical WUSNs typically have at least several number of turns and are much bigger with the mean radius in the order of hundreds of millimetres to a few metres. So, it can be envisioned that their resonant frequency and the quality factor are drastically affected by the surrounding medium due to the geometric dependence of the complex self inductance. Fig. 4.3 clearly shows the evidence of the huge change in (a) the resonant frequency and (b) the Q-factor of the coils in a practical system investigated in [51, 91].

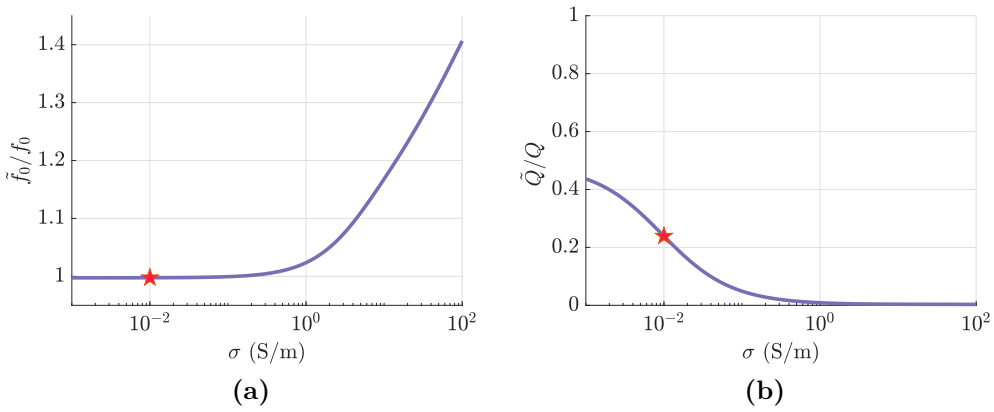


Figure 4.3: The normalised (a) resonant frequency and (b) Q-factor of a coil in a practical WUSN investigated in [51, 91]. The coil has dimensions: mean radius of $r_0 = 150$ mm, height of $l = 7.25$ mm, thickness of $w = 1.45$ mm, and five turns $N = 5$. The resonant frequency and the Q-factor in free space are: $f_0 = 7$ MHz and $Q = 1284$. The cylindrical dielectric cavity providing insulation for the coils has a height of $2h + l = 9.25$ mm. The soil's electromagnetic properties are relative permittivity of $\epsilon_r = 1$, relative permeability of $\mu_r = 1$, and variable conductivity from $\sigma = 10^{-3}$ to $\sigma = 10^{2}$ S/m. The red stars indicate the value of soil's conductivity ($\sigma = 1e-2$ S/m, dry soil) investigated in [91]. The results are normalised to those of the coil in vacuum.

4.2 Frequency Splitting

Typically, the resonance splitting occurs when the two coils are in the strongly-coupled regime, i.e., the strength of the mutual coupling between the two resonators is larger than the losses [114]. The current responses in the two coils then exhibit two peaks above and below the resonance frequency in the non-coupled case, namely the odd and even mode. At the even mode, the currents in the two coils are in phase whilst 180° out of phase at the odd mode. The two modes coalesce into one even mode when the two coils are in the lossely-coupled regime, cf. Fig. 6 in [115]. Here, the main interest of this thesis is to examine the effects of the dissipative medium on the frequency splitting phenomenon so that the two coils should be placed in the strongly-coupled regime in vacuum. The coil arrangement is illustrated in Fig. 4.4. The coils are then tuned to resonate at $f_0 = 46$ MHz.

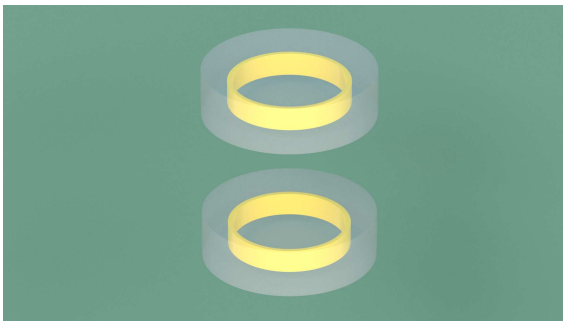


Figure 4.4: The configuration investigated consisting of two identical coils with dielectric enclosures placed inside a dissipative environment. The coils are placed coaxially with a distance of 30 mm apart from each other.

To isolate the losses added by the dissipative medium, since the Q-factor of the resonators in free space is usually high (or the damping should be small), the undamped resonant frequencies for two coupled coils can be sought by ignoring the internal resistance of the coil ($Z = j\omega L + 1/(j\omega C)$). By using (3.20), the

impedance matrix can be expressed in the following form:

$$\begin{aligned}\mathbf{Z} &= \begin{bmatrix} \tilde{Z} & j\omega\mathcal{M} \\ j\omega\mathcal{M} & \tilde{Z} \end{bmatrix} \\ &= \begin{bmatrix} \omega\Delta\mathcal{L}'' + j\omega\left(L_0 + \Delta\mathcal{L}'\right) + \dfrac{1}{j\omega C_0} & j\omega\mathcal{M} \\ j\omega\mathcal{M} & \omega\Delta\mathcal{L}'' + j\omega\left(L_0 + \Delta\mathcal{L}'\right) + \dfrac{1}{j\omega C_0} \end{bmatrix} \\ &= j\omega\left(L_0 + \Delta\mathcal{L}'\right) \begin{bmatrix} -j\dfrac{\Delta\mathcal{L}''}{L_0 + \Delta\mathcal{L}'} + 1 - \dfrac{\tilde{\omega_0}^2}{\omega^2} & \dfrac{\mathcal{M}}{L_0 + \Delta\mathcal{L}'} \\ \dfrac{\mathcal{M}}{L_0 + \Delta\mathcal{L}'} & -j\dfrac{\Delta\mathcal{L}''}{L_0 + \Delta\mathcal{L}'} + 1 - \dfrac{\tilde{\omega_0}^2}{\omega^2} \end{bmatrix} \end{aligned} \tag{4.5}$$

where $\tilde{\omega_0} = 1/\sqrt{\left(L_0 + \Delta\mathcal{L}'\right)C_0}$ is the angular frequency of the coils inside the medium. The natural response of the system can be written as:

$$j\omega\left(L_0 + \Delta\mathcal{L}'\right) \begin{bmatrix} -j\dfrac{\Delta\mathcal{L}''}{L_0 + \Delta\mathcal{L}'} + 1 - \dfrac{\tilde{\omega_0}^2}{\omega^2} & \dfrac{\mathcal{M}}{L_0 + \Delta\mathcal{L}'} \\ \dfrac{\mathcal{M}}{L_0 + \Delta\mathcal{L}'} & -j\dfrac{\Delta\mathcal{L}''}{L_0 + \Delta\mathcal{L}'} + 1 - \dfrac{\tilde{\omega_0}^2}{\omega^2} \end{bmatrix} \begin{bmatrix} I_1 \\ \\ I_2 \end{bmatrix} = \begin{bmatrix} 0 \\ \\ 0 \end{bmatrix} \tag{4.6}$$

Equation (4.6) can be rearranged as:

$$\begin{bmatrix} -j\dfrac{\Delta\mathcal{L}''}{L_0 + \Delta\mathcal{L}'} + 1 & \dfrac{\mathcal{M}}{L_0 + \Delta\mathcal{L}'} \\ \dfrac{\mathcal{M}}{L_0 + \Delta\mathcal{L}'} & -j\dfrac{\Delta\mathcal{L}''}{L_0 + \Delta\mathcal{L}'} + 1 \end{bmatrix} \begin{bmatrix} I_1 \\ \\ I_2 \end{bmatrix} = \frac{\tilde{\omega_0}^2}{\omega^2} \begin{bmatrix} I_1 \\ \\ I_2 \end{bmatrix} \tag{4.7}$$

Therefore, $\tilde{\omega_0}^2/\omega^2$ is the eigenvalue of the matrix on the left hand side of (4.7). After simple mathematical operations, the splitting frequency can be determined as:

$$\omega_{u,l} = \frac{\tilde{\omega_0}}{\sqrt{1 \pm \dfrac{\mathcal{M}}{L_0 + \Delta\mathcal{L}'} - j\dfrac{\Delta\mathcal{L}''}{L_0 + \Delta\mathcal{L}'}}} \tag{4.8}$$

where $\omega_{u,l}$ denotes the upper and lower resonance after splitting. Due to the fact that the Kirchhoff coefficients is generally complex, the eigenvalue $\tilde{\omega_0}^2/\omega^2$ and thereby, $\omega_{u,l}$ may be complex with the imaginary part representing the losses added by the dissipative surrounding medium. Also, as discussed above, the Kirchhoff coefficients exhibit frequency dependent characteristics, resulting in a computational difficulty using (4.8). The complex coefficients therefore are taken the values at the resonance frequency of the coil in the conductive medium, $\mathcal{M} = \mathcal{M}(\tilde{\omega_0})$ and

$\Delta\mathcal{L} = \Delta\mathcal{L}(\tilde{\omega_0})$. Finally, because the Q-factors of the coils in free space are high, the upper and lower resonant frequency is approximated by removing the imaginary part associated with the loss in the system:

$$\omega_{u,l} \approx \frac{\tilde{\omega_0}}{\Re\left[\sqrt{1 \pm \frac{\mathcal{M}(\tilde{\omega_0})}{L_0 + \Delta\mathcal{L}'(\tilde{\omega_0})} - j\frac{\Delta\mathcal{L}''(\tilde{\omega_0})}{L_0 + \Delta\mathcal{L}'(\tilde{\omega_0})}}\right]} \tag{4.9}$$

Fig. 4.5 compares the theoretical predictions of the splitting resonances to the simulation results. The simulation data is obtained by computing the current responses in both coils with the impedance matrix in (4.5), given that the excitation voltage of 1 V is applied to one coil. The upper and lower resonant frequency in the simulations are then detected by finding the odd and even mode in the current response of either coil.

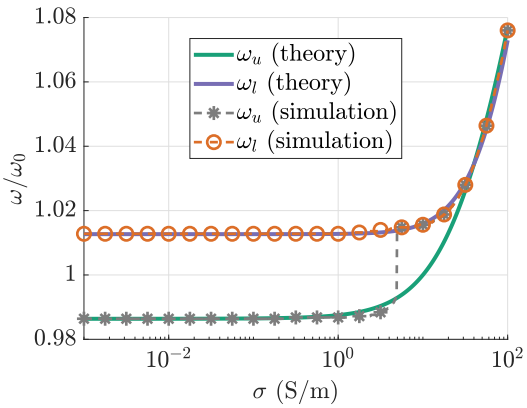


Figure 4.5: Comparison of the theoretical values and simulation results for splitting resonant frequencies of two coupled coils inside a dissipative environment. The two coils are insulated by a small dielectric cavity and immersed completely inside an infinite medium background with a relative permittivity of $\epsilon_r = 78$, relative permeability of $\mu_r = 1$, and variable conductivity from $\sigma = 10^{-3}$ to $\sigma = 10^2$ S/m. The coil has dimensions: mean radius of $r_0 = 11$ mm, height of $l = 5$ mm, thickness of $w = 1$ mm, one turn $N = 1$ and the resonant frequency of $f_0 = 46$ MHz. To isolate the effects of the medium, the internal resistance of the coils is negligible, $R_0 = 0$. The cylindrical dielectric cavity providing insulation for the coils has a height of $2h + l = 7$ mm. The results are normalised by $f_0 = 46$ MHz.

In Fig. 4.5, the theory curves and the numerical data appear to be in excellent agreement. When the medium conductivity is relatively small (less than $\sigma < 1$ S/m), the splitting frequencies are practically equal to those in the free space case.

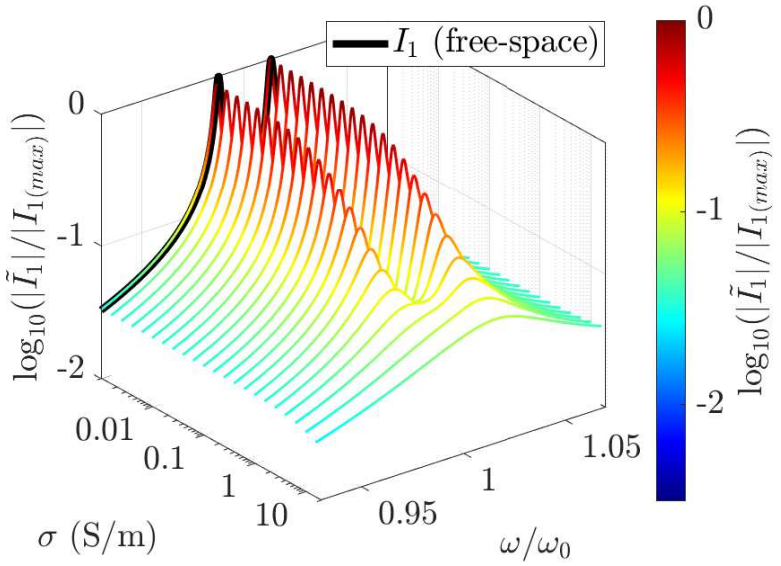
As the conductivity increases, the upper and lower resonances raise according to the original one of the coil inside the dissipative medium in the isolated case. The mutual coupling tends to zero when the medium is very conductive, resulting in the merger of the two modes. In the simulations, at $\sigma \approx 4.9$ S/m, the current response exhibits only a peak at the higher resonance instead. The phenomenon is indeed due to a very low Q-factor of the coils. The medium background lowers the Q-factor, as pointed out in the previous subsection, and therefore, spreads the current peak in the frequency domain. The resonance may be still separated but the lower resonant peak is overshadowed by the slope of the upper one. The eigenvalue method above, however, does not take into account the stretch of the current response of the coils.

4.3 Current Distribution

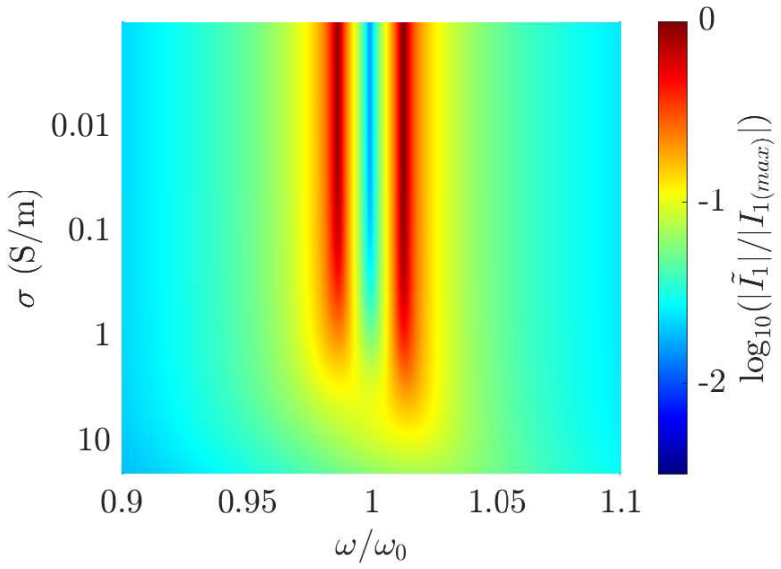
Knowing the impedance matrix of the two-coil system immersed inside a dissipative environment, it is possible to determine the current response versus frequency for a given excitation voltage. It is assumed that the excitation is a voltage $V_0 = 1$ V applied in one coil. The current matrix can be then calculated as in the following equation:

$$\begin{bmatrix} I_1 \\ I_2 \end{bmatrix} = \begin{bmatrix} Z_0 + j\omega\Delta\mathcal{L} & j\omega\mathcal{M} \\ j\omega\mathcal{M} & Z_0 + j\omega\Delta\mathcal{L} \end{bmatrix}^{-1} \begin{bmatrix} V_0 \\ 0 \end{bmatrix} \tag{4.10}$$

The coil arrangement in Fig. 4.4 is reinvestigated. Fig. 4.6 and Fig. 4.7 shows (a) the 3-D waterfall map and (b) its projection on xy-plane of the modulus of the current distribution in a pair of transmitting and receiving coils, respectively, versus frequency and medium conductivity. For the purpose of comparison, each current response of the two coils in the free space case is included as a black line. All the results are normalised to the maximum value of the corresponding currents in free space.

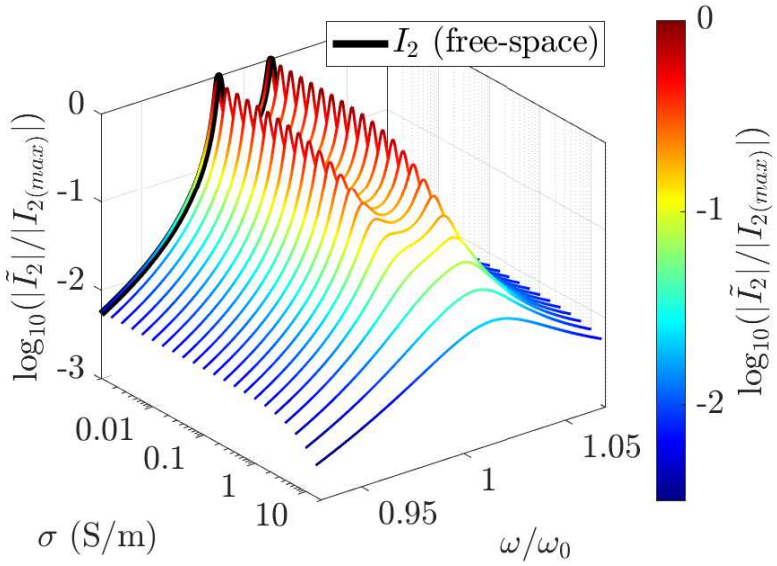


(a)

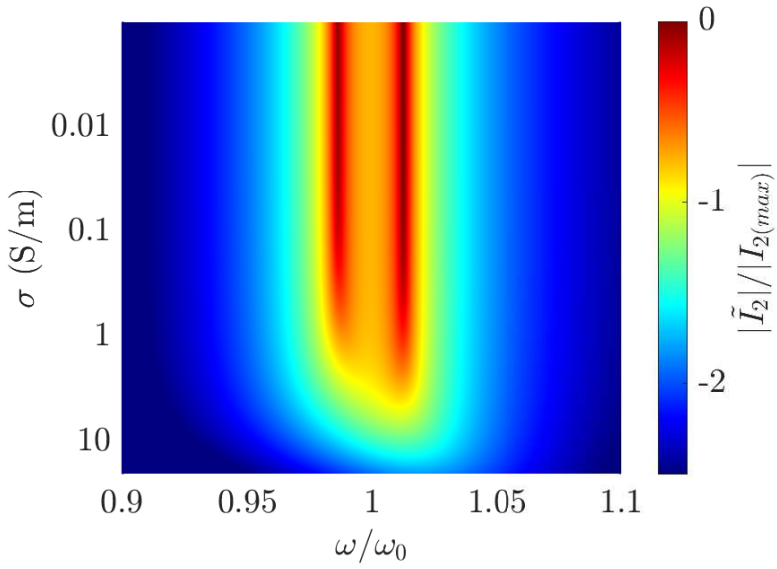


(b)

Figure 4.6: Calculated normalised magnitude of the current distribution versus frequency and medium conductivity in the transmitting coil: (a) the 3-D waterfall map and (b) colour-map for the configuration of two circular coils of mean radius $r_0 = 11$ mm, height of $l = 5$ mm, thickness of $w = 1$ mm, number of turns $N = 1$, separated by a vertical distance $d = 30$ mm and horizontal displacement $\Delta d = 0$ inside a dissipative medium with a relative permittivity of $\epsilon_r = 78$, relative permeability of $\mu_r = 1$, and conductivity $\sigma = 4$ S/m. The resonant frequency and the Q-factor in free space are: $f_0 = 46$ MHz and $Q = 432$. The cylindrical dielectric cavity providing insulation for the coils has a height of $2h + l = 7$ mm. The result is normalised to the maximum value of the transmitter current when the transmission medium is vacuum.



(a)



(b)

Figure 4.7: Calculated normalised magnitude of the current distribution versus frequency and medium conductivity in the receiving coil: (a) the 3-D waterfall map and (b) colour-map for the configuration of two circular coils of mean radius $r_0 = 11$ mm, height of $l = 5$ mm, thickness of $w = 1$ mm, number of turns $N = 1$, separated by a vertical distance $d = 30$ mm and horizontal displacement $\Delta d = 0$ inside a dissipative medium with a relative permittivity of $\epsilon_r = 78$, relative permeability of $\mu_r = 1$, and conductivity $\sigma = 4$ S/m. The resonant frequency and the Q-factor in free space are: $f_0 = 46$ MHz and $Q = 432$. The cylindrical dielectric cavity providing insulation for the coils has a height of $2h + l = 7$ mm. The result is normalised to the maximum value of the receiver current when the transmission medium is vacuum.

As expected from a pair of strongly coupled magnetic resonators, resonant peaks shift away from the original value of the self resonance. In free space, the current response splits into two almost perfectly symmetrical peaks as the two coils are ideally identical. When submerging the two coils in a surrounding conductive environment, the magnitudes of the currents decline due to the presence of induced eddy currents. Besides this phenomenon, the frequency splitting exhibits unexpected behaviours. Firstly, the symmetry of the current responses is remarkably broken as the medium conductivity is non-zero. The lower resonances tend to experience a higher loss compared to the upper resonances in both coils. Additionally, the decaying amplitude of the lower resonant peaks with increasing medium conductivity is high when compared to the upper peak. When the attenuation of the magnetic coupling is high enough, i.e., $\sigma > 4$ S/m, the eddy currents can completely suppress the lower resonant frequencies. As it happens, each current response in the two coils displays an under-coupled-like region with only one resonance. With the conductivity increasing to infinity, the Q-factor as well as the magnetic coupling tend to zero. This phenomenon is comparable to non-coupled magnetic resonators as the energy transmission from the transmitter to the receiver dissipates.

In the strongly-coupled regime, the antisymmetry of the current responses indicates that resonant peaks undergo much different amounts of damping over the frequency range. The reason behind that interesting physical occurrence can be explained with circuit theory. From (4.10), the voltage-current relationship in coil 1 can be rewritten as:

$$V_0 = \left[(Z_0 + j\omega\Delta\mathcal{L}) + \frac{(\omega\mathcal{M})^2}{Z_0 + j\omega\Delta\mathcal{L}} \right] I_1. \tag{4.11}$$

In free space, (4.11) reduces to:

$$V_0 = \left[Z_0 + \frac{(\omega M_0)^2}{Z_0} \right] I_1 \tag{4.12}$$

Recall that $Z_0 = R_0 + jX_0$, (4.12) can be rewritten as:

$$\begin{aligned} V_0 &= \left[R_0 + jX_0 + \frac{(\omega M_0)^2 R_0 - j(\omega M_0)^2 X_0}{R_0^2 + X_0^2} \right] I_1 \\ &= \left[R_0 + \frac{(\omega M_0)^2 R_0}{R_0^2 + X_0^2} + j\left(X_0 - \frac{(\omega M_0)^2 X_0}{R_0^2 + X_0^2} \right) \right] I_1 \end{aligned} \tag{4.13}$$

In practical low-frequency strongly coupled magnetic resonators, the new splitting resonances are not much different, often within a factor of one tenth of the resonance in the isolated case. The additional reflected loss from the receiving coil $(\omega M_0)^2 R_0/(R_0^2 + X_0^2)$ is then approximately constant about the resonances. The well-known symmetry of the current response in coupled magnetic circuits materializes as a result.

On the other hand, in the particular configuration shown in Fig. 3.3, the complex self inductance arises while the complex mutual inductance becomes complex, expressing in the forms of: $\mathcal{M} = \mathcal{M}' - j\mathcal{M}''$ where $0 < \mathcal{M}', \mathcal{M}'' < M_0$ due to the elliptical polarization of the magnetic field. Recall that $Z_0 + j\omega\Delta\mathcal{L} = \tilde{R}_0 + j\tilde{X}_0$. Substituting the complex forms of the complex Kirchhoff coefficients and the new coil impedance into (4.11), it results in:

$$\begin{aligned} V_0 &= \left\{ \left(\tilde{R}_0 + j\tilde{X}_0\right) + \frac{\left[\omega^2\left(\mathcal{M}'^2 - \mathcal{M}''^2\right) - j\,2\omega^2\mathcal{M}'\mathcal{M}''\right]\left(\tilde{R}_0 - j\tilde{X}_0\right)}{\tilde{R}_0{}^2 + \tilde{X}_0{}^2} \right\} I_1 \\ &= \left\{ \tilde{R}_0 + \frac{\left[\omega^2\left(\mathcal{M}'^2 - \mathcal{M}''^2\right)\tilde{R}_0 - 2\omega^2\mathcal{M}'\mathcal{M}''\tilde{X}_0\right]}{\tilde{R}_0{}^2 + \tilde{X}_0{}^2} \right. \\ &\quad \left. + j\left[\tilde{X}_0 - \frac{2\omega^2\mathcal{M}'\mathcal{M}''\tilde{R}_0 - \omega^2\left(\mathcal{M}'^2 - \mathcal{M}''^2\right)\tilde{X}_0}{\tilde{R}_0{}^2 + \tilde{X}_0{}^2}\right] \right\} I_1. \end{aligned} \tag{4.14}$$

Here, the numerator of the loss from the feedback effect is:

$$\begin{aligned} &\omega^2\left(\mathcal{M}'^2 - \mathcal{M}''^2\right)\tilde{R}_0 - 2\omega^2\mathcal{M}'\mathcal{M}''\tilde{X}_0 \\ &\qquad = \begin{cases} \omega^2\left(\mathcal{M}'^2 - \mathcal{M}''^2\right)\tilde{R}_0 + 2\omega^2\mathcal{M}'\mathcal{M}''|\tilde{X}_0|, & \text{for } \omega < \tilde{\omega_0}, \\ \omega^2\left(\mathcal{M}'^2 - \mathcal{M}''^2\right)\tilde{R}_0, & \text{for } \omega = \tilde{\omega_0}, \\ \omega^2\left(\mathcal{M}'^2 - \mathcal{M}''^2\right)\tilde{R}_0 - 2\omega^2\mathcal{M}'\mathcal{M}''|\tilde{X}_0|, & \text{for } \omega > \tilde{\omega_0}. \end{cases} \end{aligned} \tag{4.15}$$

where $\tilde{\omega_0}$ is the new resonant frequency of the coil in the medium. With the same argument above, new splitting resonances are not very separate so that the total energy loss due to the present of the complex self inductance and the Ohmic loss, $\tilde{R}_0 = R_0 + \omega\Delta\mathcal{L}''$ might still be constant. Nevertheless, from (4.14), when the working frequency proceeds through the self resonance $\tilde{\omega_0}$, the reactance of the coils, $\tilde{X}_0$, crosses the zero line, changing from capacitive (negative value) to

inductive (positive value). As it stands, the progression of the frequency indeed mitigates the reflected loss from the secondary coil. The antisymmetry of the current response therefore occur with the lower resonance facing much higher damping than the upper resonance. Likewise, the current response in the receiving coil can be explained accordingly.

4.4 Power Conservation

It is quite easy to show with the circuit theory that the power in an inductively coupled system is conserved. Now, the energy conservation is discussed with the emergence of the two complex Kirchhoff coefficients when submerging the two coils inside an attenuating medium. The coil configuration is the same as above and the excitation is a sinusoidal voltage source of 1 V. The medium however is assumed to have a conductivity of $\sigma = 1$ S/m, relative permittivity $\epsilon_r = 1$, and relative permittivity $\mu_r = 1$. The complex Kirchhoff coefficients are then calculated accordingly. Generally, the conservation of volt-ampere is derived from the equivalent circuit model (4.10):

$$\mathrm{S}_{in} = \mathrm{S}_{out} = \mathrm{S}_c + \mathrm{S}_e + \mathrm{S}_1 + \mathrm{S}_2 \tag{4.16}$$

where

$$\begin{cases} \mathrm{S}_{in} = V_0 I_1^*, & \text{is the input volt-ampere,} \\ \mathrm{S}_c = Z_0|I_1|^2 + Z_0|I_2|^2, & \text{is the dissipated volt-ampere,} \\ \mathrm{S}_f = (j\omega\Delta\mathcal{L})|I_1|^2 + (j\omega\Delta\mathcal{L})|I_2|^2, & \text{is the medium feedback volt-ampere,} \\ \mathrm{S}_1 = (j\omega\mathcal{M}I_2)I_1^*, & \text{is the volt-ampere leaving coil 1,} \\ \mathrm{S}_2 = (j\omega\mathcal{M}I_1)I_2^*, & \text{is the volt-ampere entering coil 2,} \end{cases} \tag{4.17}$$

and x^* is the conjugate number of variable x. Here, the symbol S denotes the volt-ampere (complex power) consisting of the active power P (real part) and reactive power Q (imaginary part), i.e., $\mathrm{S} = \mathrm{P} + j\mathrm{Q}$. Equally, taking the real part

of both sides of (4.16), it is possible to achieve the conservation of active powers:

$$\mathrm{P}_{in} = \mathrm{P}_{out} = \mathrm{P}_c + \underbrace{\mathrm{P}_f + \mathrm{P}_1 + \mathrm{P}_2}_{\mathrm{P}_m} \tag{4.18}$$

where P_m is the total energy loss in the ambient environment. Recall that $(Z_0 + j\omega\Delta\mathcal{L}) = \tilde{Z}_0$, it can be shown that:

$$\mathrm{S}_f = (j\omega\Delta\mathcal{L})|I_1|^2 + (j\omega\Delta\mathcal{L})|I_2|^2 = (j\omega\Delta\mathcal{L})\left(1 + \frac{\omega^2|\mathcal{M}|^2}{|\tilde{Z}_0|^2}\right)|I_1|^2 \tag{4.19}$$

$$\mathrm{S}_1 = (j\omega\mathcal{M}I_2)I_1^* = j\omega\mathcal{M}\left(\frac{-j\omega\mathcal{M}}{\tilde{Z}_0}\right)I_1 I_1^* = \frac{\omega^2\mathcal{M}^2\tilde{Z}_0{}^*}{|\tilde{Z}_0|^2}|I_1|^2 \tag{4.20}$$

$$\mathrm{S}_2 = (j\omega\mathcal{M}I_1)I_2^* = j\omega\mathcal{M}I_1\left(\frac{-j\omega\mathcal{M}}{\tilde{Z}_0}\right)^* I_1^* = \frac{-\omega^2|\mathcal{M}|^2\tilde{Z}_0}{|\tilde{Z}_0|^2}|I_1|^2 \tag{4.21}$$

In free space, eddy currents no longer exist so that $\mathcal{M} = M_0 \in \mathbb{R}$, $\Delta\mathcal{L} = 0$, and $\tilde{Z}_0 = Z_0$. Therefore, (4.19) – (4.21) can be rewritten as:

$$\mathrm{S}_f = 0 \tag{4.22}$$

$$\mathrm{S}_1 = \frac{\omega^2 M_0^2 Z_0^*}{|Z_0|^2}|I_1|^2 \tag{4.23}$$

$$\mathrm{S}_2 = \frac{-\omega^2 M_0^2 Z_0}{|Z_0|^2}|I_1|^2 \tag{4.24}$$

As is evident from (4.23) and (4.24), the active power leaving the transmitter is equal to negative value of the active power induced in the receiver while the reactive powers remain unchanged, i.e., $\mathrm{P}_1 = -\mathrm{P}_2$ and $\mathrm{Q}_1 = \mathrm{Q}_2$, as shown in Fig. 4.8. Since the active power leaving coil 1 is equal to the negative value of the active power entering coil 1 and the feedback loss due to the medium does not exist, the input active power is identical to the power dissipated as heat in the coils, see Fig. 4.9. There is no loss in the transmission medium.

$$\mathrm{P}_{in} = \mathrm{P}_{out} = \mathrm{P}_c + \underbrace{\mathrm{P}_f}_{=0} + \underbrace{\mathrm{P}_1 + \mathrm{P}_2}_{=0} = \mathrm{P}_c \tag{4.25}$$

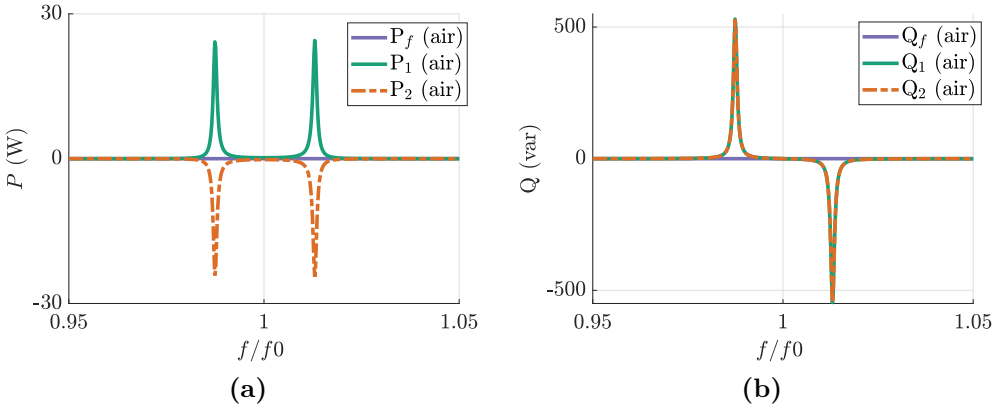


Figure 4.8: Comparison of (a) the calculated active power (real part) and (b) reactive power (imaginary part) of three volt-amperes versus frequency: S_f (feedback loss due to the medium), S_1 (leaving the transmitter), and S_2 (entering the receiver). The coil configuration is: two coaxial identical coils separated by a distance $d = 30$ mm with the resonant frequency $f_0 = 46$ MHz, the quality factor $Q = 432$, and dimensions: mean radius $r_0 = 11$ mm, height of $l = 5$ mm, thickness of $w = 1$ mm, number of turns $N = 1$. The cylindrical dielectric cavity providing insulation for the coils has a height of $2h + l = 7$ mm. The transmission medium is vacuum.

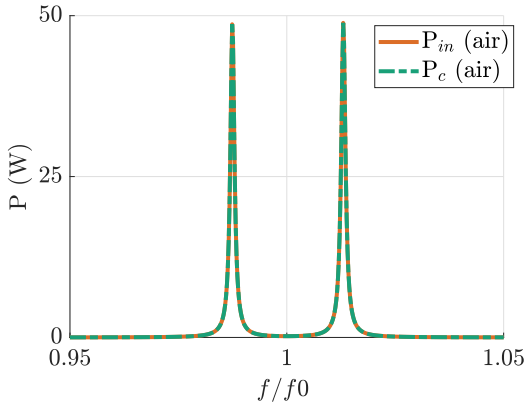


Figure 4.9: Comparison of the input active power and the power dissipated in the coils as heat versus frequency for the configuration stated in Fig. 4.8

When submerging two coupled coils inside a conductive surrounding environment, common sense suggests part of the power is dissipated in the transmission medium while transferring from transmitter to the receiver. However, interestingly, the total energy loss in the medium is not equal to the medium feedback loss. Unlike the free space case, the power leaving the transmitter is unexpectedly non-identical to the power entering the pick-up coil due to the elliptical polarization of the magnetic field. The induced eddy currents result in a complex mutual inductance, i.e., $\mathcal{M} \in \mathbb{C}$

and $\mathcal{M}^2 \neq |\mathcal{M}|^2$. Thus, it can be proven from (4.19) and (4.20) that $P_1 \neq -P_2$ and $Q_1 \neq Q_2$, but $|S_1| = |S_2|$. Fig. 4.10 shows the real part, imaginary part and modulus of three volt-amperes S_f, S_1, and S_2 as a function of frequency.

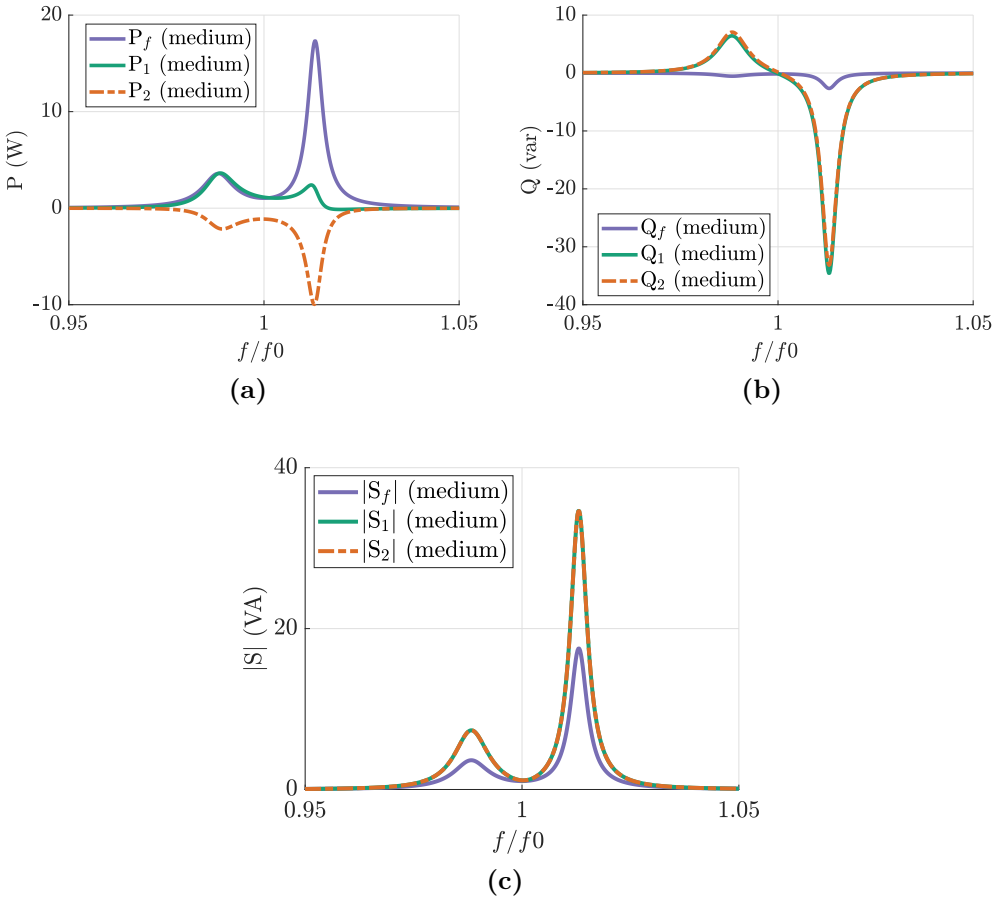


Figure 4.10: Comparison of (a) the calculated active power (real part), (b) reactive power (imaginary part), and (c) apparent power (modulus) of three volt-amperes versus frequency: S_f (feedback loss due to the medium), S_1 (leaving the transmitter), and S_2 (entering the receiver). The coil configuration is: two coaxial identical coils separated by a distance $d = 30$ mm with the resonant frequency $f_0 = 46$ MHz, the quality factor $Q = 432$, and dimensions: mean radius $r_0 = 11$ mm, height of $l = 5$ mm, thickness of $w = 1$ mm, number of turns $N = 1$. The cylindrical dielectric cavity providing insulation for the coils has a height of $2h + l = 7$ mm. The properties of the transmission medium are relative permittivity of $\epsilon_r = 78$, relative permeability of $\mu_r = 1$, and conductivity $\sigma = 1$ S/m.

It can be seen from the graphs that whereas the apparent powers $|S_1|$ and $|S_2|$ are indistinguishable, real power leaving the transmitter is not equal to negative value of the real power induced in the receiver, especially in the small range near the

resonance. As a result, the total loss is reckoned as the summation of the feedback loss and the power entering and leaving the two coils, accounting for both the extra loss in the medium and the loss due to the field polarization.

$$\mathrm{P}_{in} = \mathrm{P}_{out} = \mathrm{P}_c + \mathrm{P}_m = \mathrm{P}_c + \underbrace{\mathrm{P}_f}_{\neq 0} + \underbrace{\mathrm{P}_1 + \mathrm{P}_2}_{\neq 0} \tag{4.26}$$

It can then be rewritten in terms of the circuit parameters as:

$$\mathrm{P}_m = \Re\left\{\frac{\omega^2\left(\mathcal{M}^2\tilde{Z}_0{}^* - |\mathcal{M}|^2\tilde{Z}_0\right) + (j\omega\Delta\mathcal{L})\left(|\tilde{Z}_0|^2 + \omega^2|\mathcal{M}|^2\right)}{|\tilde{Z}_0|^2}\right\}|I_1|^2 \tag{4.27}$$

Fig. 4.11 compares the input power against the energy loss in the coils and in the medium. Apart from the heat in the coils, a significant portion of power also dissipates in the transmission environment. The power absorbed in the non-conventional medium therefore should be deserved serious attention in the job of designing and optimizing magnetic induction systems, most importantly the field of wireless power transfer.

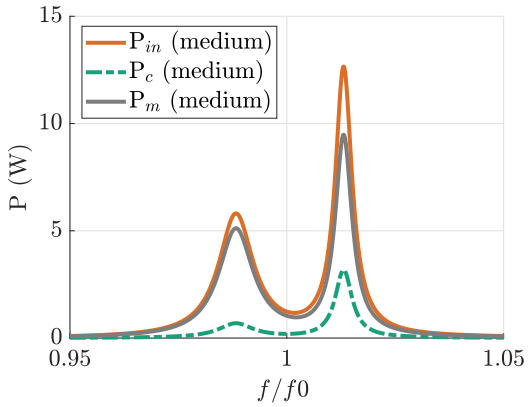


Figure 4.11: Comparison of the input active power and the power dissipated in the coils and the ambient environment versus frequency for the configuration stated in Fig. 4.10

4.5 Conclusions

With the novel circuit model being postulated, the network analysis of coupled-coil systems has been presented. Firstly, the splitting frequency phenomenon is addressed by using the eigenvalue analysis. The more conductive the medium is, the larger the

amount of opposite flux is generated by the conduction eddy currents. Thus, the resonance of the coil in isolated case is found at higher frequencies inside the medium. The position of the odd and even mode in the coupled case also follows the trend of the resonance. At the same time, the ambient environment dissipates the transferred energy between the two coils. Therefore, the two modes eventually coalesce into the resonance in the isolated case with the increasing medium conductivity.

In addition, the current responses of a two-coupled-coil system in an attenuating environment is investigated. The almost perfect symmetry of the splitting resonant peaks is noticeably broken. By contrast to the common intuition that the loss often increases with the frequency, the numerical study shows that the lower resonance encounters much larger damping and in some cases, vanishes compared to the higher resonance. This intriguing behaviour is clarified with the circuit theory with the main reason being the frequency-dependent characteristic of the complex Kirchhoff coefficients. It leads to a frequency-dependent feedback loss at one coil from another. When the conductivity is extremely high, the medium introduces more losses to the coils compared to their internal resistances, as well as attenuates all the magnetic flux towards the receiver and thus, the current responses in both coils tend to zero.

At last, to complete any electromagnetic study, the power conservation is discussed. The power is dissipated not only in the coils due to their internal resistances but also in the transmission medium due to the induced eddy currents. The total power loss in the ambient environment accounts for the feedback loss to the circuits as well as the transmission loss due to the attenuation and field polarization. Computed results show that even the conductivity is relatively small, i.e., $\sigma = 1$ S/m, a great amount of power is absorbed in the medium. It can even be larger than the power dissipated as heat in the coils. Since previous works [116–118] concentrated on the attenuation of the magnetic link and usually ignored the feedback losses from the medium, scientific community should pay more attention to investigate this issue.

5

Wireless Power Transfer via Coupled Resonators in Dissipative Media

Contents

5.1 Introduction 101
5.2 System Modelling 101
5.3 System Optimization 104
5.3.1 Optimal Load 104
5.3.2 Optimal Working Frequency 105
5.4 Simulation Results 106
5.5 Criteria for the Frequency Switching 113
5.6 Conclusions 116

Following the discussion of the network analysis for a two-coupled-resonator system in Chapter 4, this chapter considers an immediate application: wireless power transfer (WPT) via coupled resonators in dissipative media. It starts with an brief introduction of WPT in Section 5.1. Section 5.2 presents the system model while Section 5.3 shows that the working frequency for maximum transferred power is indeed a key parameter to be optimized for WPT systems in RF-challenging environments. It is followed by the simulation results in Section 5.4. Finally, Section 5.5 establishes a criteria for choosing the optimal working frequency for maximum output power at load. The main contribution of this chapter is to

investigate the WPT mechanism in attenuating media and to point out the limitation of the free-space model when applied to the attenuating media case. Some of the work in this chapter have been published in the following journals/conference proceedings:

- **S. Chu**, C. J. Stevens, and E. Shamonina, "Wireless power transfer in non-ideal media", *IEEE Transactions on Circuits and Systems II: Express Briefs*, 2020 (**in preparation**).

5.1 Introduction

WPT is an old subject of much recent interest [119, 120]. The mechanism of strongly coupled magnetic reosnators enable power to transfer efficiently through their non-radiative fields. Magnetic coupling is preferable rather than the electric coupling because of the hazards of electric fields to life forms [121]. The studies of WPT via strongly coupled magnetic resonators in the air are very mature with significant competition between standards and approaches [120, 122–124]. To date, transferring power to sensors in medical devices or in underground/underwater environments has gained increasing attention due to their short battery lifetime [125–127]. Among the various methods for wireless power and data transmission for implantable biomedical devices (ultrasonic and optical methods, capacitive coupling, intra-body communication, and etc.), near-field magnetic coupling is considered the most suitable approach because of its efficiency and harmless effects to living tissues [127]. However, the current theory for WPT using magnetically-coupled circuits has not yet included dynamic changes in the magnetic channels between resonators inside those environments. In this chapter, the theory of WPT via a pair of strongly coupled magnetic resonators inside an infinite homogeneous non-conventional environment will be elaborated.

5.2 System Modelling

The simplest practical configuration for WPT consists of two magnetically coupled resonators insulated by dielectric cavities and completely embedded in a

homogeneous conductive medium. The input excitation is a sinusoidal voltage source applied to the primary coil while the secondary coil is connected to a load. Typically, the parasitic capacitance of the resonators is very small so that to realize the WPT mechanism at lower bands, additional tuning capacitors are required to form the resonant tank circuits in both the primary and secondary sides [123]. As a result, the self capacitance is usually disregarded and the value of tuning capacitors are then determined from the desired resonant frequency and the self inductance. Concerning the capacitive compensation circuits, there are four possible simple topologies, namely parallel–parallel, parallel–series, series–series, and series–parallel, standing for the connection type of the capacitor in the transmitting and receiving coils respectively [120]. Some advanced compensation networks, for examples LLC, can be found in [128]. It can be proved by using the reflected impedance theory that the value of external capacitors in the series-series topology are independent of the coupling coefficients [120], which significantly varies with respect to the medium properties. As a result, within the scope of this thesis, series-series capacitor compensation circuit is selected to investigate the effects of medium on the wireless output power and efficiency. Besides, due to the main interest in the mechanism of the power delivery through a dissipative medium, other practical circuitries to improve the performance of inductive WPT systems, such as rectifiers, inverters, regulators are not considered. Due the interactions of the currents flowing in each coil and the eddy currents they generate, the equivalent circuit model is then constructed and illustrated in Fig. 5.1. To simplify the system, it is assumed that the dielectric cavities providing the coil insulation are free-space.

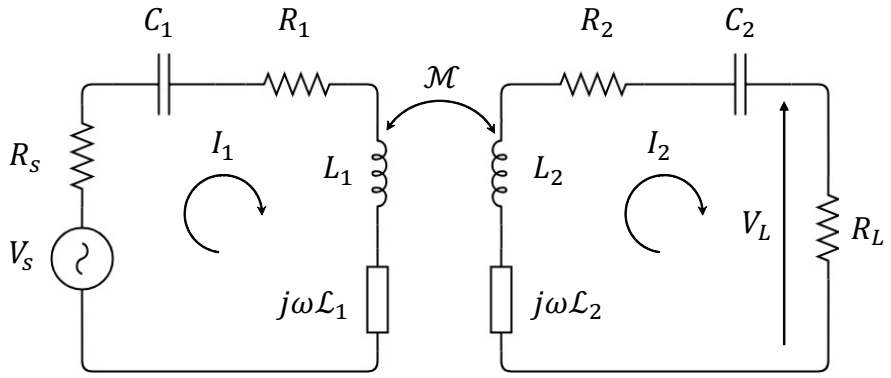


Figure 5.1: Equivalent circuit model of a WPT system consisting of two resonant coils with series-series capacitive compensation topology.

Assuming a time dependence of the form $\exp(j\omega t)$ for all variables, where $\omega = 2\pi f$ is the angular frequency, and using Kirchhoff's voltage law, the equivalent circuit model of the WPT via a pair of strongly coupled magnetic resonators inside a dissipative medium can be written as:

$$\begin{bmatrix} R_s + Z_1 + j\omega\mathcal{L}_1 & j\omega\mathcal{M} \\ j\omega\mathcal{M} & Z_2 + j\omega\mathcal{L}_1 + R_L \end{bmatrix} \begin{bmatrix} I_1 \\ I_2 \end{bmatrix} = \begin{bmatrix} V_s \\ 0 \end{bmatrix} \tag{5.1}$$

where V_s and R_s are the source voltage and the source internal resistance, R_L is the resistance of the load connected to the secondary coil; I_i, $Z_i = R_i + j\omega L_i + 1/(j\omega C_i)$, R_i, L_i, C_i are the current response, impedance, resistance, self inductance, and tuning value of tuning capacitors of the coil i respectively, $\mathcal{L}_i$ is the lossy self inductance of coil i, representing the coupling of a coil and the eddy currents it generates, $\mathcal{M} = M_0 + M_E$ is the lossy mutual inductance between two coils inside the medium, M_0 is the mutual inductance of two coils in free space (typically a purely real number), and M_E represents the coupling of a coil and the eddy currents generated by a nearby coil. In free space, the eddy currents no longer exist and hence, all the additional coupling - the lossy self inductance and the added mutual inductance - are equal to zero, i.e., $\mathcal{L}_i = 0$, $M_E = 0$ and $\mathcal{M} = M_0$. Inside the attenuating medium, the lossy Kirchhoff coefficients and $\mathcal{L}_i$ are complex quantities, i.e., $\mathcal{M} = \mathcal{M}' + j\mathcal{M}''$ and $\mathcal{L}_i = \mathcal{L}_i' - j\mathcal{L}_i''$ ($-\mathcal{L}_i'' < 0$ because it associates with the power loss in the

medium). Solving system (5.1), the currents in each coil can be derived as:

$$I_1 = \frac{V_s}{(R_s + Z_1 + j\omega\mathcal{L}_1) + \dfrac{\omega^2\mathcal{M}^2}{Z_2 + j\omega\mathcal{L}_1 + R_L}} \tag{5.2}$$

$$I_2 = \frac{\dfrac{j\omega\mathcal{M}}{Z_2 + j\omega\mathcal{L}_1 + R_L}V_s}{(R_s + Z_1 + j\omega\mathcal{L}_1) + \dfrac{\omega^2\mathcal{M}^2}{Z_2 + j\omega\mathcal{L}_1 + R_L}} \tag{5.3}$$

5.3 System Optimization

From the current expressions, the output power at the load can be then calculated as:

$$\begin{aligned} \mathrm{P}_L &= \Re\{V_L I_L^*\} = |I_2|^2 R_L \\ &= \frac{\omega^2|\mathcal{M}|^2 V_s^2 R_L}{\left|(R_s + Z_1 + j\omega\mathcal{L}_1)(Z_2 + j\omega\mathcal{L}_2 + R_L) + \omega^2\mathcal{M}^2\right|^2} \end{aligned} \tag{5.4}$$

Unlike current studies in free space [122, 129], the power loss in the medium needs to be taken into account to calculate the power transfer efficiency. The efficiency of the WPT in a conductive medium is written as:

$$\eta = \frac{\mathrm{P}_L}{\mathrm{P}_{in}} = \frac{|I_2|^2 R_L}{\Re\{V_s I_1^*\}} \tag{5.5}$$

5.3.1 Optimal Load

The useful power transferred to the load can certainly be maximized by adjusting the load resistance. Mathematically, the optimal load can be found by solving the roots of the first order derivative of (5.4) with respect to R_L. Recalling that $\mathcal{M} = \mathcal{M}' + j\mathcal{M}''$, $\mathcal{L}_i = \mathcal{L}_i' - j\mathcal{L}_i''$, and $Z_i + j\omega\mathcal{L}_i = \tilde{R}_i + j\tilde{X}_i$, where $\tilde{R}_i = R_i + \omega\mathcal{L}_i''$, $X_i = \omega L_i - 1/(\omega C_i)$ and $\tilde{X}_i = X_i + \omega\mathcal{L}_i'$, (5.4) is rewritten as:

$$\begin{aligned} \mathrm{P}_L = \frac{\omega^2(\mathcal{M}'^2 + \mathcal{M}''^2)V_s^2 R_L}{\left[2\omega^2\mathcal{M}'\mathcal{M}'' + \left(\tilde{R}_2 + R_L\right)\tilde{X}_1 + \left(\tilde{R}_1 + R_s\right)\tilde{X}_2\right]^2} \\ + \left[\left(\tilde{R}_1 + R_s\right)\left(\tilde{R}_2 + R_L\right) + \omega^2\left(\mathcal{M}'^2 - \mathcal{M}''^2\right)\tilde{X}_1\tilde{X}_2\right]^2 \end{aligned} \tag{5.6}$$

Differentiating and solving $\mathrm{d}P_L/\mathrm{d}R_L = 0$, the optimal resistive load can be obtained as follows:

$$R_L = \sqrt{\frac{\omega^4 \left(\mathcal{M}'^2 + \mathcal{M}''^2\right)^2 + 2\omega^2 \Big\{ \left(\mathcal{M}'^2 - \mathcal{M}''^2\right) \left(\tilde{R}_1\tilde{R}_2 + \tilde{R}_2 R_s - \tilde{X}_1\tilde{X}_2\right) + 2\mathcal{M}'\mathcal{M}'' \left[\tilde{R}_2\tilde{X}_1 + \left(\tilde{R}_1 + R_s\right)\tilde{X}_2\right] \Big\} + \left[\left(\tilde{R}_1 + R_s\right)^2 + \tilde{X}_1^2\right] \left(\tilde{R}_2^2 + \tilde{X}_2^2\right)}{\left(\tilde{R}_1 + R_s\right)^2 + \tilde{X}_1^2}} \tag{5.7}$$

In free space, i.e., $\mathcal{M}' = M_0$, and $\mathcal{M}'' = \mathcal{L}' = \mathcal{L}'' = 0$, it becomes:

$$R_L = \sqrt{\frac{\omega^4 M_0^4 + 2\omega^2 M_0^2 \left(R_1R_2 + R_2R_s - X_1X_2\right) + \left[\left(R_1 + R_s\right)^2 + X_1^2\right] \left(R_2^2 + X_2^2\right)}{\left(R_1 + R_s\right)^2 + X_1^2}} \tag{5.8}$$

In this chapter, the optimal load expression is not developed at the resonant frequency as in most literature but instead at an arbitrary frequency when the resonant circuits have reactive impedances, given that the circuit theory is still valid. It is noted that conjugate matching, when a complex input impedance is present, is not considered because the thesis aims to draw attention to the limitations of the current model when applied to the WPT systems in conductive media. The working frequency for those WPT systems is indeed a parameter to be optimized. It will be further clarified in the next section by examining the output power at the load over a range of frequency.

5.3.2 Optimal Working Frequency

It is well known that for WPT systems, when the coupling is fixed, the maximum output power at the load and the power transfer efficiency can be achieved when both primary and secondary circuits are tuned to the same resonant frequency, i.e., $\omega = \omega_0 = 1/\sqrt{L_iC_i}$, given the load is optimal [24]. It is easily achieved in practice by adding suitable external capacitors to the windings. However, as discussed in Chapter 3, the medium changes the self inductance of both the primary and secondary coils by absorbing some inductive energy. The resonant frequency of

the coil i, $f_{i0} = 1/\left(2\pi\sqrt{L_i C_i}\right)$, consequently shifts to $\tilde{f}_{i0}$ inside the medium, where $\tilde{f}_{i0}$ is the root of the following equation:

$$\tilde{f_{i0}}^{\,2}\left(L_i - \mathcal{L}_i'\right) - \frac{1}{4\pi^2 C_i} = 0, \tag{5.9}$$

Generally speaking, the resonance frequency of the circuits in a WPT system is inadvertently shifted due to the effects of the eddy currents in nearby external objects. The optimal working frequency for that system might not be the original resonance of the windings, f_0. To deal with this problem when considering a WPT a pair of inductively coupled resonators in the vicinity of a conducting slab, Vallecchi et al [130] suggested to retune the coil closer to the slab, which is strongly affected by the eddy currents, to the original resonant frequency by altering the external capacitors. Simulation results show that the retuning technique has the merit of increasing the useful power at the load in this case. However, as the two coils are submerged in a dissipative infinite medium, the medium detunes the two coils equally. The original resonance however may not be the most advantageous frequency for such these WPT systems.

5.4 Simulation Results

The primary and secondary coils of the WPT system are assumed to be identical ($R = R_1 = R_2$, $L = L_1 = L_2$, and $C = C_1 = C_2$) and placed coaxially at a distance from each other. The geometric and circuit parameters are summarized in Table. 5.1 whilst the radius of the dielectric boxes is assumed to be three times larger than the coil radius. The practical voltage source typically has an internal resistance of a few Ω [131], typically $R_s = 5\ \Omega$. The secondary coil is then connected with a variable resistive load R_L. It is assumed that the operating frequency of the system is the ISM band at 6.78 MHz , following the Rezence A4WP standard [132]. The lossy Kirchhoff coefficients are calculated accordingly using (3.18) and (3.19). The resistance of the coil is assumed to be constant around the resonant frequency, expressed as [133]:

$$R = \sqrt{\frac{\pi f_0 \mu_c}{\sigma_c}}\frac{N r_0}{r_w}, \tag{5.10}$$

where r_0 is the mean radius of the coil, r_w is the radius of the wire, N is the number of turns, and μ_c and σ_c is the permeability and conductivity of the conductor material.

Mean coil radius r_0	60 (mm)
Wire diameter r_w	0.6 (mm)
Coil height	12 (mm)
Number of turns N	10
Distance between coils	60 (mm)
Dielectric insulator radius	180 (mm)
Dielectric insulator height	14 (mm)
Resonance frequency f_0	6.78 (MHz)
Self inductance L	23.3464 (μH)
Parasitic resistance R	0.6793 (Ω)
Mutual inductance (free-space) M_0	2.9907 (μH)
AC voltage Source	10 (V)
Internal source resistance R_s	5 (Ω)
Medium relative permittivity ϵ_r	78
Medium relative permeability μ_r	1
Medium conductivity σ	1e-3 – 1e2 (S/m)

Table 5.1: Parameter list of the case study.

Fig. 5.2 shows the true power at the load versus frequency and load resistance for the WPT system in free space. The output power always has its maximum peaks at the resonant frequency for every load resistance as expected. When the load resistance is small, frequency splitting occurs as the output power exhibits two sharp peaks at the upper and lower resonances, ω_u and ω_l respectively. When the load resistance is large enough, the strength of the mutual inductance no longer tolerate the total loss in the system, the two coupled coils are in the lossely-coupled regime. The maximum transferred power is expectedly found at resonance where both coils are tuned to. With the working frequency being defined, the optimal load can be predicted correctly by (5.8): $R_L = 2858.7\ \Omega$ and $6.35\ \Omega$ at ω_0 and ω_u, respectively.

Now, the WPT system is embedded inside a non-conventional environment with variable conductivity. Due to the significant effects of the eddy currents, both the

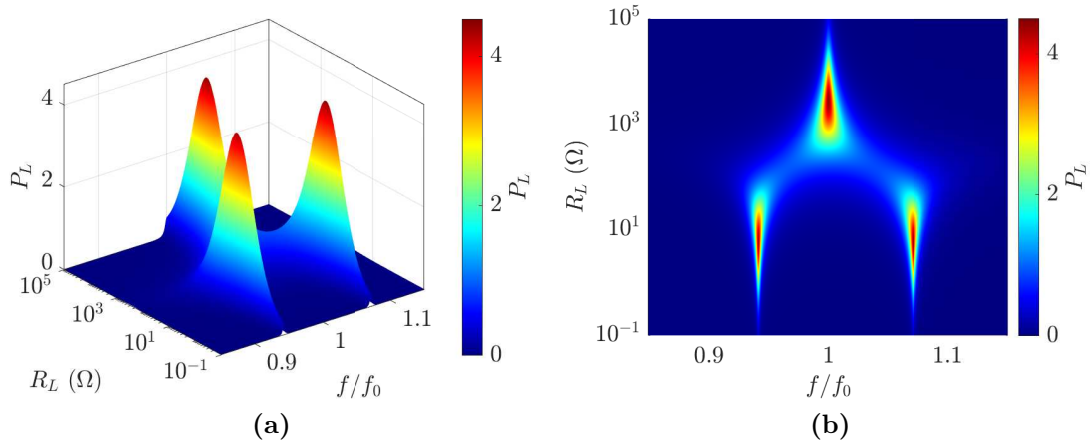


Figure 5.2: Calculated colour map of the output power P_L as a surface function of the normalised working frequency f and the load resistance R_L. The frequency is normalised by the resonance of the coils in the isolated case. The WPT system operates in free space.

primary and secondary coils are detuned and the mutual coupling between them becomes complex. Hence, it may be questionable whether the optimal frequency is still the original free-space resonance. Fig. 5.3 presents the simulation results for the output power at the original resonance and the optimal frequency versus the increment of medium conductivity. The optimal frequency and load resistance determined by the location of the maximum power are given in Fig. 5.3c and 5.3d. For the purpose of comparison, the retuning method, suggested in [130], is included. In the retuning method [130], the resonant frequency of the resonators is fixed by adding suitable additional capacitors to compensate the impacts of the eddy currents via the lossy self inductance.

In Fig. 5.3a, the retuning method appears to have certain merit of increasing the output power at load. This technique can be very applicable for system working on highly conductive medium ($\sigma > 10$) as the maximum power can be enlarged about 47% on average. However, when the conductivity of the medium is fairly low ($\sigma < 10$), retuning the coils can only boost the useful power 1% on average over the whole range of conductivity compared to the non-retuned case. Nonetheless, the typical conductivity of common propagation environments is less than $\sigma = 10$ S/m as discussed throughout this thesis. It makes the retuning approach less appealing. Also, in practice, the capacitors are not ideal and often modelled as a capacitance

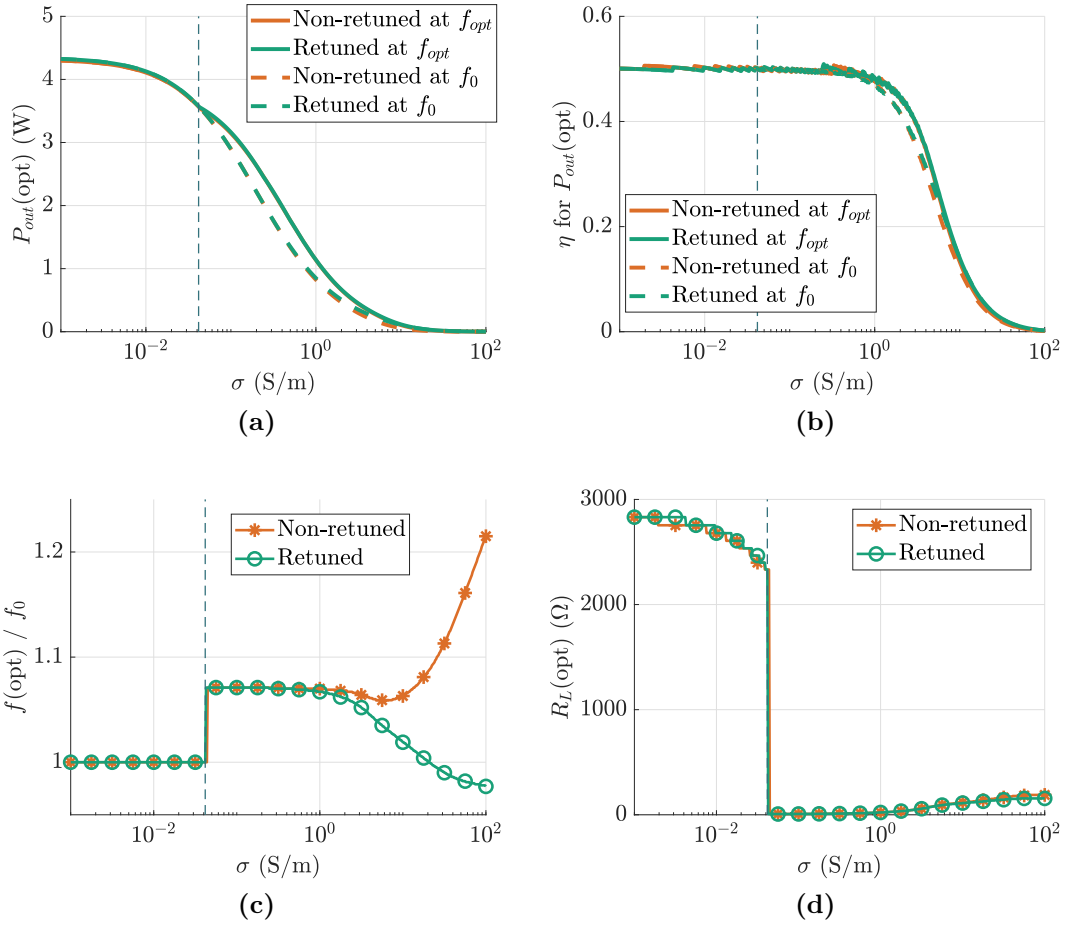
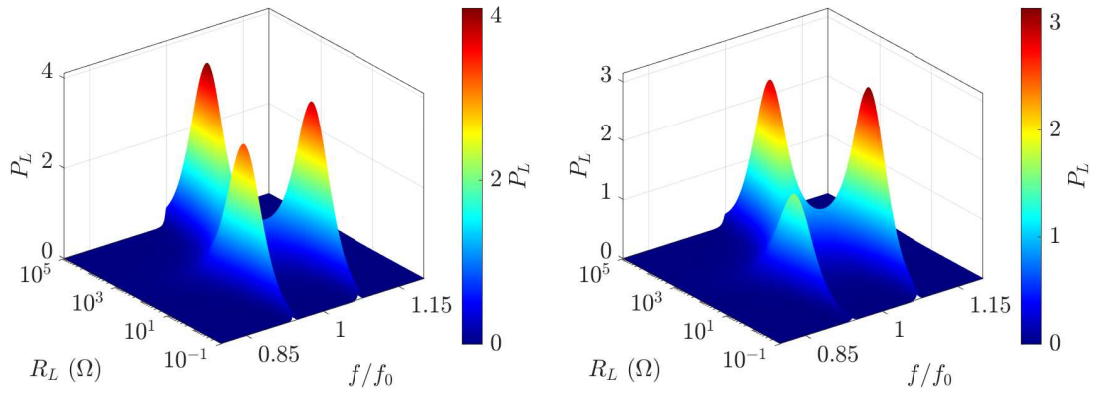


Figure 5.3: (a) Calculated active power at load at the optimal frequency and the resonance, (b) the corresponding efficiency, (c) optimal frequency, and (d) optimal load resistance. The output power in the case study is compared when the compensation capacitances are kept the same as in free space (non-retuned) and when the compensation capacitances are added according to the prediction of the detuning effect based on the novel circuit model (retuned).

in series with a resistance, called 'Equivalent Series Resistance' (ESR) [134]. Hence, a small increase in the load power cannot compensate for the losses due to ESR in the additional capacitors proposed in the retuning technique.

Additionally, the output power at the original resonance in both non-retuned and retuned case may not be the available maximum power for some particular media. When the conductivity is relatively small, the medium seems to have little-to-none effect on the output power as the optimal frequency is practically the original resonance, see Fig. 5.3c. The optimal frequency for the maximum output power then exhibits a discontinuity jump once the impact of the medium conductivity gets critical. In fact, the optimal frequency for the range of larger conductivity is now the upper resonance in the frequency splitting phenomenon. Then, the corresponding optimal load resistance is small to allow the frequency splitting to take place, as shown in Fig. 5.3d.

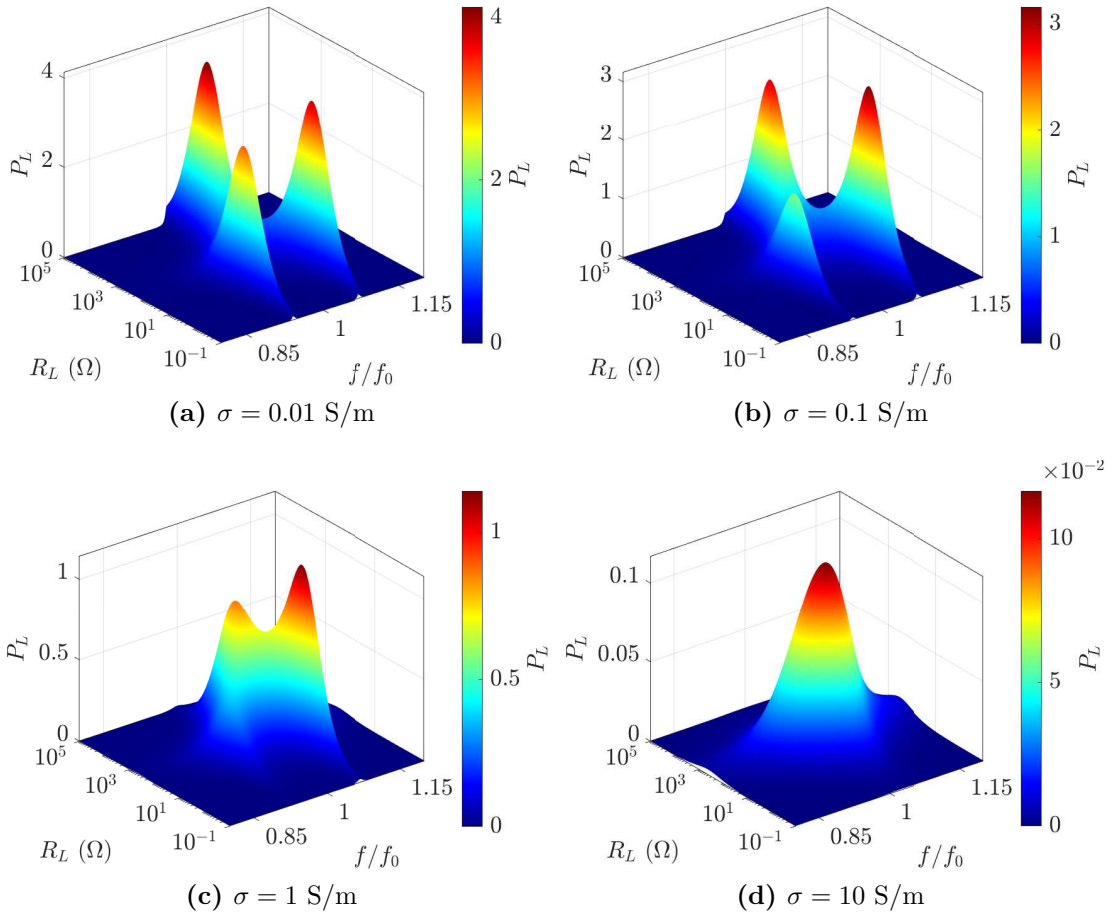
To examine the impact of medium conductivity on the change of the optimal frequency for maximum output power, Fig. 5.4 and Fig. 5.5 illustrate the 3D colour plots of the power at the load versus the frequency and load resistance for four different conductivities: $\sigma = 0.01$, 1, 4 and 10 S/m in the non-retuned and retuned case respectively. Apparently from Fig. 5.4 and Fig. 5.5, the system undergoes different amount of losses at variable frequency due to the nature of the eddy currents. The power peaks at the lower resonance and the original resonance suffer from larger attenuation with the rising of conductivity compared to the upper resonance. When the total losses are high enough, the lower resonance is completely suppressed whilst the peaks at the ω_0 and ω_u coalesce. These results are somewhat consistent with the analyses of the frequency splitting and current distribution of two coupled coils discussed in Chapter 6. A slight drop on the optimal frequency in the non-retuned case in Fig. 5.3c is the indication of the merging of these two peaks. Thereafter, the optimal frequency follows the variation of the upper resonance inside the medium with small deviation due to the damping in the coils. In addition, these two figures reaffirm that the retuning method in [130] is irrelevant to improve the maximum transferred power for WPT systems with coils immersed inside attenuating media. It is only useful to the case when one of the coils is placed closer to the conductive medium than the other, cf. Fig. 1 in [130].



(a) $\sigma = 0.01$ S/m **(b)** $\sigma = 0.1$ S/m

(c) $\sigma = 1$ S/m **(d)** $\sigma = 10$ S/m

Figure 5.4: Calculated colour map of the output power P_L as a surface function of the normalised working frequency f and the load resistance R_L. The frequency is normalised by the resonance of the coils in the isolated case. The WPT system operates inside a medium with the conductivity of (a) $\sigma = 0.01$, (b) $\sigma = 0.1$, (c) $\sigma = 1$, and $\sigma = 10$.



(a) $\sigma = 0.01$ S/m **(b)** $\sigma = 0.1$ S/m

(c) $\sigma = 1$ S/m **(d)** $\sigma = 10$ S/m

Figure 5.5: Calculated colour map of the output power P_L as a surface function of the normalised working frequency f and the load resistance R_L. The frequency is normalised by the resonance of the coils in the isolated case. The WPT system operates inside a medium with the conductivity of (a) $\sigma = 0.01$, (b) $\sigma = 0.1$, (c) $\sigma = 1$, and $\sigma = 10$. The coils are retuned to the original resonance inside the medium by adding suitable capacitors.

It is finally noted that the decline of the optimal frequency in highly conductive media in the retuned case is due to the compensation effect of the extra capacitors. The resonance of the two coils inside the dissipative medium are always ensured to be at ω_0. As a result, when the mutual inductance tends to zero at high values of conductivity, the frequency splitting no longer exist and hence, the upper resonance tends towards the original resonance. The optimal frequency, therefore, decreases progressively to ω_0 with the increment of medium conductivity. Small deviations at the end of the curve in Fig. 5.3c can be explained intuitively by the damping in the coils as well as the frequency-dependent loss added by the medium.

5.5 Criteria for the Frequency Switching

It has been shown that the total losses of the system including the damping of the coils and the frequency-dependent losses introduced by the medium are the reason underlying the switching phenomenon of the optimal frequency for the maximum load power. Also, the absorption of energy due to the eddy currents is proportional to the medium conductivity. For those reasons, it may be suggested that the quantitative relationship between the medium losses and damping in the coils itself could be used to established a criteria for the 'switching point'. Fig. 5.6 presents the simulation results for some extreme cases when (i) $R_1 = 0$, (ii) $R_2 = 0$, and (iii) both $R_1 = 0$ and $R_2 = 0$.

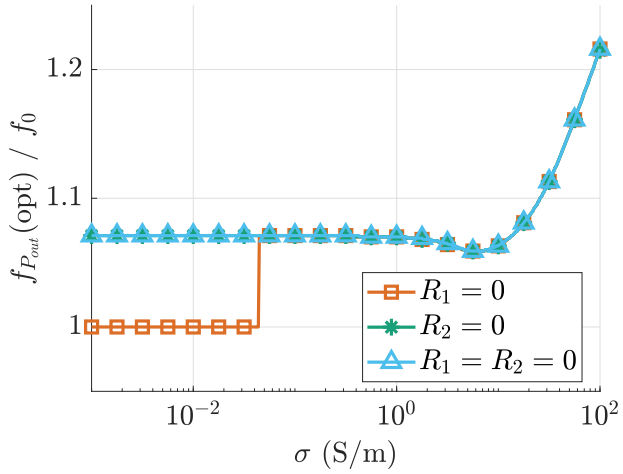


Figure 5.6: Optimal frequency for the maximum output power at load for three extreme cases of the configuration: $R_1 = 0$, $R_2 = 0$, and $R_1 = R_2 = 0$.

Interestingly, it is observed in Fig. 5.6 that the internal resistance or in other words, the damping of the receiver causes the switching point for the maximum load power. By comparing the output power at the original resonance and the upper resonance, the switching point can be determined according to the receiver resistance. Recall ω_u is the upper resonance frequency which can be calculated by (4.9), P_0 is the output power at ω_0 and P_u is the output power at ω_u. The

output power at these two frequencies can be expressed as:

$$\begin{cases} \mathrm{P}_0 = \dfrac{\omega_0^2 |\mathcal{M}_0|^2 V_s^2 R_L}{\left| \left(R_s + R_1 + j\omega_0 \mathcal{L}_{1,0}\right)\left(R_2 + j\omega_0 \mathcal{L}_{2,0} + R_L\right) + \omega_0^2 \mathcal{M}_0^2 \right|^2} \\ \mathrm{P}_u = \dfrac{\omega_u^2 |\mathcal{M}_u|^2 V_s^2 R_L}{\left| \left[R_s + R_1 + j\omega_u L_1 \left(1 - \dfrac{\omega_0^2}{\omega_u^2}\right) + j\omega_u \mathcal{L}_{1,u}\right] \right.} \\ \qquad \left. \left[R_2 + j\omega_u L_2 \left(1 - \dfrac{\omega_0^2}{\omega_u^2}\right) + j\omega \mathcal{L}_{2,u} + R_L\right] + \omega_u^2 \mathcal{M}_u^2 \right|^2 \end{cases} \tag{5.11}$$

where $\mathcal{M}_0$ and $\mathcal{M}_u$ are the lossy mutual inductance at ω_0 and ω_u respectively, and $\mathcal{L}_{i,0}$ and $\mathcal{L}_{i,u}$ are the lossy self inductance of the coil i at ω_0 and ω_u respectively. By maximizing the output power subject to the value of the resistive load using (5.7), the optimal output power at these two frequencies can be calculated as:

$$\begin{cases} \mathrm{P}_0(\max) = \dfrac{\omega_0^2 |\mathcal{M}_0|^2 V_s^2}{2\left[A_0 R_2 + B_0 + \sqrt{A_0}\sqrt{A_0 R_2^2 + 2B_0 R_2 + C_0}\right]} \\ \mathrm{P}_u(\max) = \dfrac{\omega_0^2 |\mathcal{M}_0|^2 V_s^2}{2\left[A_u R_2 + B_u + \sqrt{A_u}\sqrt{A_u R_2^2 + 2B_u R_2 + C_u}\right]} \end{cases} \tag{5.12}$$

where

$$\begin{cases} A_k &= \left(a_k^2 + b_k^2\right)\left(\dfrac{\omega_0 |\mathcal{M}_0|}{\omega_k |\mathcal{M}_k|}\right)^2, \\ B_k &= \left[\left(a_k^2 + b_k^2\right) c_k + a_k e_k + b_k g_k\right]\left(\dfrac{\omega_0 |\mathcal{M}_0|}{\omega_k |\mathcal{M}_k|}\right)^2, \\ C_k &= \Big[\left(a_k^2 + b_k^2\right)\left(c_k^2 + d_k^2\right) + e_k^2 + g_k^2 \\ &\qquad + 2c_k\left(a_k e_k + b_k g_k\right) + 2d_k\left(a_k g_k - b_k e_k\right)\Big]\left(\dfrac{\omega_0 |\mathcal{M}_0|}{\omega_k |\mathcal{M}_k|}\right)^2, \\ a_k &= R_s + R_1 + \omega_k \mathcal{L}''_{1,k}, \\ b_k &= \omega_k L_1\left(1 - \dfrac{\omega_0^2}{\omega_k^2}\right) + \omega_k \mathcal{L}'_{1,k}, \\ c_k &= \omega_k \mathcal{L}''_{2,k}, \\ d_k &= \omega_k L_2\left(1 - \dfrac{\omega_0^2}{\omega_k^2}\right) + \omega_k \mathcal{L}'_{2,k}, \\ e_k &= \omega_k^2\left(\mathcal{M}_k'^2 - \mathcal{M}_k''^2\right), \\ g_k &= 2\omega_k^2 \mathcal{M}'_k \mathcal{M}''_k, \\ k &= \{0, u\} \end{cases} \tag{5.13}$$

The switching point in the optimal frequency curve for the maximum load power occurs when the maximum output power at the upper resonance is larger or equal than that at the original resonance, $\mathrm{P}_u(\max) \geq \mathrm{P}_0(\max)$. It is equivalent to the inequality:

$$(A_u - A_0)\, R_2 + B_u - B_0 \leq \sqrt{A_0}\sqrt{A_0 R_2^2 + 2B_0 R_2 + C_0} - \sqrt{A_u}\sqrt{A_u R_2^2 + 2B_u R_2 + C_u} \tag{5.14}$$

Once the coefficients A_k, B_k and C_k are known, the inequality (5.14) is reducible to a quadratic inequality of variable R_2. The criteria for the switching point therefore can be formulated in terms of the internal resistance (the damping) of the receiver, R_2.

The case study in the previous section is reinvestigated. By solving the inequality (5.14), the region for the optimal frequency corresponding to the maximum power at load can be determined. Fig. 5.7 colour-maps the comparison between output power at the original resonance and the upper resonance, P_0 and P_u, versus the variation of the medium conductivity and the receiving coil resistance. The solid line refers to the value when the strict equality occurs in (5.14), i.e., $P_0 = P_u$.

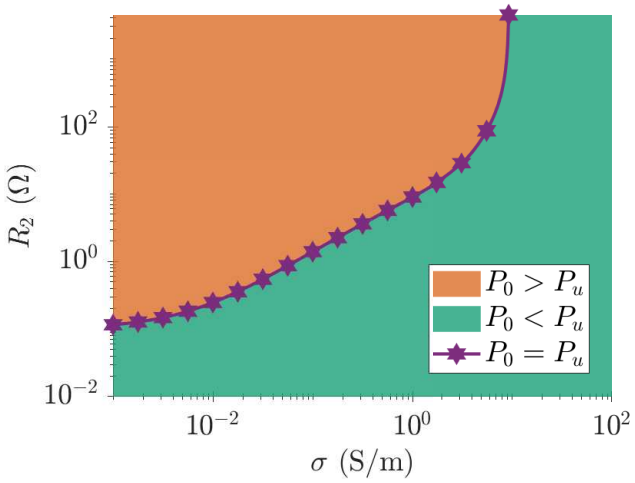


Figure 5.7: Calculated colourmap guidance by using (5.14) for the optimal frequency selection as a fuction of the receiver resistance and the medium conductivity. The solid line refers to the values when the output powers at the original resonance and upper resonance are equal.

According to Fig. 5.7, when the damping of the secondary coil is very small, the optimal frequency is always the upper resonance regardless of the medium properties. This result is indeed consistent with the simulations for some extreme cases in Fig. 5.6. On the other hand, once the medium conductivity is large enough, e.g., $\sigma \approx 9.33$ S/m for this specific coil configuration, the equilibrated line exhibits a vertical asymptote. It clearly demonstrates the optimal working frequency for the largest amount of output power in highly conductive environment is irrevocably at the upper resonance due to the insurmountable loss introduced by the medium at ω_0. Alongside this, the colour-map provides a guidance for practical coil design inside common propagation media with the conductivity varying from nearly 0 to 10 S/m. Since WPT systems often favour working at a single desired frequency, preferably the original resonance of the coils in free-space, the upper bound of the medium conductivity, where the system can function seamlessly, is computable on the basis of the receiver resistance and vice versa. In addition, on the assumption that the system design allows the flexibility in selecting the working frequency and the receiver resistance is estimated in advance, the switching point is remarkably applicable for those systems operating in time-varying environments, e.g., weather-dependent soils or human body. Otherwise, when the working frequency is fixed, employing electronically tunable coils would enable tracking the best performance for WPT systems in variable-conductivity media.

5.6 Conclusions

With the use of the comprehensive equivalent circuit model, the mechanism of the wireless power transfer in conductive media has been theorised in details for the first time. While the resistance of the load can always be optimized for the maximum output power, the working-frequency selection needs attention when designing systems operating in non-conventional environments. Unlike the free-space case, even though the primary and secondary coils inside the medium are retuned to the original resonance, that frequency may not be superlative for maximum output power at load. Simulation results have indicated that the optimal

frequency is either the original resonance or the upper resonance due to the frequency splitting. Surprisingly, the criteria for choosing the best frequency is shown to be the quantitative relationship between the damping in the receiving coil and the loss by virtue of the eddy currents, intuitively represented by the conductivity. The upper resonance is thoughtlessly the best choice for maximizing output power when the secondary coil's resistance tends to zero or when the environment is highly conductive. Neither of these conditions, however, is applicable in real-world scenarios. Generally speaking, the regions containing common ranges of the coil resistance and the medium conductivity experience a switch between the two frequencies with the deviation of one of the two factors while other is fixed. The formula for the switching point, which is reducible to a solvable quadratic inequality, can be used to construct a colour-map of the frequency selection based on the receiving coil resistance and medium property. It indeed offers insights to design and operate the WPT systems in non-conventional ambient environments.

6

Magnetoinductive Waves in Homogeneous Dissipative Media

Contents

6.1 Dispersion Equation 119
6.2 Simulation Results 121
6.3 Laboratory Experiments 126
6.3.1 Experimental Design 126
6.3.2 Retrieving Dispersion Constants 135
6.3.3 Experimental Results 136
6.4 Conclusions 139

The characteristics of MI waves have been discussed briefly in Chapter 1. When the dimensions of the waveguide are small relative to the free space wavelength, the dispersion equation (1.6) is derived straightforward from the circuit model. Nevertheless, this formula only holds true for the case where the transmission medium is free space. Here, in Section 6.1, the dispersion equation of MI waves in an arbitrary surrounding environment is generalised by using the novel circuit model in Chapter 3. Simulation results are then presented in Section 6.2. Finally, Section 6.3 shows the experimental results to verify the theory. The main contribution of this chapter is to propose a general dispersion equation for MI waves travelling in a homogeneous non-ideal medium. Some of the work in this chapter have been

published in the following journals/conference proceedings:

- **S. Chu**, M. S. Luloff, J. Yan, C. J. Stevens, and E. Shamonina "Magnetoinductive waves in attenuating media", *Nature Communications*, 2020 (**submitted**).

6.1 Dispersion Equation

Fig. 6.1 illustrates the configuration of a coaxial MI waveguide with a finite number of elements completely immersed in an infinite, linear, isotropic, homogeneous, and dissipative medium. Each element is a capacitively-loaded split ring resonator insulated by a small dielectric cavity to prevent current leakage to the environment. The dielectric cavities having no significant impact on the magnetic channels are assumed to be vacuum.

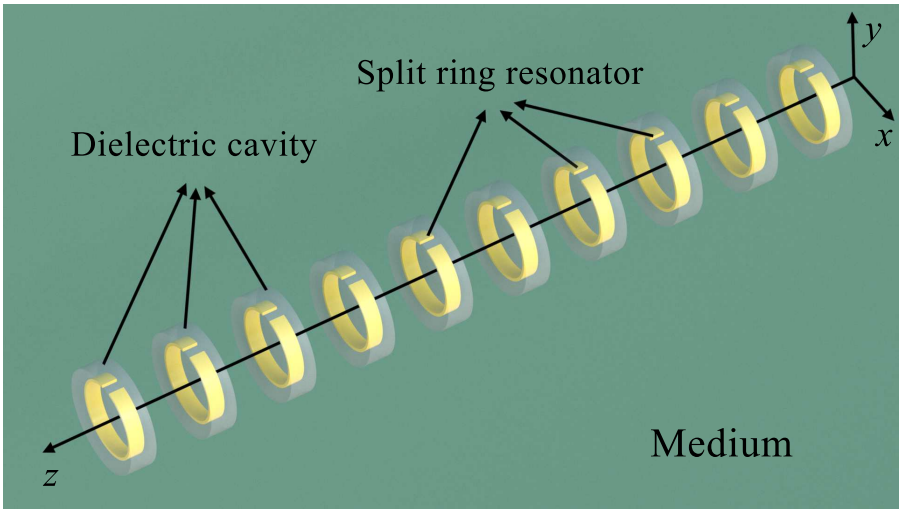


Figure 6.1: General schematic diagram of a coaxial MI waveguide consisting of a finite number of capacitively-loaded split ring resonators immersed in a dissipative environment. Each element is placed centrally in an insulating volume.

Fundamentally, each coil can be modelled as a RLC series resonator, whose impedance is given by:

$$Z_n = R_n + j\omega L_n + \frac{1}{j\omega C_n} \tag{6.1}$$

where a time variation of the form $\exp(j\omega t)$ has been assumed for variables, ω is the working frequency, R_n is the resistance, L_n are the self inductance, and C_n is the capacitance of the n-th coil, respectively. Applying the Kirchhoff's voltage law in combination with the new circuit model for coupled coils in a dissipative medium, the relationship between current and voltage in the n-th coil is obtained as:

$$\left(Z_n + j\omega\Delta\mathcal{L}_n\right) I_i + \sum_{m\neq n} j\omega\mathcal{M}_{m,n} I_m = V_n \tag{6.2}$$

where I_n and I_m are the currents in n-th and m-th coils respectively, V_n is the voltage applied to the n-th coil, $\Delta\mathcal{L}_n$ is the lossy self-inductance of n-th coil, $\mathcal{M}_{m,n} = M_{m,n} + M_{E,m,n}$ is the lossy mutual inductance between n-th coil and m-th coil through the medium, $M_{m,n}$ and $M_{E,m,n}$ are the mutual inductance in the free space between n-th coil and m-th coil and its additive factor due to the eddy currents inside the medium. The general relationship of the waveguide thus can be rewritten in the matrix form:

$$\mathbf{V} = \mathbf{ZI} \tag{6.3}$$

$$\begin{bmatrix} V_0 \\ \dots \\ V_n \\ \dots \\ V_{\mathcal{N}} \end{bmatrix} = \begin{bmatrix} Z_1 + j\omega\Delta\mathcal{L}_1 & \dots & j\omega\mathcal{M}_{1,n} & \dots & j\omega\mathcal{M}_{1,\mathcal{N}} \\ \dots & \dots & \dots & \dots & \dots \\ j\omega\mathcal{M}_{n,1} & \dots & Z_n + j\omega\Delta\mathcal{L}_n & \dots & j\omega\mathcal{M}_{n,\mathcal{N}} \\ \dots & \dots & \dots & \dots & \dots \\ j\omega\mathcal{M}_{\mathcal{N},1} & \dots & j\omega\mathcal{M}_{\mathcal{N},n} & \dots & Z_{\mathcal{N}} + j\omega\Delta\mathcal{L}_{\mathcal{N}} \end{bmatrix} \begin{bmatrix} I_1 \\ \dots \\ I_n \\ \dots \\ I_{\mathcal{N}} \end{bmatrix} \tag{6.4}$$

where $\mathbf{Z}$ is the symmetrical $\mathcal{N} \times \mathcal{N}$ impedance matrix of the configuration, $\mathbf{V}$ is the $\mathcal{N} \times 1$ applied voltage vector, and $\mathbf{I}$ is the $\mathcal{N} \times 1$ current vector. As a result, if the Kirchhoff coefficients of the circuit and the excitation signal are known, the currents in each coil can be easily determined by matrix inversion.

Assuming that the excitation is an external voltage V_0 applied to the first element of the MI waveguide. To simplify the configuration, it is assumed that all elements in the chain are identical ($R = R_n$, $L = L_n$ and $C = C_n$). As a consequence, the lossy Kirchhoff coefficients are identical due to the symmetry ($\Delta\mathcal{L} = \Delta\mathcal{L}_n$ and $\mathcal{M} = \mathcal{M}_n$). Hence, the current of the n-th coil can be rewritten in a general exponential form by taking an infinite wave solution due to the attenuation of magnetic field:

$$I_n = I_0 e^{-n\gamma d} \tag{6.5}$$

where I_0 is a constant, $\gamma = \alpha + j\beta$ is the propagation constant, α is the attenuation coefficient, β is the phase constant, and d is the separation between two adjacent elements. Finally, by substituting (6.5) into (6.2), a new dispersion relationship is derived to take into account the effects of the additional couplings in the medium background:

$$\frac{\omega_0^2}{\omega^2} + \frac{j}{Q}\frac{\omega_0}{\omega} - \left(\frac{\Delta\mathcal{L}}{L} + 1\right) = \sum_{n=1}^{p} \kappa_n \cosh(n\gamma d) \tag{6.6}$$

where $\omega_0 = 1/\sqrt{LC}$ and $Q = \omega_0 L/R$ are the fundamental resonant frequency and the Q-factor of the capacitively-loaded coil in free space, and $\kappa_n = 2\mathcal{M}_n/L$ is the mutual coupling coefficient, $\mathcal{M}_n$ are the lossy mutual inductance between two coils located at a distance of nd apart from each other, p is the upper limits of the summation, depending on how far the elements can interact magnetically before coupling becomes negligible. When the medium is vacuum, i.e., $\sigma = 0$ S/m, $\mu = \mu_0$, and $\epsilon = \epsilon_0$, the lossy self-inductance and the added mutual inductance no longer exist, $\Delta\mathcal{L} = 0$ and $\mathcal{M} = M_0$ where M_0 are the mutual inductance in vacuum. Consequently, (6.6) reduces to the well-known dispersion equation (1.6) for MI waves in free-space.

6.2 Simulation Results

The excitation is assumed to be a sinusoidal voltage amplitude $V_0 = 1$ V applied to the first element of the waveguide. Fig. 6.2 depicts the dispersion constants: (a) attenuation and (b) phase constant of MI waves travelling in a coaxial waveguide in free space and in an attenuating medium with a conductivity of $\sigma = 1.5$ S/m (similar to that of human blood [81, 107]). The waveguide comprises an infinite number of split ring resonators loaded with suitable capacitors with the element interval being $d = 30$ mm. The split ring has the following characteristic parameters: mean radius of $r = 11$ mm, height of $l = 5$ mm, width of $w = 1$ mm, resonant frequency of $f_0 = 46$ MHz, Q-factor of $Q = 1000$. The insulating cavities are assumed to be made of vacuum with a height of $2h + l = 7$ mm. The self inductance and the

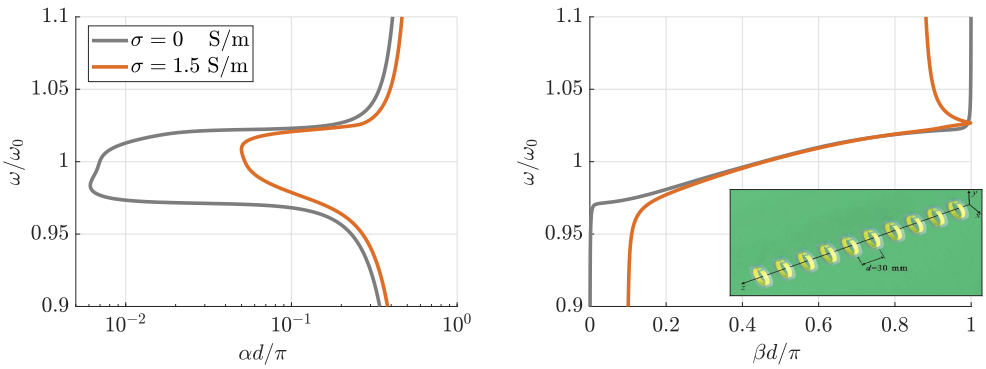


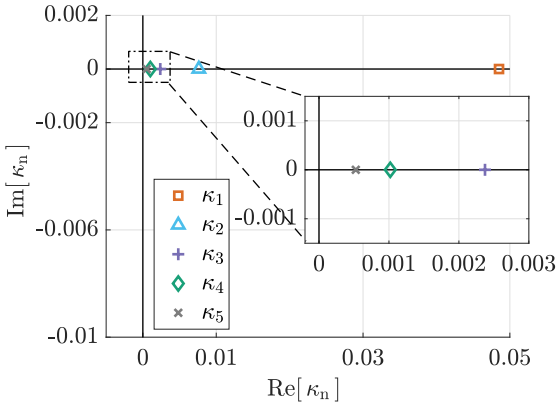
Figure 6.2: Calculated dispersion relationship (a) attenuation and (b) phase constant in a coaxial 1-D waveguide with a distance between two adjacent resonators of $d = 30$ mm embedded in free-space ($\sigma = 0$ S/m) and a dissipative medium with relative permittivity of $\epsilon_r = 78$, relative permeability $\mu_r = 1$ and conductivity of $\sigma = 1.5$ S/m in a very low-loss case ($Q = 1000$). Each element is placed centrally in an insulating cavity. The magnetic interaction is taken up to the fifth nearest neighbour.

lossy coefficients are then calculated according to the geometric parameters. The magnetic interaction is taken up to the fifth nearest neighbour.

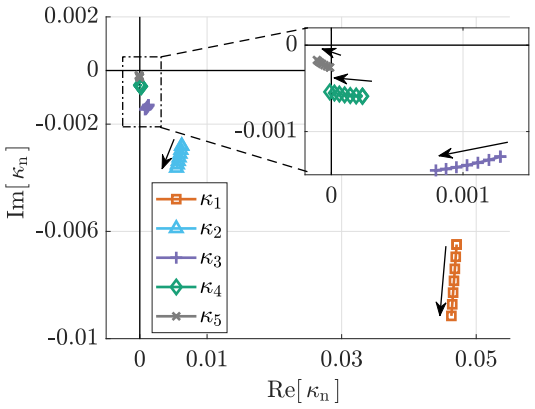
Inside the conductive medium, two effects are observed. The Q-factor of the resonators significantly decreases and their resonant peaks are slightly shifted to higher frequencies. In turn, MI waves when penetrating in an attenuating medium suffer a larger attenuation. The attenuation of MI waves in a medium with conductivity of $\sigma = 1.5$ S/m is nearly 5 times higher in the passband than that of MI waves in vacuum. In addition, they exhibit a peak in the passband at higher frequency, as shown in Fig 6.2. In terms of the phase constant, the MI waves in two cases coincide in most of the passband. In the stopband at lower frequencies, MI waves in the medium exhibit a non-zero phase constant due to the extra phase introduced by the eddy currents. Curiously, at the end of the passband, MI waves change from forward waves to backward waves. Previously, MI waves once were reported to change their type from backward waves to forward waves in biatomic metamaterial structures with co-directional power flow [135]. In [135], two coupled identical planar lines with one shifted by a half of the period are the platforms to support MI waves. When the coupling constant between unit

cells of two lines is sufficiently larger in magnitude than the coupling constant within a unit cell of a line, the positive coupling can suppress the negative coupling. Forward MI waves may occur for a certain range of frequency as a result. Here, on the other hand, the reason why the backward MI waves exist is entirely due to the phase rotation rather than the disparity in modulus of the mutual couplings. With the magnetic interactions between elements being complex quantities, the phase difference between currents in two neighbours is now not equal to $\beta d = \pi$ at the higher stopband as in free space case.

Fig. 6.3 illustrates the coupling constants $\kappa_n = 2M_n/L$ between the n-th nearest neighbours in the complex plane as a function of frequency among five adjacent split rings for the MI waveguide configuration shown in Fig. 6.2, inside (a) free space and (b) the medium above. The coupling constants are calculated by using (3.19) and the calculated self-inductance of the coil is $L = 30.46$ nH. As expected, the coupling constants between coaxial microwave resonators separated by a small electrical distance in free space are real and positive. Otherwise in an attenuating environment, those coupling constants with a negative imaginary part due to the field polarization exhibit frequency complex amplitude. In particular, the 1^{st} and 2^{nd} order coupling constants are largely real. On the other hand, the real and imaginary part of the 3^{rd} and 4^{th} order couplings have relatively comparable magnitudes. The fifth nearest neighbour coupling even moves to Quadrant **III**, revealing a real part being neither positive nor larger than its counterpart, as shown in Fig. 6.3b. With further observation, the real parts of the fourth and fifth nearest neighbour couplings even vanish in some parts of the frequency range. Hence, the unorthodox complex and frequency-dependent coupling constants between adjacent resonators makes the phase constant of MI waves when penetrating through a dissipative environment far more complicated over a wide range of frequency, and in the same way trigger the switch of the wave type at the end of the pass band.



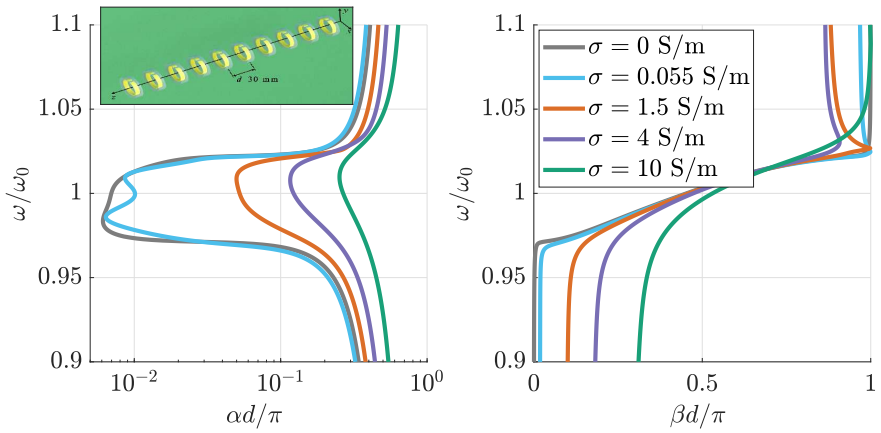
(a) Free space ($\epsilon_r = 1$ and $\sigma = 0$ S/m)



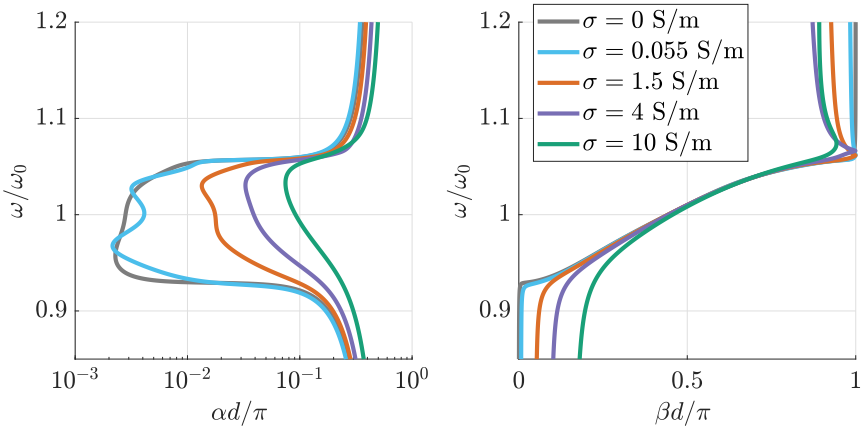
(b) Medium ($\epsilon_r = 78$ and $\sigma = 1.5$ S/m)

Figure 6.3: Calculated coupling constants $\kappa_n = 2M_n/L$ in the complex plane as a function of frequency between five neighbour resonant elements in the MI waveguide configurations shown in Fig. 6.2. The surrounding medium is (a) free space and (b) a dissipative medium with relative permittivity of $\epsilon_r = 78$, relative permeability $\mu_r = 1$ and conductivity of $\sigma = 1.5$ S/m. The working frequency is from $0.9\omega_0$ to $1.1\omega_0$. Black arrows indicate the progression of the frequency.

This trend can also be observed with media of different conductivities. Fig. 6.4 shows the dispersion relationship of the MI waveguide with an interelement distance of (a) $d = 30$ mm and (b) $d = 20$ mm respectively. Both the waveguides are embedded in a dissipative medium with varying conductivity. The conductivity is set to be $\sigma = 0.055$, 1.5, 4, and 10 S/m (corresponding to that of tap water, blood, sea water, massive sulfide minerals respectively [79–81, 107]). As shown in both dispersion diagrams, the larger the medium conductivity is, the stronger the induced eddy currents are, the higher the attenuation constant is. Besides that, all MI waves turn from forward to backward waves at the higher end of the



(a) $d = 30$ mm



(b) $d = 20$ mm

Figure 6.4: Calculated dispersion relationship of (left) attenuation and (right) phase constant in a coaxial 1-D waveguide with a distance between two adjacent resonators of (a) $d = 30$ mm and (b) $d = 20$ mm embedded in free-space ($\sigma = 0$ S/m) and a dissipative medium with relative permittivity of $\epsilon_r = 78$, relative permeability $\mu_r = 1$ and different conductivity of $\sigma = 0.055$, 1.5, 4, and 10 S/m in a very low-loss case ($Q = 1000$). Each element is placed centrally in an insulating cavity.

passband. The reason as pointed out above is because of the combination of the phase rotation of coupling constants between adjacent elements in the waveguide. It can be concluded that the phase difference of the mutual coupling has been a key factor for the interesting behaviour of the dispersion constants of MI waves inside non-conventional media. If the phase difference between adjacent elements is nearer to π than 0 (rad), backward MI waves exist, else forward MI waves. Therefore, this feature may open up an opportunity to tailor the dispersion relationship of MI waves by adjusting the phase of the coupling constants, which can be done by

inserting non-conventional media with different relative permittivity, conductivity or even relative permeability between components of the waveguide. However, the additional losses introduced by the media may be the trade-off in this scenario. The final noteworthy observation is that in Fig. 6.4b, MI waves travelling in a volume with conductivity of $\sigma = 0.055$ S/m have lower attenuation at some parts of the passband. Considering the conductivity is fairly low, the medium is now a low-loss material with high permittivity so that it can magnify the mutual coupling in virtue of the displacement currents while introduce tolerant losses.

6.3 Laboratory Experiments

In the previous section, the dispersion characteristics of MI waves have been studied analytically. The dispersion equation is generalised by using the new circuit model for two magnetically coupled circuits inside an arbitrary medium. To validate the dispersion equation expressed in (6.6), laboratory measurements for the propagation constants of a 1-D MI waveguides embedded in a conductive medium have been conducted.

6.3.1 Experimental Design

Section 6.3 outlines the measurement apparatus in the laboratory. Fig. 6.5 illustrates the schematic diagram of the experimental set-up to measure the transmission parameters of a MI waveguide. In the experiments, two magnetic loop probes connecting to two ports of a VNA (Keysight E5061B) are used to provide a transmitting-receiving scheme. The transmitting and receiving probe is manufactured from a semirigid RG402/U 50 Ω coaxial cable with one end being a 10-mm-diameter loop and a 15-mm-diameter loop made from their inner conductors, respectively. They are insulated to prevent direct contacts with the attenuating medium to improve the measurement accuracy.

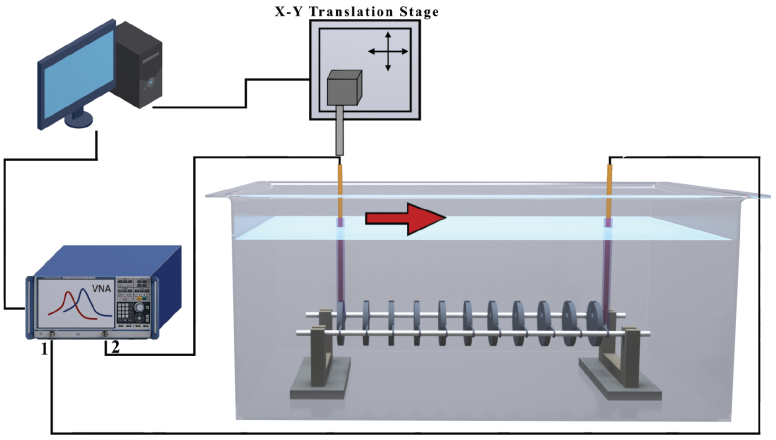


Figure 6.5: Schematic diagram of the experiment set-up to measure the dispersion constants of MI waveguides inside a dissipative surrounding medium.

The MI waveguide under test is immersed inside a tank containing a dissipative medium of suitable conductivities. The tank is made of polymethyl methacrylate with a dimension of 230 mm×480 mm×260mm. The MI waveguide consists of 11 capacitively loaded split rings placed inside insulating cylindrical cavities. Two symmetric rings attached to the sides of insulating cavities are designed for minimizing misalignment errors. The insulators are then interconnected via two polytetrafluoroethylene rods through these rings. The MI waveguide is aligned within a 0.1 mm accuracy along the rods. The whole frame is then mounted on U-shaped cantilevers that are taped to the bed of the tank.

Throughout the experiments, the transmitting probe was placed centrally aligned behind the first coil to excite the MI waveguide whilst the receiving probe was attached to the arm of a computer-controlled translation stage mover. By using the mover control software, the receiving probe is moved to the top of each ring scan the near-field magnetic fields which proportionally correspond to the current following in the rings. The propagation constants are then extracted from the measured currents.

6.3.1.1 Dissipative Media

The media in the experiments are made of aqueous solutions of sodium chloride (salt) with variable concentration to represent different conductivities. The conductivity is assessed with a conductivity-meter calibrated with standard calibration solutions

(HANNA HI-70030 12880 μS/cm). The relative permittivity of the solutions is assumed to be about $\epsilon_r = 78$ at room temperature at radio frequency [84, 85].

6.3.1.2 Split Ring Resonators

A large number of identical split ring resonators were manufactured and tested. They are fabricated by slicing a cylindrical copper tube (diameter of 22 mm) and soldering a suitable tuning capacitor at the gap to tune to a desired frequency. Fig. 6.6 shows a diagram with detailed dimensions and the photograph of the split ring. It has a mean radius of $r_0 = 11$ mm, width of $w = 1$ mm, height of $l = 5$ mm while the gap width is $g = 1$ mm. The rings are then tuned to work at a resonant frequency of interest $f_0 = 46$ MHz by loading nominally identical 330 pF capacitors of type of polystyrene film at the gap.

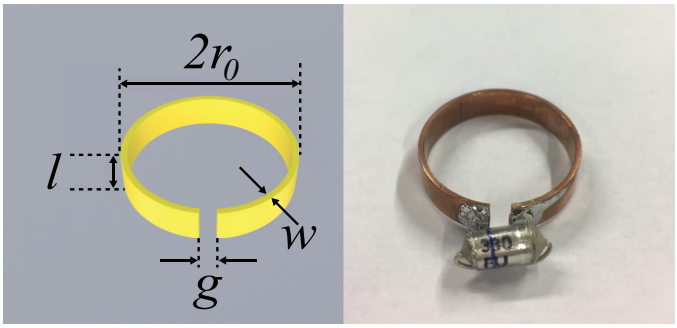
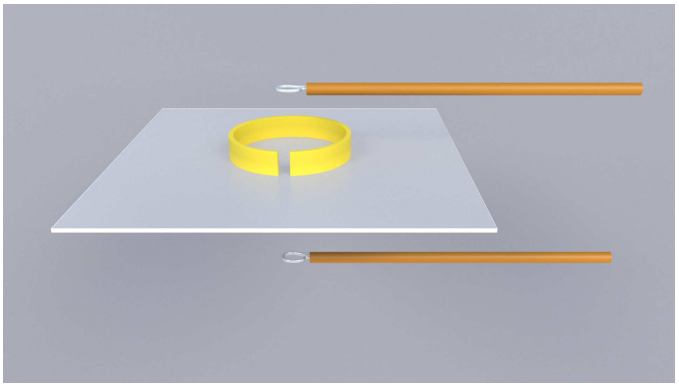
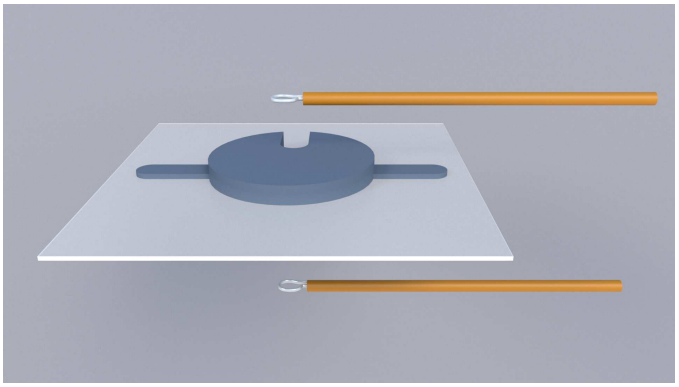


Figure 6.6: (a) Schematic diagram of a split ring resonator and (b) its actual photograph. The ring is loaded with a capacitor of polystyrene film type at the gap.

The characteristics of split rings are usually defined by two important parameters, such as the resonant frequency and Q-factor. Each ring is then measured to satisfy the desired resonant frequency $f_0 = 46$ MHz. Only the rings that exhibit a resonant frequency within 0.5% of f_0 are used to construct MI waveguides. Additionally, when insulating the split rings by placing them inside non-magnetic cavities, the material that the cavities are made of having a dielectric constant different from that of vacuum may introduce a small capacitance to the circuits. Predictably, it leads to a small decrease in the self resonance of the rings. The impact of the dielectric therefore should be considered in the microwave resonator characteristic. Fig. 6.7 illustrates the schematic diagram of the experimental set-up. Two weakly-coupling



(a)



(b)

Figure 6.7: Measurement set-up to measure the quality factor of the fabricated split ring resonators (a) alone and (b) in combination with their corresponding insulating cavities.

magnetic probes connected to a VNA are used to measure the responses of the resonators with and without their corresponding insulators.

The modulus of the transmission coefficient S_{21} is then fit to the Lorentzian curve using nonlinear least-squares analysis to determinedly eliminate uncertainty under realistic experimental conditions. The resonant frequency and the Q-factor, therefore, are calculated from fitting curve, see Appendix C. This method is known as one of the most reliable procedures to estimate these crucial parameters of a microwave resonators [136]. After filtering substandard resonators, the satisfactory ones are employed to determine the impacts of dielectric cavity on the resonant frequency and Q-factor. Fig. 6.8 presents the measured broadband transmission coefficient for the split ring resonators with their insulating cavities.

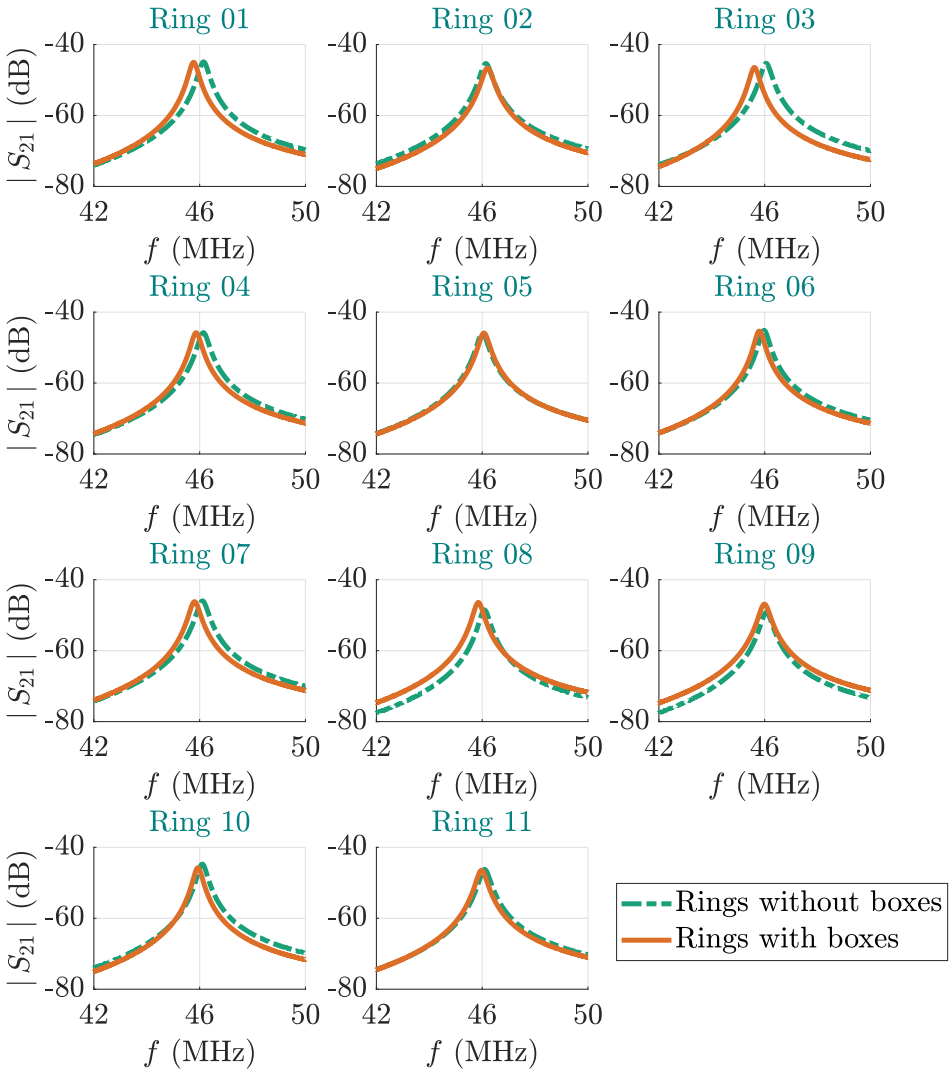


Figure 6.8: The modulus of the measured transmission coefficients for manufactured split ring resonators with and without their corresponding insulating cavities.

As can be seen from the graph, the insulators tend to shift the resonant peaks to slightly lower frequencies, about $0.05 - 0.3$ MHz. Performing the same fitting procedure above, the new resonant frequency and Q-factor of the rings inside their corresponding insulators are evaluated. Table. 6.1 summaries the results obtained from Fig. 6.8 by fitting the Lorentzian curve.

Ring Number	Without Insulator		With Insulator	
	Resonant Frequency (f_0)	Q-factor (Q)	Resonant Frequency (f_0)	Q-factor (Q)
01	46.1500	126.9444	45.7750	132.3387
02	46.1425	115.5577	46.2025	115.5041
03	45.0600	121.9614	45.6175	127.1722
04	46.1425	121.8710	45.8725	127.0703
05	46.0150	117.9900	46.0675	120.9647
06	45.9775	129.2496	45.7975	132.8813
07	46.1125	115.5605	45.8125	118.8790
08	46.0900	125.8105	45.8575	124.5727
09	46.0675	115.6414	45.9925	114.9579
10	46.1050	129.7646	45.9325	136.2901
11	46.0975	115.5573	45.9775	117.3607
Average	46.0762	119.8355	45.9025	122.5285

Table 6.1: The resonant frequency and Q-factors of split ring resonators with and without their corresponding insulators calculated from the Lorentzian fit of the experimental data presented in Fig. 6.8.

6.3.1.3 Dielectric Cavities, Cantilevers, and Immersion Level

The formula estimating the lossy Kirchhoff coefficients provides the most accuracy when the radius of dielectric cavities tends to infinity. Yet, the size of the insulators must be finite for practical applications. In order to obtain a reasonable match to the analytical conditions, the radius of the insulators is chosen to be three times the radius of the coil, as discussed in Chapter 3. Therefore, the insulating cavities are designed with cylindrical shapes with the dimensions: a radius of $R = 3r_0 = 33$ mm, height of $h = 7$ mm, and thickness of 1 mm. There is a small centrally-aligned hollow cylindrical pipe for fixing the position of split ring resonators, as shown in Fig. 6.9. In addition, to measure the near fields generated by the split ring resonators, the dielectric cavity has been made with a small notch. The notch should be long enough for the measuring probe to access within several millimetres from the edge of the rings while its size should be as small as possible to avoid a larger

volume of the conductive solution in proximity to the rings. Thus, the diameter and the length of the notch are $D_n = 14$ mm and $l_n = 12$ mm, respectively.

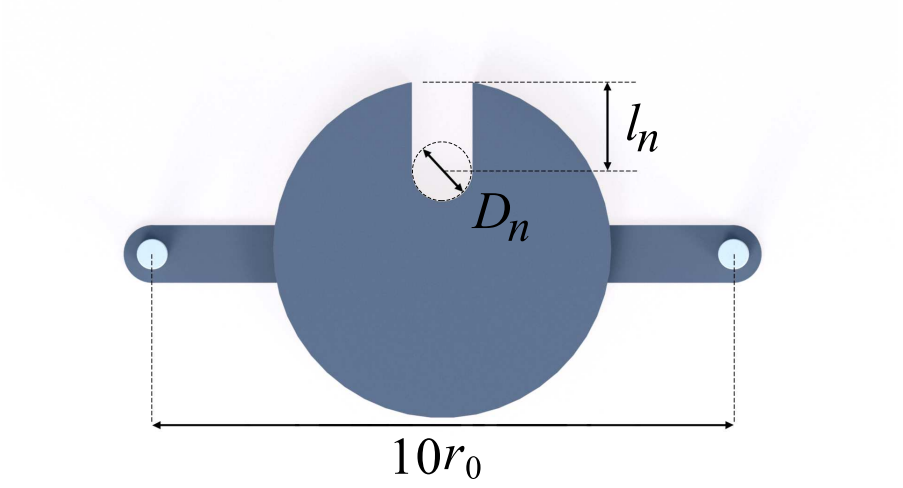


Figure 6.9: Schematic diagram of the dielectric cavity providing the insulation for the split ring resonators.

Clearly, having a notch on the insulating cavities has a certain impact on the lossy self inductance as well as the lossy mutual inductance between two split ring resonators because it causes more volume of the medium near the rings and in turn larger eddy current effects. Also, as a further consideration for the experiment design, the novel circuit model in Chapter 3 is developed for the configuration where the coils are embedded in a boundless dissipative medium. However, the aqueous solution in the experiments is limited by the size of the container. To mimic the effects of an infinite environment, the immersion level is a key parameter to consider in designing the experimental framework. Fig 6.10 depicts the definition of the immersion level, i_v. It refers to the distance from the edge of the insulating cavity to the medium surface. The region above the medium is vacuum.

Now, the combination effects of the notch and the immersion levels is simulated with CST EMS. Fig. 6.11 and Fig. 6.12 show the normalised (a) modulus and (b) phase of the lossy self and mutual coefficients as a function of the immersion levels with the actual design for insulating cavities at the resonance frequency, respectively. The results are normalised to the simulated values for the configuration when the two coils are immersed in an infinite dissipative medium and the insulators

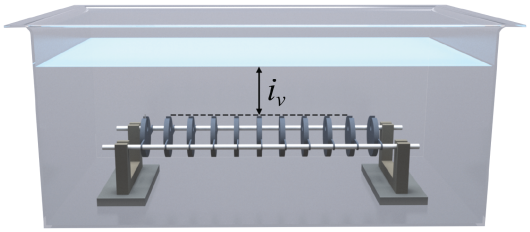


Figure 6.10: Vertical immersion level of the split ring resonators in the experiment.

are in perfectly cylindrical shape, cf. Fig. 3.3. In conjunction with the notch, the immersion level modifies both lossy coefficients. However, when the coils are submerged with a depth of $i_v \geq 60$ mm, it plays a less important role as the relative errors in both the modulus and phase are less 3% compared to the reference value. The immersion level therefore should be larger than 60 mm for this particular coil and insulator design to corroborate the accuracy of the analytical model. As a result, the U-shaped cantilevers used to support the rods interconnecting the dielectric insulator has a height of $h_c = 100$ mm to satisfy the immersion level conditions.

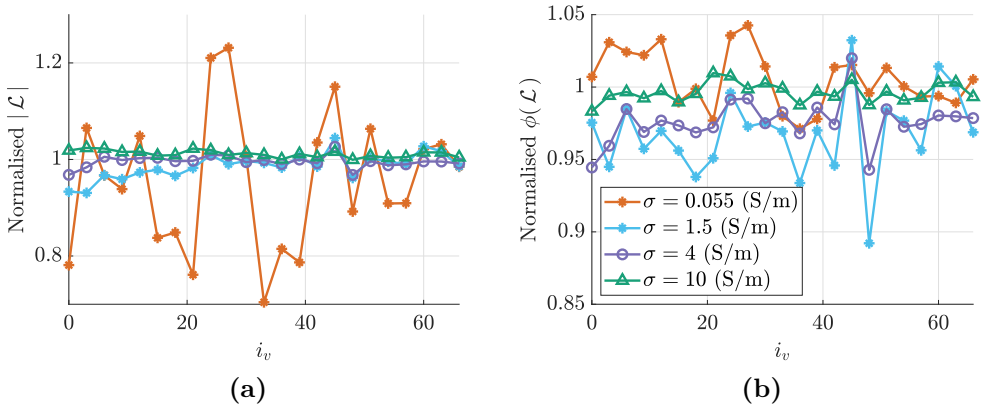


Figure 6.11: Normalised (a) modulus and (b) phase of the lossy self inductance as a function of the immersion level for the configuration of two coaxial identical circular coils shown in Fig. 6.6, separated by a vertical distance $d = 30$ mm inside a dissipative medium with a relative permittivity of $\epsilon_r = 78$, relative permeability of $\mu_r = 1$, and variable conductivity $\sigma = 0.055$, 1.5, 4, and 10 S/m. The insulating cavities shown in Fig. 6.9 have a height of 7 mm. CST EMS simulation results are normalised to that of the case when the surrounding dissipative medium is infinite and the insulators are in perfectly cylindrical shape.

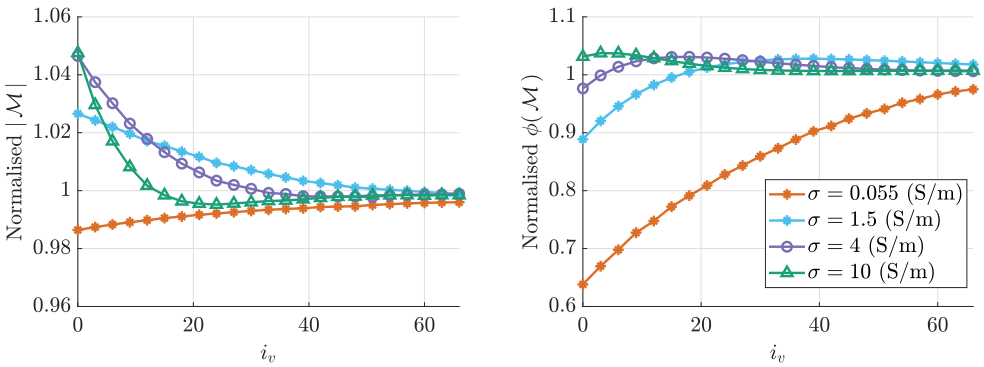


Figure 6.12: Normalised (a) modulus and (b) phase of the lossy mutual inductance as a function of the immersion level for the configuration of two coaxial identical circular coils shown in Fig. 6.6, separated by a vertical distance $d = 30$ mm inside a dissipative medium with a relative permittivity of $\epsilon_r = 78$, relative permeability of $\mu_r = 1$, and variable conductivity $\sigma = 0.055$, 1.5, 4, and 10 S/m. The insulating cavities shown in Fig. 6.9 have a height of 7 mm. CST EMS simulation results are normalised to that of the case when the surrounding dissipative medium is infinite and the insulators are in perfectly cylindrical shape.

Finally, the insulating cavities and the U-shaped cantilevers are realized by using 3D printing with acrylonitrile butadiene styrene (ABS) filament, see Fig. 6.13. To prevent water leakage, the dielectric cavities are sealed with silicone adhesive sealant (LOCTITE SI 595).

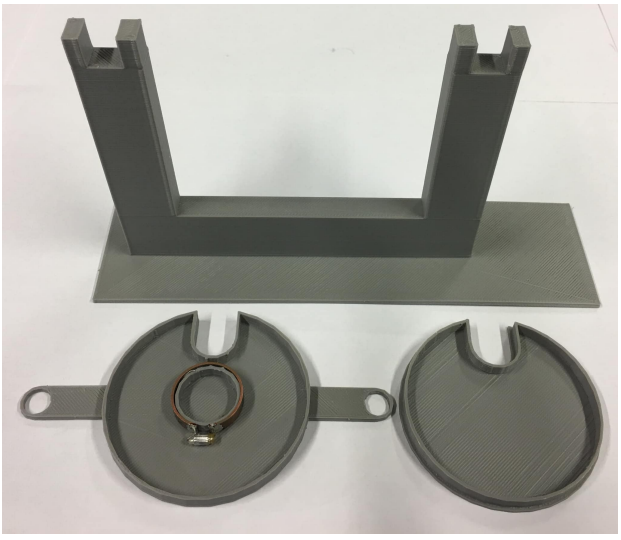


Figure 6.13: 3D printed (top) U-shaped cantilevers, the (bottom right) body and (bottom left) cap of an insulating cylindrical cavity with a split ring resonator inside.

6.3.2 Retrieving Dispersion Constants

To extract the propagation constants, the retrieving procedure is as follows. It is assumed that the transfer coefficient recorded by the measuring probes at the split ring n is proportional only to the current flowing in that ring, i.e., $S_{21|n} \propto I_n$. It is assumed that the MI waveguide supports two complex modes with two complex values of the propagation constant γd. In reality, the MI waveguide has a finite length. Thus, there is a reflected wave at the end of the waveguide when the waveguide is not matched. Taking the reflected waves into account, the measured transfer function at n-th element of the array can be rewritten in the form:

$$S_{21|n} \propto I_n = \left(a_1 e^{-n\gamma_1 d} + b_1 e^{n\gamma_1 d}\right) + \left(a_2 e^{-n\gamma_2 d} + b_1 e^{n\gamma_2 d}\right) \tag{6.7}$$

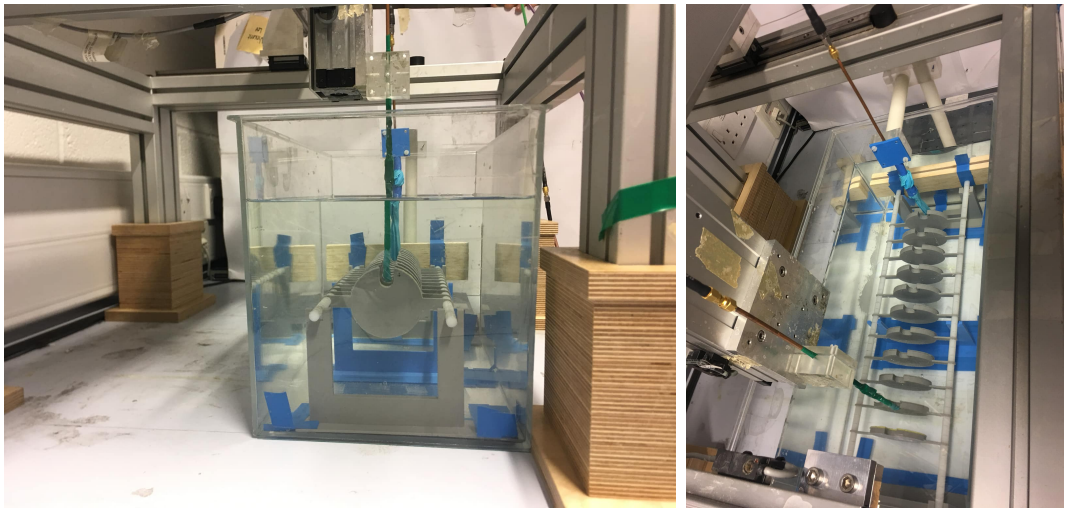
where a_1, a_2, b_1, and b_2 are constant, and d is the distance between 2 elements. After a few algebraic operations (see Appendix D), the value of $\gamma_1 d$ and $\gamma_2 d$ can be determined by considering the ratios between S_{21} at ring n and its six neighbour resonators.

$$\begin{cases} \cosh(\gamma_1 d) = \dfrac{1}{2}\left(\dfrac{2uv-u-w}{2(2u^2-v-1)} \pm \sqrt{\left[\dfrac{2uv-u-w}{2(2u^2-v-1)}\right]^2 - 4\dfrac{(v+1)^2-u(3u+w)}{2(2u^2-v-1)}}\right) \\ \cosh(\gamma_2 d) = \dfrac{1}{2}\left(\dfrac{2uv-u-w}{2(2u^2-v-1)} \mp \sqrt{\left[\dfrac{2uv-u-w}{2(2u^2-v-1)}\right]^2 - 4\dfrac{(v+1)^2-u(3u+w)}{2(2u^2-v-1)}}\right) \end{cases} \tag{6.8}$$

where $u = (S_{21|n+1} + S_{21|n-1})/(2S_{21|n})$, $v = (S_{21|n+2} + S_{21|n-2})/(2S_{21|n})$, and $w = (S_{21|n+3} + S_{21|n-3})/(2S_{21|n})$. One of two modes is the propagation mode while the other is non-propagating. It is worth noting that this method is best utilized for seven elements about the middle of the waveguides because the measurements at the beginning of the waveguide are strongly affected by the direct coupling between the transmitting and receiving probes while those towards the end of the line are strongly affected by reflected waves from the unmatched condition.

6.3.3 Experimental Results

In this section, the laboratory measurements are reported. The actual experiment in the laboratory is shown in Fig. 6.14. The MI waveguide under test consisted of 11 elements for an inter-element distance of 30 mm. The aqueous solution is made with different conductivities, such as $\sigma = 0.055, 1.5, 4, 10$ S/m. In the measurement, the VNA recorded the transfer functions, S_{21}, between two magnetic probes for 1601 frequency points in the range from 40 MHz ($\approx 0.9f_0$) to 52 MHz ($\approx 1.1f_0$) with an averaging factor of 64. The VNA is calibrated up the connection with the probes with a set of standard terminations.

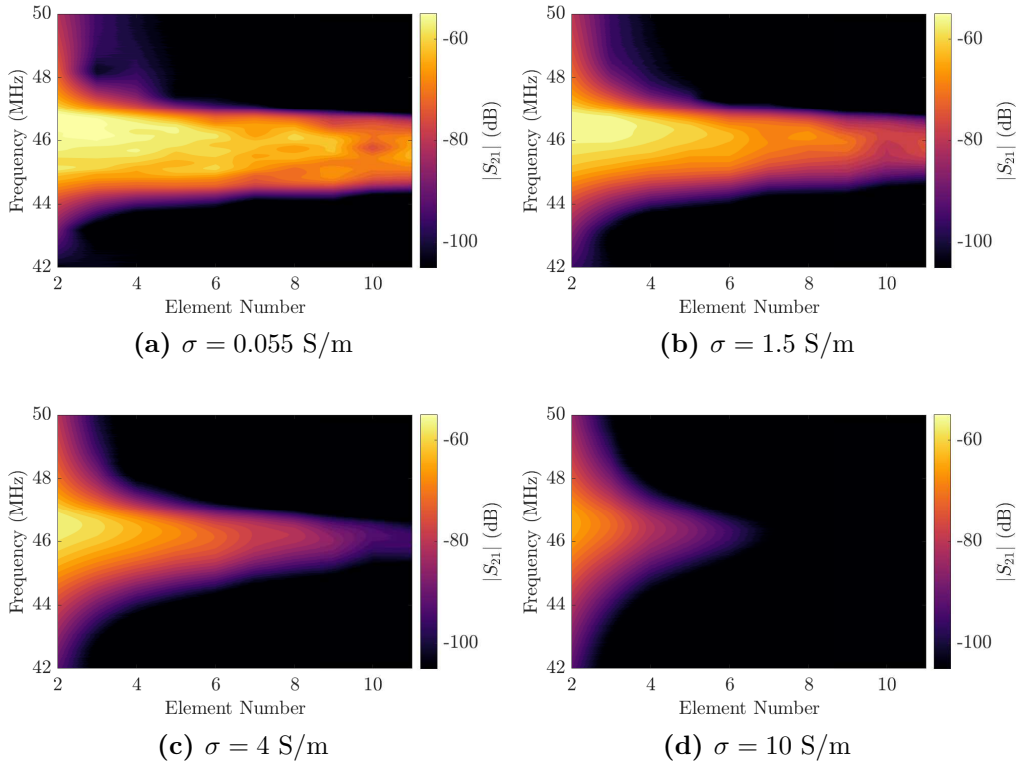


(a) **(b)**

Figure 6.14: Laboratory measurement of an MI waveguide consisting of 11 elements with the distance between two adjacent elements of $d = 30$ mm submerged in an aqueous solution of sodium chloride with suitable conductivity. (a) Side view, and (b) top view.

Fig. 6.15 illustrates the modulus of the measured S_{21} in logarithmic scale along the waveguide in four different solutions. The result for the first element of the waveguide is excluded due to the strong direct coupling between the transmitting and receiving probes. For $\sigma = 0.055$ S/m, it can be shown that MI waves can travel through the dissipative solution via a moderate bandwidth around the resonance of the split ring resonators. The bandwidth reduces rapidly with the increasing conductivity which corresponds to the stronger attenuating effects of the eddy

currents. When the medium conductivity is equal to $\sigma = 4$ S/m, similar to that of common sea water, the signals barely reach the tenth resonators. To a greater degree, MI waves completely vanish after penetrating through 6 elements in the medium with conductivity of $\sigma = 10$ S/m. In addition, the centre of the passband of MI waves noticeably moves up in the frequency spectrum. It is due to the shift of the resonance of the split rings inside a conductive medium as discussed in Chapter 3.



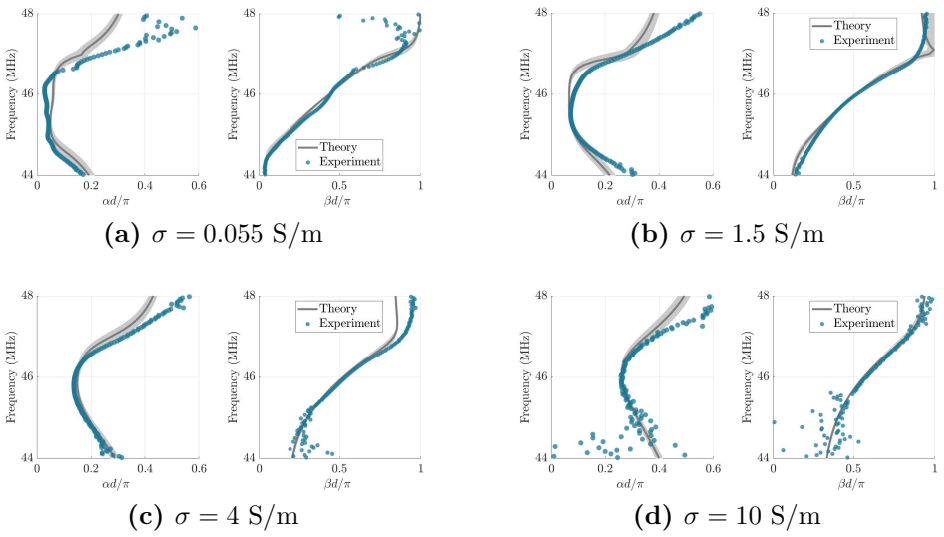
(a) $\sigma = 0.055$ S/m **(b)** $\sigma = 1.5$ S/m

(c) $\sigma = 4$ S/m **(d)** $\sigma = 10$ S/m

Figure 6.15: Log-magnitude of transmission coefficients, S_{21} in dB scale measured along the waveguide shown in Fig. 6.14 submerged in an aqueous solution with different conductivity of (a) $\sigma = 0.055$, (b) $\sigma = 1.5$, (c) $\sigma = 4$, and (d) $\sigma = 10$ S/m.

By using the retrieving procedure stated in the previous Section, the dispersion constants can be extracted from the transfer coefficients at elements about the middle of the waveguide. Fig. 6.16 shows experimental results for the attenuation and phase constant per unit cell, αd and βd respectively, versus the frequency for four different medium conductivities. For the purpose of comparison, the predicted dispersion constants based on (6.6) considering magnetic interactions up to the fifth nearest neighbours will be presented along with the experimental data. As discussed,

the analytical solutions for the lossy Kirchhoff coefficients yield an average relative error of 7% compared to the full-wave simulation under the condition that the radius of the insulators is three times larger than the coil radius. In addition, the immersion level and the notch on the dielectric insulators are shown to modify the lossy Kirchhoff coefficients by a maximum relative error of 3% with respect to the simulation results for an infinite medium background and perfectly cylindrical insulators. Those uncertainties therefore are encapsulated by attributing a 7% variability to both lossy coefficients, $\Delta\mathcal{L}$ and $\mathcal{M}$, in the (6.6).



(a) $\sigma = 0.055$ S/m **(b)** $\sigma = 1.5$ S/m

(c) $\sigma = 4$ S/m **(d)** $\sigma = 10$ S/m

Figure 6.16: Comparison of the experimental and theoretical (left) attenuation constant and (right) phase constant in a coaxial 1-D waveguide with a distance between two adjacent resonators of $d = 30$ mm embedded in an aqueous solution with different conductivity of (a) $\sigma = 0.055$, (b) $\sigma = 1.5$, (c) $\sigma = 4$, and (d) $\sigma = 10$ S/m. Each element is placed centrally in an insulating cavity with the radius equalling to three times ring radius. The shaded area represents the spread in the theoretical results due to the 7% uncertainty in the lossy Kirchhoff coefficients ($\Delta\mathcal{L}$ and $\mathcal{M}$).

Within the pass band, the experimental and theoretical curves for the phase change of MI waves in the medium with variable conductivity are shown to be in excellent agreement, although towards the edges of the passband there is some deviation. The agreement for the attenuation diagram is satisfactorily good. The likely reasons for the discrepancy are the multiple fields on the measuring probe, and most importantly, the mutual coupling between the measuring probes and the

rings being strongly affected by the eddy currents in the medium. The former reason can be seen clearly as the attenuation curve in the medium of 0.055 S/m exhibits modest oscillations at the pass band. When the magnetic probe is placed at one element, the measured signal is polluted by strong couplings from its neighbours. This phenomenon is less pronounced for increasing conductivities because the eddy currents attenuate those couplings from the neighbours, as shown in Fig. 6.16c-6.16d. The latter reason is indeed systematic and unavoidable in the measurements.

The interesting phenomenon when MI waves switches from forward waves to backward waves at the higher end of the pass band however cannot be observed in the measurements. The experimental points in the stop bands had magnitudes close to or less than the noise floor so they are probably spurious. As things currently stand, the dispersion equation (6.6) provides an excellent understanding of the propagation of MI waves in non-conventional media.

6.4 Conclusions

In the previous chapter, a novel analytical circuit model for two low frequency coupled resonators is postulated. Even though the full-wave simulation results have confirmed the existence of the lossy Kirchhoff coefficients, no experience is conducted to verify the model. In this chapter, a general dispersion relationship of MI waves travelling in an attenuating medium has been theorized from the novel circuit model. When the medium is non-dissipative, the general equation turns into the established one in free space. With increasing medium conductivity, MI waves attenuate proportionally, and also the switch of wave type can be seen at the higher branch of the stop band. The complex nature of the lossy Kirchhoff coefficients is responsible for the change in the phase constant. By virtue of their imaginary parts, they introduce extra phase shift to the currents between two adjacent elements. Thus, currents of neighbouring elements are not in anti-phase as in the free space case.

Laboratory experiments have been conducted to validate the general dispersion relationship. A chain of capacitively-loaded split ring resonators is the platform to support MI waves. Each resonator is insulated by placing into a 3D-printed

cylindrical dielectric cavity. The waveguide is then submerged in aqueous solutions of sodium chloride (salt) with different concentration representing four conductivities, namely $\sigma = 0.055$, 1.5, 4, and 10 S/m. By measuring the transfer coefficient along the waveguide, MI waves evidently propagate through the dissipative medium while suffer from huge attenuation. Signals can only travel through 6 unit cells inside the medium of conductivity $\sigma = 10$ S/m as an example.

The dispersion constants extracted from the measurements show excellent agreement with the theoretical values attributing to $\pm 7\%$ uncertainty in the lossy Kirchhoff coefficients for the β-ω diagram, and acceptably good for the α-ω diagram. The effect of eddy currents on the coupling between measuring probes and split ring resonators is likely the main reason for the discrepancy in the attenuation graph. Nevertheless, the turning point that MI waves change from forward to backward type cannot be shown in the experiment because the results are specious in the branch of evanescent waves where the signals are at or below the noise floor. Having validated the general dispersion equation, the experimental data also obliquely corroborate the circuit theory for two coupled coils in non-conventional media with the existence of the lossy Kirchhoff coefficients. To conclude this Chapter, the general dispersion equation offers insights to the propagation properties of MI waves in an arbitrary medium, and allows the design and optimization of various applications utilizing MI waves in non-conventional media.

7 Conclusions and Future Work

Contents

7.1 Conclusions 141
7.2 Future Work 145
7.2.1 Possible Model Improvement 145
7.2.2 Possible Applications 147

7.1 Conclusions

The study of near-field coupling is a long-standing topic of much interest. Since the beginning of the *21st* century, with the emergence of metamaterials, this near-field coupling has attracted more attention from scientists and researchers worldwide as a key design element to numerous practical applications such as wireless power transfer, near field imaging, antenna and waveguide, and light manipulation. Free space or the earth's atmosphere is the most common environment where these applications are operating. Nevertheless, there seems to be a lack of literature on near field coupling in less-ideal media like the earth, concrete, ocean, or biological tissues. The aim of this thesis has been to investigate the near-field coupling of magnetic metamaterials in those environments. Especially it centres on understanding the impact of the ambient

environment on two or more magnetically coupled circuits and hence, developing an analytical model for the propagation of MI waves in a non-ideal medium.

Since MI waves require a magnetic coupling between the elements forming the waveguide, Chapter 2 starts with a literature survey on how an intervening slab affects the mutual coupling between two low frequency coils. In most current literature, the plane-wave approximation model has been the most common model for the magnetic channel linking an inductive source to a receiver. The computational results show that in the presence of an intervening conductive block, the magnetic field becomes elliptically polarized due to the emergence of the reaction field generated by the eddy currents in the block. As a result, the mutual inductance exhibits a non-negligible imaginary part referring to the field rotation. Laboratory experiments were conducted to compare three other approaches: the plane-wave approximation, the generalised D&D field solution, CST EMS simulation results. Doubtlessly, the plane-wave approximation shows the worst agreement with the experimental data since it has neglected completely the imaginary part while overestimated the attenuation of the real part of the mutual inductance. On the other hand, the generalised D&D field solution are in satisfactory agreement with the CST simulations and measurements. It can then be concluded that the simple PW approximation, which has no theoretical foundation, is truly impractical for actual applications in common wireless propagation environments.

However, in most applications involving non-conventional media, the coils acting as transmitting-receiving antennas are often immersed partly or completely in those environments, like in underground/underwater wireless sensor networks and in vivo communications systems. Therefore, Chapter 3 investigates the case when the two coils insulated by small dielectric cavities are completely immersed in an infinite homogeneous dissipative medium. A novel equivalent circuit model for this case has been developed. It is concluded that there exists a change in the self-inductances of the coils as well as in their mutual coupling. The former is called complex self-inductance while the latter is called complex mutual inductance. These complex terms depend on the working frequency, geometry of the coils and electromagnetic

characteristics of the medium. To calculate the complex Kirchhoff coefficients, a mathematical method is developed for time-harmonic voltage excitation sources. Compared to the mathematical method in the D&D solution that considers one coil driven by a constant amplitude alternating current and the other coil left open-circuited, the analytical method originated in this thesis not only reduce the mathematical complexity but also directly calculate the complex self inductance from the magnetic vector potential. This approach is very versatile and can be easily adapted to various application scenarios, such as where the coils are partly submerged or the medium has layers of different conductivities. Intensive finite element simulations with CST EMS has been performed to examine the validity of the complex Kirchhoff coefficients. It is confirmed that when the radius of the insulating box is sufficiently large with respect to the coil radius, i.e., at least three times larger than the coil radius $R \geqslant 3r_0$, the field solutions can provide exceptional accuracy with an average relative error not exceeding 7% in comparison to the numerical simulations for reasonable values of the parameters. As previous works have concentrated on the attenuation of the magnetic link and usually ignoring the feedback losses from the medium, the new circuit model incorporates for the first time all electromagnetic coupling and feedback effects for two coupled coils in infinite homogeneous non-conventional media.

Taking the complex Kircchoff coefficients into account, circuit analysis is addressed in Chapter 4. When immersing a magnetic resonant circuit in an arbitrary environment, the resonant frequency indeed varies with the real part of the complex self inductance, whereas the Q-factor is lowered because of the additional losses symbolized by the imaginary part. For a simple system of two coupled coils, the almost perfect symmetry of the splitting resonant peaks in the current response is noticeably broken with the lower frequency peak smaller than the higher one. It can be explained with the circuit theory with the main reason being the phase of the complex mutual inductance. Additionally, the positions of the even and odd modes inside a particular propagation medium are predictable by performing the eigenvalue method. The power conversation of the coupled coil system is then

explicated. The loss due to the medium can be accurately estimated given the knowledge of the medium electromagnetic properties.

Using the novel circuit model, Chapter 5 reports a general dispersion relationship of the MI waves supported by a chain of resonators inside an arbitrary medium. The conductivity of the ambient environment results in a significant attenuation to the MI waves as expected. Interestingly, the analysis in this thesis suggests a switch of the wave type from forward waves to backward waves at the higher end of the passband for a coaxial MI waveguide. The complex nature of the complex Kirchhoff coefficients are responsible for that phenomenon, causing the currents flowing in two adjacent elements not being in anti-phase as seen in the free space case. The laboratory experiments were conducted to verify the dispersion equation. In the experiment, the dissipative medium is aqueous solutions of sodium chloride with different concentration representing four conductivities, such as $\sigma = 0.055$, 1.5, 4, 10 S/m similar to that of tap water, human blood, sea water and massive sulfide minerals. In comparison to the theoretical values, the measured data is in excellent agreement and acceptably good for the phase and attenuation constant, although towards both ends of the passband there is some deviation. The main reason for the discrepancy in the attenuation constant diagram is that the eddy currents have a strong impact on coupling between the measuring magnetic probes and the elements. The measurement however is not able to capture the point where the MI waves change the type from forward to backward waves due to low signal-to-noise ratio at the stop band. Having demonstrated that the experimental data for the dispersion constant are in accord with the theoretical values, the importance of including the complex Kirchhoff coefficients is highlighted. The novel circuit model for two coupled inductive circuits inside a non-ideal medium is indirectly validated. With the general dispersion of MI waves available, the propagation of MI waves in an arbitrary ambient environment has been fully understood. This work offers insights to the design, analysis, and optimization of various immediate applications utilizing MI waves in non-conventional media.

Finally, Chapter 6 considers one immediate application with the novel equivalent circuit model: wireless power transfer. The behaviour of wireless power transfer via strongly-coupled magnetic resonators in conductive environments is established. Numerical simulations for a case study have shown that the operating frequency should be selected carefully in order to maximize the transferred power to the load. Interestingly, the optimal frequency can be either the original resonance in the isolated case or the upper resonance in the no-load coupled case. The load resistance, therefore, will be optimized corresponding to the chosen frequency. To choose the optimal working frequency, an implicit quadratic inequality of the receiver internal resistance is solved to construct a guided map. In the common ranges of the coil resistance, given that the resistance is fixed, the optimal frequency encounters a switch at a suitable medium conductivity and vice versa. These findings are very applicable when designing and operating systems functioning in real-time dynamic environments.

7.2 Future Work

7.2.1 Possible Model Improvement

In spite of the facts that the circuit model in this thesis illustrates the physics clearly with all the electromagnetic interactions being addressed, the way to calculate the complex Kirchhoff coefficients arose naturally from theory indeed need to be improved. Positively, the mathematical method in this thesis has certain merits on estimating these complex terms, as discussed thoroughly. Negatively, it has some limitations at the same time. The mathematically method in this thesis accepts an assumption, which models the finite insulating cavities as infinitely wide layers, in order to derive closed form solutions for the electromagnetic fields. Since the split ring resonators forming the MI waveguide under test are quite small in size, the dimensions of the dielectric cavities seem to be reasonable and practical. For the same reason, the model can be also applied for tiny implantable devices, such as neural recording and swallowable capsule technology. However, for other applications, it would encounter a problematic issue in the system design. For

example, the inductive coils used in wireless power transfer systems are usually much bigger than the split ring resonators, typically their radius is in the order of hundreds of millimetres to a few meters. For the model to be relevant for this typical application, the insulating cavities would be enormous because the model provides its best accuracy when the radius of the box is at least three times larger than the coil radius. Thus, the box would occupy so much space as well as become very expensive and impractical. A possible solution for this problem is to introduce a correction factor as a function of the radius of the insulators to rectify the complex terms.

$$\begin{cases} \mathcal{L} = \alpha_{\mathcal{L}} \mathcal{L}_0 \\ \mathcal{M} = \alpha_{\mathcal{M}} \mathcal{M}_0 \end{cases} \tag{7.1}$$

where $\mathcal{L}_0$ and $\mathcal{M}_0$ are the complex Kirchhoff coefficients calculated from the model developed in this thesis, $\alpha_{\mathcal{L}}$ and $\alpha_{\mathcal{M}}$ are the correction factors for those coefficients, and $\lim_{R\to\infty} \alpha_{\mathcal{L}} = 1$ and $\lim_{R\to\infty} \alpha_{\mathcal{M}} = 1$ where R is the radius of the insulators. It is suggested that the correction factors may be found through empirical methods with the aid of machine learning.

In addition, from the theoretical point of view, the assumption above presents another challenging problem when the vertical distance between coils is very small, especially when the two coils are in a coplanar configuration. The approach of replacing the dielectric cavities by infinitely wide layers will fail to describe the electromagnetic field of the system because two layers of dielectric overlap each other in the theoretical model. The boundary value problem therefore becomes: two layers of a dissipative material sandwiches a dielectric region containing two coupled coils. It would cause a significant inaccuracy in the prediction of complex coefficients.

If these two problems can be tackled, the general circuit model for two low-frequency inductive circuits inside an arbitrary medium will be completed. Then, various practical application of MI waves in the field of sensing, imaging, cloaking, and wireless power and data transfer, to name but a few, can be studied, analysed and optimized according to the theoretical model.

7.2.2 Possible Applications

Chapter 5 discussed the applicability of the novel equivalent circuit model to the field of wireless power transfer in harsh environments. It is pointed out that the model for free space case should not be applied for systems operating in attenuating media. With a better equivalent circuit model proposed in this thesis, there is a need to reinvestigate the analysis and design for WPT systems inside those environments. In particular, with the effects of eddy currents, the input impedance is always complex even at the resonant frequency. The conjugate matching, which is not considered in this thesis should be studied. In addition, to increase the transmission range of the system in those media, relaying-coil arrangements have been widely proposed. Interestingly, such relaying-coil arrays are identical to the structure of MI waveguides. In Chapter 6, the dispersion equation of MI waves has been generalised for the case when the whole waveguide is embedded in a non-conventional media. The wireless power transfer mechanism therefore can be discussed from the perspective of wave propagation [49, 50].

Appendices

A

Field Solutions for a Coil above an Infinitely Wide Slab

To solve (2.5), the mathematical method is as follows. Since filamentary coils are considered, the total driving current in the transmitting coil is taken as:

$$I = \frac{J_0}{\delta(\rho - r_1)\delta(z - z_1)} \tag{A.1}$$

where r_1 and z_1 is the radius and axial coordinate of the transmitting coil respectively, $\delta(x)$ is the delta function of variable x. A sinusoidal function of time e^{jwt} is applied to all variables. Taking the Fourier transform of (2.5), the general differential equation of the magnetic vector potential can be written in the frequency domain:

$$\frac{\partial^2 A_\varphi^{(n)}}{\partial z^2} + \frac{\partial^2 A_\varphi^{(n)}}{\partial \rho^2} + \frac{1}{\rho}\frac{\partial A_\varphi^{(n)}}{\partial \rho} - \frac{A_\varphi^{(n)}}{\rho^2} - j\omega\mu^{(n)}\sigma^{(n)}A_\varphi^{(n)} + \omega^2\mu^{(n)}\epsilon^{(n)}A_\varphi^{(n)} = -\mu_0 I\delta(\rho - r_0)\delta(z - z_0) \tag{A.2}$$

where $A_\varphi^{(n)}$ is the vector potential in the n-th region, which only depends on the cylindrical coordinates ρ and z due to the symmetry assumption, $\omega = 2\pi f$ is the transformed variable of time t, f is the working frequency. The partial differential equation (A.2) can be solved with the separation of variables method [71]. The magnetic vector potential in each region is expressed in the general form:

$$A_\varphi^{(n)}(\rho, z, \omega) = \int_0^\infty \left(X^{(n)}e^{-\alpha_n z} + Y^{(n)}e^{\alpha_n z}\right) \mathrm{J}_1(\alpha\rho)\,\mathrm{d}\alpha \tag{A.3}$$

where $X^{(n)}$ and $Y^{(n)}$ are functions of the separation constant α, J_1 is the Bessel function of the first kind and the first order, and $\alpha_n = \sqrt{\alpha + j\omega\mu^{(n)}\sigma^{(n)} - \omega^2\mu^{(n)}\epsilon^{(n)}}$. In general, $X^{(n)}$ and $Y^{(n)}$ are found by solving (A.3) subject to the boundary conditions shown below:

$$A_\varphi^{(n)}(\rho, z, \omega)\Big|_{z=z^{n\to n+1}} = A_\varphi^{(n+1)}(\rho, z, \omega)\Big|_{z=z^{n\to n+1}} \tag{A.4}$$

$$\frac{\partial A_\varphi^{(n)}(\rho, z, \omega)}{\partial z}\bigg|_{z=z^{n\to n+1}} = \frac{\partial A_\varphi^{(n+1)}(\rho, z, \omega)}{\partial z}\bigg|_{z=z^{n\to n+1}} \tag{A.5}$$

$$z^{n\to n+1} = \begin{cases} h, & \text{for interface } \textbf{I-II}, \\ 0, & \text{for interface } \textbf{II-III}, \\ -c, & \text{for interface } \textbf{III-IV}. \end{cases} \tag{A.6}$$

where $z^{n\to n+1}$ is the location of the interface between consecutive zones n and $n+1$. In particular, $Y^{\mathbf{I}} = 0$ and $X^{\mathbf{IV}} = 0$ to ensure the vanishing of the vector magnetic potential in regions (**I**) and (**IV**) when z goes to plus and minus infinity, respectively, and $X^{(\mathbf{I})}, X^{(\mathbf{II})}, ..., Y^{(\mathbf{III})}$ and $Y^{(\mathbf{IV})}$ are solutions of the system of 6 linear equations (A.7) derived from the boundary conditions (A.4) – (A.6), ensuring the continuity for the electric and magnetic field components at the layer interfaces.

$$\begin{cases} X^{(\mathbf{I})}\, e^{-\alpha_{\mathbf{I}}(h)} - X^{(\mathbf{II})}\, e^{-\alpha_{\mathbf{I}}(h)} - Y^{(\mathbf{II})}\, e^{\alpha_{\mathbf{I}}(h)} &= 0 \\ X^{(\mathbf{I})}\, \alpha_{\mathbf{I}} e^{-\alpha_{\mathbf{I}}(h)} - X^{(\mathbf{II})}\, \alpha_{\mathbf{I}} e^{-\alpha_{\mathbf{I}}(h)} + Y^{(\mathbf{II})}\, \alpha_{\mathbf{I}} e^{\alpha_{\mathbf{I}}(h)} &= \alpha\, \mu_0\, I\, r_0\, \mathrm{J}(\alpha r_0) \\ X^{(\mathbf{II})} + Y^{(\mathbf{II})} - X^{(\mathbf{III})} - Y^{(\mathbf{III})} &= 0 \\ X^{(\mathbf{II})}\, \alpha_{\mathbf{I}} + Y^{(\mathbf{II})}\, \alpha_{\mathbf{I}} - X^{(\mathbf{III})}\, \alpha_{\mathbf{III}} - Y^{(\mathbf{III})}\, \alpha_{\mathbf{III}} &= 0 \\ X^{(\mathbf{III})}\, e^{-\alpha_{\mathbf{III}}(-c)} + Y^{(\mathbf{III})}\, e^{\alpha_{\mathbf{I}}(-c)} - Y^{(\mathbf{IV})}\, e^{\alpha_{\mathbf{I}}(-c)} &= 0 \\ X^{(\mathbf{III})}\, \alpha_{\mathbf{III}} e^{-\alpha_{\mathbf{III}}(-c)} - Y^{(\mathbf{III})}\, \alpha_{\mathbf{III}} e^{\alpha_{\mathbf{I}}(-c)} + Y^{(\mathbf{IV})}\, \alpha_{\mathbf{III}} e^{\alpha_{\mathbf{I}}(-c)} &= 0 \end{cases} \tag{A.7}$$

By solving the system (A.7), the coefficients are obtained as follows:

$$\begin{cases} X^{\mathbf{I}} &= \alpha\,\mu_0\,I\,r_0\,\mathrm{J}_1(\alpha r_0)\left[\dfrac{e^{\alpha_{\mathbf{I}}h}}{2\alpha_{\mathbf{I}}}+\dfrac{e^{-\alpha_{\mathbf{I}}h}}{2\alpha_{\mathbf{I}}}\dfrac{(\alpha_{\mathbf{I}}+\alpha_{\mathbf{III}})(\alpha_{\mathbf{I}}-\alpha_{\mathbf{III}})(e^{2\alpha_{\mathbf{III}}c}-1)}{(\alpha_{\mathbf{I}}+\alpha_{\mathbf{III}})^2e^{2\alpha_{\mathbf{III}}c}-(\alpha_{\mathbf{I}}-\alpha_{\mathbf{III}})^2}\right] \\ X^{\mathbf{II}} &= \alpha\,\mu_0\,I\,r_0\,\mathrm{J}_1(\alpha r_0)\dfrac{e^{-\alpha_{\mathbf{I}}h}}{2\alpha_{\mathbf{I}}}\dfrac{(\alpha_{\mathbf{I}}+\alpha_{\mathbf{III}})(\alpha_{\mathbf{I}}-\alpha_{\mathbf{III}})(e^{2\alpha_{\mathbf{III}}c}-1)}{(\alpha_{\mathbf{I}}+\alpha_{\mathbf{III}})^2e^{2\alpha_{\mathbf{III}}c}-(\alpha_{\mathbf{I}}-\alpha_{\mathbf{III}})^2} \\ Y^{\mathbf{II}} &= \alpha\,\mu_0\,I\,r_0\,\mathrm{J}_1(\alpha r_0)\dfrac{e^{-\alpha_{\mathbf{I}}h}}{2\alpha_{\mathbf{I}}} \\ X^{\mathbf{III}} &= \alpha\,\mu_0\,I\,r_0\,\mathrm{J}_1(\alpha r_0)\dfrac{-(\alpha_{\mathbf{I}}-\alpha_{\mathbf{III}})e^{-\alpha_{\mathbf{I}}h}}{(\alpha_{\mathbf{I}}+\alpha_{\mathbf{III}})^2e^{2\alpha_{\mathbf{III}}c}-(\alpha_{\mathbf{I}}-\alpha_{\mathbf{III}})^2} \\ Y_{\mathbf{III}} &= \alpha\,\mu_0\,I\,r_0\,\mathrm{J}_1(\alpha r_0)\dfrac{-(\alpha_{\mathbf{I}}+\alpha_{\mathbf{III}})e^{-\alpha_{\mathbf{I}}h+2\alpha_{\mathbf{III}}c}}{(\alpha_{\mathbf{I}}+\alpha_{\mathbf{III}})^2e^{2\alpha_{\mathbf{III}}c}-(\alpha_{\mathbf{I}}-\alpha_{\mathbf{III}})^2} \\ Y_{\mathbf{IV}} &= \alpha\,\mu_0\,I\,r_0\,\mathrm{J}_1(\alpha r_0)\dfrac{2\alpha_{\mathbf{III}}e^{\alpha_{\mathbf{I}}(c-h)}e^{\alpha_{\mathbf{III}}c}}{(\alpha_{\mathbf{I}}+\alpha_{\mathbf{III}})^2e^{2\alpha_{\mathbf{III}}c}-(\alpha_{\mathbf{I}}-\alpha_{\mathbf{III}})^2} \end{cases} \tag{A.8}$$

Substituting (A.8) into (A.3), the analytical solution for the magnetic vector potential of a coil above an infinitely wide conducting slab over all space regions is then expressed by:

$$\begin{aligned} A_\varphi^{(n)}(\rho,z,\omega) &= \int_0^\infty \left(X^{(n)}e^{-\alpha_n z}+Y^{(n)}e^{\alpha_n z}\right)\mathrm{J}_1(\alpha\rho)\,\mathrm{d}\alpha \\ &= \mu_0\,I\,r_0\int_0^\infty \alpha\,\mathrm{J}_1(\alpha r_0)\,\mathrm{J}_1(\alpha\rho)\,F^{(n)}(z,\omega)\,\mathrm{d}\alpha \end{aligned} \tag{A.9}$$

where $F^{(n)}(z,\omega)$ is the spectral function for each region:

$$\begin{cases} F^{(\mathbf{I})}(z,\omega) &= \dfrac{e^{-\alpha_{\mathbf{I}}(z-h)}}{2\alpha_{\mathbf{I}}}+\dfrac{e^{-\alpha_{\mathbf{I}}(z+h)}}{2\alpha_{\mathbf{I}}}\dfrac{(\alpha_{\mathbf{I}}+\alpha_{\mathbf{III}})(\alpha_{\mathbf{I}}-\alpha_{\mathbf{III}})(e^{2\alpha_{\mathbf{III}}c}-1)}{(\alpha_{\mathbf{I}}+\alpha_{\mathbf{III}})^2e^{2\alpha_{\mathbf{III}}c}-(\alpha_{\mathbf{I}}-\alpha_{\mathbf{III}})^2} \\ F^{(\mathbf{I})}(z,\omega) &= \dfrac{e^{\alpha_{\mathbf{I}}(z-h)}}{2\alpha_{\mathbf{I}}}+\dfrac{e^{-\alpha_{\mathbf{I}}(z+h)}}{2\alpha_{\mathbf{I}}}\dfrac{(\alpha_{\mathbf{I}}+\alpha_{\mathbf{III}})(\alpha_{\mathbf{I}}-\alpha_{\mathbf{III}})(e^{2\alpha_{\mathbf{III}}c}-1)}{(\alpha_{\mathbf{I}}+\alpha_{\mathbf{III}})^2e^{2\alpha_{\mathbf{III}}c}-(\alpha_{\mathbf{I}}-\alpha_{\mathbf{III}})^2} \\ F^{(\mathbf{III})}(z,\omega) &= \dfrac{\left[(\alpha_{\mathbf{I}}+\alpha_{\mathbf{III}})e^{2\alpha_{\mathbf{III}}(z+c)}-(\alpha_{\mathbf{I}}-\alpha_{\mathbf{III}})\right]e^{-\alpha_{\mathbf{I}}h-\alpha_{\mathbf{III}}z}}{(\alpha_{\mathbf{I}}+\alpha_{\mathbf{III}})^2e^{2\alpha_{\mathbf{III}}c}-(\alpha_{\mathbf{I}}-\alpha_{\mathbf{III}})^2} \\ F^{(\mathbf{IV})}(z,\omega) &= \dfrac{2\alpha_{\mathbf{III}}e^{\alpha_{\mathbf{I}}(z+c-h)}e^{\alpha_{\mathbf{III}}c}}{(\alpha_{\mathbf{I}}+\alpha_{\mathbf{III}})^2e^{2\alpha_{\mathbf{III}}c}-(\alpha_{\mathbf{I}}-\alpha_{\mathbf{III}})^2} \end{cases} \tag{A.10}$$

B

Field Solutions for a Coil inside a Dissipative Medium

B.1 Transmitting coil problem

To solve (3.4), the mathematical method is as follows. The magnetic vector potential produced by a Dirac-coil (an infinitely thin coil with infinite conductivity) of radius r, is calculated in terms of an infinite integral of Bessel functions [106]:

$$\mathbf{\Psi}_{\boldsymbol{\delta}}(\rho, z, t) = i(t)\frac{\mu}{2}\int_0^\infty r\, \mathrm{J}_1(\alpha r)\, \mathrm{J}_1(\alpha\rho)\, e^{-\alpha|z-z'|}\, \mathrm{d}\alpha \tag{B.1}$$

where α is the separation constant, and J_x is the Bessel function of the first kind and the x-th order. By substituting $i(t)$ for $\delta(t)$ and taking the integral sum of all the Dirac-delta contributions over the volume of the coil 1 and then by multiplying the term by its appropriate turn density, the time-dependent unit impulse response of coil 1 can be determined as:

$$\widehat{\Psi}_1(\rho, z, t) = \frac{\mu^{(\mathbf{II})}\, \delta(t)\, N_1}{2\, w_1\, l_1}\int_0^\infty \int_{r_1-w_1/2}^{r_1+w_1/2} \int_{(-h_1-l_1)}^{(-h_1)} r\, \mathrm{J}_1(\alpha r)\, \mathrm{J}_1(\alpha\rho)\, e^{-\alpha|z-z'|}\, \mathrm{d}\alpha\, \mathrm{d}r\, \mathrm{d}z' \tag{B.2}$$

where r_1, l_1, w_1 and N_1 are the mean radius, thickness, width and number of turns of the coil 1 respectively, and $2h_1 + l_1$ is the height of the insulating cavity of coil 1. Taking the Fourier Transform in t and Hankel Transform in ρ, the unit impulse

response of coils can be rewritten in frequency domain and α-space:

$$\widehat{\Psi}_1(\alpha, z, \omega) = \frac{\mu^{(\mathbf{II})}\, N_1}{2\,\alpha\, w_1\, l_1} \int_{r_1 - w_1/2}^{r_1 + w_1/2} \int_{(-h_1 - l_1)}^{(-h_1)} r\, \mathrm{J}_1(\alpha r)\; e^{-\alpha |z - z'|}\, \mathrm{d}r\, \mathrm{d}z' \tag{B.3}$$

where ω and α are the transformed variables of t and ρ, respectively. Next, the unit impulse response induced by eddy currents in n-th region, $\widehat{E}_1^{(n)}(r, z, t)$, is derived from the field solutions:

$$\left(\frac{\partial^2}{\partial z^2} + \frac{\partial^2}{\partial r^2} + \frac{1}{\rho}\frac{\partial}{\partial \rho} - \frac{1}{\rho^2}\right) \widehat{E}_1^{(n)}(\rho, z, t) = \left(\mu^{(n)}\sigma^{(n)}\frac{\mathrm{d}}{\mathrm{d}\,t} + \mu^{(n)}\epsilon^{(n)}\frac{\mathrm{d}^2}{\mathrm{d}\,t^2}\right) \widehat{E}_1^{(n)}(\rho, z, t) \tag{B.4}$$

Applying the Fourier Transform and Hankel Transform,

$$\frac{\partial^2}{\partial z^2}\widehat{E}_1^{(n)}(\alpha, z, \omega) = \left(\alpha^2 + j\omega\mu^{(n)}\sigma^{(n)} - \omega^2\mu^{(n)}\epsilon^{(n)}\right) \widehat{E}_1^{(n)}(\alpha, z, \omega) \tag{B.5}$$

The solutions of equation (B.5) can be expressed in the general form:

$$\widehat{E}_1^{(n)}(\alpha, z, \omega) = X_1^{(n)}(\alpha, \omega)\, e^{\alpha_n z} + Y_1^{(n)}(\alpha, \omega)\, e^{-\alpha_n z} \tag{B.6}$$

where $\alpha^{(n)} = \sqrt{\alpha^2 + j\omega\mu^{(n)}\sigma^{(n)} - \omega^2\mu^{(n)}\epsilon^{(n)}}$ is the separation constant in the n-th zone, and $X_1^{(n)}(\alpha, \omega)$ and $Y_1^{(n)}(\alpha, \omega)$ are unknown constants. In this particular configuration, cf. Fig. 3.2, $\alpha^{(\mathbf{II})} = \alpha^{(\mathbf{IV})} = \sqrt{\alpha^2 - \omega^2\mu^{(\mathbf{II})}\epsilon^{(\mathbf{II})}}$ and $\alpha^{(\mathbf{I})} = \alpha^{(\mathbf{III})} = \alpha^{(\mathbf{V})} = \sqrt{\alpha^2 + j\omega\mu^{(\mathbf{I})}\sigma^{(\mathbf{I})} - \omega^2\mu^{(\mathbf{I})}\epsilon^{(\mathbf{I})}}$. Finally, the solutions for MVPIR for coil 1 problem in each region are expressed as in 3.5.

The boundary conditions (3.6) – (3.8) ensure the continuity of the electromagnetic fields across layer interfaces of the configuration shown in Fig. 3.2. By expanding those equations, the unknown coefficients $X_1^{(n)}$ and $Y_1^{(n)}$ for the transmitting coil problem are the solutions of the system of 8 linear equations below:

$$
\begin{cases}
\widehat{\Psi}_1(\alpha, z^{\mathbf{I}\to\mathbf{II}}, \omega) &= X_1^{(\mathbf{I})}\, e^{\alpha_1 z^{\mathbf{I}\to\mathbf{II}}} \\
&\quad - \left[X_1^{(\mathbf{II})}\, e^{\alpha_2 z^{\mathbf{I}\to\mathbf{II}}} + Y_1^{(\mathbf{II})}\, e^{-\alpha_2 z^{\mathbf{I}\to\mathbf{II}}}\right] \\
\dfrac{\alpha}{\mu_2}\widehat{\Psi}_1(\alpha, z^{\mathbf{I}\to\mathbf{II}}, \omega) &= \dfrac{1}{\mu_1} X_1^{(\mathbf{I})}\, \alpha_1\, e^{\alpha_1 z^{\mathbf{I}\to\mathbf{II}}} \\
&\quad - \dfrac{1}{\mu_2}\left[X_1^{(\mathbf{II})}\, \alpha_2\, e^{\alpha_2 z^{\mathbf{I}\to\mathbf{II}}} - Y_1^{(\mathbf{II})}\, \alpha_2\, e^{-\alpha_2 z^{\mathbf{I}\to\mathbf{II}}}\right] \\
-\widehat{\Psi}_1(\alpha, z^{\mathbf{II}\to\mathbf{III}}, \omega) &= X_1^{(\mathbf{II})}\, e^{\alpha_2 z^{\mathbf{II}\to\mathbf{III}}} + Y_1^{(\mathbf{II})}\, e^{-\alpha_2 z^{\mathbf{II}\to\mathbf{III}}} \\
&\quad - \left[X_1^{(\mathbf{III})}\, e^{\alpha_1 z^{\mathbf{II}\to\mathbf{III}}} + Y_1^{(\mathbf{III})}\, e^{-\alpha_1 z^{\mathbf{II}\to\mathbf{III}}}\right] \\
\dfrac{\alpha}{\mu_2}\widehat{\Psi}_1(\alpha, z^{\mathbf{II}\to\mathbf{III}}, \omega) &= \dfrac{1}{\mu_2}\left[X_1^{(\mathbf{II})}\, \alpha_2\, e^{\alpha_2 z^{\mathbf{II}\to\mathbf{III}}} - Y_1^{(\mathbf{II})}\, \alpha_2\, e^{-\alpha_2 z^{\mathbf{II}\to\mathbf{III}}}\right] \\
&\quad - \dfrac{1}{\mu_1}\left[X_1^{(\mathbf{III})}\, \alpha_1\, e^{\alpha_1 z^{\mathbf{II}\to\mathbf{III}}} - Y_1^{(\mathbf{III})}\, \alpha_1\, e^{-\alpha_1 z^{\mathbf{II}\to\mathbf{III}}}\right] \\
0 &= X_1^{(\mathbf{III})}\, e^{\alpha_1 z^{\mathbf{III}\to\mathbf{IV}}} + Y_1^{(\mathbf{III})}\, e^{-\alpha_1 z^{\mathbf{III}\to\mathbf{IV}}} \\
&\quad - \left[X_1^{(\mathbf{IV})}\, e^{\alpha_2 z^{\mathbf{III}\to\mathbf{IV}}} + Y_1^{(\mathbf{IV})}\, e^{-\alpha_2 z^{\mathbf{III}\to\mathbf{IV}}}\right] \\
0 &= \dfrac{1}{\mu_1}\left[X_1^{(\mathbf{III})}\, \alpha_1\, e^{\alpha_1 z^{\mathbf{III}\to\mathbf{IV}}} - Y_1^{(\mathbf{III})}\, \alpha_1\, e^{-\alpha_1 z^{\mathbf{III}\to\mathbf{IV}}}\right] \\
&\quad - \dfrac{1}{\mu_2}\left[X_1^{(\mathbf{IV})}\, \alpha_2\, e^{\alpha_2 z^{\mathbf{III}\to\mathbf{IV}}} + Y_1^{(\mathbf{IV})}\, \alpha_2\, e^{-\alpha_2 z^{\mathbf{III}\to\mathbf{IV}}}\right] \\
0 &= X_1^{(\mathbf{IV})}\, e^{\alpha_2 z^{\mathbf{IV}\to\mathbf{V}}} + Y_1^{(\mathbf{IV})}\, e^{-\alpha_2 z^{\mathbf{IV}\to\mathbf{V}}} \\
&\quad - Y_1^{(\mathbf{V})}\, e^{-\alpha_1 z^{\mathbf{IV}\to\mathbf{V}}} \\
0 &= \dfrac{1}{\mu_2}\left[X_1^{(\mathbf{IV})}\, \alpha_2\, e^{\alpha_2 z^{\mathbf{IV}\to\mathbf{V}}} - Y_1^{(\mathbf{IV})}\, \alpha_2\, e^{-\alpha_2 z^{\mathbf{IV}\to\mathbf{V}}}\right] \\
&\quad - \dfrac{1}{\mu_1}\left[Y_1^{(\mathbf{V})}\, \alpha_1\, e^{-\alpha_1 z^{\mathbf{IV}\to\mathbf{V}}}\right]
\end{cases}
\tag{B.7}
$$

B.2 Receiving coil problem

By proceeding analogously, the unknown coefficients $X_2^{(n)}$ and $Y_2^{(n)}$ for the receiving coil problem are the solutions of the system of 8 linear equations below:

$$
\left\{
\begin{array}{lcl}
\widehat{\Psi}_2(\alpha, z^{\mathbf{I}\to\mathbf{II}}, \omega) & = & X_2^{(\mathbf{I})}\, e^{\alpha_1 z^{\mathbf{I}\to\mathbf{II}}} \\
 & & -\left[X_2^{(\mathbf{II})}\, e^{\alpha_2 z^{\mathbf{I}\to\mathbf{II}}} + Y_2^{(\mathbf{II})}\, e^{-\alpha_2 z^{\mathbf{I}\to\mathbf{II}}}\right] \\
\dfrac{\alpha}{\mu_2}\widehat{\Psi}_2(\alpha, z^{\mathbf{I}\to\mathbf{II}}, \omega) & = & \dfrac{1}{\mu_1} X_2^{(\mathbf{I})}\, \alpha_1\, e^{\alpha_1 z^{\mathbf{I}\to\mathbf{II}}} \\
 & & -\dfrac{1}{\mu_2}\left[X_2^{(\mathbf{II})}\, \alpha_2\, e^{\alpha_2 z^{\mathbf{I}\to\mathbf{II}}} - Y_2^{(\mathbf{II})}\, \alpha_2\, e^{-\alpha_2 z^{\mathbf{I}\to\mathbf{II}}}\right] \\
-\widehat{\Psi}_2(\alpha, z^{\mathbf{II}\to\mathbf{III}}, \omega) & = & X_2^{(\mathbf{II})}\, e^{\alpha_2 z^{\mathbf{II}\to\mathbf{III}}} + Y_2^{(\mathbf{II})}\, e^{-\alpha_2 z^{\mathbf{II}\to\mathbf{III}}} \\
 & & -\left[X_2^{(\mathbf{III})}\, e^{\alpha_1 z^{\mathbf{II}\to\mathbf{III}}} + Y_2^{(\mathbf{III})}\, e^{-\alpha_1 z^{\mathbf{II}\to\mathbf{III}}}\right] \\
\dfrac{\alpha}{\mu_2}\widehat{\Psi}_2(\alpha, z^{\mathbf{II}\to\mathbf{III}}, \omega) & = & \dfrac{1}{\mu_2}\left[X_2^{(\mathbf{II})}\, \alpha_2\, e^{\alpha_2 z^{\mathbf{II}\to\mathbf{III}}} - Y_2^{(\mathbf{II})}\, \alpha_2\, e^{-\alpha_2 z^{\mathbf{II}\to\mathbf{III}}}\right] \\
 & & -\dfrac{1}{\mu_1}\left[X_2^{(\mathbf{III})}\, \alpha_1\, e^{\alpha_1 z^{\mathbf{II}\to\mathbf{III}}} - Y_2^{(\mathbf{III})}\, \alpha_1\, e^{-\alpha_1 z^{\mathbf{II}\to\mathbf{III}}}\right] \\
0 & = & X_2^{(\mathbf{III})}\, e^{\alpha_1 z^{\mathbf{III}\to\mathbf{IV}}} + Y_2^{(\mathbf{III})}\, e^{-\alpha_1 z^{\mathbf{III}\to\mathbf{IV}}} \\
 & & -\left[X_2^{(\mathbf{IV})}\, e^{\alpha_2 z^{\mathbf{III}\to\mathbf{IV}}} + Y_2^{(\mathbf{IV})}\, e^{-\alpha_2 z^{\mathbf{III}\to\mathbf{IV}}}\right] \\
0 & = & \dfrac{1}{\mu_1}\left[X_2^{(\mathbf{III})}\, \alpha_1\, e^{\alpha_1 z^{\mathbf{III}\to\mathbf{IV}}} - Y_2^{(\mathbf{III})}\, \alpha_1\, e^{-\alpha_1 z^{\mathbf{III}\to\mathbf{IV}}}\right] \\
 & & -\dfrac{1}{\mu_2}\left[X_2^{(\mathbf{IV})}\, \alpha_2\, e^{\alpha_2 z^{\mathbf{III}\to\mathbf{IV}}} + Y_2^{(\mathbf{IV})}\, \alpha_2\, e^{-\alpha_2 z^{\mathbf{III}\to\mathbf{IV}}}\right] \\
0 & = & X_2^{(\mathbf{IV})}\, e^{\alpha_2 z^{\mathbf{IV}\to\mathbf{V}}} + Y_2^{(\mathbf{IV})}\, e^{-\alpha_2 z^{\mathbf{IV}\to\mathbf{V}}} \\
 & & -Y_2^{(\mathbf{V})}\, e^{-\alpha_1 z^{\mathbf{IV}\to\mathbf{V}}} \\
0 & = & \dfrac{1}{\mu_2}\left[X_2^{(\mathbf{IV})}\, \alpha_2\, e^{\alpha_2 z^{\mathbf{IV}\to\mathbf{V}}} - Y_2^{(\mathbf{IV})}\, \alpha_2\, e^{-\alpha_2 z^{\mathbf{IV}\to\mathbf{V}}}\right] \\
 & & -\dfrac{1}{\mu_1}\left[Y_2^{(\mathbf{V})}\, \alpha_1\, e^{-\alpha_1 z^{\mathbf{IV}\to\mathbf{V}}}\right]
\end{array}
\right. \tag{B.8}
$$

C
Lorentzian Fit

This appendix describes the Lorentzian fit used to determine the resonant frequency and Q-factor of the coils in section 6.3.1. The complex transmission coefficient of two weakly-coupling magnetic probes via a nearby microwave resonators is given by [136]:

$$S_{21}(f) = \frac{S_{21(max)}}{1 + jQ\left(\frac{f}{f_0} - \frac{f_0}{f}\right)} \tag{C.1}$$

where $S_{21(max)}$ is the maximum transmission coefficient which arises at the resonant frequency, f_0 and Q are the resonant frequency and Q-factor of the circuit respectively, and f is the frequency. Near the resonant peak, the variable frequency f can be approximated as f_0, simplifying the frequency dependence of the denominator of in the left-hand side of (C.1):

$$S_{21}(f) = \frac{S_{21(max)}}{1 + j2Q\left(\frac{f}{f_0} - 1\right)} \tag{C.2}$$

The magnitude of the complex transmission coefficient is then calculated by:

$$|S_{21}(f)| = \frac{|S_{21(max)}|}{\sqrt{1 + 4Q^2\left(\frac{f}{f_0} - 1\right)^2}} \tag{C.3}$$

For Lorentzian fitting method, the modulus of the measured S_{21} as a function of frequency is fit to a distribution using a nonlinear least-squares analysis. The Lorentzian distribution are expressed by:

$$|S_{21,fitting}(f)| = A_1 + A_2 f + \frac{|S_{(max)}| + A_3 f}{\sqrt{1 + \left(\frac{f - f_0}{\Delta f_{Lorent}}\right)^2}} \tag{C.4}$$

where the fitting parameters are as follows: f_0 is the resonant frequency, Δf_{Lorent} is the bandwidth, $|S_{max}|$ is the maximum magnitude, A_1 is the constant background, A_2 is the slope on the background, and A_3 is the skew. The Q-factor is then determined using the fitting parameters f_0 and Δf_{Lorent}:

$$Q = \frac{f_0}{\Delta f_{Lorent}} \tag{C.5}$$

D

Retrieving Dispersion Constants from Experimental Data

Recall from Section 6.3.2 that the ratios u, v, and w are expressed as:

$$\begin{cases} u = (S_{21|n+1} + S_{21|n-1})/(2S_{21|n}) \\ v = (S_{21|n+2} + S_{21|n-2})/(2S_{21|n}) \\ w = (S_{21|n+3} + S_{21|n-3})/(2S_{21|n}) \end{cases} \tag{D.1}$$

Substituting (6.7) into (D.1), the ratios of transfer functions in seven neighbour elements are rewritten as:

$$\begin{cases} u = \dfrac{\left(a_1 e^{-n\gamma_1 d} + b_1 e^{n\gamma_1 d}\right)\cosh(\gamma_1 d) + \left(a_2 e^{-n\gamma_2 d} + b_1 e^{n\gamma_2 d}\right)\cosh(\gamma_1 d)}{(a_1 e^{-n\gamma_2 d} + b_1 e^{n\gamma_1 d}) + (a_2 e^{-n\gamma_2 d} + b_1 e^{n\gamma_2 d})} \\ v = \dfrac{\left(a_1 e^{-n\gamma_1 d} + b_1 e^{n\gamma_1 d}\right)\cosh(2\gamma_2 d) + \left(a_2 e^{-n\gamma_2 d} + b_1 e^{n\gamma_2 d}\right)\cosh(2\gamma_1 d)}{(a_1 e^{-n\gamma_1 d} + b_1 e^{n\gamma_1 d}) + (a_2 e^{-n\gamma_2 d} + b_1 e^{n\gamma_2 d})} \\ w = \dfrac{\left(a_1 e^{-n\gamma_1 d} + b_1 e^{n\gamma_1 d}\right)\cosh(3\gamma_2 d) + \left(a_2 e^{-n\gamma_2 d} + b_1 e^{n\gamma_2 d}\right)\cosh(3\gamma_1 d)}{(a_1 e^{-n\gamma_1 d} + b_1 e^{n\gamma_1 d}) + (a_2 e^{-n\gamma_2 d} + b_1 e^{n\gamma_2 d})} \end{cases} \tag{D.2}$$

Using trigonometry expansion and deriving the system of non-linear equations (D.2) with respect to the sum and multiplication of $\cosh(\gamma_1 d)$ and $\cosh(\gamma_2 d)$, the relationship between them is determined as:

$$\begin{cases} u\left[\cosh(\gamma_1 d) + \cosh(\gamma_2 d)\right] - \cosh(\gamma_1 d)\cosh(\gamma_2 d) = \dfrac{1}{2}(v+1) \\ u\left\{\left[\cosh(\gamma_1 d) + \cosh(\gamma_2 d)\right]^2 - \cosh(\gamma_1 d)\cosh(\gamma_2 d)\right\} \\ \quad - \left[\cosh(\gamma_1 d) + \cosh(\gamma_2 d)\right]\cosh(\gamma_1 d)\cosh(\gamma_2 d) = \dfrac{1}{4}(w+3u) \end{cases} \tag{D.3}$$

Therefore,

$$\begin{cases} cosh(\gamma_1 d) + \cosh(\gamma_2 d) = \dfrac{2uv - u - w}{2(2u^2 - v - 1)} \\ \cosh(\gamma_1 d)\cosh(\gamma_2 d) = \dfrac{(v+1)^2 - u(3u + w)}{2(2u^2 - v - 1)} \end{cases} \tag{D.4}$$

Finally, solving the system (D.4), $\cosh(\gamma_1 d)$ and $\cosh(\gamma_2 d)$ can be calculated as in (6.8)

References

[1] D. R. Smith, J. B. Pendry, and M. C. K. Wiltshire. "Metamaterials and Negative Refractive Index". In: *Science* 305.5685 (2004), pp. 788–792.

[2] J. B. Pendry, D. Schurig, and D. R. Smith. "Controlling electromagnetic fields". In: *Science* 312.5781 (2006), pp. 1780–1782.

[3] N. Engheta and R. W. Ziolkowski. *Metamaterials: Physics and Egineering Explorations*. John Wiley & Sons, 2006.

[4] L. Solymar and E. Shamonina. *Waves in Metamaterials*. Oxford University Press, 2009.

[5] W. H. Bragg and W. L. Bragg. "The reflection of X-rays by crystals". In: *Proc. R. Soc. Lond. A* 88.605 (1913), pp. 428–438.

[6] P. B. Johnson and R. W. Christy. "Optical constants of the noble metals". In: *Phys. Rev. B* 6.12 (1972), pp. 4370–4379.

[7] R. X. Wu. "Effective negative refraction index in periodic metal–ferrite–metal film composite". In: *J. Appl. Phys.* 97.7 (2005), pp. 076105-1–076105-4.

[8] K. M. Ho, C. T. Chan, and C. M. Soukoulis. "Existence of a photonic gap in periodic dielectric structures". In: *Phys. Rev. Lett.* 65.25 (1990), pp. 3152–3155.

[9] E. Yablonovitch. "Photonic band-gap structures". In: *J. Opt. Soc. Am. B* 10.2 (1993), pp. 283–295.

[10] J. D. Joannopoulos, P. R. Villeneuve, S. Fan, et al. "Photonic crystals: putting a new twist on light". In: *Nature* 386.6621 (1997), pp. 143–149.

[11] V. G. Veselago. "The electrodynamics of substances with simultaneously negative values of ϵ and μ". In: *Phys. Usp* 10.4 (1968), pp. 509–514.

[12] J. B. Pendry et al. "Extremely low frequency plasmons in metallic mesostructures". In: *Phys. Rev. Lett.* 76.25 (1996), pp. 4773–4776.

[13] J. B. Pendry et al. "Magnetism from conductors and enhanced nonlinear phenomena". In: *IEEE Trans. Microw. Theory Tech.* 47.11 (1999), pp. 2075–2084.

[14] D. R. Smith et al. "Composite medium with simultaneously negative permeability and permittivity". In: *Phys. Rev. Lett.* 84.18 (2000), pp. 4184–4187.

[15] R. A. Shelby, D. R. Smith, and S. Schultz. "Experimental verification of a negative index of refraction". In: *Science* 292.5514 (2001), pp. 77–79.

[16] J. B. Pendry. "Negative refraction makes a perfect lens". In: *Phys. Rev. Lett.* 85.18 (2000), pp. 3966–3969.

[17] N. Fang et al. "Sub–diffraction-limited optical imaging with a silver superlens". In: *Science* 308.5721 (2005), pp. 534–537.

[18] D. Schurig et al. “Metamaterial electromagnetic cloak at microwave frequencies”. In: *Science* 314.5801 (2006), pp. 977–980.

[19] W. Cai et al. “Optical cloaking with metamaterials”. In: *Nat. Photon.* 1.4 (2007), pp. 224–227.

[20] C. Caloz, T. Itoh, and A. Rennings. “CRLH metamaterial leaky-wave and resonant antennas”. In: *IEEE Antennas Propag. Mag.* 50.5 (2008), pp. 25–39.

[21] M. C. Johnson et al. “Sidelobe canceling for reconfigurable holographic metamaterial antenna”. In: *IEEE Trans. Antennas Propag.* 63.4 (2015), pp. 1881–1886.

[22] N. I. Landy et al. “Perfect metamaterial absorber”. In: *Phys. Rev. Lett.* 100.20 (2008), pp. 207402-1–207402-4.

[23] M. C. Tran et al. “Controlled defect based ultra broadband full-sized metamaterial absorber”. In: *Sci. Rep.* 8.1 (2018), pp. 1–9.

[24] A. Kurs et al. “Wireless power transfer via strongly coupled magnetic resonances”. In: *Science* 317.5834 (2007), pp. 83–86.

[25] G. Lipworth et al. “Magnetic metamaterial superlens for increased range wireless power transfer”. In: *Sci. Rep.* 4 (2014), pp. 1–6.

[26] M. J. Freire, R. Marques, and L. Jelinek. “Experimental demonstration of a μ=- 1 metamaterial lens for magnetic resonance imaging”. In: *Appl. Phys. Lett.* 93.23 (2008), pp. 231108-1–231108-3.

[27] Z. Geng et al. “A route to terahertz metamaterial biosensor integrated with microfluidics for liver cancer biomarker testing in early stage”. In: *Sci. Rep.* 7.1 (2017), pp. 1–11.

[28] J. S. Hong. “Couplings of asynchronously tuned coupled microwave resonators”. In: *IEE Proc.-Microw. Antennas Propag.* 147.5 (2000), pp. 354–358.

[29] F. Hesmer et al. “Coupling mechanisms for split ring resonators: Theory and experiment”. In: *Phys. Status Solidi B* 244.4 (2007), pp. 1170–1175.

[30] V. Lomanets et al. “Electrical circuit model of arrays of resonant elements”. In: *Phys. Rev. B* 85.12 (2012), pp. 125110-1–125110-9.

[31] E. Tatartschuk et al. “Mapping inter-element coupling in metamaterials: Scaling down to infrared”. In: *J. Appl. Phys.* 111.9 (2012), pp. 094904-1–094904-9.

[32] E. Shamonina et al. “Magneto-inductive waveguide”. In: *Electron. Lett.* 38.8 (2002), pp. 371–373.

[33] M. Beruete et al. “Electroinductive waves in chains of complementary metamaterial elements”. In: *Appl. Phys. Lett.* 88.8 (2006), pp. 083503-1–083503-3.

[34] E. Shamonina. “Slow waves in magnetic metamaterials: History, fundamentals and applications”. In: *Phys. Status Solidi B* 245.8 (2008), pp. 1471–1482.

[35] M. C. K. Wiltshire et al. “Dispersion characteristics of magneto-inductive waves: comparison between theory and experiment”. In: *Electron. Lett.* 39.2 (2003), pp. 215–217.

[36] E. Shamonina et al. “Magnetoinductive waves in one, two, and three dimensions”. In: *J. Appl. Phys.* 92.10 (2002), pp. 6252–6261.

[37] E. Shamonina and L. Solymar. “Magneto-inductive waves supported by metamaterial elements: components for a one-dimensional waveguide”. In: *J. Phys. D* 37.3 (2004), pp. 362–367.

[38] O. Sydoruk et al. “Analytical formulation for the resonant frequency of split rings”. In: *J. Appl. Phys.* 105.1 (2009), pp. 014903-1–014903-4.

[39] L. D. Landau et al. *Electrodynamics of Continuous Media.* Vol. 8. Elsevier, 2013.

[40] P. A. Belov and C. R. Simovski. “Subwavelength metallic waveguides loaded by uniaxial resonant scatterers”. In: *Phys. Rev. E* 72.3 (2005), pp. 036618-1–036618-11.

[41] M. J. Freire and R. Marques. “Planar magnetoinductive lens for three-dimensional subwavelength imaging”. In: *Appl. Phys. Lett.* 86.18 (2005), pp. 182505-1–182505-3.

[42] O. Zhuromskyy, E. Shamonina, and L. Solymar. “2D metamaterials with hexagonal structure: spatial resonances and near field imaging”. In: *Opt. Express* 13.23 (2005), pp. 9299–9309.

[43] O. Sydoruk et al. “Mechanism of subwavelength imaging with bilayered magnetic metamaterials: Theory and experiment”. In: *J. Appl. Phys.* 101.7 (2007), pp. 073903-1–073903-8.

[44] M. J. Freire et al. “Planar magnetoinductive wave transducers: Theory and applications”. In: *Appl. Phys. Lett.* 85.19 (2004), pp. 4439–4441.

[45] I. S. Nefedov and S. A. Tretyakov. “On potential applications of metamaterials for the design of broadband phase shifters”. In: *Microw. Opt. Technol. Lett.* 45.2 (2005), pp. 98–102.

[46] R. R. A. Syms and L. Solymar. “Magneto-inductive phase-shifters and interferometers”. In: *Metamaterials* 5.4 (2011), pp. 155–161.

[47] C. J. Stevens et al. “Magnetic metamaterials as 1-D data transfer channels: an application for magneto-inductive waves”. In: *IEEE Trans. Microw. Theory Tech.* 58.5 (2010), pp. 1248–1256.

[48] C. W. T. Chan and C. J. Stevens. “Two-dimensional magneto-inductive wave data structures”. In: *Proc. the 5th European Conference on Antennas and Propagation (EUCAP).* 2011, pp. 1071–1075.

[49] C. J. Stevens. “A magneto-inductive wave wireless power transfer device”. In: *Wireless Power Transfer* 2.1 (2015), pp. 51–59.

[50] C. J. Stevens. “Magnetoinductive waves and wireless power transfer”. In: *IEEE Trans. Power Electron.* 30.11 (2015), pp. 6182–6190.

[51] Z. Sun and I. F. Akyildiz. “Magnetic induction communications for wireless underground sensor networks”. In: *IEEE Trans. Antennas Propag.* 58.7 (2010), pp. 2426–2435.

[52] M. C. Domingo. “Magnetic induction for underwater wireless communication networks”. In: *IEEE Trans. Antennas Propag.* 60.6 (2012), pp. 2929–2939.

[53] S. Movassaghi et al. “Wireless body area networks: A survey”. In: *IEEE Commun. Surv. Tutor.* 16.3 (2014), pp. 1658–1686.

[54] I. F. Akyildiz and E. P. Stuntebeck. “Wireless underground sensor networks: Research challenges”. In: *Ad Hoc Netw.* 4.6 (2006), pp. 669–686.

[55] H. G. Doll et al. “Introduction to induction logging and application to logging of wells drilled with oil base mud”. In: *J. Petroleum Technol.* 1.06 (1949), pp. 148–162.

[56] R. R. A. Syms et al. “Magnetic resonance imaging using linear magneto-inductive waveguides”. In: *J. Appl. Phys.* 112.11 (2012), pp. 114911-1–114911-7.

[57] M. Patel and J. Wang. “Applications, challenges, and prospective in emerging body area networking technologies”. In: *Wireless Commun.* 17.1 (2010), pp. 80–88.

[58] M. Seyedi et al. “A survey on intrabody communications for body area network applications”. In: *IEEE Trans. Biomed. Eng.* 60.8 (2013), pp. 2067–2079.

[59] K. Kalantar-Zadeh et al. “Intestinal gas capsules: a proof-of-concept demonstration”. In: *Gastroenterology* 150.1 (2016), pp. 37–39.

[60] D. Jordane et al. *Electromagnetic waves and radiating systems*. Prentice-Hall Of Lndia Private Limited; New Delhi, 1967.

[61] R. R. A. Syms et al. “Thin-film magneto-inductive cables”. In: *J. Phys. D* 43.5 (2010), pp. 1–7.

[62] A. Ahlbom et al. “Epidemiology of health effects of radiofrequency exposure”. In: *Environ. Health Perspect.* 112.17 (2004), pp. 1741–1754.

[63] I. Yakymenko et al. “Long-term exposure to microwave radiation provokes cancer growth: evidences from radars and mobile communication systems”. In: *Exp. Oncol.* 33.2 (2011), pp. 62–70.

[64] E. Cardis et al. “Risk of brain tumours in relation to estimated RF dose from mobile phones: results from five Interphone countries”. In: *Occup. Environ. Med.* 68.9 (2011), pp. 631–640.

[65] Z. Sun and I. F. Akyildiz. “Underground wireless communication using magnetic induction”. In: *Proc. IEEE International Conference on Communications (ICC)*. 2009, pp. 1–5.

[66] Z. Sun and I. F. Akyildiz. “Optimal deployment for magnetic induction-based wireless networks in challenged environments”. In: *IEEE Trans. Wireless Commun.* 12.3 (2013), pp. 996–1005.

[67] B. Gulbahar and O. B. Akan. “A communication theoretical modeling and analysis of underwater magneto-inductive wireless channels”. In: *IEEE Trans. Wireless Commun.* 11.9 (2012), pp. 3326–3334.

[68] Z. Sun et al. “Increasing the capacity of magnetic induction communications in RF-challenged environments”. In: *IEEE Trans. Commun.* 61.9 (2013), pp. 3943–3952.

[69] S. Kisseleff et al. “Channel capacity of magnetic induction based wireless underground sensor networks under practical constraints”. In: *Proc. 2013 IEEE Wireless Communications and Networking Conference (WCNC)*. 2013, pp. 2603–2608.

[70] J. Ma et al. “Experimental study on the impact of soil conductivity on underground magneto–inductive channel”. In: *IEEE Antennas Wirel. Propag. Lett.* 14 (2015), pp. 1782–1785.

[71] C. V. Dodd and W. E. Deeds. “Analytical Solutions to Eddy-Current Probe-Coil Problems”. In: *J. Appl. Phys* 39.6 (1968), pp. 2829–2838.

[72] J. C. Moulder, E. Uzal, and J. H. Rose. “Thickness and conductivity of metallic layers from eddy current measurements”. In: *Rev. Sci. Instrum.* 63.6 (1992), pp. 3455–3465.

[73] B. A. Auld and J. C. Moulder. “Review of advances in quantitative eddy current nondestructive evaluation”. In: *J. Nondestruct. Eval.* 18.1 (1999), pp. 3–36.

[74] Y. Li, T. Theodoulidis, and G. Y. Tian. “Magnetic field-based eddy-current modeling for multilayered specimens”. In: *IEEE Trans. Magn.* 43.11 (2007), pp. 4010–4015.

[75] A. Yin et al. “Physical interpretation and separation of eddy current pulsed thermography”. In: *J. Appl. Phys* 113.6 (2013), pp. 064101-1–064101-8.

[76] T. Wu, J. R. Bowler, and T. P. Theodoulidis. “Eddy-Current Induction by a Coil Whose Axis is Perpendicular to that of a Tube”. In: *IEEE Trans. on Magn.* 53.7 (2017), pp. 1–9.

[77] M. Lu et al. “Reducing the Lift-Off Effect on Permeability Measurement for Magnetic Plates From Multifrequency Induction Data”. In: *IEEE Trans. Instrum. Meas.* 67.1 (2018), pp. 167–174.

[78] J. Larsson. “Electromagnetics from a quasistatic perspective”. In: *American Journal of Physics* 75.3 (2007), pp. 230–239.

[79] G. J. Palacky. “Resistivity Characteristics of Geologic Targets”. In: *Electromagnetic Methods in Applied Geophysics*. 1988. Chap. 3, pp. 52–129.

[80] D. Miklavcic, N. Pavselj, and F. X. Hart. “Electric Properties of Tissues”. In: *Wiley Encyclopedia of Biomedical Engineering*. American Cancer Society, 2006.

[81] D. U. J. Keller et al. “Ranking the influence of tissue conductivities on forward-calculated ECGs”. In: *IEEE Trans. Biomed. Eng.* 57.7 (2010), pp. 1568–1576.

[82] D. J. Griffiths. *Introduction to Electrodynamics*. 4th. Pearson Education, 2014.

[83] Computer Simulation Technology AG. *CST – Computer Simulation Technology*. URL: `https://www.cst.com`.

[84] C. G. Malmberg and A. A. Maryott. “Dielectric constant of water from 0° to 100° C”. In: *J. Res. Nat. Bureau. Stand.* 56 (1956), pp. 1–8.

[85] V. Komarov, S. Wang, and J. Tang. “Permittivity and Measurements”. In: *Encyclopedia of RF and Microwave Engineering*. American Cancer Society, 2005.

[86] C. A. Balanis. *Antenna Theory: Analysis and Design*. 4th. Wiley, 2015.

[87] C. A. Balanis. *Advanced Engineering Electromagnetics*. John Wiley & Sons, 1999.

[88] T. H. Le, Y. Kim, and H. Yoon. “Electrical and electrochemical properties of conducting polymers”. In: *Polymers* 9.4 (2017), p. 150.

[89] Keysight Technologies Inc. *Advanced Design System (ADS)*. URL: https://www.keysight.com/gb/en/products/software/pathwave-design-software/pathwave-advanced-design-system.html.

[90] S. Kisseleff, I. F. Akyildiz, and W. H. Gerstacker. "Throughput of the magnetic induction based wireless underground sensor networks: Key optimization techniques". In: *IEEE Trans. Commun.* 62.12 (2014), pp. 4426–4439.

[91] S. Lin et al. "Distributed cross-layer protocol design for magnetic induction communication in wireless underground sensor networks". In: *IEEE Trans. Wirel. Commun.* 14.7 (2015), pp. 4006–4019.

[92] B. Gulbahar. "A communication theoretical analysis of multiple-access channel capacity in magneto-inductive wireless networks". In: *IEEE Trans. Commun.* 65.6 (2017), pp. 2594–2607.

[93] V. Kumar et al. "Design of magnetic induction based energy-efficient WSNs for nonconventional media using multilayer transmitter-enabled novel energy model". In: *IEEE Syst. J.* 13.2 (2019), pp. 1285–1296.

[94] C. T. Tai and R. E Collin. "Radiation of a Hertzian dipole immersed in a dissipative medium". In: *IEEE Trans. Antennas Propag.* 48.10 (2000 (reprinted)), pp. 1501–1506.

[95] J. R. Wait. "The magnetic dipole antenna immersed in a conducting medium". In: *Proceedings of the IRE* 40.10 (1952), pp. 1244–1245.

[96] R. James. "Insulated loop antenna immersed in a conducting medium". In: *J. Res. Natl. Bur. Stand.* 59.2 (1957), pp. 133–137.

[97] R Moore. "Effects of a surrounding conducting medium on antenna analysis". In: *IEEE Transactions on Antennas and Propagation* 11.3 (1963), pp. 216–225.

[98] G. S. Smith. "A theoretical and experimental study of the insulated loop antenna in a dissipative medium". In: *Radio Sci.* 8.7 (1973), pp. 711–725.

[99] R. W. P King. "Theory of the terminated insulated antenna in a conducting medium". In: *IEEE Trans. Antennas Propag.* 12.3 (1964), pp. 305–318.

[100] R. W. P. King et al. "Insulated linear antenna: Theory and experiment". In: *J. Appl. Phys.* 45.4 (1974), pp. 1688–1697.

[101] R. W. P Prasad S.King. "Experimental study of embedded insulated antennas". In: *IEEE Trans. Antennas Propag.* 30.5 (1982), pp. 1013–1017.

[102] R. W. P King, B. S. Trembly, and J. W. Strohbehn. "The electromagnetic field of an insulated antenna in a conducting or dielectric medium". In: *IEEE Trans. Microw. Theory Tech.* 31.7 (1983), pp. 574–583.

[103] M. S. Luloff et al. "Solution for a transmit-receive eddy current probe above a layered planar conductive structure". In: *NDT & E International* 96 (2018), pp. 1–8.

[104] D. R. Desjardins et al. "Concerning the derivation of exact solutions to inductive circuit problems for eddy current testing". In: *NDT & E Int.* 68 (2014), pp. 128–135.

[105] J. T. Conway. "Inductance calculations for noncoaxial coils using bessel functions". In: *IEEE Trans. Magn* 43.3 (2007), pp. 1023–1034.

[106] J. T. Conway. "Mutual Inductance for an Explicitly Finite Number of Turns". In: *Prog. Electromagn. Res. B* 28 (2011), pp. 273–287.

[107] H. McCann, G. Pisano, and L. Beltrachini. "Variation in reported human head tissue electrical conductivity values". In: *Brain Topogr.* 32.5 (2019), pp. 825–858.

[108] P. Yeon et al. "Fabrication and microassembly of a mm-sized floating probe for a distributed wireless neural interface". In: *Micromachines* 7.9 (2016), pp. 154–171.

[109] P. Feng et al. "Chip-scale coils for millimeter-sized bio-implants". In: *IEEE Trans. Biomed. Circuits Syst.* 12.5 (2018), pp. 1088–1099.

[110] T. Asada et al. "A study on basic characteristics of the proximity effect on conductors". In: *IEEE Trans. Power Del.* 32.4 (2017), pp. 1790–1799.

[111] D. H. Kim, J. Kim, and Y. J. Park. "Optimization and design of small circular coils in a magnetically coupled wireless power transfer system in the megahertz frequency". In: *IEEE Trans. Microw. Theory Techn.* 64.8 (2016), pp. 2652–2663.

[112] Z. Pantic and S. Lukic. "Computationally-efficient, generalized expressions for the proximity-effect in multi-layer, multi-turn tubular coils for wireless power transfer systems". In: *IEEE Trans. Magn.* 49.11 (2013), pp. 5404–5416.

[113] H. Igarashi. "Semi-analytical approach for finite-element analysis of multi-turn coil considering skin and proximity effects". In: *IEEE Trans. Magn.* 53.1 (2017), pp. 1–7.

[114] D. Ahn and S. Hong. "A study on magnetic field repeater in wireless power transfer". In: *IEEE Trans. Ind. Electron.* 60.1 (2012), pp. 360–371.

[115] X. Wei, Z. Wang, and H. Dai. "A critical review of wireless power transfer via strongly coupled magnetic resonances". In: *Energies* 7.7 (2014), pp. 4316–4341.

[116] J. S. Ho, S. Kim, and A. S. Poon. "Midfield wireless powering for implantable systems". In: *Proc. IEEE* 101.6 (2013), pp. 1369–1378.

[117] A. Ibrahim and M. Kiani. "A figure-of-merit for design and optimization of inductive power transmission links for millimeter-sized biomedical implants". In: *IEEE Trans. Biomed. Circuits Syst.* 10.6 (2016), pp. 1100–1111.

[118] M. R. Basar et al. "Stable and high-efficiency wireless power transfer system for robotic capsule using a modified Helmholtz coil". In: *IEEE Trans. Ind. Electron.* 64.2 (2017), pp. 1113–1122.

[119] J. Garnica, R. A. Chinga, and J. Lin. "Wireless power transmission: From far field to near field". In: *Proc. IEEE* 101.6 (2013), pp. 1321–1331.

[120] Zhen Zhang et al. "Wireless power transfer—An overview". In: *IEEE Trans. Ind. Electron.* 66.2 (2019), pp. 1044–1058.

[121] L. Sun, D. Ma, and H. Tang. "A review of recent trends in wireless power transfer technology and its applications in electric vehicle wireless charging". In: *Renew. Sustain. Energy Rev.* 91 (2018), pp. 490–503.

[122] A. P. Sample, D. T. Meyer, and J. R. Smith. "Analysis, experimental results, and range adaptation of magnetically coupled resonators for wireless power transfer". In: *IEEE Trans. Ind. Electron.* 58.2 (2010), pp. 544–554.

[123] Bingnan Wang, William Yerazunis, and Koon Hoo Teo. "Wireless power transfer: Metamaterials and array of coupled resonators". In: *Proc. IEEE* 101.6 (2013), pp. 1359–1368.

[124] D. Bululukova and M. Kramer. "Application of existing wireless power transfer standards in automotive applications". In: *Proc. 2014 International Conference on Connected Vehicles and Expo (ICCVE)*. 2014, pp. 863–864.

[125] T. Orekan, P. Zhang, and C. Shih. "Analysis, design, and maximum power-efficiency tracking for undersea wireless power transfer". In: *IEEE Trans. Emerg. Sel. Topics Power Electron.* 6.2 (2017), pp. 843–854.

[126] Z. Yan et al. "Frequency optimization of a loosely coupled underwater wireless power transfer system considering eddy current loss". In: *IEEE Trans. Ind. Electron.* 66.5 (2018), pp. 3468–3476.

[127] H. J. Kim et al. "Review of near-field wireless power and communication for biomedical applications". In: *IEEE Access* 5 (2017), pp. 21264–21285.

[128] W. Zhang and C. C. Mi. "Compensation topologies of high-power wireless power transfer systems". In: *IEEE Trans. Veh. Technol.* 65.6 (2016), pp. 4768–4778.

[129] W. X. Zhong and S. Y. R. Hui. "Maximum energy efficiency tracking for wireless power transfer systems". In: *IEEE Trans. Power Electron.* 30.7 (2014), pp. 4025–4034.

[130] A. Vallecchi, E. Shamonina, and C. J. Stevens. "Wireless power transfer in the presence of a conducting interface: Analytical solution". In: *IET Microw. Antenna Propag.* 13.6 (2019), pp. 725–731.

[131] *Commercial grade AC-DC power supplies*. URL: `https://unipowerco.com/product-industry/power-supplies-commercial-grade-ac-dc/`.

[132] R. Tseng et al. "Introduction to the alliance for wireless power loosely-coupled wireless power transfer system specification version 1.0". In: *Proc. 2013 IEEE Wireless Power Transfer (WPT)*. 2013, pp. 79–83.

[133] D. M. Pozar. *Microwave Engineering*. John Wiley & Sons, 2009.

[134] X. S. Pu et al. "Fault diagnosis of DC-link capacitors in three-phase AC/DC PWM converters by online estimation of equivalent series resistance". In: *IEEE Trans. Ind. Electron.* 60.9 (2012), pp. 4118–4127.

[135] O. Sydoruk et al. "Tailoring the near-field guiding properties of magnetic metamaterials with two resonant elements per unit cell". In: *Phys. Rev. B* 73.22 (2006), pp. 224406-1–224406-12.

[136] P. J. Petersan and S. M. Anlage. "Measurement of resonant frequency and quality factor of microwave resonators: Comparison of methods". In: *J. Appl. Phys.* 84.6 (1998), pp. 3392–3402.